



# **Structural control in metal-organic frameworks**

**Corey Leigh Jones**

Thesis submitted to Cardiff University for the degree of Doctor of  
Philosophy

September 2019



## Abstract

This thesis explores the ways in which structural control can be exhibited in metal-organic frameworks.

Chapter 1 describes the history of MOFs, particularly highlighting the importance of the structure-function relationship. The various ways in which the structural control can be exacted by synthesis, component design or external stimuli are outlined, forming the basis of the work in the subsequent chapters.

Chapter 2 discusses the use of the CLASSIC NMR technique, carried out using the facilities at the UK 850 MHz Solid-State NMR Facility, to monitor the in-situ formation of five different frameworks containing NMR active nuclei. This approach enabled simultaneous monitoring of the liquid and solid phases during syntheses, highlighting its advantage as an alternative method to traditional diffraction studies to study the in-situ crystallisation processes.

Chapter 3 summaries the syntheses of a novel series of coordination polymers with a benzimidazole-based linker ( $H_2L^1$ ). The linker has limited flexibility and the coordination geometry with various metal ions was explored. Crystal structures of the seven materials were obtained ( $MgL^1$ ,  $CaL^1$ ,  $SrL^1$ ,  $BaL^1$ ,  $MnL^1$ ,  $Cu_3(L^1)_2$ ,  $ZnL^1$ ) that showed the linker can bind to the metal nodes in two distinct conformations.

Chapter 4 details the synthesis and photochemical characterisation of two spiropyran-based carboxylate linkers ( $H_2L^2$  and  $H_4L^3$ ) that can undergo a structural change upon exposure to multiple stimuli. The linkers were reacted with various metal salts in combinatorial reactions, with powder X-ray diffraction used to screen for promising crystalline frameworks. Seven materials ( $Zn-L^2$ ,  $Mg-L^3$ ,  $Ca-L^3$ ,  $Sr-L^3$ ,  $Ba-L^3$ ,  $Zn-L^3$  and  $Cu-L^3$ ) showed promise of spiropyran incorporation. Initial structural characterisation of  $Cu-L^3$  has been obtained crystallographically. UV-visible absorption spectroscopy was used to further understand the SP/MC equilibrium of  $H_4L^3$  in solution under MOF reaction conditions, with the aim of predicting the conditions that can form crystalline materials in future syntheses.

## Table of Contents

List of figures .....	vi
List of schemes .....	xiii
List of tables .....	xiii
List of abbreviations.....	xiv
Contributions .....	xvi
Acknowledgements.....	xvii
<b>1 Structure-function relationship in porous materials .....</b>	<b>2</b>
1.1 Introduction.....	2
1.2 Structural control by synthesis.....	5
1.3 Structural control by component design .....	10
1.4 Post-synthetic structural control by external stimuli .....	15
1.5 Summary .....	26
1.6 Thesis scope.....	26
1.7 References.....	28
<b>2 CLASSIC NMR Studies of the Formation Processes of MOFs .....</b>	<b>36</b>
2.1 Introduction.....	36
2.2 Aim and objectives .....	39
2.3 Results and discussion .....	41
2.3.1 MFM-500(Ni).....	41
2.3.1.1 Synthesis .....	41
2.3.1.2 CLASSIC NMR of MFM-500(Ni).....	44
2.3.1.2.1 <sup>1</sup> H results.....	45
2.3.1.2.2 <sup>31</sup> P results .....	51
2.3.1.3 Reaction kinetics .....	52
2.3.1.4 Ex-situ and in-situ XRD results.....	55
2.3.1.5 SAXS results .....	58
2.3.1.6 Summary.....	60
2.3.2 AlPO-5.....	61
2.3.2.1 Synthesis.....	61
2.3.2.2 CLASSIC NMR of AlPO-5.....	62
2.3.2.2.1 <sup>1</sup> H data.....	62
2.3.2.2.2 <sup>31</sup> P data .....	63
2.3.2.3 Summary.....	64

2.3.3	Lithium-tartrate MOFs.....	65
2.3.3.1	Synthesis .....	65
2.3.3.2	CLASSIC NMR of lithium-tartrate MOF.....	66
2.3.3.2.1	<sup>1</sup> H results .....	66
2.3.3.2.2	<sup>13</sup> C results .....	67
2.3.3.3	NMR of ex-situ lithium-tartrate MOF samples .....	69
2.3.3.4	Ex-situ and in-situ PXRD results.....	71
2.3.3.5	Summary.....	73
2.3.4	MOF-5 .....	74
2.3.4.1	Synthesis .....	74
2.3.4.2	CLASSIC NMR of MOF-5 .....	75
2.3.4.2.1	<sup>1</sup> H results .....	75
2.3.4.2.2	<sup>13</sup> C results .....	76
2.3.4.3	PXRD results .....	77
2.3.4.3	Summary.....	77
2.3.5	Spiropyran-MOFs .....	78
2.3.5.1	Synthesis .....	79
2.3.5.2	NMR of ex-situ spiropyran-MOF samples .....	79
2.3.5.2.1	<sup>1</sup> H results .....	80
2.3.5.3.2	<sup>13</sup> C results .....	80
2.3.5.3	PXRD results .....	82
2.3.5.4	Summary.....	83
2.4	Conclusions .....	84
2.5	Experimental .....	85
2.5.1	MFM-500(Ni).....	86
2.5.2	AlPO-5.....	87
2.5.3	Lithium-tartrate MOFs.....	88
2.5.4	MOF-5 .....	89
2.5.5	Spiropyran-MOFs .....	89
2.6	References.....	91
<b>3</b>	<b>Syntheses of benzimidazolone-based coordination polymers.....</b>	<b>96</b>
3.1	Introduction.....	96
3.2	Aim and objectives.....	99
3.3	Results and discussion .....	100
3.3.1	Linker synthesis .....	100

3.3.2	Benzimidazolone-based coordination polymer synthesis .....	100
3.3.2.1	Crystal structures of group 2 coordination polymers .....	101
3.3.2.2	Group 2 coordination polymers structural discussion .....	105
3.3.2.3	Crystal structures of transition metal coordination polymers.....	107
3.3.2.4	Transition metal coordination polymers structural discussion.....	110
3.3.3	Group 2 vs. transition metal coordination polymer comparison .....	111
3.3.4	Bulk characterisation of coordination polymers.....	112
3.3.4.1	PXRD results .....	112
3.3.4.2	TGA results .....	114
3.4	Conclusions.....	116
3.5	Experimental.....	117
3.5.1	Synthesis of benzimidazolone diacetic acid ( $H_2L^1$ ) .....	118
3.5.2	Single crystal syntheses of coordination polymers .....	120
3.6	References.....	122
3.7	Appendix.....	125
<b>4</b>	<b>Spiropyran-incorporated metal-organic frameworks .....</b>	<b>140</b>
4.1	Introduction.....	140
4.2	Aims and objectives.....	143
4.3	Results and discussion .....	144
4.3.1	Spiropyran-based carboxylate linkers for MOF synthesis .....	144
4.3.1.1	Synthesis.....	144
4.3.1.2	Photophysical characterisation .....	145
4.3.1.2.1	Dissolution in polar solvents.....	146
4.3.1.2.2	pH dependence.....	147
4.3.1.2.3	Irradiation.....	154
4.3.2	Photoactive MOF syntheses .....	155
4.3.2.1	PXRD results .....	157
4.3.2.1.1	Syntheses with $H_2L^2$ and $H_4L^3$ in <i>absence</i> of co-linker .....	158
4.3.2.1.2	Syntheses with $H_2L^2$ and co-linker .....	159
4.3.2.1.3	Syntheses with $H_4L^3$ and co-linker .....	160
4.3.2.2	Cu- $L^3$ SCXRD results.....	164
4.3.2.3	UV-vis absorption spectra of “MOF condition” solutions .....	167
4.4	Conclusions.....	181
4.5	Experimental.....	183
4.5.1	Synthesis of spiropyran-based linkers .....	184

4.5.2	Synthesis of spiropyran-based MOFs .....	187
4.5.2.1	Crystalline products with $H_2L^2$ .....	187
4.5.2.2	Crystalline products with $H_4L^3$ .....	188
4.5.2.3	Crystal structure details of Cu- $L^3$ .....	189
4.5.3	Photophysical characterisation experiments .....	190
4.5.3.1	Dissolution of $H_2L^2$ in DMSO .....	190
4.5.3.2	pH study of $H_4L^3$ .....	190
4.5.3.3	Irradiation of $H_2L^2$ and $H_4L^3$ .....	190
4.5.3.4	UV-vis spectra of ‘MOF’ condition samples .....	191
4.6	References .....	192
4.7	Appendix .....	195

## List of figures

**Figure 1.1** Schematic of self-assembly reaction of metal ions with organic linkers to form a MOF.....2

**Figure 1.2** Schematic highlighting the multiple synthetic methods (*top*), reaction temperatures (*middle*) and the product outcomes (*bottom*) in the synthesis of framework materials.....3

**Figure 1.3** Crystallographic structure of Ni-MOF-74 upon dosing with CO<sub>2</sub>. The gas molecules coordinate to the exposed Ni cations at the pore surface.....4

**Figure 1.4** Components used to optimise the conditions for successful MOF synthesis.....6

**Figure 1.5** Phase diagram showing H<sub>2</sub>O/temperature dependence between Mn-sdc-1 and Mn-sdc-2.....7

**Figure 1.6** Perspective views of the 3D cadmium frameworks showing the changing pore size and shape when using DMF (*left*), DEF (*middle*) and PrOH (*right*) as reaction solvents.....8

**Figure 1.7** Infographic showing the different techniques that can be used to monitor the formation of MOFs. The phase regime each technique is sensitive to is given along with the information that can be collected.....9

**Figure 1.8** The 16 structures of the IRMOF series, with yellow spheres showing the largest Van der Waals spheres that fit into the pores without touching the framework itself.....11

**Figure 1.9** Syntheses of NOTT-10x series with the various tetracarboxylate linkers and copper nitrate in a solvent mixture with small quantities of acid.....11

**Figure 1.10** Zr nodes shown with the extended linkers used in the three UiO MOFs: 1,4-benzenedicarboxylate (BDC) in UiO-66; 4,4' biphenyl-dicarboxylate (BPDC) in UiO-67 and terphenyl dicarboxylate (TPDC) in UiO-68.....12

**Figure 1.11** Multiple modes that can be adopted (due to the flexible {O-CH<sub>2</sub>-} portion of the molecule) by 5,5'-(1,4-phenylenebis(methylene))bis(oxy)diisophthalic acid in a series of zinc frameworks under different synthesis conditions.....13

**Figure 1.12** The flexible linkers, CSA and PDG, used to synthesise two indium frameworks ([In(OH)CSA]<sub>∞</sub> and [In(OH)PDG]<sub>∞</sub>) reported by Haddad *et al.*.....14

**Figure 1.13** Pressure-induced reaction of Cd(APP)<sub>2</sub>NO<sub>3</sub>·NO<sub>3</sub> (APP = 1,4-bis(3-aminopropyl)-piperazine) under 0.4 GPa, which leads to an increase in coordination number to the 7-coordinated Cd<sup>2+</sup> in Cd(APP)<sub>2</sub>(NO<sub>3</sub>)<sub>2</sub>. ....15

**Figure 1.14** Structural changes that occur due to the loss of different solvents in SHF-61 which significantly affects the gas adsorption capacity.....17

**Figure 1.15** LED ring schematic (top view, *left*) and set-up when attached to cyrostream nozzle (*right*) of diffractometer for photocrystallographic experiments on Beamline 11.3.1 at the Advances Light Source (ALS), Berkeley, CA.....19

**Figure 1.16** Conversion from ground-state structure  $[\text{Ni}(\text{dppe})(\eta^1\text{-NO}_2)\text{Cl}]$  (*left*) to the metastable structures  $[\text{Ni}(\text{dppe})(\text{NO}_2)\text{Cl}]$  (*middle*) and  $[\text{Ni}(\text{dppe})(\eta^1\text{-ONO})\text{Cl}]$  (*right*) at 100 K upon irradiation with UV LEDs mounted 1 cm away from the crystal.....**19**

**Figure 1.17** Schematic of the  $\text{Mn}(\text{diamine-dicarboxylic acid})(\text{CO})_3\text{Cl}$  linker (*left*). i) Upon incorporation into a MOF with Mn(II) centres (black spheres) (*middle*) and the crystal structure shows the *fac* isomer shown in red. ii) After UV irradiation, rearrangement to the *mer* isomer occurs shown in blue, with no effect to the crystallinity of the framework.....**20**

**Figure 1.18** Isomerisation of *trans*-azobenzene upon irradiation with UV light to the *cis*-isomer.....**20**

**Figure 1.19** Zinc paddlewheel motif in CAU-5, showing the 2D sheets of metal nodes connected by NDC linkers in the *a,b*-plane. The azo-containing bipyridine linkers are coordinated to the zinc ions in the axial positions.....**21**

**Figure 1.20** Schematic of the reversible photoinduced  $\text{CO}_2$  uptake in  $\text{Zn}(\text{AzDC})(4,4'\text{-BPE})_{0.5}$ .....**22**

**Figure 1.21** Schematic of  $^{\text{Azo}}$ MOF highlighting the *trans-cis* isomerisation upon UV irradiation, with the *cis*-azobenzene pendent groups circled in purple (*far right*)....**23**

**Figure 1.22** Dithienylethene molecules undergoing ring-closure upon exposure to UV light.....**23**

**Figure 1.23** Reversible photo-isomerisation of a spiropyran molecule.....**24**

**Figure 1.24** Transformations of neutral and protonated spiropyran and merocyanine molecules upon irradiation and through acid–base equilibria.....**25**

**Figure 2.1** Structure of *m*-aminobenzoic acid (*right*) and the schematic of alternating  $^{13}\text{C}$  and  $^1\text{H} \rightarrow ^{13}\text{C}$  CP pulses sequences in the CLASSIC NMR experiment to record the liquid and solid-state respectively....**39**

**Figure 2.2**  $^1\text{H}$  NMR spectra showing BTPPA aromatic resonances (*left*) in  $d_6$ -DMSO (*middle*) and the reaction solvents,  $\text{D}_2\text{O}/d_7$ -DMF (*right*). The relative integrations of each peak are given, along with the corresponding proton environment.....**42**

**Figure 2.3** VT NMR spectra of BTPPA in  $\text{D}_2\text{O}/d_7$ -DMF at room temperature and upon heating the sample from 60 – 90 °C.....**43**

**Figure 2.4** BTPPA “dimers” in the reported crystal structure of MFM-500(Ni).<sup>29</sup> The chains of metal ions run in the *c*-direction and the ligands arrange in the AB...BA...AB motif (hydrogen atoms, DMSO molecules and some phosphonic acid groups have been omitted for clarity) (*left*). The dimer pairs have been coloured in blue and green (*right*) for clarity.....**44**

**Figure 2.5** Assignment of  $^1\text{H}$  NMR peaks in CLASSIC NMR experiment, including the three aromatic resonances in the BTPPA linker.....**45**

**Figure 2.6** Individual  $^1\text{H}$  spectrum (*left*) with red dashed line depicting the set ‘height’ for the level on the contour plot which is two-dimensional showing the shifts with time (*right*).....**46**

**Figure 2.7** 2D  $^1\text{H}$  NMR spectra from the in-situ experiments collected at 60 °C, 70 °C, 80 °C, 90 °C and 100 °C, with individual spectra at selected time points acquired during the CLASSIC NMR syntheses of MFM-500(Ni).....47

**Figure 2.8**  $^1\text{H}$  peak positions vs. time of the three aromatic resonances attributed to the BTPPA linker during the CLASSIC NMR experiment. The  $\text{H}_a$  and  $\text{H}_b$  fitting artefacts at 80 and 90 °C respectively are a result of the fit struggling with the low intensity peaks.....48

**Figure 2.9**  $^1\text{H}$  liquid-phase time series of laboratory synthesised MFM-500(Ni), in which a spectrum of the reaction solution was recorded every hour.....49

**Figure 2.10** Laboratory synthesised MFM-500(Ni) post-reaction solution VT NMR spectra.....50

**Figure 2.11** Difference IR spectrum (*left*) of  $\text{Ni}(\text{NO}_3)_2 \cdot 6\text{H}_2\text{O}$  in the  $\text{D}_2\text{O}/d_7\text{-DMF}$  reaction mixture and the change in absorbance of peaks at  $3167\text{ cm}^{-1}$  ( $\text{H}_2\text{O}$ ) and  $2488\text{ cm}^{-1}$  ( $\text{D}_2\text{O}$ ) over time (*right*).....50

**Figure 2.12**  $^{31}\text{P}$  direct excitation 2D contour plot from CLASSIC NMR experiment performed at 60 °C (*left*). Intensity vs. time plot for  $^{31}\text{P}$  signal which follows a similar trend to the  $^1\text{H}$  data at 60 °C (*right*).....51

**Figure 2.13** 2D  $^{31}\text{P}$  HPDEC spectra showing 3 weak peaks at 80 °C (*left*) and 90 °C (*right*) from the 2016 set of experiments.....52

**Figure 2.14** Intensity vs. time plots for the three aromatic peaks attributed to the BTPPA linker, to which Gualtieri models have been fitted for each temperature and proton position (*red lines*).....54

**Figure 2.15** Arrhenius plot for the calculation of activation energies for the nucleation and growth factors of MFM-500(Ni). The trendline has been fitted to only the first four data points (60 – 90 °C) for both the nucleation and the growth; the omitted 100 °C data points are plotted in green.....55

**Figure 2.16** Ex-situ PXRD patterns ( $\lambda = 1.54056\text{ \AA}$ ) of phase-pure MFM-500(Ni) synthesised in both the in-situ laboratory scale (*left*) and CLASSIC NMR experiments (*right*).....56

**Figure 2.17** Individual PXRD patterns taken from the in-situ XRD experiment ( $\lambda = 0.23417\text{ \AA}$ ). The appearance of MFM-500(Ni) occurs between 80 – 90 minutes, with only one crystalline phase forming.....56

**Figure 2.18** Data points (*left*) were produced by Dr Yeung using a Pawley refinement on the in-situ XRD pattern collected at a given time and integrating the area under the diffraction peaks to give a combined "intensity", with the red trace showing the unsuccessful attempt at the Gualtieri fit. The red stars indicate where material is falling out of the beam path and MFM-500(Ni) collected at the bottom of the sample tube (*right*).....57

**Figure 2.19**  $I(Q)$  vs  $Q$  plot for aliquots taken from 80 °C MFM-500(Ni) reaction solution over 4 hours (*left*) with an expansion of the high  $Q$  region, offset for clarity (*right*).....58

**Figure 2.20** The measured intensities have been scaled by factors of 1, 2, 4, 8, 16, 32 and 64 in intensity for presentation purposes. Solid lines represent fits to a core-shell rod model; dashed line corresponds to a power law of  $Q^{-1.5}$ .....59

- Figure 2.21** Crystal structure of AlPO-5.....61
- Figure 2.22** 2D  $^1\text{H}$  direct excitation spectra from the in-situ AlPO-5 experiment.....62
- Figure 2.23** 2D  $^{31}\text{P}$  direct excitation NMR spectrum from in-situ formation of AlPO-5, in which four species are present during the reaction.....63
- Figure 2.24** PXRD pattern of the ex-situ AlPO-5 product formed after 24 hours of heating at 120 °C, compared with the literature reported pattern (*red lines*) after 48 hours.....64
- Figure 2.25** Multiple phases form during the lithium-tartrate MOF reaction.....65
- Figure 2.26**  $^1\text{H}$  spectra from the in-situ NMR experiment in which the rotor was heated at three different temperatures over the course of 18 hours (the individual spectra collected at 80 and 105 °C have been summed) .....66
- Figure 2.27**  $^{13}\text{C}$  HPDEC summed spectra from the in-situ CLASSIC NMR experiment at 40, 80 and 105 °C.....67
- Figure 2.28** Sum of  $^{13}\text{C}$  CP spectra from in-situ CLASSIC NMR experiment at 40, 80 and 105 °C.....68
- Figure 2.29** Summed  $^{13}\text{C}$  CP spectra of lithium-tartrate MOFs at 40, 80 and 105 °C prepared ex-situ in deuterated (*left*) and non-deuterated (*right*) solvent mixtures. ....69
- Figure 2.30** Expanded high ppm region of  $^{13}\text{C}$  CP spectra for the deuterated sample (*left*) and non-deuterated samples (*right*).....70
- Figure 2.31**  $^{13}\text{C}$  CP spectra recorded at room temperature (RT) and high temperature (HT) of lithium-tartrate samples prepared at 105 °C in both deuterated (*left*) and (*right*) normal solvents.....71
- Figure 2.32** PXRD pattern of the solid prepared in the in-situ reaction (background has been corrected).....72
- Figure 2.33** PXRD patterns of lithium-tartrate MOFs formed at 40, 80 and 105 °C prepared in non-deuterated (H) and deuterated (D) solvent mixtures. The two phases **2a** (*black circles*) and **2b** (*red triangles*) are indicated.....72
- Figure 2.34** Synthesis of MOF-5.....74
- Figure 2.35** 2D  $^1\text{H}$  NMR spectrum for in-situ MOF-5 reaction.....75
- Figure 2.36** 2D  $^{13}\text{C}$  HPDEC spectra during in-situ MOF-5 reaction.....76
- Figure 2.37** PXRD comparison of simulated MOF-5 (black), MOF-2-DMF (red) and the product synthesised during the CLASSIC NMR experiment (blue).....77
- Figure 2.38** Reaction of zinc nitrate,  $\text{L} = 1',3',3''\text{-trimethylspiro}[\text{chromene-2,2'}\text{-indoline}]\text{-5',6-dicarboxylic acid}$  and  $\text{P} = \text{N}^l, \text{N}^d\text{-di(pyridin-4-yl)-terephthalamide}$  in DMF/EtOH producing colourless crystals of  $\{\text{Zn}(\text{L}_3)(\text{syn-P})\cdot(\text{DMF})_3(\text{H}_2\text{O})\}_n$  (*left*) and  $\{\text{Zn}(\text{L}_3)(\text{anti-P})\cdot(\text{DMF})_{3.5}(\text{H}_2\text{O})_{1.5}\}_n$  (*right*).....78

**Figure 2.39**  $^1\text{H}$  spectra of spiropyran-MOF 8-day reaction sample at the original concentration (black) and increased concentration (red).....**80**

**Figure 2.40**  $^{13}\text{C}$  CP spectra of spiropyran-MOF 8-day reaction sample at the original concentration (black) and increased concentration (red) compared with the solid-state spectrum of the spiropyran linker only (blue).....**81**

**Figure 2.41**  $^{13}\text{C}$  CP spectra of timed spiropyran-MOF syntheses (coloured traces) compared with the spiropyran linker (black trace).....**82**

**Figure 2.42** PXRD patterns of the spiropyran-MOFs synthesised using the adapted method compared with the simulated patterns for the known *syn*- and *anti*- crystalline phases.....**83**

**Figure 3.1** The reversible transition between the hydrated phase (MIL-53lt) and the anhydrous phase (MIL-53ht) results in the pore dimension changing by more than 5 Å.....**96**

**Figure 3.2** The GGH linker is tetratopic and is connected to four different  $\text{Zn}^{2+}$  centres. Multiple conformations can be adopted due to three torsion angles ( $\varphi_1$ ,  $\psi$  and  $\varphi_2$ ).....**98**

**Figure 3.3** Crystal structure of  $\text{MgL}^1$  showing the asymmetric unit (*right*) and the view along the *a*-axis (*left*).....**102**

**Figure 3.4** Crystal structure of  $\text{CaL}^1$  showing the asymmetric unit (*right*), the view along the *b*-axis showing the metal chain (*top left*) and the view along the *a*-axis in which the H-atoms have been omitted (*bottom left*).....**103**

**Figure 3.5** Crystal structure of  $\text{SrL}^1$  showing the asymmetric unit (*right*), the view along the *b*-axis showing the metal chain (*top left*) and the view along the *a*-axis in which the H-atoms have been omitted (*bottom left*).....**104**

**Figure 3.6** Crystal structure of  $\text{BaL}^1$  showing the asymmetric unit (*right*), the view along the *b*-axis showing the metal chain (*top left*) and the view along the *a*-axis in which the H-atoms have been omitted (*bottom left*). Structure solving and refinement was carried out by Adam Nevin.....**105**

**Figure 3.7** 2D layers are present in the four group 2 metal coordination polymers.....**105**

**Figure 3.8** The limited flexibility of  $\text{L}^1$  allows for binding to a metal centre in either a *cis* (*left*) or *trans* configuration (*right*). .....**106**

**Figure 3.9** Crystal structure of  $\text{MnL}^1$  showing the asymmetric unit (*right*), view along the *b*-axis (*top left*) and the view along the *a*-axis in which the H-atoms have been omitted (*bottom left*).....**108**

**Figure 3.10** Crystal structure of  $\text{Cu}_3(\text{L}^1)_2$  showing the asymmetric unit (*right*), view along the *a*-axis (*top left*) and the copper chain running throughout the coordination polymer, in which the linker has been omitted (*bottom left*).....**109**

**Figure 3.11** Crystal structure of  $\text{ZnL}^1$  showing the asymmetric unit (*right*) view along the *c*-axis (*top left*) and the view along the *a*-axis (*bottom left*). Structure solving and refinement was carried out by Benson Kariuki.....**110**

**Figure 3.12** PXRD patterns of the synthesised seven coordination polymers and  $H_2L^1$  (*blue traces*) compared with the simulated patterns from SCXRD (*red traces*). The powder patterns for synthesised  $CaL^1$  and  $Cu_3(L^1)_2$  have been background corrected.....113

**Figure 3.13** TGA data of the seven coordination polymers and  $H_2L^1$ .....115

**Figure 4.1** Single-crystal structures of  $[Zn_2(DBTD)(TNDS)]$  (**1**) and  $[Zn_2(DBTD)(HDDDB)]$  (**2**) with the simulated location of the spiropyran moieties in the pores of the framework.....141

**Figure 4.2** UV-vis spectra monitoring the MC→SP conversion of  $H_2L^2$  in DMSO (0.08 mM) at room temperature over one minute.....146

**Figure 4.3** UV-vis spectra showing the pH dependence of  $H_4L^3$  in ethanol upon addition of various concentrations of HCl covering a pH range from 1 – 7. Spectra were recorded at  $t = 0, 1$  and 24 hr.....148

**Figure 4.4** UV-vis spectra of extinction coefficient vs. wavelength as the concentration of the spiropyran in ethanol changes upon addition of HCl. Spectra were recorded at  $t = 0, 1$  and 24 hr.....148

**Figure 4.5** The reversible transitions between four different species of a spiropyran as a result of irradiation and acidochromism.....149

**Figure 4.6** Changes in the extinction coefficient of the 301 nm peak upon addition of HCl to  $H_4L^3$  in ethanol at  $t = 0, 1$  and 24 hours.....149

**Figure 4.7** Corrected absorbance values of the 450 nm peak with increasing acid concentration at  $t = 0, 1$  and 24 hours.....150

**Figure 4.8** Absorption difference spectra at  $t = 0$  and 24 hr for the 0.020 M HCl (*left*) and 0.023 M HCl solutions (*right*).....151

**Figure 4.9** UV-vis spectra showing the pH dependence of  $H_4L^3$  upon addition of various concentrations of NaOH covering an equivalent pH range from 7 – 14. Spectra were recorded at  $t = 0, 1$  and 24 hr.....152

**Figure 4.10** Corrected absorbance values of the SP peak with increasing  $[NaOH]$  after  $t = 0, 1$  and 24 hours.....152

**Figure 4.11** Corrected absorbance values of the 400 nm peak with increasing  $[NaOH]$  after  $t = 0, 1$  and 24 hours.....153

**Figure 4.12** Absorption difference spectra at  $t = 0$  and 24 hr upon addition of 0.0020 M NaOH (*left*) and 0.0023 M NaOH solutions.....153

**Figure 4.13** UV-vis spectra of  $H_2L^2$  after a total of 4 and 24 hours of irradiation (*left*) and the difference spectra after 24 hours (*right*).....154

**Figure 4.14** UV-vis spectra of  $H_4L^3$  after a total of 4, 5 and 9 hours of irradiation (*left*) and the difference spectra after 9 hours (*right*).....155

**Figure 4.15** PXRD patterns obtained from initial combinatorial syntheses with  $H_4L^3$  and group 2 metal salts – magnesium (II) (*left*) and calcium (II) (*right*).....158

**Figure 4.16** PXRD pattern of  $Zn-L^2$ . The powder diffraction pattern of  $H_2L^2$  and zinc acetate are shown for comparison.....159

**Figure 4.17** PXRD patterns of four crystalline products obtained from combinatorial syntheses with  $H_4L^3$ , 4,4'-dipyridyl and group 2 metal salts. The PXRD patterns of the metal salts are shown (*red trace*).....161

**Figure 4.18** PXRD comparison of crystalline material formed with magnesium or calcium (II) ions and  $H_4L^3$ , *with* and *without* a co-linker present in the reaction solution.....162

**Figure 4.19** PXRD patterns of two crystalline products obtained from combinatorial syntheses with  $H_4L^3$ , 4,4'-dipyridyl and first row transition metal salts. The PXRD patterns of the metal salts are also shown.....163

**Figure 4.20** 1,3-BDC-based linkers can exhibit partial flexibility by twisting and bending (*left*) which when reacted with  $Cu^{2+}$  ions results in the formation of a Kagomé lattice (*2D layer shown right*).....165

**Figure 4.21** Modelling of the possible four-way disorder of the spiropyran core in  $Cu-L^3$ .....165

**Figure 4.22** Proposed structure of  $Cu-L^3$ . *Top*: Kagomé layers in *ab* plane – the disordered spiropyran core has been removed from the image for clarity. *Left (middle and bottom)*: View of hexagonal channel in which the linkers can be seen bending towards the centre. *Right (middle and bottom)*: View of triangular channel in which the linkers can be seen bending away from the centre of the pore forming a capsule. The disorder around the spiropyran cores is not shown in order to clearly display the proposed network connectivity....166

**Figure 4.23** Simulated and experimental PXRD patterns of  $Cu-L^3$ ; the powder pattern of copper oxide is also shown.....168

**Figure 4.24** Samples of  $H_4L^3$  spanning a wide range of “MOF reaction conditions” (see Table 4.1) in the absence of metal ions prepared for UV-vis spectroscopy, shown immediately after preparation (*top*) and after leaving to equilibrate for 48 hours (*bottom*).....169

**Figure 4.25** VT UV-vis absorption spectra of vials 1 – 10; expanded region of low intensity showing weak peaks at 450 and 550 nm (*inset*).....171

**Figure 4.26** VT UV-vis absorption spectra of vials 11 – 20; expanded region of low intensity showing weak peaks at 450 and 550 nm (*inset*).....174

**Figure 4.27** Plot of SP/MC ratio against the observed outcome in the combinatorial reactions using the conditions from vials 1 – 20.....179

**Figure 4.28** Plot of SP/MCH<sup>+</sup> ratio against the observed outcome in the combinatorial reactions using the conditions from vials 1 – 20.....180

**Figure 4.29** Plot of MCH<sup>+</sup>/MC ratio against the observed outcome in the combinatorial reactions using the conditions from vials 1 – 20.....180

## List of schemes

**Scheme 2.1** Reported reaction conditions for the synthesis of MFM-500(Ni).....41

**Scheme 2.2** Adapted MFM-500(Ni) synthesis in which Ni(NO<sub>3</sub>)<sub>2</sub>·6H<sub>2</sub>O and BTPPA were added to deuterated solvents (D<sub>2</sub>O/*d*<sub>7</sub>-DMF) and inserted into a 20 μL Kel-F tube which was placed inside a rotor (*shown right*).....42

**Scheme 3.1** Structure of tetrakis[4-(carboxyphenyl)oxamethyl]methane acid (H<sub>4</sub>cm).....97

**Scheme 3.2** Three-step synthesis of benzimidazolone diacetic acid (H<sub>2</sub>L<sup>1</sup>).....100

**Scheme 4.1** Structures of three functionalised spiropyran-based linkers synthesised by Dr Magdalene Chong in 2016.....141

**Scheme 4.2** Synthesis of **3** to form the dibrominated spiropyran core **4**.....144

**Scheme 4.3** Suzuki-Miyaura cross-coupling of the dibrominated spiropyran with ethyl ester functionalised boronic acids to give **5** and **6**, followed by the subsequent hydrolysis with a mild base to give H<sub>2</sub>L<sup>2</sup> and H<sub>4</sub>L<sup>3</sup> respectively. ....145

**Scheme 4.4** Schematic representation of combinatorial syntheses with either H<sub>2</sub>L<sup>2</sup> or H<sub>4</sub>L<sup>3</sup> using two different approaches (*with* and *without* a co-linker) under various reaction conditions.....156

## List of tables

**Table 3.1** Summary of ionic radii of the metal ions in the +2 oxidation state and their metal oxide bond lengths *vs.* the configuration of L<sup>1</sup> in the corresponding benzimidazolone-based coordination polymer.....112

**Table 4.1** Quantities per vial of “MOF reaction conditions” for UV-vis absorption analysis.....170

**Table 4.2** Absorbance maxima for the SP (311 nm), MCH<sup>+</sup> (455 nm) and MC (573 nm) peaks from the VT UV-vis spectra for vials 1 – 10 for H<sub>4</sub>L<sup>3</sup> under different “MOF conditions”.....172

**Table 4.3** Absorbance values for the SP (310 nm), MCH<sup>+</sup> (450 nm) and MC form (550 nm) of H<sub>4</sub>L<sup>3</sup> under different “MOF conditions”.....175

## List of abbreviations

### Spectroscopy and techniques

AFM	Atomic force microscopy
CLASSIC NMR	Combined Liquid and Solid-State <i>In-situ</i> Crystallization Nuclear Magnetic Resonance
CP	Cross-polarisation
DFT	Density functional theory
FTIR	Fourier-transform infrared spectroscopy
LCTEM	Liquid Cell Transmission Electron Microscopy
HPDEC	High-power decoupling
IR	Infrared
MAS	Magic angle spinning
NMR	Nuclear magnetic resonance
PSM	Post-synthetic modification
PXRD	Power X-ray diffraction
QENS	Quasielastic neutron scattering
SAXS	Small-angle X-ray scattering
SCXRD	Single crystal X-ray diffraction
SPR	Surface plasmon resonance
TGA	Thermogravimetric analysis
TLC	Thin layer chromatography
UV	Ultraviolet
UV-vis	Ultraviolet-visible
VT	Variable temperature
WAXS	Wide-angle X-ray scattering
XRD	X-Ray diffraction

### Porous materials

AlPO	Aluminophosphates
COF	Covalent-organic framework

CAU	Christian-Albrechts-University
HKUST	Hong Kong University of Science and Technology
IRMOF	Isoreticular metal-organic framework
MFM	Manchester Framework Material
MIL	Materials of Institut Lavoisier
MOF	Metal-organic framework
NOTT	Nottingham
SBU	Secondary building unit
UiO	Universitetet i Oslo
ZIF	Zeolitic imidazolate framework

### **Solvents and chemicals**

BDC	Benzene dicarboxylate
BTC	Benzene tricarboxylate
BTPPA	1,3,5-benzene-tri- <i>p</i> -phenyl phosphonic acid
DCM	Dichlorometane
DEF	Diethyl formamide
DMF	Dimethyl formamide
DMSO	Dimethyl sulfoxide
4,4'-DP	4,4'-dipyridyl
EtOH	Ethanol
HCl	Hydrochloric acid
MC	Merocyanine
MCH <sup>+</sup>	Protonated merocyanine
MeOH	Methanol
NaOH	Sodium hydroxide
PrOH	Isopropanol
SP	Spiropyran
THF	Tetrahydrofuran
TPAOH	Tetrapropylammonium hydroxide

## Contributions

There are many people I would like to acknowledge for their scientific contributions to the work described in this thesis.

For the work in Chapter 2, I cannot thank Dr Colan Hughes enough for his help. He has been responsible for setting up the spectrometer at the UK 850 MHz Solid-State NMR Facility in the University of Warwick and recording the experiments that were ran. He also kindly processed and fit all the NMR data that is presented in the chapter for the five different frameworks that were studied. For the MFM-500(Ni) study, Dr Hughes modelled the Gualtieri data to obtain the activation energies for the process and Dr Alison Paul was responsible for aiding me with the *ex-situ* SAXS experiments and all the analysis of the data obtained. Finally, Dr Hamish Yeung (University of Oxford) and his students carried out the *in-situ* SAXS experiment at Diamond Light Source and was responsible for analysing the results obtained.

For the work in Chapter 3, I would like to thank Dr Adam Martin (UNSW, Sydney) for the linker synthesis procedure and synthesis of the initial Cu-benzimidazolone structure which provided the concept for the project; Dr Mohan Bhadbhade (UNSW) solved the crystal structure. At Cardiff, a big thank you to BSc student Elizabeth Marsden for being a wonderful student and her contribution to the scale-up of the linker synthesis and many combinatorial reactions to obtain the benzimidazolone-based structures. Dr Benson Kariuki solved two of the seven crystal structures, while Dr Adam Nevin was vital for his contribution in solving the remaining crystal structures and helping me to analyse the coordination geometry and the crystal structure descriptions.

For the work in Chapter 4, Dr Magdalene Chong reported the synthetic methods for linker syntheses in her own thesis under the supervision of Dr Timothy Easun; the spiropyran-containing zinc framework was also synthesised by Dr Chong (which is also discussed in Chapter 2). I would like to thank MChem students Joe Alemzadeh and James Down. Both students provided their synthetic input with bulk syntheses of the photoactive linkers. Joe carried out many MOF combinatorial reactions and PXRD analysis of the materials made, while James contributed to the UV-vis spectroscopy experiment to monitor the dissolution of spiropyrans.

## Acknowledgements

Firstly, I would like to thank Dr Timothy Easun for being a wonderful supervisor. Your support, guidance and encouragement over the last four years has been invaluable and thank you for allowing me to have many fantastic opportunities during my PhD. Thank you to all the Easun group members (past and present) including the undergraduate, visiting and summer students along the way.

A huge thank you to Alex for being the best work husband and friend – we’ve finally made it to the end! I couldn’t have asked for a more wonderful person to spend practically every day of the last four years with (both in and out of work), keeping me sane with a constant supply of laughter, cake and gin. Our trip to MOF2018 will forever hold amazing memories!

Thank you to the PhD students and post-docs in the inorganic department for providing the most enjoyable working atmosphere - you have all been a great support system for the days in which we all need to moan and to cheer each other up. I would like to thank the many School of Chemistry staff (technical and admin) for all their help during my PhD. I would also like to thank the members of staff who have given me the opportunity to participate in outreach activities – I have had many great experiences and now I get to enjoy doing it full-time in my new job!

My last thanks go to my incredible friends and family – especially my parents and grandparents – for your endless support in everything I have ever done and always believing in me. And finally, Michael – I don’t even have enough words to thank you for your love and encouragement every single day of the last eight years...here’s to our next chapter!



---

# **Chapter 1**

## **Structure-function relationship in porous materials**

---

# 1 Structure-function relationship in porous materials

---

## 1.1 Introduction

Coordination polymers, with 1, 2 or 3D structures, have been reported as early as the 1960s.<sup>1</sup> Coordination networks are a subset of coordination polymers, and metal-organic frameworks (MOFs) can be described as either a 2D or 3D coordination network with organic ligands containing potential voids.<sup>2</sup> The self-assembly of metal ions with organic linkers in solution forms a supramolecular thermodynamically stable product (Figure 1.1).<sup>3</sup> MOFs have become a thriving field of research over the last 20 years, with over 70,000 reported MOF structures in the Cambridge Structural Database (CSD) as of 2017.<sup>4</sup>

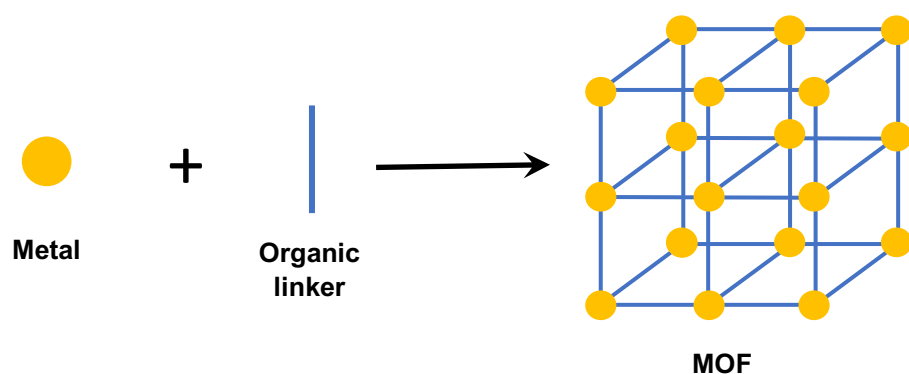


**Figure 1.1** Schematic of self-assembly reaction of metal ions with organic linkers to form a MOF.

MOFs fall into the class of crystalline porous materials which also include materials such as zeolites, activated carbons and covalent organic frameworks (COFs).<sup>5</sup> Compared with zeolites, which consist of aluminosilicate tetrahedra, MOFs are composed of secondary building units (SBUs) that are linked by multidentate organic molecules,<sup>6</sup> and it is this tuneable nature that makes them attractive materials. They can be synthesised to suit a range of applications due to the limitless ways in which metals and linkers can be combined leading to structures with variable pore sizes, topologies and increased internal surface area.<sup>7,8</sup> Although there is mainly focus on crystalline frameworks, there has been growing interest in amorphous MOFs (aMOFs) in the last five years.<sup>9</sup> These materials are formed by applying stress to crystalline frameworks destroying any long-range periodic order, whilst still retaining the connectivity of the molecular components.

There are several methods that can be used to synthesise crystalline frameworks (Figure 1.2).<sup>10</sup> The most conventional method is that of solvothermal synthesis, in which the reaction mixture is sealed in a pressure vessel and heated to a temperature greater than the boiling point of the solvent mixture.<sup>11</sup> The increased pressures generated in the system increases the solubility of the reagents in the solution thereby increasing the likelihood of reaction, resulting in products with greater crystallinity and high yields.<sup>12</sup> Non-solvothermal reactions take place below the boiling point of the solvent mixture, and there are even some examples in the literature of MOFs that have precipitated upon mixing of the starting reagents at room temperature.<sup>13</sup>

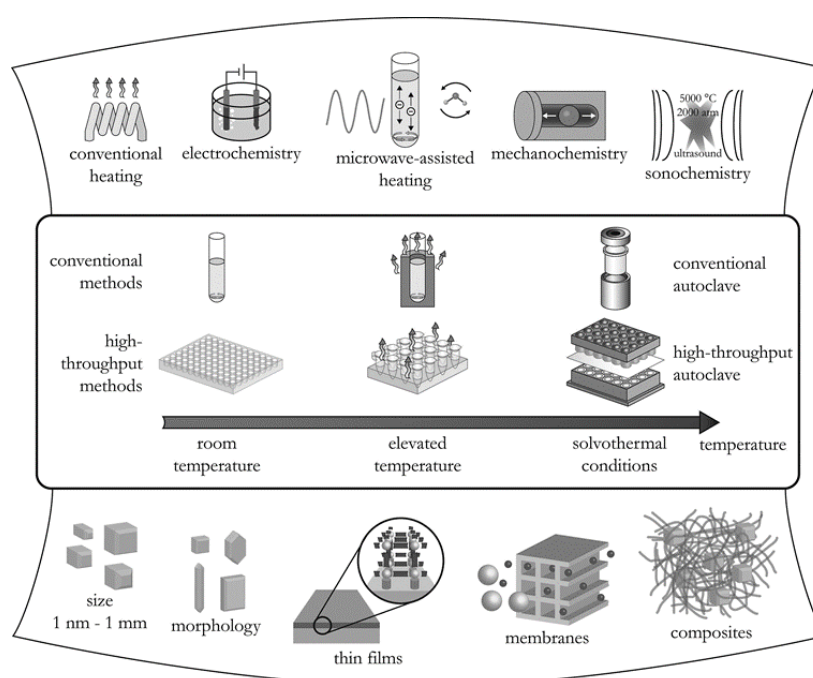


**Figure 1.2** Schematic highlighting the multiple synthetic methods (*top*), reaction temperatures (*middle*) and the product outcomes (*bottom*) in the synthesis of framework materials. Reproduced from reference 10.

Alternative synthetic methods have also been the subject of interest in recent years,<sup>14</sup> such as use of microwaves,<sup>15</sup> electrochemical,<sup>16</sup> mechanochemical<sup>17</sup> and sonochemical methods.<sup>18</sup> Many of these syntheses are investigated as possible methods for scaling-up production as they offer advantages such as quicker time-scale and lower temperatures for commercial purposes compared with solvothermal methods.

Syntheses can be very sensitive to small changes in reaction conditions; the variables commonly altered are temperature, time, solvent mixture, reagent concentration and pH,<sup>11</sup> which can lead to products of different crystal sizes and morphology forming. In order to control the nucleation and growth rate, modulators can also be added to the reaction mixture that are commonly monodentate linkers which results in competitive binding at the metal sites during the self-assembly process.<sup>19</sup> Unfortunately, there is much trial and error involved with most syntheses in order to form highly ordered crystalline materials of suitable quality for structural analysis methods.

Early coordination networks could not be classed as ‘MOFs’ because they did not retain permanent porosity; removal of solvent molecules caused the frameworks to collapse and they were referred to as ‘first generation’ materials.<sup>20</sup> Consequently, the ‘second generation’ of MOFs developed in the late 1990s were found to have greater stability to solvent removal and retained significant porosity upon desorption of guest molecules. The high surface areas (calculated to be up to a theoretical maximum of  $14600 \text{ m}^2 \text{ g}^{-1}$ )<sup>21</sup> and porosity of these materials have led to them being used for gas storage and separation.<sup>22–24</sup> Many MOFs have been widely studied as a potential solution for adsorbing  $\text{CO}_2$  and other harmful greenhouse gases (Figure 1.3),<sup>25</sup>  $\text{H}_2$  storage for fuel uses<sup>26,27</sup> or as an absorbent for toxic gases.<sup>28</sup>

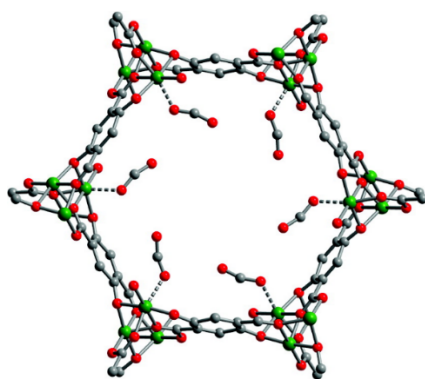


**Figure 1.3** Crystallographic structure of Ni-MOF-74 upon dosing with  $\text{CO}_2$ . The gas molecules coordinate to the exposed Ni cations at the pore surface. Reproduced from reference 25.

In recent years, many unusual applications of MOFs have been considered.<sup>29</sup> MOFs as chemical sensors<sup>30–32</sup> and catalysts<sup>33</sup> have become more common, and other niche applications for drug delivery<sup>34</sup> and in batteries and supercapacitors<sup>35</sup> are appearing in the literature. These applications are all possible as a result of tuning the functionality in the framework; this can be introduced by either pre-design of the organic linkers

for a suitable purpose or by post-synthetic modification (PSM) of the framework after synthesis.<sup>25</sup> However, the direct synthesis approach is not always the best method due to the challenges of limited linker solubility and functional group compatibility that can occur during solvothermal reactions.<sup>14</sup> The PSM method is therefore often preferred leading to alteration of the physical and chemical properties of the framework.<sup>36</sup>

The defined structures of MOFs makes it relatively straightforward to examine their “structure-function” relationships.<sup>37</sup> Allendorf and Stavila reviewed the field in 2015 to summarise various MOF series that have established these relationships, indicating how understanding this complex relationship can help with the synthesis of new materials.<sup>38</sup> Moghadam *et al.* have recently highlighted how machine-learning can be used to predict the mechanical properties of over 3000 MOFs.<sup>39</sup> This is crucial information that can be used to identify the most robust topologies that are necessary for scale-up of these materials for industrial applications. The way in which syntheses can control the functionality of frameworks forms the basis of this thesis, and the various aspects of monitoring the formation and the different design aspects leading to flexible frameworks will be discussed in greater detail in the subsequent sections in the chapter.

## 1.2 Structural control by synthesis

At the beginning of 2019, work by Berend Smit and co-workers highlighted how the reported literature only states the reaction conditions that yield successful MOF products meaning that a very large number of unsuccessful reactions often remain unreported.<sup>40</sup> By reporting the multiple failed conditions that were trialled along the way, they have analysed a successful pathway to synthesise HKUST-1, composed of Cu<sup>2+</sup> ions and 1,3,5-benzenetricarboxylic (BTC) acid,<sup>41</sup> with the highest surface area reported to date. This was achieved by using a method of machine learning to capture ‘chemical intuition’, which can be described as the way in which scientists develop an understanding and use this to optimise the conditions needed for a successful reaction. The various components that make up this process are shown in Figure 1.4. The group have developed an online programme, Materials Cloud,<sup>42</sup> which enables users to input

their partially successful and unsuccessful conditions so that genetic algorithms can calculate the next suitable attempts in order to synthesise high quality crystals suitable for analysis.

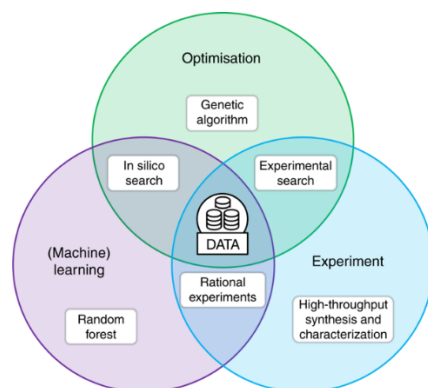


**Figure 1.4** Components used to optimise the conditions for successful MOF synthesis. Reproduced from reference 40.

The syntheses of MOFs need to be very carefully controlled as multiple (and sometimes unwanted) phases can often be formed. There are many variables that can be altered (including temperature, pH, solvent or molar ratio) that result in a structural or phase change.<sup>43</sup>

In an interesting example of changing the solvent *and* temperature, Qian and co-workers monitored the nucleation stage of two Mn-based MOFs.<sup>44</sup> They were able to gain understanding into the reversible transformation between the two frameworks and produce a phase diagram of the process (Figure 1.5). It can be seen that although the two phases are clearly separated, there is an area between in which both of the phases can co-exist. The two phases can be independently synthesised using manganese chloride and 4,4'-stilbenedicarboxylic acid (sdc) with DMF/acetic acid or DMF/H<sub>2</sub>O to form Mn-sdc-1 and Mn-sdc-2 respectively. The transformation from Mn-sdc-1 to Mn-sdc-2 is induced by the presence of water, with Mn-sdc-2 showing very good water stability; the reversible transformation back to Mn-sdc-1 was found to occur upon heating in DMF.

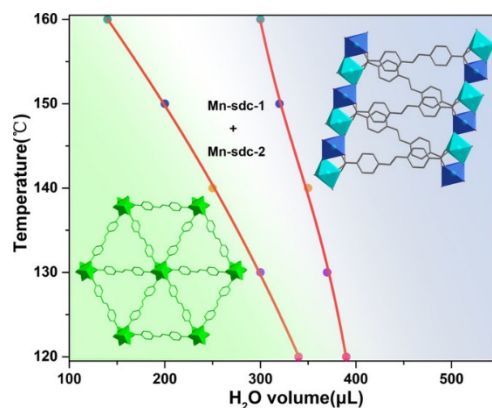


**Figure 1.5** Phase diagram showing H<sub>2</sub>O/temperature dependence between Mn-sdc-1 and Mn-sdc-2. Reproduced from reference 44.

An interesting example by Cheetham and co-workers in 2004 showed how five different phases of Co-succinate coordination polymers could be formed by changing the reaction temperature from 60 to 250 °C, whilst keeping all other variables the same.<sup>45</sup> It was found that as the temperature of the synthesis increased, the density and number of coordinated Co<sup>2+</sup> ions per linker increased whilst the hydration was found to decrease. In a different example, de Oliveira *et al.* synthesised two Tm-based frameworks under aqueous conditions at 100 and 180°C; the different temperatures resulted in the frameworks crystallising in a monoclinic and triclinic space group respectively.<sup>46</sup> This was also the first example of synthesising lanthanide-succinate structures with different space groups but identical empirical formulae.

The succinate-based linkers can form different structures at various temperatures due to the flexible nature of the molecule, which results in a range of different coordination modes – this aspect will be examined in more detail in Section 1.3. Altering the reaction conditions, *i.e.* temperature, can not only lead to materials with different structures but a significant change in properties too. An example by Wu and co-workers showed that altering the hydrothermal conditions when forming two cobalt coordination polymers using cobalt sulphate and 1H-benzimidazole-5,6-dicarboxylate led to one structure exhibiting ferromagnetic coupling whilst the other was antiferromagnetic.<sup>47</sup>

Variation of the solvent used during MOF syntheses can also have huge structure-directing effects. Ghosh and Kitagawa found that when a tripodal ligand (tris(2-carboxyethyl)isocyanurate) was reacted with a cadmium salt, upon altering the

reaction solvent from DMF to DEF to PrOH resulted in the synthesis of three different structures with a range of pore shapes and sizes (Figure 1.6).<sup>48</sup> The solvents were found to have a templating effect, resulting in an anionic framework being formed with DMF whilst the frameworks synthesised with DEF and PrOH were neutral. As mentioned previously, the ligand flexibility plays a large part in determining the structure and demonstrates the interplay between component design and synthesis conditions.

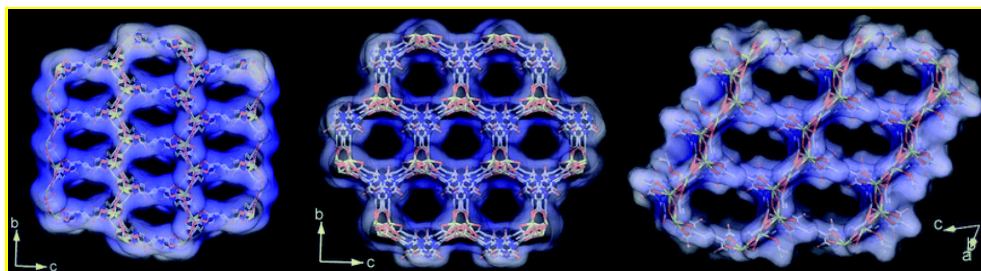


**Figure 1.6** Perspective views of the 3D cadmium frameworks showing the changing pore size and shape when using DMF (*left*), DEF (*middle*) and PrOH (*right*) as reaction solvents. Reproduced from reference 48.

Additionally, pH effects can impact on MOF structure. In 2013, Luo *et al.* found that by altering pH between 5 and 9, three different cobalt frameworks were formed with differing colour crystals.<sup>49</sup> Crystal structure analysis showed that the trimesic acid linker was partially deprotonated in the framework synthesised with the most acidic conditions, but was fully deprotonated in the other two frameworks synthesised at pH 7 and 9. Phase pure materials could be isolated when the pH of the reaction mixture was either 5 or 9, however when the pH was adjusted to a range of 6 – 8 a mixture of phases was obtained. This emphasises how critical the reaction conditions are during the self-assembly process.

Due to the number of factors that can influence MOF syntheses, the whole process from the initial nucleation and growth to the final product is still not fully understood with many studies attempting to further progress this limited understanding. A comprehensive review by Van Vleet *et al.* provided great detail on the in-situ, time-resolved and mechanistic studies of the MOF crystallisation process using a number of different techniques, which include scattering methods, microscopy, spectroscopy and computational simulation.<sup>50</sup> Each technique has its advantages and limitations (Figure 1.7), with the various scattering and microscopy approaches being

explored in more depth in Chapter 2 of this thesis. Spectroscopic techniques are often less reported, and are used in combination with other methods, as they can only be used to study structures of complexes in the reaction solution.

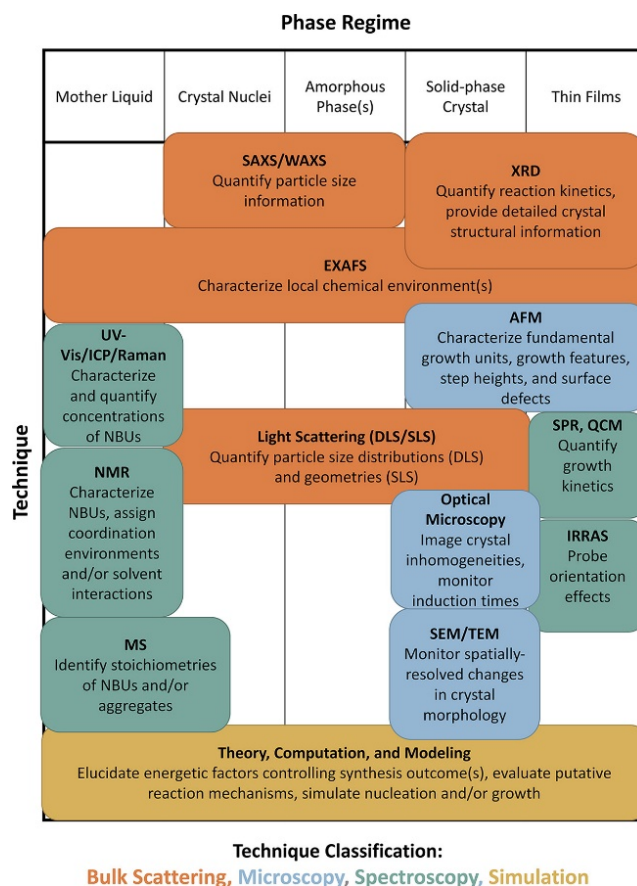


**Figure 1.7** Infographic showing the different techniques that can be used to monitor the formation of MOFs. The phase regime each technique is sensitive to is given along with the information that can be collected. Reproduced from reference 50.

An NMR technique has been developed by the Harris group at Cardiff University to study crystallisation processes which has been exploited as a potential new method to monitor the in-situ formation of several frameworks for this thesis; this is discussed in detail in Chapter 2. In this thesis we have investigated both novel and widely reported materials in order to further understand how we can control difficult syntheses. In the case of a novel framework, we have observed the synthesis resulting in the formation of multiple phases that we wish to disentangle (also discussed in Chapter 4).

### 1.3 Structural control by component design

The formation of MOF materials can be unpredictable due to factors that can affect the structural outcome, including the choice of metal ion or linker. For the self-assembly process of the reactants to occur in solution, labile metal ions are typically used including  $\text{Cu}^+$ ,  $\text{Cu}^{2+}$ ,  $\text{Zn}^{2+}$ ,  $\text{Co}^{2+}$  and  $\text{Ni}^{2+}$ .<sup>51</sup> As particular elements will have their own coordination preferences for a particular valency, this can be viewed as way of controlling the intrinsic structure of framework materials.<sup>52</sup>

This metal-directed effect has been observed in a novel MOFs series when Hu *et al.* synthesised six MOFs with a combination of polycarboxylate linkers, a V-shaped imidazole-based linker and a range of different metal salts.<sup>53</sup> The crystal structures obtained were compared and varying metal node geometries were observed, from  $\text{Cd}^{2+}$  6-coordinate metal centres with a distorted octahedral geometry to a  $\text{Co}^{2+}$  framework with 5-coordinate distorted trigonal bipyramidal nodes. The  $\text{Zn}^{2+}$  framework consists of two types of coordination: distorted tetrahedral nodes and an octahedrally coordinated node. The  $\text{Mn}^{2+}$  structure is interesting as it contains two types of Mn ions (5- and 6-coordinate) bridged by the carboxylate linker to give a binuclear cluster. Finally, two  $\text{Ni}^{2+}$  frameworks were synthesised with different linkers which resulted in 6-coordinate metal centres in both cases.

The choice of linker can also have a significant influence on the final structure. One of the most common synthetic strategies is the process of ‘reticular synthesis’ (a term devised by Yaghi in the early 2000s).<sup>54</sup> He described the concept of rigid building blocks that can be assembled by the formation of strong bonds with linkers or spacers; these prearranged highly crystalline ordered networks produce a series of structures that have the same net (or topology) and are ‘isorecticular’. Using this process, it has been possible to construct molecules by design to give frameworks with a predetermined pore size and functionalisation.<sup>6</sup>

MOF-5 is the archetypal framework (described in more detail in Chapter 2) and formed the basis of a series of frameworks (IRMOFs) in which the pore functionality and size were increased whilst retaining the same cubic topology upon altering the linker.<sup>55</sup> The IRMOF series consists of 16 frameworks originally synthesised in 2002 by Yaghi and co-workers for high capacity methane storage. The linkers contain a

range of different functional groups in the central portion of the molecule that ultimately affected the pore structure and gas storage capacity (Figure 1.8). IRMOF-6 was found to have the highest CH<sub>4</sub> uptake in the series as a result of the appropriate pore size dimensions (*ca.* 5.9 Å).

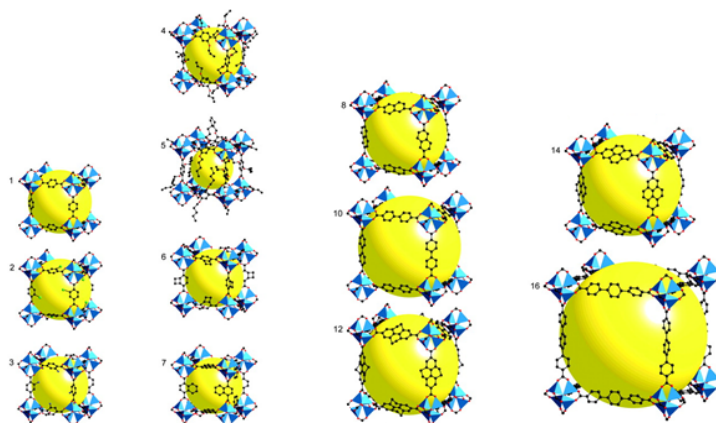


**Figure 1.8** The 16 structures of the IRMOF series, with yellow spheres showing the largest Van der Waals spheres that fit into the pores without touching the framework itself. Reproduced from reference 55.

Schröder and co-workers synthesised a well-known series of isorecticular MOFs which were an example of developing materials via *design* to extensively study the H<sub>2</sub> adsorption capacities.<sup>56</sup> The NOTT-10x frameworks are all constructed of the same Cu(II) paddlewheel motif but different polyphenyl tetracarboxylate linkers. This resulted in structures with a range of pore sizes from 6.5 – 8.3 Å and the projection of various functional groups into the pores altered the gas uptake (Figure 1.9).

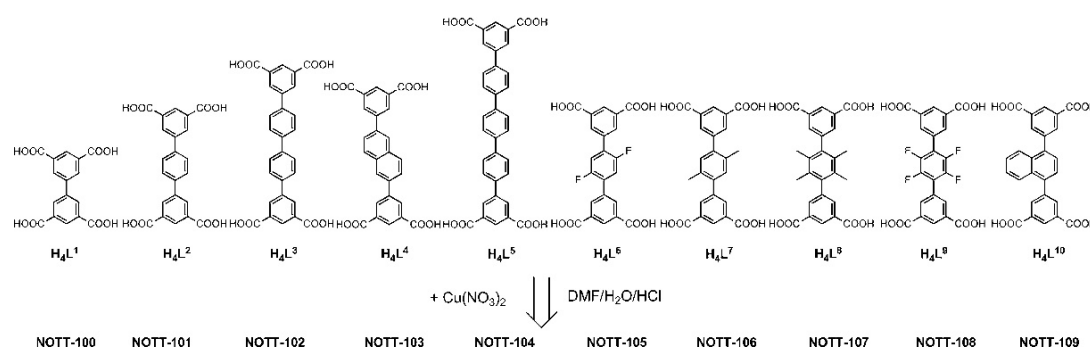


**Figure 1.9** Syntheses of NOTT-10x series with the various tetracarboxylate linkers and copper nitrate in a solvent mixture with small quantities of acid. Reproduced from reference 56.

NOTT-100 – 108 are isorecticular due to the formation of two types of planar 4-connected nodes, which gives a NbO type network due to the packing and combination of two types of metal-ligand cages, whilst NOTT-109 was found to have a different topology of PtS.

The UiO series was first reported in 2008 and all the frameworks contain the  $Zr_6O_4(OH)_4(CO_2)_{12}$  building block.<sup>57</sup> The zirconium node is extremely stable (both thermally and chemically) and has the highest coordination number (12) in any MOF. The three different linkers used in the isorecticular series are shown in Figure 1.10. The pore window increases in length from 6, 8 to 10 Å as the number of benzene rings in the linker increases in UiO-66, UiO-67 to UiO-68 respectively.

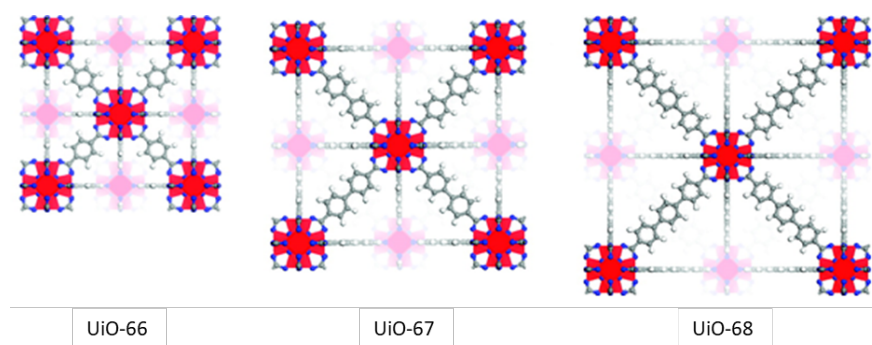


**Figure 1.10** Zr nodes shown with the extended linkers used in the three UiO MOFs: 1,4-benzenedicarboxylate (BDC) in UiO-66; 4,4' biphenyl-dicarboxylate (BPDC) in UiO-67 and terphenyl dicarboxylate (TPDC) in UiO-68. Reproduced from reference 57.

The isorecticular approach was used in 2014 by the Forgan group to create a series of frameworks with the same topology.<sup>58</sup> However, when the functionality of the linker group was altered to allow for non-covalent interactions such as hydrogen bonding between linkers, the topology of the resulting framework was altered. This work reveals how these interactions can also have substantial structure-directing effects that allows the framework to be tuned for attractive properties such as sensing and catalysis.

The reticular synthetic approach is becoming quite outdated, with the formation of more MOFs containing linkers that can adopt multiple conformations. This leads to frameworks with varying structures and a change of properties as a result. Many

examples include a linker that contains an  $sp^3$  carbon that allows for bond rotation, such as the 5,5'-(1,4-phenylenebis(methylene))bis(oxy)diisophthalic acid linker used by Li and co-workers to synthesis a novel series of ten zinc frameworks.<sup>59</sup> This molecule could not only assume various coordination modes (Figure 1.11) due to the {O-CH<sub>2</sub>-} group which can twist in response to influencing factors during the self-assembly process, but it can also act as a H-bond acceptor or donor. Various N-donor ligands were used also used in the syntheses to yield the different structures resulting in changes to the emission wavelengths studied by solid-state photoluminescence. The  $\pi$ - $\pi$  stacking interactions were present in the observed crystal structures and the emissions for the ten frameworks were ascribed to be either ligand-centred (LC) transitions or a ligand-to-ligand charge transfer (LLCT).

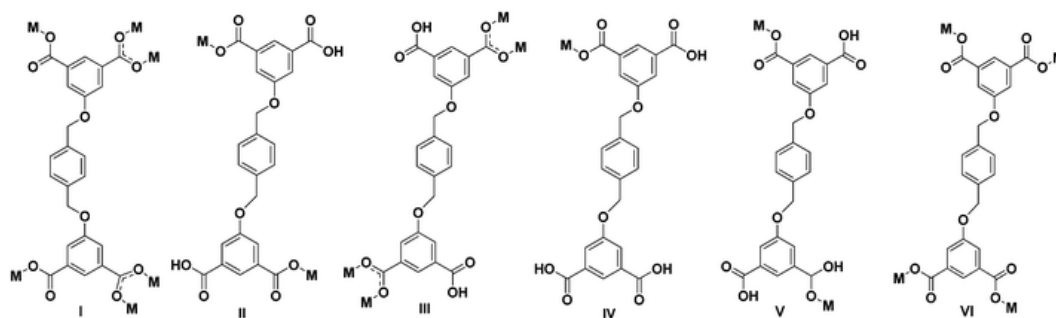


**Figure 1.11** Multiple modes that can be adopted (due to the flexible {O-CH<sub>2</sub>-} portion of the molecule) by 5,5'-(1,4-phenylenebis(methylene))bis(oxy)diisophthalic acid in a series of zinc frameworks under different synthesis conditions. Reproduced from reference 59.

Another type of flexible linker that has become more common in recent years are peptide-based molecules. As these types of linkers can adopt various conformations, there is increased possibility of formation of low energy states that can be accessed under changes in environmental conditions. Non-coordinating pendent groups in the peptide chain also allow for supramolecular interactions within the frameworks causing structure-directing transformations.<sup>60</sup> Several examples of this research have been reported by Rosseinsky and co-workers. In 2010 they synthesised a framework with a dipeptide glycine-alanine linker to form the framework [Zn(Gly-Ala)<sub>2</sub>] $\cdot$ (solvent).<sup>61</sup> The linker has several degrees of freedom, similar to those seen in protein folding with Zn<sup>2+</sup> cations.<sup>62</sup> A range of coordination environments were adopted within the MOF which led to changes in pore conformation; the solvent accessible pore area was calculated to almost double from 15.6 Å<sup>2</sup> to 29.2 Å<sup>2</sup>.

A different example by the same research group reported two flexible amide functionalised linkers (Figure 1.12), *N*-(4-carboxyphenyl)succinamic acid (CSA) and *N,N'*-(1,4-phenylenedicarbonyl)diglycine (PDG) were used to synthesise the indium frameworks  $[\text{In}(\text{OH})\text{CSA}]_{\infty}$  and  $[\text{In}(\text{OH})\text{PDG}]_{\infty}$ .<sup>63</sup>

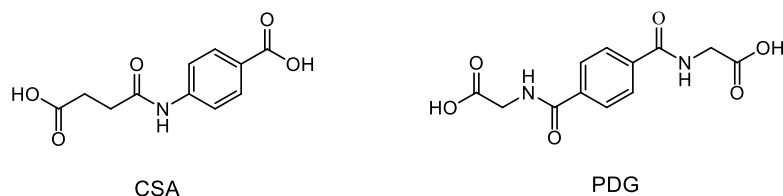


**Figure 1.12** The flexible linkers, CSA and PDG, used to synthesise two indium frameworks ( $[\text{In}(\text{OH})\text{CSA}]_{\infty}$  and  $[\text{In}(\text{OH})\text{PDG}]_{\infty}$ ) reported by Haddad *et al.*

The frameworks consist of indium hydroxide chains of corner-sharing octahedra  $\{\text{InO}_4(\text{OH})_2\}$  interconnected by rigid dicarboxylate linkers forming stacked 2-dimensional layers. Due to the different supramolecular interactions between the linkers, the conformational configurations result in the two structures having different pore shapes and a variation in the functional group orientation.<sup>63</sup> The flexibility of the PDG linker with  $\text{sp}^3$  carbon tails at either end of the molecule resulted in a structure with hydrogen-bonding between the linkers which prevented the layers from being close-packed, creating large cylindrical pores that were accessible by solvents. In the framework with the CSA linker, the asymmetric molecule does not allow for hydrogen-bonding to occur therefore Van der Waals interactions dominated and the layers were close-packed.

The concept of introducing flexibility into a framework has been applied in Chapter 3 of this thesis. A biologically active carboxylate-containing molecule with a  $-\{\text{CH}_2\}$ -spacer group has been used to demonstrate the flexibility exhibited when forming structures using a range of group 2 and transition metal ions.

## 1.4 Post-synthetic structural control by external stimuli

The previous sections have summarised how we can impart structural control in MOFs during the synthesis stage and by particular component design. We can also impose a structural change in a framework as a result of exposing materials to an external stimulus. An excellent review by Coudert in 2015 highlighted a number of stimuli-responsive frameworks that can undergo a large structural change upon exposure to heat, light, pressure and guest adsorption/removal.<sup>64</sup> A MOF that can even respond to multiple stimuli has been reported by Shivanna *et al.* in which the framework undergoes four types of structural transformation forming six discrete phases.<sup>65</sup> The subsequent sections describe various frameworks that have been found to be responsive to the following stimuli.

### Pressure

High pressure single-crystal diffraction studies on MOFs are typically carried out in a diamond-anvil cell, in which pressures of 0.1 – 10 GPa can be reached.<sup>66</sup> It has been found that this can induce phase-transitions, such as an example by Lapidus *et al.* in which the conversion between a dense phase interpenetrated zinc cyanide MOF to three new porous phases occurred at pressures of 0.9 – 1.8 GPa.<sup>67</sup> In 2018 Katrusiak and co-workers reported the increasing coordination number of a cadmium-based framework upon increasing pressures.<sup>68</sup> At room temperature, the linkers bind to the  $\text{Cd}^{2+}$  centre in a distorted octahedron which then underwent an associative reaction upon the pressure reaching 0.4 GPa. Due to the decrease of the linker radii a 7-coordinate metal centre was formed (Figure 1.13).

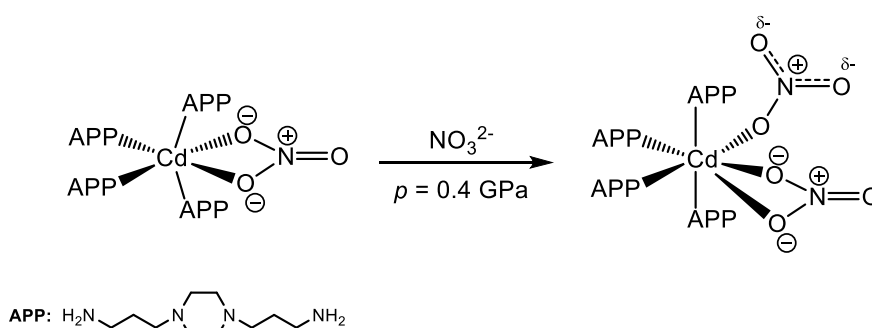


**Figure 1.13** Pressure-induced reaction of  $\text{Cd}(\text{APP})_2\text{NO}_3 \cdot \text{NO}_3$  (APP = 1,4-bis(3-aminopropyl)-piperazine) under 0.4 GPa, which leads to an increase in coordination number to the 7-coordinated  $\text{Cd}^{2+}$  in  $\text{Cd}(\text{APP})_2(\text{NO}_3)_2$ .

High pressures can also result in amorphisation of MOFs. This was once considered a negative property, but recently these amorphous MOF phases have been found to retain some porosity and even have improved mechanical strength when compared to the crystalline parent material.<sup>9,66</sup>

### *Temperature*

The ability to retain the framework structure while acting responsively to temperature changes is highly desirable. It has been shown that three flexible MOFs (FJI-H11-R) could respond reversibly to temperature whilst displaying an extremely high anisotropic thermal expansion.<sup>69</sup> In-situ X-ray diffraction showed that the mechanism was a result of the organic linkers rotating and bending upon heating from 100 K to 293 K, highlighting the interplay between external stimuli and flexible linkers (as mentioned in the previous section). In 2018, Wang and co-workers reported a thermoresponsive amphoteric MOF with incorporation of a polymer with tertiary amine groups in the pores, PDMVBA-MIL-121.<sup>70</sup> The framework showed uptake of metal salts at room temperature and the ability to release them into solution at 80 °C. The ease of regeneration showed potential to reduce the environmental impact of purifying water, with the aim of using the material to produce low-cost potable desalination cups to provide a fresh water supply in an emergency.

### *Guest adsorption/removal*

An early example of MOFs responding to solvent adsorption is the MIL-88 series in which the unit cells can undergo a large expansion and exhibit a 'breathing' motion without disrupting the connectivity of the framework.<sup>71</sup> The extent of pore opening was dependent upon the polarity of the solvent. Water and methanol are small polar molecules and induced an increase of *ca.* 7% in pore volume. Pyridine and DEF are hydrophobic polar liquids resulting in a dramatic cell volume increase of 170%; this is due to the favourable CH- $\pi$  interactions with the organic component of the pores.

In 2017, the Brammer group synthesised a 3D diamondoid structure (SHF-61) by the solvothermal reaction of InCl<sub>3</sub> and 2-aminoterephthalic acid in DMF.<sup>72</sup> The structure exhibited a continuous breathing mechanism, which differs depending on desolvation in two different solvents (Figure 1.14).

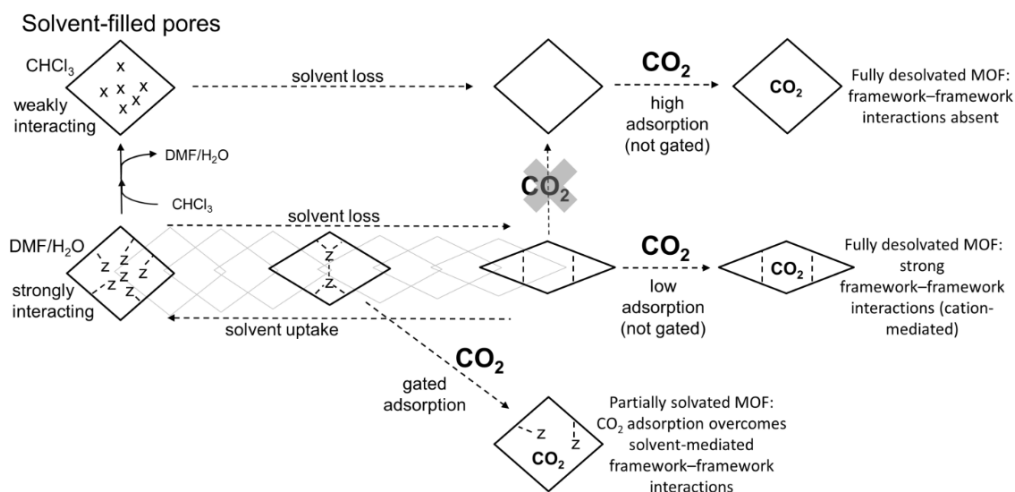


**Figure 1.14** Structural changes that occur due to the loss of different solvents in SHF-61 which significantly affects the gas adsorption capacity. Reproduced from reference 72.

In the as-synthesised material (SHF-61-DMF) the solvent is strongly bound and upon removal from the pores of the framework the structure contracts. This process is reversible upon solvent uptake, hence giving a breathing motion. CO<sub>2</sub> uptake is very low in the narrow pore form as there are strong framework-framework interactions. However, if SHF-61-DMF is only partially solvated, CO<sub>2</sub> adsorption is possible as the framework-framework interactions can be overcome. When SHF-61-DMF is solvent-exchanged with chloroform to give SHF-61-CHCl<sub>3</sub>, the structure is retained upon removal of the solvent allowing for high CO<sub>2</sub> uptake due to the absence of framework-framework interactions.

### Light

There are many examples of photoactive frameworks, particularly frameworks containing components with inherent ‘static’ luminescent properties that have been widely reported as sensors of metal ions and small molecules.<sup>73–77</sup> However, the use of light to evoke a structural change in a framework has become of great interest in the recent decade, highlighting the importance of design strategy for functional materials.<sup>78</sup> This section goes into greater depth, compared to the use of other stimuli in the previously aforementioned paragraphs, as it is ultimately important to the main aims of this thesis.

In 2015, we reviewed various photoresponsive frameworks and classified them by four different design strategies which were:<sup>78</sup>

- i) inclusion of a photoresponsive guest;
- ii) post-synthetic modification (PSM) of frameworks to add in photoresponsive groups;
- iii) synthesis of MOFs with linkers containing pendent photoresponsive groups;
- iv) synthesis of MOFs from linkers that themselves have intrinsic structural photoresponsivity such that their structure is altered upon irradiation.

In order to examine the structural changes in these materials, X-ray photocrystallography can be used. The technique uses single-crystal X-ray diffraction (SCXRD) methods to determine the 3D structure after irradiation with UV or visible light that cause the molecular components to adopt a photoactivated metastable or short-lived high-energy state.<sup>79</sup> The use of light as a stimulus is advantageous due to the high temporal and spatial control that can be achieved.<sup>80</sup>

Some of the first reports of solid-state photochemical reactions were published in the 1950s and 1960s by Schmidt and co-workers. Since that time, the development of the technique has dramatically improved due to the technological advances of lasers for irradiation and the use of synchrotron sources for time-resolved experiments on extremely fast timecales.<sup>81,82</sup> Work by Coppens and co-workers in the 1990s and early 2000s used photocrystallography to determine the structures of photoactive metastable linkage isomers in metal nitrosyl,<sup>83</sup> nitrite<sup>84</sup> and sulfur dioxide complexes.<sup>85</sup>

Using lasers as an irradiation source can be expensive and potentially hazardous; therefore, over the last decade LEDs have become more widely used (Figure 1.15). Their decreased intensities can allow greater control of the photoactivation and conversion rate of a species, preventing fast crystal degradation.<sup>86,87</sup>

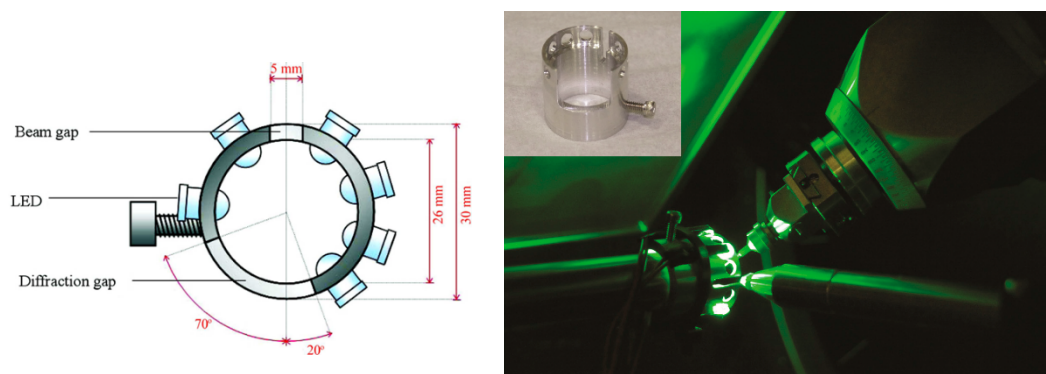


**Figure 1.15** LED ring schematic (top view, *left*) and set-up when attached to cryostream nozzle (*right*) of diffractometer for photocrystallographic experiments on Beamline 11.3.1 at the Advances Light Source (ALS), Berkeley, CA. Reproduced from references 86 and 87.

There are limitations of photocrystallography such as low photoconversion due to lack of laser penetration into samples or unfavourable strain energy within the MOF as the crystal structure changes.<sup>88</sup> Warren *et al.* have made progress in this area by taking advantage of compounds with bulky ligands or large counterions in metal salts to reduce lattice strain and enhance the percentage conversion upon irradiation.<sup>88</sup> A nickel nitro complex with a 1,2-bis(diphenylphosphino-ethane) (dppe) ligand was reported to undergo a single-crystal to single-crystal transformation upon irradiation with UV light (400 nm) to give the nickel nitrito complex (Figure 1.16). The transformation was found to be 100% reversible under photocrystallographic conditions; the bulky dppe ligands dominate the crystal packing allowing for ease of rearrangement due to the areas of free space within the crystal.

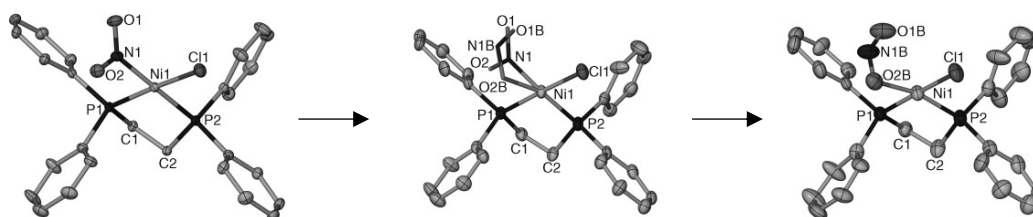


**Figure 1.16** Conversion from ground-state structure  $[\text{Ni}(\text{dppe})(\eta^1\text{-NO}_2)\text{Cl}]$  (*left*) to the metastable structures  $[\text{Ni}(\text{dppe})(\text{NO}_2)\text{Cl}]$  (*middle*) and  $[\text{Ni}(\text{dppe})(\eta^1\text{-ONO})\text{Cl}]$  (*right*) at 100 K upon irradiation with UV LEDs mounted 1 cm away from the crystal. Reproduced from reference 88.

The photocrystallographic approach has been applied to MOFs by Champness, George and co-workers to study the local structural changes around photoactive centres.<sup>89</sup> They reported the incorporation of a  $\text{M}(\text{diimine})\text{CO}_3\text{X}$  complex (where  $\text{M} = \text{Re}, \text{Mn}$  and  $\text{X} = \text{Cl}, \text{Br}$ ) into a manganese-based MOF to form two isostructural frameworks

(ReMn and MnMn). Upon irradiation of the frameworks (with a 300 W Xe lamp at low temperatures), the M(diimine)(CO)<sub>3</sub>Cl unit underwent isomerisation from the *fac* to the *mer* isomer with *ca.* 10% conversion for ReMn and 25% for MnMn (Figure 1.17).<sup>90</sup> The MOF structure provided an environment to study the photochemical nature of this process without affecting the crystal integrity. The mechanism and intermediates involved in this process were later investigated by Easun *et al.* using FTIR and Raman mapping techniques.<sup>91</sup>

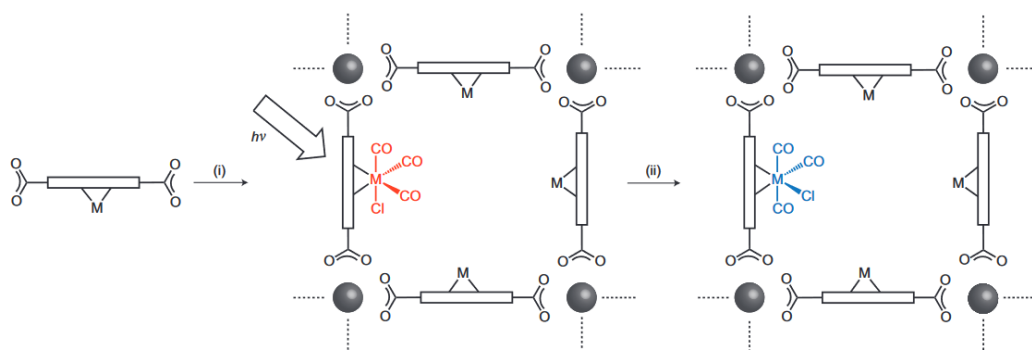


**Figure 1.17** Schematic of the Mn(diimine-dicarboxylic acid)(CO)<sub>3</sub>Cl linker (*left*). i) Upon incorporation into a MOF with Mn(II) centres (black spheres) (*middle*) and the crystal structure shows the *fac* isomer shown in red. ii) After UV irradiation, rearrangement to the *mer* isomer occurs shown in blue, with no effect to the crystallinity of the framework. Taken from reference 90.

This method of incorporating photochemically active groups directly into the framework, rather than as guest molecules in the pores, has been well-studied with azobenzene. There are more publications with the incorporation of azobenzene into MOFs than any other photoswitch (especially as pendent groups in the organic linkers) due to its well-understood photoswitchable nature (Figure 1.18). The *trans*-isomer is the most stable form, which can be converted to the *cis*-isomer upon exposure to UV light.<sup>92</sup>

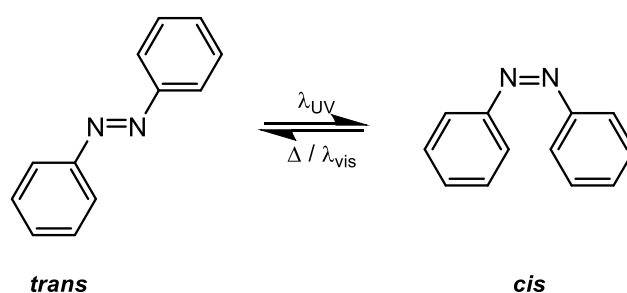


**Figure 1.18** Isomerisation of *trans*-azobenzene upon irradiation with UV light to the *cis*-isomer.

Azo-functionalised linkers in MOFs have been reported since the early 2000s,<sup>93</sup> however photo-induced switching between the *trans* and *cis* states in MOFs was not achieved until 2011 when a mixed linker approach was used.<sup>94</sup> CAU-5 was synthesised by solvothermal reaction of zinc nitrate hexahydrate, 2,6-naphthalenedicarboxylic acid (NDC) and 3-azophenyl-4,4'-bipyridine to give the final product as orange crystals. The zinc paddlewheel motif in the crystal structure is shown in Figure 1.19. The solid-state photoswitching of CAU-5 upon irradiation with UV light (365 nm) was observed using PXRD. There were no notable shifts in peak positions apart from the appearance of two broad reflections were seen associated with the *cis*-isomer, which disappeared upon conversion back to the *trans*-isomer.

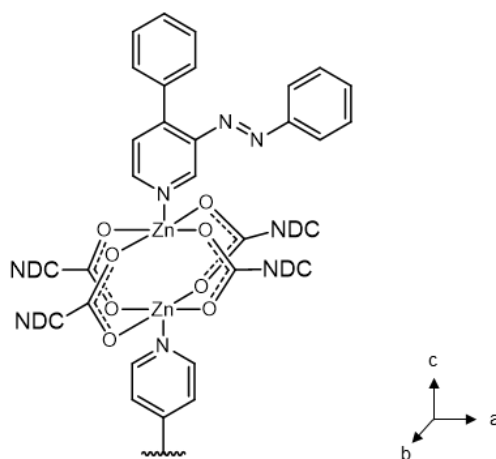


**Figure 1.19** Zinc paddlewheel motif in CAU-5, showing the 2D sheets of metal nodes connected by NDC linkers in the *a,b*-plane. The azo-containing bipyridine linkers are coordinated to the zinc ions in the axial positions. Adapted from reference 94.

A particular interest has grown around the use of photoswitchable MOFs for controlled gas uptake and release. The potential applications include a low-energy method for gas capture and release, particularly if sunlight could be used as a stimulus to trigger release of gas from the framework which would drastically reduce energy costs. Lyndon *et al.* synthesised a zinc-based framework that contains two photoswitchable linkers,<sup>95</sup> including a dicarboxylate linker with azobenzene functionality incorporated in the ‘backbone’ of the linker rather than as a pendent group.<sup>96</sup>  $\text{Zn}(\text{AzDC})(4,4'\text{-BPE})_{0.5}$  (AzDC = 4,4'-azodicarboxylic acid and BPE = *trans*-1,2-bis(4-pyridyl)ethylene) is a triply interpenetrated MOF that exhibits dynamic structural flexibility when exposed to UV light (Figure 1.20). Photoisomerisation occurs in both

linkers resulting in instant release of up to 64% of adsorbed CO<sub>2</sub> as it is effectively ‘squeezed’ from the pores.<sup>95</sup>



**Figure 1.20** Schematic of the reversible photoinduced CO<sub>2</sub> uptake in Zn-(AzDC)(4,4'-BPE)<sub>0.5</sub>. Taken from reference 95.

Another example of CO<sub>2</sub> uptake in a photoactive MOF was reported in 2017 by Huang *et al.* who explored the photoswitching properties of a zirconium framework (AzoMOF).<sup>97</sup> Photoconversion with UV light ( $365 \pm 10$  nm) for 45 minutes followed by irradiation with visible light (420–480 nm) for 20 minutes was repeated for three photoisomerisation cycles without the structural integrity of the sample being affected. A photostationary state was observed after 30 mins of UV irradiation giving a 21% conversion from the *trans* to *cis* isomer (Figure 1.21). To study the polarity of the nanochannels in the framework erythrosine B (EB) was incorporated as a guest molecule (undergoing a red shift in the absorbance spectrum in a less polar environment), which confirmed that the pores becomes more polar as the conversion to the *cis* isomer increased. However, EB is a significantly larger molecule than compared to CO<sub>2</sub> so the usefulness of this approach may be debated. The diffusion kinetics of CO<sub>2</sub> and Ar were investigated and it was reported how the isomerisation in AzoMOF led to changes on the kinetics of CO<sub>2</sub>, but not Ar; this is likely to be a result of argon not possessing a permanent dipole or quadruple moment. Due to the kinetic diameters of both gases being almost equal to one another, this suggested that carbon dioxide is subject to a polar effect from the azobenzene pendent group as it diffuses into the MOF.

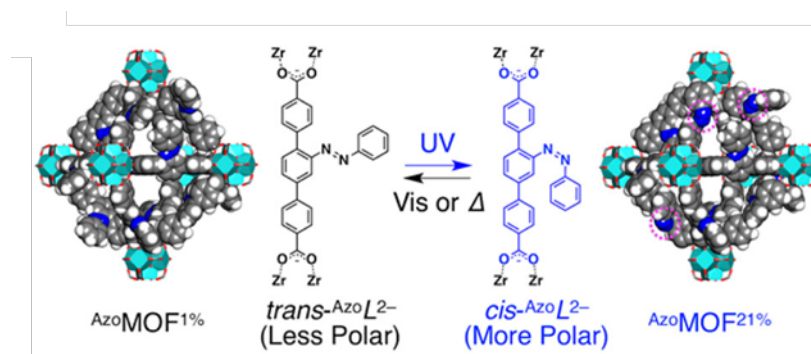


**Figure 1.21** Schematic of <sup>Azo</sup>MOF highlighting the trans-cis isomerisation upon UV irradiation, with the *cis*-azobenzene pendent groups circled in purple (*far right*). Reproduced from reference 97.

Diarylethenes have also been studied in MOFs for their photoswitching properties. For instance, dithienylethenes (Figure 1.22) can undergo a structural ring-closure which results in the two species having very different absorption profiles with an associated colour change.<sup>98</sup> Unlike the azobenzene systems which exhibit large structural changes but only show subtle differences in their UV-visible absorption spectra, dithienylethenes do not have such a significant structural transformation but are extremely stable to photodegradation.<sup>99</sup> This is advantageous for studying these systems via photocrystallographic methods.

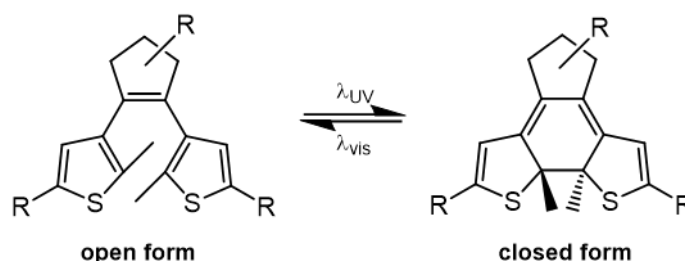


**Figure 1.22** Dithienylethene molecules undergoing ring-closure upon exposure to UV light.

Guo and co-workers used a similar approach to Lyndon *et al.* (Figure 1.21) to synthesise a neutral photoresponsive diarylethene MOF from zinc nitrate, biphenyl-4,4'-dicarboxylic acid and 1,2-bis(2'-methyl-5'-(pyrid-4''-yl)thien-3'-yl)perfluorocyclopentene.<sup>100</sup> Upon irradiation with UV light (300 nm) a colour change from yellow to blue was observed, with a fourfold change in CO<sub>2</sub> adsorption capacity also seen. When irradiated with visible light (600 nm), there was instantaneous release of the adsorbed CO<sub>2</sub>. This work highlighted the possibility of low-energy gas capture and release in an extremely thermostable framework.

The use of an external stimulus to control the gas adsorption selectivity in MOFs had not been reported before 2017 until Guo and co-workers also proved that the above-mentioned framework could be used as a dual temperature and light-responsive C<sub>2</sub>H<sub>2</sub>/C<sub>2</sub>H<sub>4</sub> switch.<sup>101</sup> Upon irradiation with UV light, weak separation occurred giving a mixed gas output as the ring-closing occurred. However, when irradiated with visible light the ring-opening reaction led to a high gas separation with pure C<sub>2</sub>H<sub>2</sub> being generated.

The final class of photoactive switches to be discussed in this section are spiropyrans, which were reported as early as 1948.<sup>102</sup> They are typically made up of a heterocyclic fragment and a pyran fragment connected by an asymmetric spiro-centre. The C–O bond can be cleaved upon irradiation with UV light, resulting in a structural change from the asymmetric ‘closed’ (SP) form to the ‘open’ planar merocyanine (MC) form shown in Figure 1.23. The merocyanine name is given due to the two terminal heteroatoms connected by a polymethine chain.<sup>103</sup>

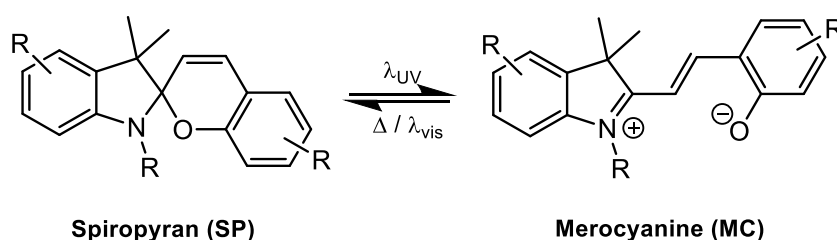


**Figure 1.23** Reversible photo-isomerisation of a spiropyran molecule.

The MC state has a single transition in the visible region (*ca.* 550 – 600 nm) when dissolved in most non-polar solvents.<sup>99</sup> This transformation is also associated with a colour change due to the shift in absorption as a result of the increased conjugation in the molecule. The recovery from MC→SP can occur under irradiation with visible light, as well as thermally.<sup>104</sup> Protonated species of the SP and MC forms have been found to exist.<sup>99</sup> Photoswitching of these isomers in the gas phase has been investigated using combined laser spectroscopy and ion mobility spectrometry by Markworth *et al.* in which the multiple conformations were observed (Figure 1.24).<sup>105</sup>

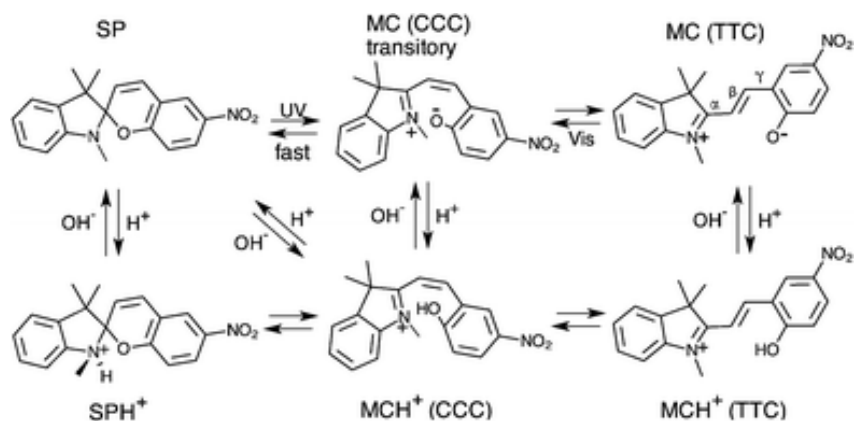


**Figure 1.24** Transformations of neutral and protonated spiropyran and merocyanine molecules upon irradiation and through acid–base equilibria. Reproduced from reference 105.

As well as exhibiting photochromism upon irradiation with UV light, spiropyrans have also been found to be solvatochromic, electrochromic, mechanochromic and acidochromic.<sup>106–108</sup> The zwitterionic form has been found to bind to metal ions,<sup>109,110</sup> therefore spiropyran-based molecules have found applications as different types of sensors.<sup>111–113</sup> Other applications have been summarised by Lukyanov *et al.*<sup>12</sup> which include the use of these compounds in photochromic optical lenses,<sup>106</sup> in the cosmetic industry in nail varnishes and in materials that have been used for recording optical data.

In the last five years, there have been more reports of spiropyran incorporation into MOFs, some of which are described in Chapter 4. These molecules are of specific interest due to the flexibility of the open merocyanine form which can result in potential reduction of strain on a framework upon photoswitching (particularly when compared with azobenzene). The aim of the final chapter in this thesis was to use functionalised spiropyran linkers in the syntheses of frameworks, with the expectation of exhibiting structural control upon irradiation of the framework with UV light.

## 1.5 Summary

The self-assembly and crystallisation of metal-organic frameworks can be very unpredictable with the structural outcomes affected by several different factors. Section 1.2 demonstrated how altering the synthetic conditions can influence the topology of frameworks simply by changing the temperature, reaction solvents or the pH of a solution. MOF design using the isorecticular process based on the structure of the metal nodes was very common during the early 2000s, however Section 1.3 emphasised the newer approaches to using flexible linkers which, when combined with different metals result in a variety of structures due to the metal- and linker-directing effects. One of the most interesting ways of controlling structure in MOFs is exposure to an external stimulus. Section 1.4 highlighted many examples of stimuli-responsive frameworks with fascinating properties, with those responsive to light being the most relevant to the area of work described in the subsequent chapters of this thesis.

## 1.6 Thesis scope

The effort of this research was to determine the numerous ways in which structural control can be exhibited within metal-organic frameworks; the goal was to synthesise frameworks with spiropyran-based linkers in which the guest uptake and release can be controlled by exposure to light.

Chapter 2 describes the application of an in-situ NMR technique to study the formation processes of metal-organic frameworks, in collaboration with colleagues at Cardiff University. Five frameworks, MFM-500(Ni), AlPO-5, lithium-tartrate MOFs, MOF-5, and a novel spiropyran-based framework were chosen due to the multiple NMR active nuclei present in the syntheses ( $^1\text{H}$ ,  $^{13}\text{C}$  and  $^{31}\text{P}$ ) and for reasons described in more depth in the chapter.

Chapter 3 describes a series of coordination polymers that were synthesised using a linker with limited conformational flexibility. Benzimidazolone diacetic acid contains two carboxylic acid binding sites that are connected to a planar core via  $-\{\text{CH}_2\}-$  spacers which can rotate freely in solution. Four group 2 and three transition

metal-based materials were formed and structural analysis was obtained using single-crystal X-ray diffraction. The coordination geometries observed were found to be an interplay of linker and metal coordination preferences.

Chapter 4 details the combinatorial attempts to synthesise metal-organic frameworks that incorporate spiropyran-functionalised linkers ( $H_2L^2$  and  $H_4L^3$ ) into the backbone of the frameworks. Seven promising materials have been formed and initial PXRD analysis confirms their crystallinity. SXCRD analysis of the copper-based material provides evidence of spiropyran incorporation into a metal-organic framework. The factors influencing the ring-opening of spiropyrans in solution have also been investigated using UV-vis spectroscopy, with the aim of attempting to predict the reaction conditions under which crystalline products can form.

## 1.7 References

- 1 S. Kitagawa, R. Kitaura and S. Noro, *Angew. Chemie Int. Ed.*, 2004, **43**, 2334–2375.
- 2 S. R. Batten, N. R. Champness, X.-M. Chen, J. Garcia-Martinez, S. Kitagawa, L. Öhrström, M. O’Keeffe, M. Paik Suh and J. Reedijk, *Pure Appl. Chem.*, 2013, **85**, 1715–1724.
- 3 T. R. Cook, Y.-R. Zheng and P. J. Stang, *Chem. Rev.*, 2013, **113**, 734–777.
- 4 P. Z. Moghadam, A. Li, S. B. Wiggin, A. Tao, A. G. P. Maloney, P. A. Wood, S. C. Ward and D. Fairen-Jimenez, *Chem. Mater.*, 2017, **29**, 2618–2625.
- 5 N. Hosono and S. Kitagawa, *Acc. Chem. Res.*, 2018, **51**, 2437–2446.
- 6 M. O’Keeffe, *Chem. Soc. Rev.*, 2009, **38**, 1215–1217.
- 7 S. R. Venna and M. A. Carreon, *Chem. Eng. Sci.*, 2015, **124**, 3–19.
- 8 H. B. Tanh Jeazet, C. Staudt and C. Janiak, *Dalton Trans.*, 2012, 41, 14003–14027.
- 9 T. D. Bennett and A. K. Cheetham, *Acc. Chem. Res.*, 2014, **47**, 1555–1562.
- 10 N. Stock and S. Biswas, *Chem. Rev.*, 2012, **112**, 933–969.
- 11 A. J. Howarth, A. W. Peters, N. A. Vermeulen, T. C. Wang, J. T. Hupp and O. K. Farha, *Chem. Mater.*, 2017, **29**, 26–39.
- 12 V. V Butova, M. A. Soldatov, A. A. Guda, K. A. Lomachenko and C. Lamberti, *Russ. Chem. Rev.*, 2016, **85**, 280–307.
- 13 D. J. Tranchemontagne, J. R. Hunt and O. M. Yaghi, *Tetrahedron*, 2008, **64**, 8553–8557.
- 14 Y. Sun and H. C. Zhou, *Sci. Technol. Adv. Mater.*, 2015, 16, 054202.
- 15 Z. Ni and R. I. Masel, *J. Am. Chem. Soc.*, 2006, **128**, 12394–12395.
- 16 H. Al-Kutubi, J. Gascon, E. J. R. Sudhölter and L. Rassaei, *ChemElectroChem*, 2015, **2**, 462–474.
- 17 A. Pichon, A. Lazuen-Garay and S. L. James, *CrystEngComm*, 2006, **8**, 211–214.
- 18 W. J. Son, J. Kim, J. Kim and W. S. Ahn, *Chem. Commun.*, 2008, **0**, 6336–6338.
- 19 A. Schaate, P. Roy, A. Godt, J. Lippke, F. Waltz, M. Wiebcke and P. Behrens, *Chem. - A Eur. J.*, 2011, **17**, 6643–6651.
- 20 S. Kitagawa, *Acc. Chem. Res.*, 2017, **50**, 514–516.
- 21 O. K. Farha, I. Eryazici, N. C. Jeong, B. G. Hauser, C. E. Wilmer, A. A. Sarjeant, R. Q. Snurr, S. T. Nguyen, A. Ö. Yazaydin and J. T. Hupp, *J. Am. Chem. Soc.*, 2012, **134**, 15016–15021.
- 22 J. R. Li, R. J. Kuppler and H. C. Zhou, *Chem. Soc. Rev.*, 2009, **38**, 1477–1504.
- 23 H. Li, K. Wang, Y. Sun, C. T. Lollar, J. Li and H.-C. Zhou, *Mater. Today*, 2018, **21**, 108–121.
- 24 R. E. Morris and P. S. Wheatley, *Angew. Chemie Int. Ed.*, 2008, **47**, 4966–4981.

- 25 K. Sumida, D. L. Rogow, J. A. Mason, T. M. McDonald, E. D. Bloch, Z. R. Herm, T.-H. Bae and J. R. Long, *Chem. Rev.*, 2012, **112**, 724–781.
- 26 D. Sun, S. Ma, Y. Ke, D. J. Collins and H. C. Zhou, *J. Am. Chem. Soc.*, 2006, **128**, 3896–3897.
- 27 S. Ma, D. Sun, M. Ambrogio, J. A. Fillinger, S. Parkin and H. C. Zhou, *J. Am. Chem. Soc.*, 2007, **129**, 1858–1859.
- 28 E. Barea, C. Montoro and J. A. R. Navarro, *Chem. Soc. Rev.*, 2014, **43**, 5419–5430.
- 29 A. J. Tansell, C. L. Jones and T. L. Easun, *Chem. Cent. J.*, 2017, 11, 100.
- 30 L. E. Kreno, K. Leong, O. K. Farha, M. Allendorf, R. P. Van Duyne and J. T. Hupp, *Chem. Rev.*, 2012, **112**, 1105–1125.
- 31 F.-Y. Yi, D. Chen, M.-K. Wu, L. Han and H.-L. Jiang, *Chempluschem*, 2016, **81**, 675–690.
- 32 Y. Zhang, S. Yuan, G. Day, X. Wang, X. Yang and H.-C. Zhou, *Coord. Chem. Rev.*, 2018, **354**, 28–45.
- 33 J. Lee, O. K. Farha, J. Roberts, K. A. Scheidt, S. T. Nguyen and J. T. Hupp, *Chem. Soc. Rev.*, 2009, **38**, 1450–1459.
- 34 L. Wang, M. Zheng and Z. Xie, *J. Mater. Chem. B*, 2018, **6**, 707–717.
- 35 R. Zhao, Z. Liang, R. Zou and Q. Xu, *Joule*, 2018, **2**, 2235–2259.
- 36 S. M. Cohen, *Chem. Rev.*, 2012, **112**, 970–1000.
- 37 L. Jiao, J. Y. R. Seow, W. S. Skinner, Z. U. Wang and H.-L. Jiang, *Mater. Today*, 2019, **27**, 43–68.
- 38 M. D. Allendorf and V. Stavila, *CrystEngComm*, 2015, **17**, 229–246.
- 39 P. Z. Moghadam, S. M. J. Rogge, A. Li, C.-M. Chow, J. Wieme, N. Moharrami, M. Aragonés-Anglada, G. Conduit, D. A. Gomez-Gualdron, V. Van Speybroeck and D. Fairen-Jimenez, *Matter*, 2019, **1**, 219–234.
- 40 S. M. Moosavi, A. Chidambaram, L. Talirz, M. Haranczyk, K. C. Stylianou and B. Smit, *Nat. Commun.*, 2019, **10**, 539.
- 41 S. S.-Y. Chui, S. M.-F. Lo, J. P. H. Charmant, A. G. Orpen and I. D. Williams, *Science (80-. )*, 1999, **283**, 1148–1150.
- 42 T. M. C. Team, Materials Cloud, <https://www.materialscloud.org/>, (accessed 29 March 2019).
- 43 R. Seetharaj, P. V. Vandana, P. Arya and S. Mathew, *Arab. J. Chem.*, 2019, **12**, 295–315.
- 44 Y. Huang, J. Zhang, D. Yue, Y. Cui, Y. Yang, B. Li and G. Qian, *Chem. - A Eur. J.*, 2018, **24**, 13231–13237.
- 45 P. M. Forster, A. R. Burbank, C. Livage, G. Férey and A. K. Cheetham, *Chem. Commun.*, 2004, 368–369.

- 46 C. A. F. de Oliveira, F. F. da Silva, I. Malvestiti, V. R. dos S. Malta, J. D. L. Dutra, N. B. da Costa, R. O. Freire and S. A. Júnior, *J. Solid State Chem.*, 2013, **197**, 7–13.
- 47 Y. Wei, Y. Yu, R. Sa, Q. Li and K. Wu, *CrystEngComm*, 2009, **11**, 1054–1060.
- 48 S. K. Ghosh and S. Kitagawa, *CrystEngComm*, 2008, **10**, 1739–1742.
- 49 L. Luo, G. C. Lv, P. Wang, Q. Liu, K. Chen and W. Y. Sun, *CrystEngComm*, 2013, **15**, 9537–9543.
- 50 M. J. Van Vleet, T. Weng, X. Li and J. R. Schmidt, *Chem. Rev.*, 2018, **118**, 3681–3721.
- 51 S. L. James, *Chem. Soc. Rev.*, 2003, **32**, 276–288.
- 52 K. Shen, M. Zhang and H. Zheng, *CrystEngComm*, 2015, **17**, 981–991.
- 53 J. Hu, L. Huang, X. Yao, L. Qin, Y. Li, Z. Guo, H. Zheng and Z. Xue, *Inorg. Chem.*, 2011, **50**, 2404–2414.
- 54 O. M. Yaghi, M. O’Keeffe, N. W. Ockwig, H. K. Chae, M. Eddaoudi and J. Kim, *Nature*, 2003, 423, 705–714.
- 55 M. Eddaoudi, J. Kim, N. Rosi, D. Vodak, J. Wachter, M. O’Keeffe and O. M. Yaghi, *Science (80-. )*, 2002, **295**, 469–472.
- 56 X. Lin, I. Telepeni, A. J. Blake, A. Dailly, C. M. Brown, J. M. Simmons, M. Zoppi, G. S. Walker, K. M. Thomas, T. J. Mays, P. Hubberstey, N. R. Champness and M. Schröder, *J. Am. Chem. Soc.*, 2009, **131**, 2159–2171.
- 57 J. H. Cavka, S. Jakobsen, U. Olsbye, N. Guillou, C. Lamberti, S. Bordiga and K. P. Lillerud, *J. Am. Chem. Soc.*, 2008, **130**, 13850–13851.
- 58 R. S. Forgan, R. J. Marshall, M. Struckmann, A. B. Bleine, D.-L. Long, M. C. Bernini and D. Fairen-Jimenez, *CrystEngComm*, 2015, **17**, 299–306.
- 59 X. He, X. P. Lu, Z. F. Ju, C. J. Li, Q. K. Zhang and M. X. Li, *CrystEngComm*, 2013, **15**, 2731–2744.
- 60 J. Navarro-Sánchez, I. Mullor-Ruíz, C. Popescu, D. Santamaría-Pérez, A. Segura, D. Errandonea, J. González-Platas and C. Martí-Gastaldo, *Dalton Trans.*, 2018, **47**, 10654–10659.
- 61 J. Rabone, Y.-F. Yue, S. Y. Chong, K. C. Stylianou, J. Bacsá, D. Bradshaw, G. R. Darling, N. G. Berry, Y. Z. Khimyak, A. Y. Ganin, P. Wiper, J. B. Claridge and M. J. Rosseinsky, *Science (80-. )*, 2010, **329**, 1053–1057.
- 62 E. H. Cox and G. L. McLendon, *Curr. Opin. Chem. Biol.*, 2000, **4**, 162–165.
- 63 J. Haddad, G. F. S. Whitehead, A. P. Katsoulidis and M. J. Rosseinsky, *Faraday Discuss.*, 2017, **201**, 327–335.
- 64 F.-X. Coudert, *Chem. Mater.*, 2015, **27**, 1905–1916.
- 65 M. Shivanna, Q. Y. Yang, A. Bajpai, E. Patyk-Kazmierczak and M. J. Zaworotko, *Nat. Commun.*, 2018, **9**, 3080.

- 66 F.-X. Coudert, *Acta Crystallogr. Sect. B Struct. Sci. Cryst. Eng. Mater.*, 2015, **71**, 585–586.
- 67 S. H. Lapidus, G. J. Halder, P. J. Chupas and K. W. Chapman, *J. Am. Chem. Soc.*, 2013, **135**, 7621–7628.
- 68 A. Półrolniczak, S. Sobczak and A. Katrusiak, *Inorg. Chem.*, 2018, **57**, 8942–8950.
- 69 J. Pang, C. Liu, Y. Huang, M. Wu, F. Jiang, D. Yuan, F. Hu, K. Su, G. Liu and M. Hong, *Angew. Chemie*, 2016, **128**, 7604–7608.
- 70 R. Ou, H. Zhang, J. Wei, S. Kim, L. Wan, N. S. Nguyen, Y. Hu, X. Zhang, G. P. Simon and H. Wang, *Adv. Mater.*, 2018, **30**, 1802767.
- 71 C. Serre, C. Mellot-Draznieks, S. Surble, N. Audebrand, Y. Filinchuk and G. Férey, *Science (80-. )*, 2007, **315**, 1828–1831.
- 72 E. J. Carrington, C. A. McAnally, A. J. Fletcher, S. P. Thompson, M. Warren and L. Brammer, *Nat. Chem.*, 2017, **9**, 882–889.
- 73 A. Lan, K. Li, H. Wu, D. H. Olson, T. J. Emge, W. Ki, M. Hong and J. Li, *Angew. Chemie Int. Ed.*, 2009, **48**, 2334–2338.
- 74 M. D. Allendorf, C. A. Bauer, R. K. Bhakta and R. J. T. Houk, *Chem. Soc. Rev.*, 2009, **38**, 1330–1352.
- 75 Y. Cui, Y. Yue, G. Qian and B. Chen, *Chem. Rev.*, 2012, **112**, 1126–1162.
- 76 S. A. Diamantis, A. Margariti, A. D. Pournara, G. S. Papaefstathiou, M. J. Manos and T. Lazarides, *Inorg. Chem. Front.*, 2018, **5**, 1493–1511.
- 77 W. P. Lustig, S. Mukherjee, N. D. Rudd, A. V. Desai, J. Li and S. K. Ghosh, *Chem. Soc. Rev.*, 2017, **46**, 3242–3285.
- 78 C. L. Jones, A. J. Tansell and T. L. Easun, *J. Mater. Chem. A*, 2016, **4**, 6714–6723.
- 79 P. R. Raithby, *IUCrJ*, 2015, **2**, 5–6.
- 80 A. A. Beharry and G. A. Woolley, *Chem. Soc. Rev.*, 2011, **40**, 4422–4437.
- 81 P. Coppens, D. V. Fomitchev, M. D. Carducci and K. Culp, *J. Chem. Soc. Dalton Trans.*, 1998, **0**, 865–872.
- 82 P. Coppens, *Struct. Dyn. (Melville, N.Y.)*, 2017, **4**, 032102.
- 83 D. V. Fomitchev and P. Coppens, *Inorg. Chem.*, 2002, **35**, 7021–7026.
- 84 A. Y. Kovalevsky, G. King, K. A. Bagley and P. Coppens, *Chem. - A Eur. J.*, 2005, **11**, 7254–7264.
- 85 A. Y. Kovalevsky, K. A. Bagley and P. Coppens, *J. Am. Chem. Soc.*, 2002, **124**, 9241–9248.
- 86 S. K. Brayshaw, J. W. Knight, P. R. Raithby, T. L. Savarese, S. Schiffers, S. J. Teat, J. E. Warren, M. R. Warren and IUCr, *J. Appl. Crystallogr.*, 2010, **43**, 337–340.
- 87 L. J. McCormick, N. Giordano, S. J. Teat and C. M. Beavers, *Crystals*, 2017, **7**, 382.

- 88 M. R. Warren, S. K. Brayshaw, A. L. Johnson, S. Schiffers, P. R. Raithby, T. L. Easun, M. W. George, J. E. Warren and S. J. Teat, *Angew. Chemie Int. Ed.*, 2009, **48**, 5711–5714.
- 89 A. J. Blake, N. R. Champness, T. L. Easun, D. R. Allan, H. Nowell, M. W. George, J. Jia and X.-Z. Sun, *Nat. Chem.*, 2010, **2**, 688–694.
- 90 M. D. Ward, *Nat. Chem.*, 2010, **2**, 610–611.
- 91 T. L. Easun, J. Jia, J. A. Calladine, D. L. Blackmore, C. S. Stapleton, K. Q. Vuong, N. R. Champness and M. W. George, *Inorg. Chem.*, 2014, **53**, 2606–2612.
- 92 J. Griffiths, *Chem. Soc. Rev.*, 1972, **1**, 481–493.
- 93 Y. Liu, J. F. Eubank, A. J. Cairns, J. Eckert, V. C. Kravtsov, R. Luebke and M. Eddaoudi, *Angew. Chemie Int. Ed.*, 2007, **46**, 3278–3283.
- 94 A. Modrow, D. Zargarani, R. Herges and N. Stock, *Dalton Trans.*, 2011, **40**, 4217–4222.
- 95 R. Lyndon, K. Konstas, B. P. Ladewig, P. D. Southon, P. C. J. Kepert and M. R. Hill, *Angew. Chem. Int. Ed. Engl.*, 2013, **52**, 3695–3698.
- 96 L. Wang and Q. Li, *Chem. Soc. Rev.*, 2018, **47**, 1044–1097.
- 97 H. Huang, H. Sato and T. Aida, *J. Am. Chem. Soc.*, 2017, **139**, 8784–8787.
- 98 E. A. Dolgoplova, A. M. Rice, C. R. Martin and N. B. Shustova, *Chem. Soc. Rev.*, 2018, **47**, 4710–4728.
- 99 R. Klajn, *Chem. Soc. Rev.*, 2014, **43**, 148–184.
- 100 F. Luo, C. Bin Fan, M. B. Luo, X. L. Wu, Y. Zhu, S. Z. Pu, W.-Y. Xu and G.-C. Guo, *Angew. Chemie Int. Ed.*, 2014, **53**, 9298–9301.
- 101 C. Bin Fan, L. Le Gong, L. Huang, F. Luo, R. Krishna, X. F. Yi, A. M. Zheng, L. Zhang, S. Z. Pu, X. F. Feng, M. B. Luo and G. C. Guo, *Angew. Chemie Int. Ed.*, 2017, **56**, 7900–7906.
- 102 A. Mustafa, *Chem. Rev.*, 1948, **43**, 509–523.
- 103 A. V Kulinich and A. A. Ishchenko, *Russ. Chem. Rev.*, 2009, **78**, 141–164.
- 104 S. V. Paramonov, V. Lokshin and O. A. Fedorova, *J. Photochem. Photobiol. C Photochem. Rev.*, 2011, **12**, 209–236.
- 105 P. B. Markworth, B. D. Adamson, N. J. A. Coughlan, L. Goerigk and E. J. Bieske, *Phys. Chem. Chem. Phys.*, 2015, **17**, 25676–25688.
- 106 V. I. Minkin, *Chem. Rev.*, 2004, **104**, 2751–2776.
- 107 D. A. Davis, A. Hamilton, J. Yang, L. D. Cremar, D. Van Gough, S. L. Potisek, M. T. Ong, P. V. Braun, T. J. Martínez, S. R. White, J. S. Moore and N. R. Sottos, *Nature*, 2009, **459**, 68–72.
- 108 W. Tian and J. Tian, *Dye. Pigment.*, 2014, **105**, 66–74.
- 109 J. Ren and H. Tian, *Sensors*, 2007, **7**, 3166–3178.

- 110 J. T. C. Wojtyk, E. Buncel and P. M. Kazmaier, *Chem. Commun.*, 1998, **0**, 1703–1704.
- 111 N. Shao, Y. Zhang, S. M. Cheung, R. H. Yang, W. H. Chan, T. Mo, K. A. Li and F. Liu, *Anal. Chem.*, 2005, **77**, 7294–7303.
- 112 M. Natali, L. Soldi and S. Giordani, *Tetrahedron*, 2010, **66**, 7612–7617.
- 113 A. Abdollahi, A. Mouraki, M. H. Sharifian and A. R. Mahdavian, *Carbohydr. Polym.*, 2018, **200**, 583–594.



---

## **Chapter 2**

# **CLASSIC NMR Studies of the Formation Processes of MOFs**

---

## 2 CLASSIC NMR Studies of the Formation Processes of MOFs

---

### 2.1 Introduction

MOFs can be formed either by conventional solvothermal synthesis or more modern microwave-assisted syntheses,<sup>1-3</sup> leading to many reports on the formation of new materials and their properties. To date, the majority of the characterisation is carried out post-synthetically meaning that the mechanistic aspects of the formation process are often sparsely investigated. This chapter sets out to discuss examples of in-situ monitoring using various techniques before focussing on our use of a novel NMR approach to study the entire reaction of framework materials.

The formation of SBUs as a key step in the assembly of MOFs was described back in 2001 by Férey,<sup>4</sup> but it was not experimentally reported until 2009 by Shekhah *et al.* using surface plasmon resonance (SPR) spectroscopy.<sup>5</sup> In recent years, there have been further developments into understanding the solvothermal synthesis of inorganic materials as structural information is normally obtained *post hoc*. The literature mostly reports the use of X-ray diffraction techniques to study the crystallisation processes that influence the syntheses of MOFs.<sup>6,7</sup>

In-situ energy dispersive X-ray diffraction was used to study the formation of zirconium-fumarate (Zr-fum) MOFs in 2014 by Zahn *et al.* using a coordination modulation synthetic approach to increase the crystallinity of the final products.<sup>8</sup> The addition of formic acid as a modulator in a water-based system was found to decrease the rate of reaction. The opposite effect was seen when formic acid was used in DMF-based conditions; the small amount of water in the formic acid was found to have strong accelerating effect, dramatically increasing the kinetic rate of formation of Zr-fum MOF. The effect of temperature was also monitored leading to the conclusion that the nucleation stage appears to be the rate-limiting step.

In another example using synchrotron radiation, Wu and co-workers have shown that it is possible to gain high-quality structural information with in-situ X-ray diffraction measurements on reactions under laboratory conditions using beamline I12 at Diamond Light Source; this ultimately provides significant new insights into the formation of MOF materials.<sup>9-11</sup> In 2015, Wu *et al.* described how angular dispersive

XRD was used to study the synthesis of a cobalt-containing MOF, in which a cation-exchanged polymer resin was both a template and metal ion source.<sup>12</sup> Their findings detailed the first reported observation of a rapid solid-state rearrangement of intermediate to product during the formation of  $(\text{H}_2\text{NMe}_2)_2[\text{Co}_3(\text{BDC})_4] \cdot y\text{DMF}$ ; this is different to syntheses of, for example, MIL-53(Al)<sup>6</sup> and MIL-47,<sup>13</sup> in which the intermediates can undergo a dissolution-recrystallisation process that ultimately leads to the thermodynamically stable product. In 2017, the in-situ monitoring of a continuous MOF synthesis was reported by Polyzoidis *et al.*<sup>14</sup> Time-resolved powder X-ray diffraction (PXRD) was used to monitor the crystallite formation of ZIF-8, where the MOF was found to form in eight seconds; crystal growth occurred immediately with nucleation and the kinetic measurements proposed a diffusion-controlled growth mechanism.

One of the biggest challenges is that diffraction data gives information about the crystallinity of a material but does not provide information about the changes occurring in the reaction solution prior to solid formation. Over the past twenty years, there has been significant progress in understanding some of the parameters that control the crystallisation of MOFs in solution. The developments in density functional theory (DFT) and enhancements with in-situ synchrotron X-ray methods have been summarised in a recent review by Cheetham, Kieslich and Yeung, shedding light on the possible challenges in this field of research.<sup>15</sup> Scattering techniques can offer a useful insight to the crystal growth and nucleation steps of nano- or microscale particles in solution.<sup>16</sup> Small- and wide-angle X-ray scattering (SAXS and WAXS) techniques have been combined in time-resolved in-situ studies, including those by Stavitski *et al.* to monitor the crystallisation of two aluminium frameworks<sup>17</sup> and Wiebcke and co-workers to monitor the rapid formation of ZIF-8.<sup>18</sup>

Microscopy techniques have also been exploited to study the growth of various types of MOF. Liquid cell transmission electron microscopy (LCTEM) can be advantageous as it allows for the internal structural features of materials in liquids to be studied. Patterson *et al.* used the technique in 2015 to observe the real time growth of metal-organic frameworks with a high magnification.<sup>19</sup> More recently, atomic force microscopy (AFM) has become a popular technique to use in combination with spectroscopic methods to understand the growth mechanisms of molecular materials

on a nanometre scale. In 2017, Weckhuysen and co-workers used a combined AFM-vibrational spectroscopy method to understand the nucleation and growth of ZIF thin films, allowing the size and number of ZIF nuclei deposited during the synthetic procedure to be quantified.<sup>20</sup> In 2018 they reported the use of infrared reflection absorption spectroscopy along with AFM to examine the assembly process of surface mounted MOF (SURMOF) films in which they were able to optimise the synthesis of (100) oriented HKUST-1 thin-films.<sup>21</sup> The above-mentioned microscopy techniques are extremely useful when combined with other X-ray experiments and spectroscopy methods as various length scales are probed, providing a complete picture of the MOF crystallisation process once nucleation begins.

NMR techniques can also be used; Hoffmann *et al.* reviewed the field of solid-state NMR spectroscopy applications to study the structure, dynamics and flexibility of framework materials and as a method to characterise host–guest interactions with adsorbed species.<sup>22</sup> In addition, the structural and dynamic studies of small molecule binding in MOFs by a range of techniques including pulsed field gradient NMR have been described in a review by Schröder and co-workers,<sup>23</sup> in which diffusion studies of guest molecules within the pores and channels of porous MOFs (such as CO<sub>2</sub> in MOF-74-Mg) show that such NMR experiments offer important information on the kinetics of gas loading.<sup>24,25</sup> Another example is that by Moreau *et al.* in which <sup>2</sup>H NMR has been used to investigate the rotational and flipping dynamics of the phenyl groups, in the solid state, within selectively deuterated MFM-180-d<sub>16</sub> and MFM-181-d<sub>16</sub>.<sup>26</sup>

The methods described in this section thus far do not look at the pre-nucleation stages *or* the “whole system” of a reaction, therefore a new approach is needed. Combined Liquid- And Solid-State In-situ Crystallisation (CLASSIC) NMR is able to provide the time-evolution of the polymorphic forms observed in the solid phase, in combination with an understanding of the time-dependent changes that occur in the modes of molecular aggregation and speciation in the liquid phase.<sup>27</sup> The first example using this technique was reported in 2014 by Hughes *et al.* to study the crystallisation of *m*-aminobenzoic acid. Four of the five polymorphs were already known, and it was hoped that the experiment could provide information on tautomeric forms that exist in the liquid and solid-state during the crystallisation process in DMSO. The sample was heated to 120 °C, then cooled to 33 °C over fifteen minutes before the CLASSIC NMR

strategy was applied over 15 hours (Figure 2.1). The time to record the solid-state  $^1\text{H} \rightarrow ^{13}\text{C}$  cross-polarisation (CP) with high-power  $^1\text{H}$  decoupling spectrum was 38.4 minutes and 6.4 minutes for  $^{13}\text{C}$  direct excitation measurement with no decoupling for the liquid-state, giving an effective time resolution of 44.8 minutes for the experiment.

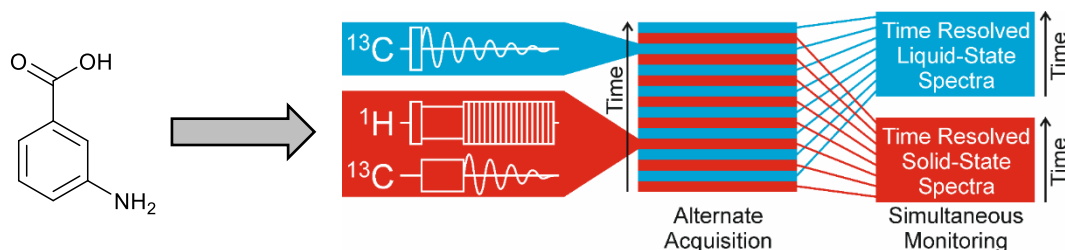


**Figure 2.1** Structure of *m*-aminobenzoic acid (right) and the schematic of alternating  $^{13}\text{C}$  and  $^1\text{H} \rightarrow ^{13}\text{C}$  CP pulses sequences in the CLASSIC NMR experiment to record the liquid and solid-state respectively. Reproduced from reference 27.

The technique allows for detection of only the solid phase in a heterogeneous solid-liquid system, with the liquid phase “invisible” to the measurement, and vice versa.<sup>28</sup> It is a promising approach to study the initial liquid state conversion to solid product from the start to the end of a reaction for a wide variety of MOF syntheses, providing time evolution of formation process.<sup>27</sup>

## 2.2 Aim and objectives

This chapter describes application of the CLASSIC NMR approach to the study of MOF growth from the very beginning of the reaction through to the end. The objectives were to:

- i) Apply the CLASSIC NMR technique to several known MOF systems to test its capabilities and limitations.

The formation of different frameworks containing NMR active nuclei, such as  $^1\text{H}$ ,  $^{13}\text{C}$  and  $^{31}\text{P}$  were monitored to determine if the concentrations needed for NMR experiments resulted in different framework structures from those reported in the literature.

- ii) Investigate the stages of the reaction prior to nucleation.

The reactant dissolution and chemical changes of the linkers occurring in the liquid-state of the reaction prior to formation of solid material was monitored.

- iii) Obtaining the rate constants for the reactions.

The nucleation and growth stages of the syntheses were quantified experimentally.

- iv) Compare these findings with literature values.

Our results were compared to the kinetic values obtained using other reported methods to study the formation processes of MOFs to allow for comparison of the effectiveness of the CLASSIC NMR technique.

The technique was applied to four known materials and a novel spiropyran-based MOF (which will form the basis of discussion in Chapter 4). These are MFM-500(Ni)<sup>29</sup> and AIPO-5<sup>30</sup> which both contain hydrogen and phosphorus nuclei that can be studied by NMR. We have also investigated a lithium-tartrate MOF which has interesting phase behaviour and has been studied extensively by diffraction methods.<sup>31</sup> We have studied MOF-5 as the archetypal MOF,<sup>32</sup> and finally we described an attempt to understand the phase behaviour of the synthesis of a spiropyran-based framework.<sup>33</sup>

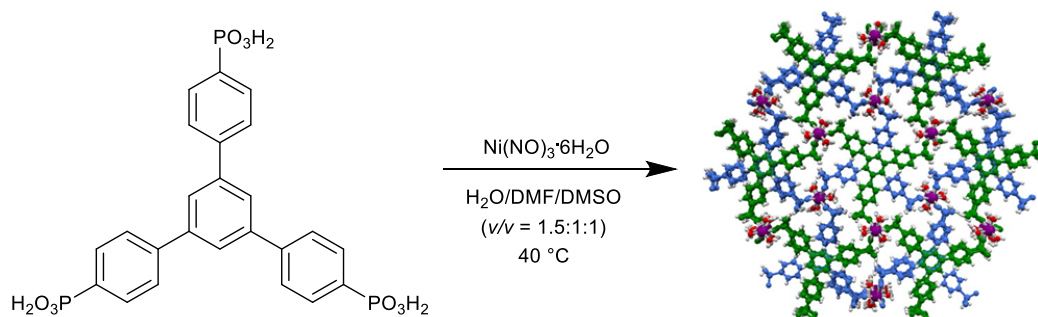
This work in this chapter has been performed in collaboration with Professor Kenneth Harris and Dr Alison Paul at Cardiff University, and Dr Hamish Yeung at University of Oxford. I would like to acknowledge Dr Colan Hughes (Harris Group) for his assistance in creating the NMR pulse sequences and control of the spectrometer during the visits to the UK 850 MHz Solid-State NMR Facility at the University of Warwick. He has also processed the NMR data collected for the five different frameworks and modelled the kinetic data for the MFM-500(Ni) set of experiments.

The MFM-500(Ni) work in Section 2.3.1 has been prepared for publication and uploaded to ChemRxiv (*Exploiting in-situ NMR to monitor the formation of a metal-organic framework*). The figures, NMR peak assignments, fitting of reaction kinetics and ex-situ SAXS data are reproduced from the manuscript, of which the thesis author is first author.

## 2.3 Results and discussion

### 2.3.1 MFM-500(Ni)

MFM-500(Ni) is a proton-conducting nickel-phosphonate framework originally reported by Pili *et al.* in 2016.<sup>29</sup> Scheme 2.1 shows the synthesis involving nickel nitrate hexahydrate and 1,3,5-benzene-tri-*p*-phenyl phosphonic acid (BTPPA) in a solvent mixture of water, dimethylformamide and dimethyl sulfoxide (1.5 : 1 : 1) heated to 40 °C for two days yielding green hexagonal crystals. There are 2D networks of overlapping ligand pairs laying in the *ab* plane, and in the *c*-axis direction the stacks of pairs are offset by 60° with respect to the pairs of ligands above and below. Chains of disordered nickel metal centres with pseudo-octahedral geometry run down the *c*-axis to complete the 3D structure of this MOF.



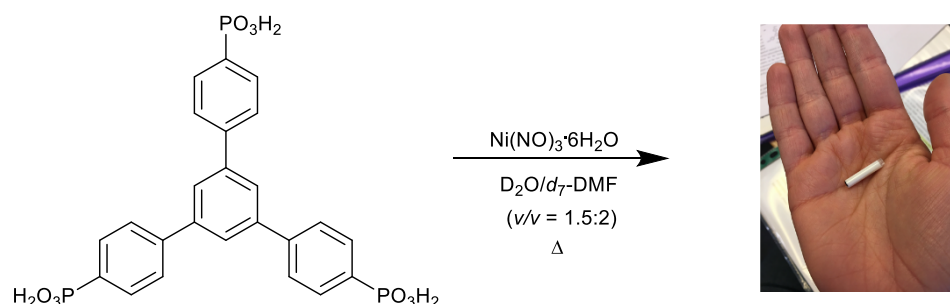
**Scheme 2.1** Reported reaction conditions for the synthesis of MFM-500(Ni). The crystal structure is reproduced from reference 29.

The tris-phosphonate linker was found to be only 50% deprotonated in the reported structure and bound to the nickel metal centres enabling free protons to move within the framework. AC impedance spectroscopy was used to calculate the proton conductivity of  $4.5 \times 10^{-4} \text{ S cm}^{-1}$  at room temperature with a room humidity of 98%. Quasi-elastic neutron scattering (QENS) was used to study the mechanism of proton diffusion in which the first model of “free diffusion inside a sphere” was reported, compared to the more common “jump diffusion between sites” model.<sup>29</sup>

#### 2.3.1.1 Synthesis

The reaction conditions have been adapted from the reported synthesis to enable the formation process of MFM-500(Ni) to be monitored using the CLASSIC NMR approach. This included increasing the reaction solution concentration (due to the

small quantity of material used in 20  $\mu\text{L}$  tube insert for rotor), simplifying the number of solvents in the system and using deuterated solvents (Scheme 2.2).



**Scheme 2.2** Adapted MFM-500(Ni) synthesis in which  $\text{Ni}(\text{NO}_3)_2 \cdot 6\text{H}_2\text{O}$  and BTTPA were added to deuterated solvents ( $\text{D}_2\text{O}/d_7\text{-DMF}$ ) and inserted into a 20  $\mu\text{L}$  Kel-F tube which was placed inside a rotor (shown right).

Figure 2.2 shows the  $^1\text{H}$  NMR spectrum of the BTTPA linker, which was synthesised via a reported method.<sup>34</sup>

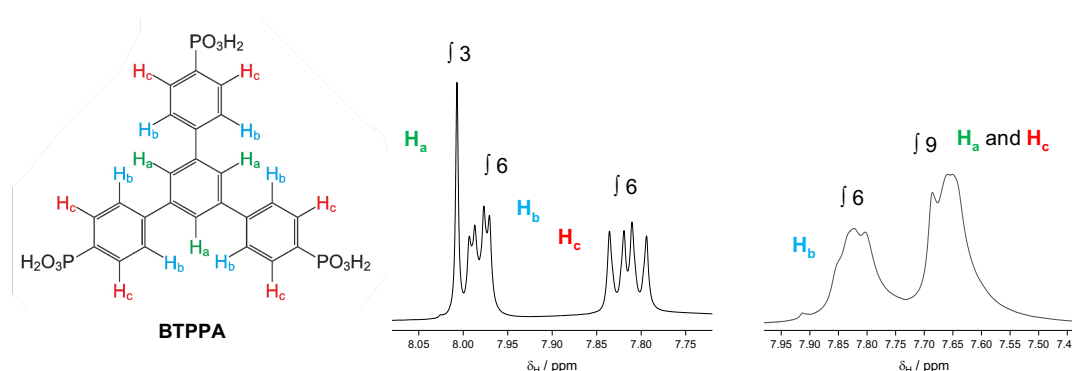


**Figure 2.2**  $^1\text{H}$  NMR spectra showing BTTPA aromatic resonances (left) in  $d_6\text{-DMSO}$  (middle) and the reaction solvents,  $\text{D}_2\text{O}/d_7\text{-DMF}$  (right). The relative integrations of each peak are given, along with the corresponding proton environment.

When dissolved in  $d_6\text{-DMSO}$  the aromatic region of the spectrum is very different to when the molecule is dissolved in the reaction solution mixture ( $\text{D}_2\text{O}/d_7\text{-DMF}$ ) for the CLASSIC NMR experiment. Three proton environments at 8.01, 7.99 and 7.81 ppm ( $\text{H}_a$ ,  $\text{H}_b$  and  $\text{H}_c$ ) are seen in the aromatic region for  $d_6\text{-DMSO}$  which integrate to 3:6:6 protons respectively. However, in the  $\text{D}_2\text{O}/d_7\text{-DMF}$  reaction mixture the aromatic peaks shift upfield and broaden; only two peaks are resolved between 7.5 – 8 ppm and integrate to 6:9 protons respectively. Notably the three core protons ( $\text{H}_a$ ) are shifted upfield relative to the  $\text{H}_b$  and  $\text{H}_c$  protons, meaning that there is an overlap of two of

the proton environments. These shifts, combined with the peak broadening, suggests possible aggregation of the linker in solution. The  $^3\text{P}\{^1\text{H}\}$  NMR spectra show only one phosphorus environment in the both  $d_6$ -DMSO and  $\text{D}_2\text{O}/d_7$ -DMF.

It is possible that at the increased concentration in the  $\text{D}_2\text{O}/d_7$ -DMF mix, aggregation of the linker is occurring ( $\pi$ - $\pi$  stacking arises between molecules that are maximum 3 – 4 Å apart<sup>35</sup> as seen in the MFM-500(Ni) structure). This is consistent with the observed relative shift of the  $\text{H}_a$  protons as the central part of the molecule becomes more shielded from the polar solvent.

In order to investigate this further, variable temperature (VT) NMR was carried out on a sample of BTPPA in  $\text{D}_2\text{O}/d_7$ -DMF with addition of 30  $\mu\text{L}$  of (natural isotopic abundance) DMF to enable identification of the solvent peak (Figure 2.3). At room temperature the peaks are very broad but become more well-resolved by the time the sample reaches 90 °C suggesting dissolution and separation of the aggregates. A mixture of species is clearly present (most probably aggregates, dimers and single molecules) as the peaks do not integrate correctly for a single molecule.

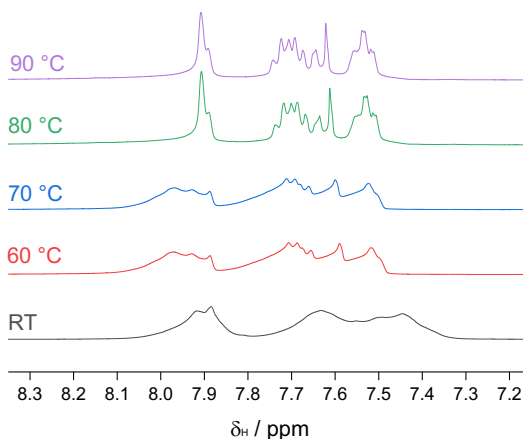


**Figure 2.3** VT NMR spectra of BTPPA in  $\text{D}_2\text{O}/d_7$ -DMF at room temperature and upon heating the sample from 60 – 90 °C.

In the reported crystal structure, the ligands appear in dimeric pairs in which the BTPPA are staggered to each other in an AB arrangement in which the distance between the layer is approximately 3.6 Å. These are adjacent to another dimeric pair but eclipsed with a distance between the atoms approximately 3.9 Å. This is repeated throughout the structure giving an overall AB...BA...AB motif (Figure 2.4). It is

possible that this dimer formation in the published MFM-500(Ni) structure<sup>29</sup> originates from ligand aggregation in solution prior to metal complexation which is consistent with these NMR spectra.

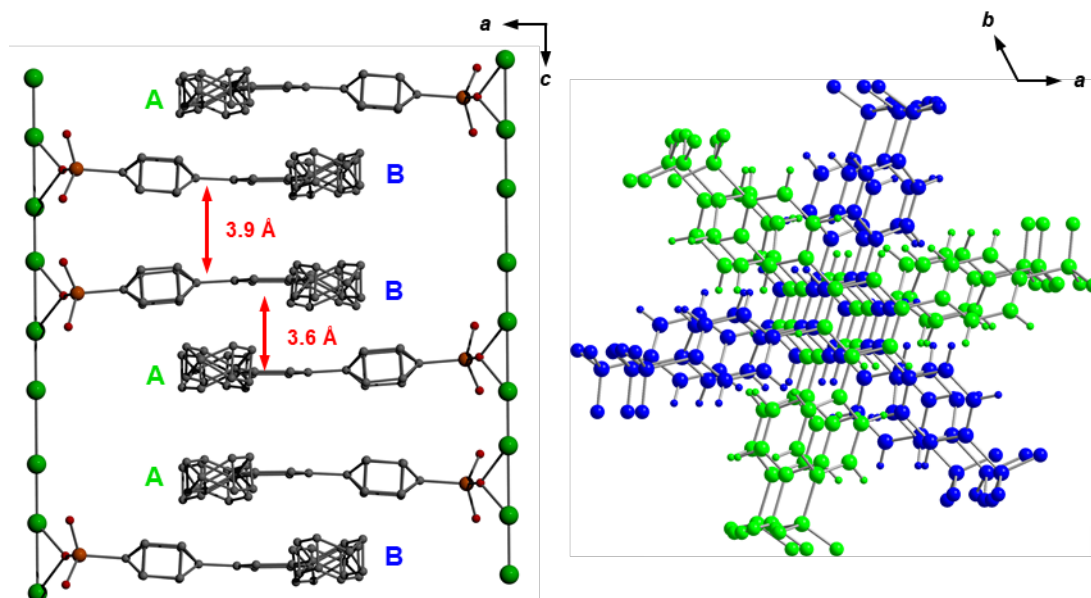


**Figure 2.4** BTPPA “dimers” in the reported crystal structure of MFM-500(Ni).<sup>29</sup> The chains of metal ions run in the *c*-direction and the ligands arrange in the AB...BA...AB motif (hydrogen atoms, DMSO molecules and some phosphonic acid groups have been omitted for clarity) (*left*). The dimer pairs have been coloured in blue and green (*right*) for clarity.

The five temperatures chosen to study the formation process of MFM-500(Ni) were 60, 70, 80 90 and 100 °C, with the experimental times ranging from 36 hours at 60 °C to 4 hours at 100 °C. These temperatures were chosen as they were within the accessible temperature range for the NMR probe. The rotor was then heated to the reaction temperature and spun at a magic angle spinning (MAS) frequency of 12 kHz for the duration of the experiment to reduce line broadening.<sup>28</sup>

In a separate laboratory control experiment, the reaction solutions were heated (without spinning) in Wheaton vials at the five temperatures discussed above, with green crystalline product forming around 16 hours at 60 °C, decreasing to only 1 hour at 100 °C.

### 2.3.1.2 CLASSIC NMR of MFM-500(Ni)

Two separate experimental runs using the 850 MHz spectrometer were carried out for this framework in 2016 and 2018. The results presented here are from 2018, due to the

more informative data, unless otherwise stated. Three sets of data were recorded in each experiment:  $^1\text{H}$  direct excitation,  $^{31}\text{P}$  direct excitation *without* decoupling and  $^{31}\text{P}$  direct excitation *with* decoupling; the effective time resolution for this CLASSIC NMR study was 7.1 minutes. The chemical changes of coordination and the loss of BTPPA linker from the solution were monitored, whilst observing the growth of solid product.

### 2.3.1.2.1 $^1\text{H}$ results

In all the CLASSIC NMR experiments seven  $^1\text{H}$  resonances are observed at all temperatures which have been assigned (Figure 2.5). The description has been taken from the completed manuscript.

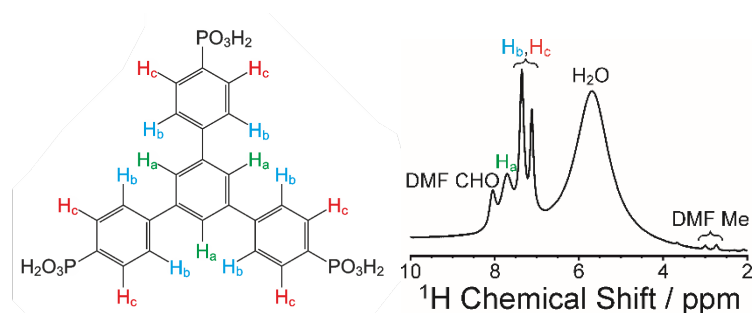
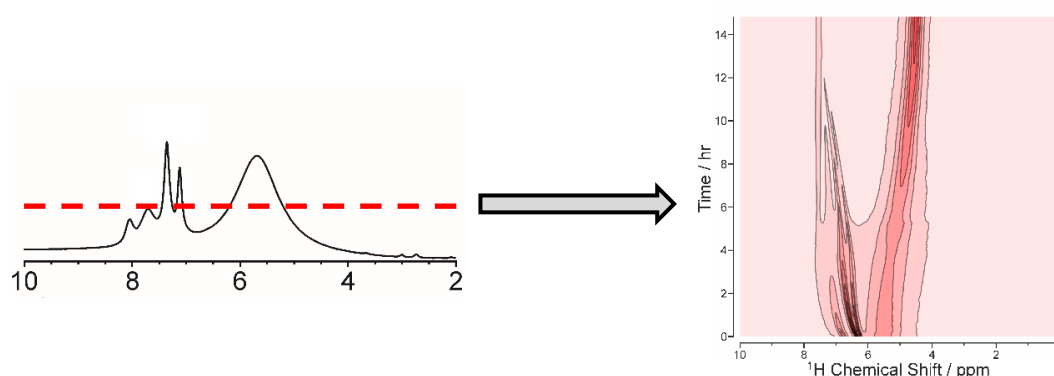


**Figure 2.5** Assignment of  $^1\text{H}$  NMR peaks in CLASSIC NMR experiment, including the three aromatic resonances in the BTPPA linker.

The two weak peaks between 2.5 – 3.0 ppm can be ascribed to the residual methyl group protons from the  $d_7$ -DMF reaction mixture. All subsequent spectra are referenced relative to the furthest downfield of these two peaks, which was taken as 3.0 ppm. At *ca.* 5.8 ppm an intense broad peak is present at the start of all of the experiments, and as time progresses the peak moves upfield to 4.0 – 4.5 ppm; it is assigned to partially protonated water (having started as  $\text{D}_2\text{O}$ ) as a result of the proton exchange the acidic linker and release of the coordinated water from  $\text{Ni}(\text{NO}_3)_2 \cdot 6\text{H}_2\text{O}$ . The three aromatic resonances between 7.0 – 8.0 ppm are assigned to the three proton environments of the BTPPA linker, which integrate to 1:2:2 ratio as expected. The most downfield of the three peaks, and the lowest integral, corresponds to the protons on the core benzene ring ( $\text{H}_a$ ) and the remaining two peaks are attributed to the two proton environments on the outer benzene rings ( $\text{H}_b$  and  $\text{H}_c$ ). The final peak observed at highest chemical shift, to the left of  $\text{H}_a$  protons, is assigned to the aldehyde group

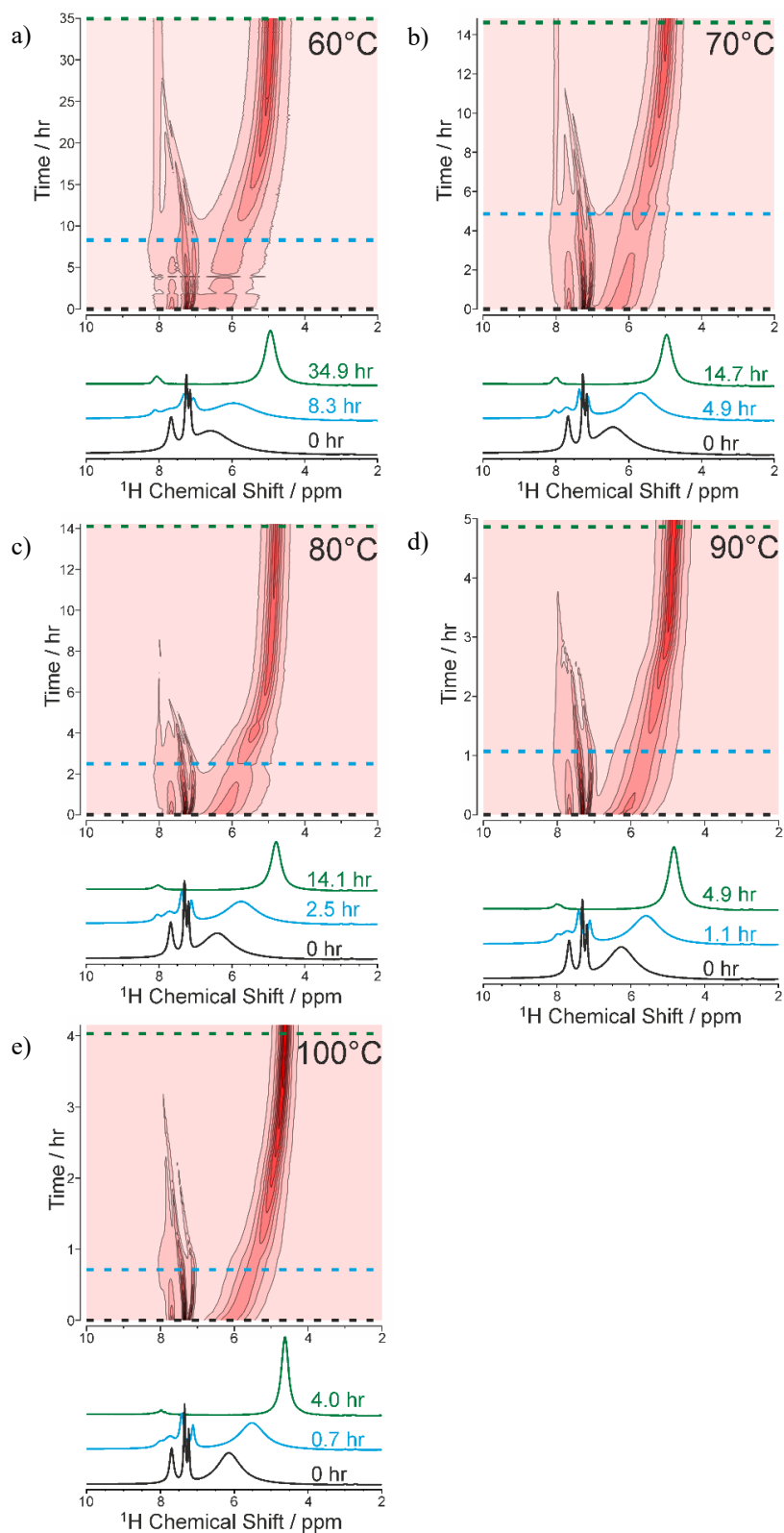
of the  $d_7$ -DMF solvent. It appears very weak in the first spectrum of each experiment as all of protons are initially deuterated, but as they can undergo proton exchange with the BTPPA linker and water in the early part of the experiment, the intensity is seen to increase relative to the methyl group peaks as time progress.

The spectra recorded during the in-situ experiments are displayed as a 2D contour plot (time vs. frequency), in which the intensity of the peaks is represented by contour lines drawn at suitable intervals, in the same way as a topographical map (Figure 2.6).



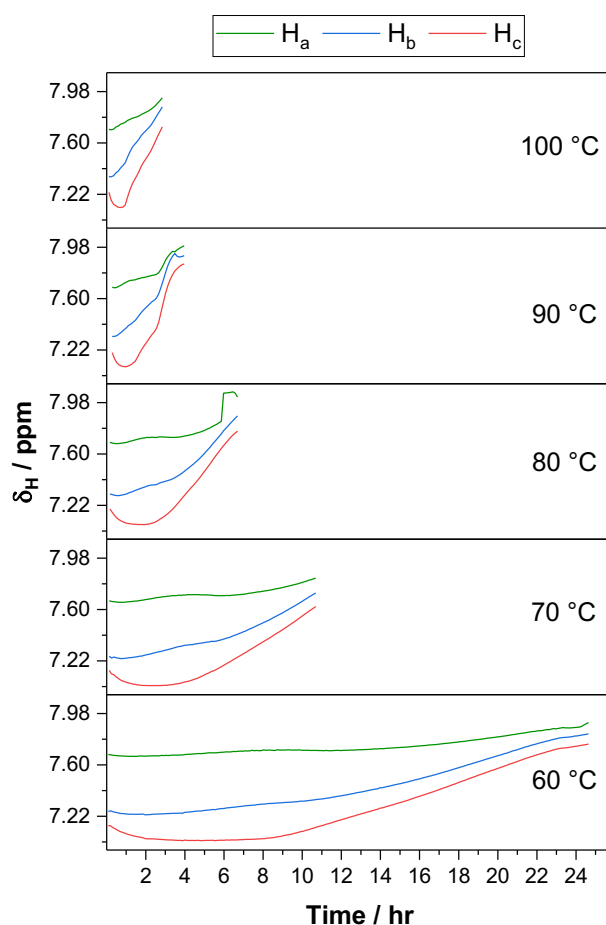
**Figure 2.6** Individual  $^1\text{H}$  spectrum (*left*) with red dashed line depicting the set 'height' for the level on the contour plot which is two-dimensional showing the shifts with time (*right*).

Figure 2.7 shows the 2D  $^1\text{H}$  NMR spectra of the five experiments. The experiments were stopped after 35, 15, 14, 5 and 4 hours for 60, 70, 80, 90 and 100  $^\circ\text{C}$  respectively. Individual spectra from three time points (start, during and end) of the reactions are shown below each contour plot at each given temperature. The spectra are taken from the manuscript and the image was produced by Dr Colan Hughes.



**Figure 2.7** 2D  $^1\text{H}$  NMR spectra from the in-situ experiments collected at 60 °C, 70 °C, 80 °C, 90 °C and 100 °C, with individual spectra at selected time points acquired during the CLASSIC NMR syntheses of MFM-500(Ni). This plot was produced by Dr Colan Hughes.

The broad water peak during the synthesis of MFM-500(Ni) that moves to a lower chemical shift is tentatively assigned to the change in the solvent mixture over the course of the reaction. Water molecules released from the nickel nitrate hexahydrate salt make up a significant proportion of the final solvent, meaning that the reaction finishes with the nominal solvent ratio of *ca.* 4:3:1 (v/v/v)  $d_7$ -DMF:D<sub>2</sub>O:H<sub>2</sub>O; H/D exchange would also be occurring. However, the most important peak shifts during the experiment are those of the BTPPA linker (Figure 2.8).



**Figure 2.8**  $^1\text{H}$  peak positions vs. time of the three aromatic resonances attributed to the BTPPA linker during the CLASSIC NMR experiment. The  $H_a$  and  $H_b$  fitting artefacts at 80 and 90 °C respectively are a result of the fit struggling with the low intensity peaks.

The three aromatic resonances shift non-monotonically as a function of time during the reaction, initially moving slightly upfield before shifting back downfield. The  $H_c$  signal exhibits the largest movement to lower chemical shift, before curving back to a higher chemical shift. These shifts can cautiously be ascribed to the deprotonation of

the phosphonic acid groups, aggregation of the linker molecules and then successive complexation to the nickel ions. The aggregation of the linker molecules in solution (discussed in Section 2.3.1.1) also cause the core ( $H_a$ ) protons to shift upfield, before de-aggregating as reaction reaches temperature. The “induction period” appears to conclude as the maximum shift downfield is reached, which also coincides with the water peak moving upfield to *ca.* 4.5 ppm. This suggests that either nucleation is dependent on enough metal complexation or the formation of a suitably acidic environment for precipitation of metal-linker complexes that can then grow as crystals.

In order to interpret the CLASSIC NMR experiment, a comparative laboratory synthesis at 80 °C was performed. The synthetic conditions were matched as closely as possible, but with a larger volume of reagents used. The reaction of BTPPA and nickel nitrate was set up in a Wheaton vial at 80 °C, and a 0.1 mL aliquot of reaction solution was removed every hour and diluted with 0.3 mL  $D_2O/d_7$ -DMF in the same ratio as the reaction solution. The  $^1H$  spectra shown in Figure 2.9 were referenced to the peak at 3 ppm (the most downfield of the two methyl groups in DMF).

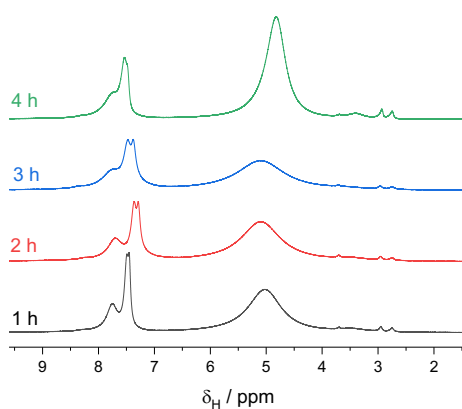


**Figure 2.9**  $^1H$  liquid-phase time series of laboratory synthesised MFM-500(Ni), in which a spectrum of the reaction solution was recorded every hour.

Similar peak behaviour to that seen in the CLASSIC NMR spectra were noted; as time progresses the aromatic peaks attributed to the linker can be seen to shift upfield by 2 hours, before shifting downfield between 2 – 3 hours. The peaks begin to merge into the residual DMF peak and decrease in intensity around 4 hours when solid particulate was noted to start forming, as the large water peak shifts to a lower chemical shift and the intensity increases.

To investigate the chemical changes in the liquid phase after solid formation, 0.1 mL of supernatant from the 80 °C laboratory synthesis was removed and added to 0.4 mL of D<sub>2</sub>O/*d*<sub>7</sub>-DMF (*v/v* = 1.5:2). The <sup>1</sup>H spectra shown in Figure 2.10 have been referenced to the methyl peak of DMF at 3 ppm. The NMR spectra of the supernatant was recorded at room temperature, before increasing the temperature from 60 to 90 °C as in the CLASSIC NMR experiment. The aromatic peaks and the large broad peak move further apart with increasing temperature, with the distance ( $\Delta\delta$ ) increasing from *ca.* 2.5 ppm at room temperature to 3.3 ppm at 90 °C.

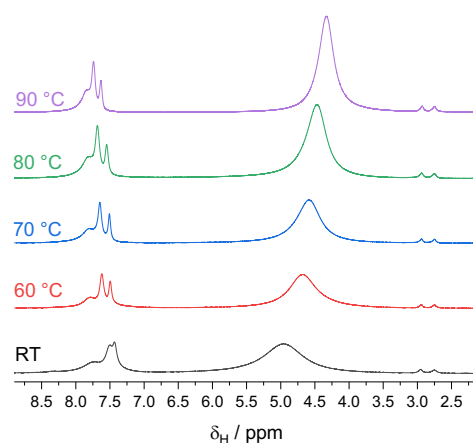


**Figure 2.10** Laboratory synthesised MFM-500(Ni) post-reaction solution VT NMR spectra.

To understand the peak shift of the broad water signal, infrared spectroscopy was used to monitor exchange of the coordinated water molecules in the nickel nitrate hexahydrate salt in the D<sub>2</sub>O/*d*<sub>7</sub>-DMF reaction mixture (Figure 2.11). The metal salt was added to the solvent mixture and a droplet was loaded onto the ATR stage and covered to prevent evaporation during the experiment.

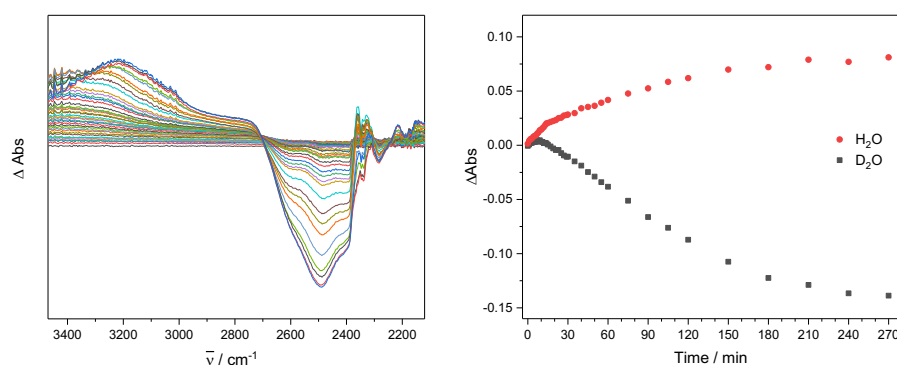


**Figure 2.11** Difference IR spectrum (*left*) of Ni(NO<sub>3</sub>)<sub>2</sub>·6H<sub>2</sub>O in the D<sub>2</sub>O/*d*<sub>7</sub>-DMF reaction mixture and the change in absorbance of peaks at 3167 cm<sup>-1</sup> (H<sub>2</sub>O) and 2488 cm<sup>-1</sup> (D<sub>2</sub>O) over time (*right*).

The difference spectra were collected over a period of 4.5 hours which show the growth of the peak at  $3167\text{ cm}^{-1}$  (attributed to the  $\text{H}_2\text{O}$  signal) and the loss of the  $\text{D}_2\text{O}$  signal at  $2488\text{ cm}^{-1}$ . Plotting the change in absorbance against time for the two peaks shows that the system is still equilibrating over four hours later at room temperature. It can be assumed that there are three processes occurring: DMF/ $\text{H}_2\text{O}$  exchange on Ni centre;  $\text{H}_2\text{O}$  exchange on Ni centre; and H/D exchange with water. During the CLASSIC NMR experiments, it can be assumed that these processes will occur much faster at the higher reaction temperatures.

### 2.3.1.2.2 $^{31}\text{P}$ results

The  $^{31}\text{P}$  NMR data (both liquid and solid-phase) were less conclusive than the  $^1\text{H}$  spectra for the higher temperature experiments ( $70 - 100\text{ }^\circ\text{C}$ ). Figure 2.12 shows the 2D liquid-phase  $^{31}\text{P}$  spectra (acquired *without*  $^1\text{H}$  decoupling) which shows a single broad peak during the  $60\text{ }^\circ\text{C}$  experiment. Distinct  $^{31}\text{P}$  resonances from different environments were not observed from the BTTPA linker deprotonating and complexing to the nickel ions. The signal intensity begins to decrease from *ca.* 9 hr which is consistent with loss of the linker from the solution. The solid-state  $^{31}\text{P}$  spectra (acquired *with*  $^1\text{H}$  decoupling) from the  $60\text{ }^\circ\text{C}$  did not show any additional signals to those observed in the liquid-state spectra.

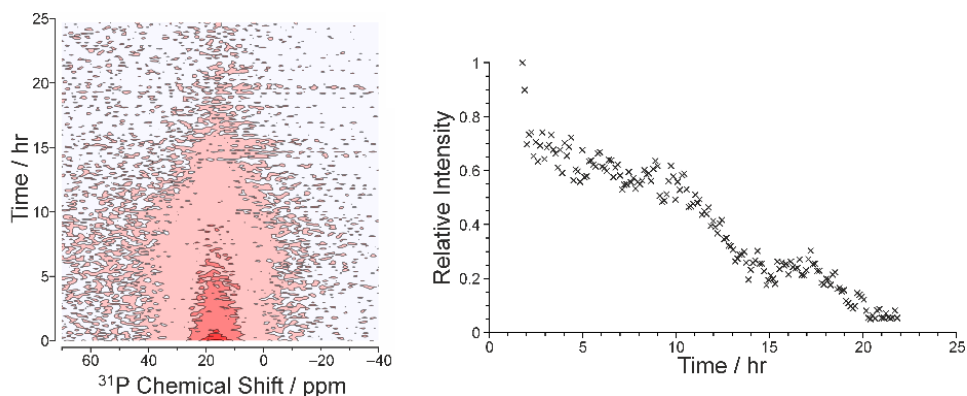


**Figure 2.12**  $^{31}\text{P}$  direct excitation 2D contour plot from CLASSIC NMR experiment performed at  $60\text{ }^\circ\text{C}$  (*left*). Intensity vs. time plot for  $^{31}\text{P}$  signal which follows a similar trend to the  $^1\text{H}$  data at  $60\text{ }^\circ\text{C}$  (*right*). This plot was produced by Dr Colan Hughes.

From the first set of experiments in 2016, the  $^{31}\text{P}$  high-power decoupling (HPDEC) spectra show us the combined liquid- and solid-state signal. At  $60\text{ }^\circ\text{C}$  a very weak signal appears at the beginning of the reaction which then diminishes over time, that

can be attributed to dissolution of the BTPPA linker at the reaction temperature increases due to the high concentration of material used. Figure 2.13 shows the 80 and 90 °C 2D spectra, both showing three very weak peaks between 30 and -20 ppm.

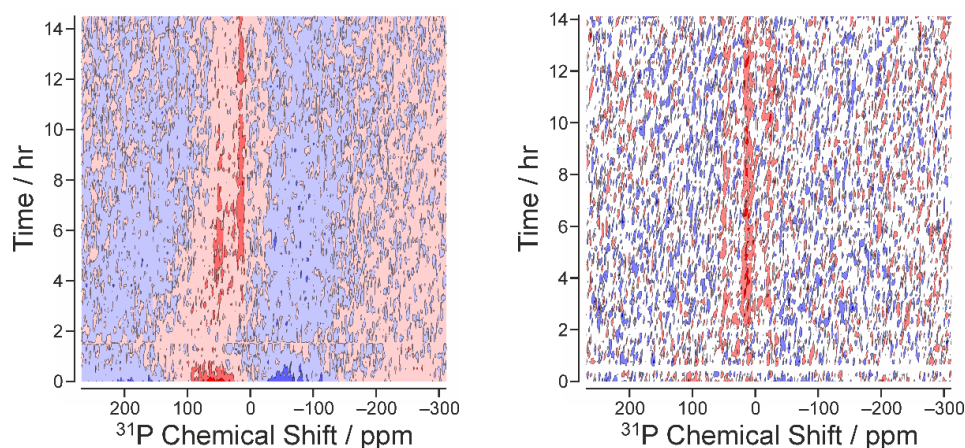


**Figure 2.13** 2D  $^{31}\text{P}$  HPDEC spectra showing 3 weak peaks at 80 °C (*left*) and 90 °C (*right*) from the 2016 set of experiments. This plot was produced by Dr Colan Hughes.

It is possible that this is due to a combination of deprotonated phosphonic acid group, mono-coordination and bi-coordination to the nickel ions. Well-resolved spectra are not observed in both cases because as solid particulates form, the signal becomes broader and weaker due to the reduced motion in solution.

### 2.3.1.3 Reaction kinetics

The  $^1\text{H}$  liquid-state spectra showed a decrease in peak intensity with reaction time as the linker reacted with the metal ions to form MFM-500(Ni), from which the three aromatic BTPPA  $^1\text{H}$  resonances attributed to the linker were successfully fitted using the two-stage model of Gualtieri<sup>36</sup> by Dr Colan Hughes. The following description of this fitting is taken from the completed manuscript and outlines the method of calculation of the nucleation and growth rate constants, and therefore the activation energies for the formation of MFM-500(Ni).

The decrease in peak intensity as a function of time for the data at the five temperatures were fitted to seven Lorentzian lineshapes, with the five overlapping peaks at higher chemical shift being fitted simultaneously. Each Lorentzian was defined by its chemical shift, linewidth and intensity, with polynomial functions used to fit the baselines. From these fits, intensities for the three linker peaks ( $\text{H}_a$ ,  $\text{H}_b$  and  $\text{H}_c$ ) were

established which were normalised by scaling the values so that the largest intensity for each peak was set to unity. We took the Gualtieri model for nucleation and growth and applied it to our peak intensities, subtracting the original model from unity to allow for the disappearance of reactant rather than the appearance of product. This gave us the equation:

$$I_{rel}(k_n, k_g, b) = 1 - \left( \frac{1 - \exp(-k_g t)}{1 + \exp(-(t - 1/k_n)/b)} \right)$$

for the relative intensity of each peak. For each temperature, we simultaneously fitted all three peak intensities to this model, using the same values of  $k_n$ ,  $k_g$  and  $b$ , allowing only a scaling factor to vary independently for each peak. The final model for the  $j^{\text{th}}$  peak at temperature  $T$ , giving a total of six fitting parameters per temperature, is:

$$I^{(j)}(s_j, k_n^{(T)}, k_g^{(T)}, b^{(T)}) = s_j I_{rel}(k_n^{(T)}, k_g^{(T)}, b^{(T)})$$

The resulting fits (red traces) are shown in Figure 2.14.

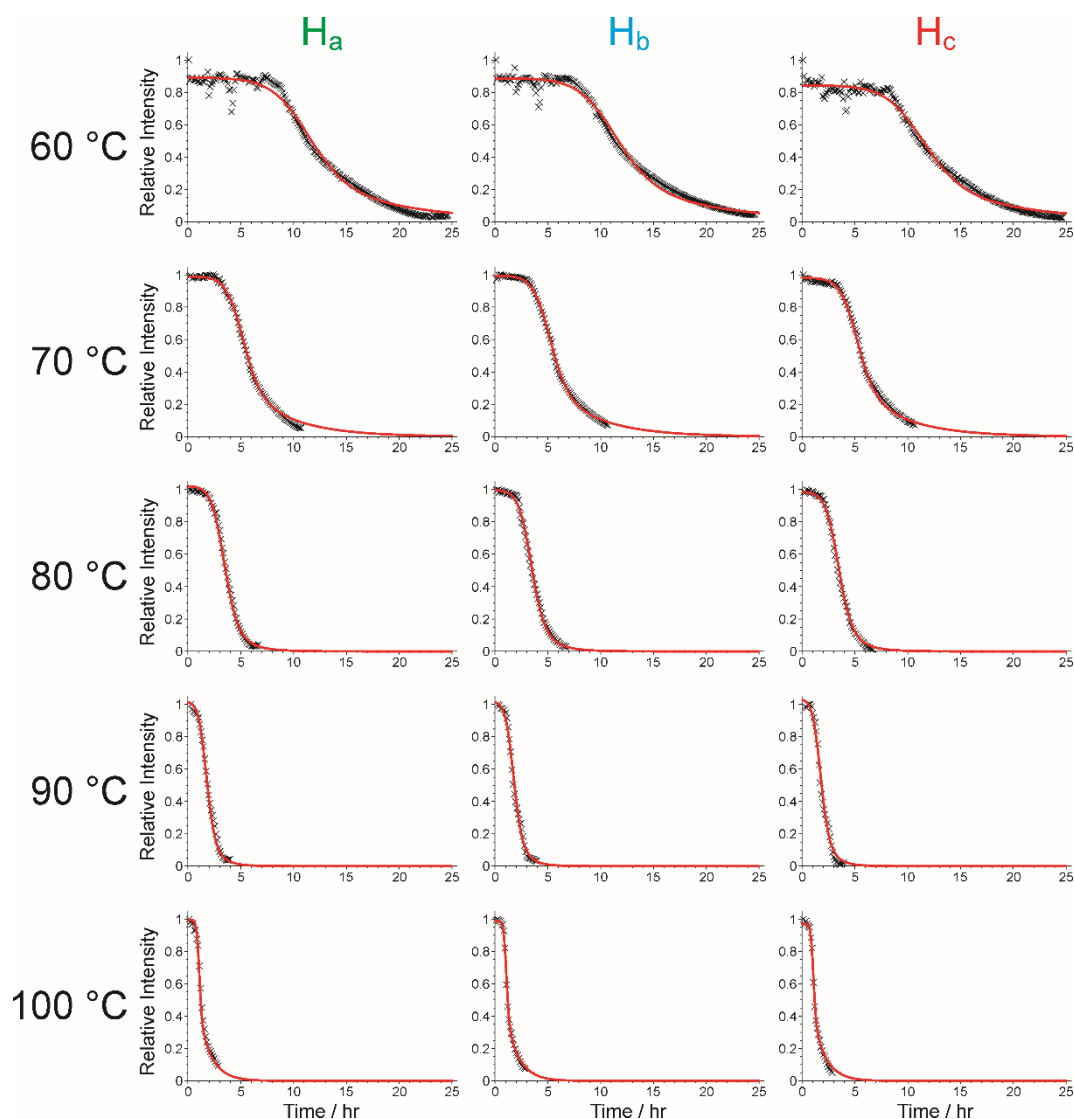


**Figure 2.14** Intensity vs. time plots for the three aromatic peaks attributed to the BTPPA linker, to which Guaitieri models have been fitted for each temperature and proton position (*red lines*). This plot was produced by Dr Colan Hughes.

Unexpectedly, growth during the 100 °C experiment is much slower than at 90 °C, with the nucleation and growth rates being virtually identical. The shape of the fit is very different to the other four temperatures, suggesting that nucleation is dominating such that the particles are not able to grow. It is also important to recognise that the reaction will already be underway by the time the rotor reaches temperature; the time taken from the point of heating to the start of the first measurement after tuning the probe was *ca.* 7 minutes. Even though the growth is limited, and the model begins to fail at the higher temperatures, the reaction is still sufficiently fast that the experiment still completes in the shortest time.

Therefore, omitting the 100 °C data, an Arrhenius plot (Figure 2.15) allowed the activation energies for both nucleation and growth of the MFM-500(Ni) formation process to be estimated as  $E_a^{(n)} = 61.4 \pm 9.7 \text{ kJ mol}^{-1}$  and  $E_a^{(g)} = 72.9 \pm 8.6 \text{ kJ mol}^{-1}$  respectively. These values are very similar when taking into account the errors, and are comparable to the activation energies of other single-phase forming examples within a similar temperature range in the literature.<sup>37-41</sup>

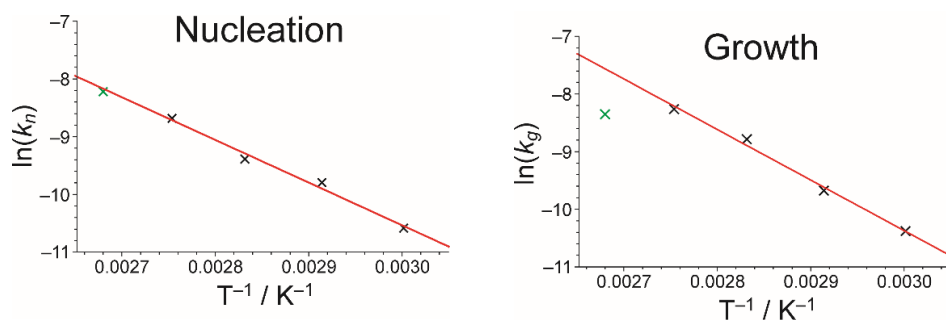


**Figure 2.15** Arrhenius plot for the calculation of activation energies for the nucleation and growth factors of MFM-500(Ni). The trendline has been fitted to only the first four data points (60 – 90 °C) for both the nucleation and the growth; the omitted 100 °C data points are plotted in green. This plot was produced by Dr Colan Hughes.

### 2.3.1.4 Ex-situ and in-situ XRD results

PXRD analysis was used to characterise the green crystalline material formed at the five temperatures from both the CLASSIC NMR experiments and laboratory syntheses. The powder patterns shown in Figure 2.16 were collected post-NMR synthesis and show that MFM-500(Ni) was formed at all five temperatures, with no other phases present.

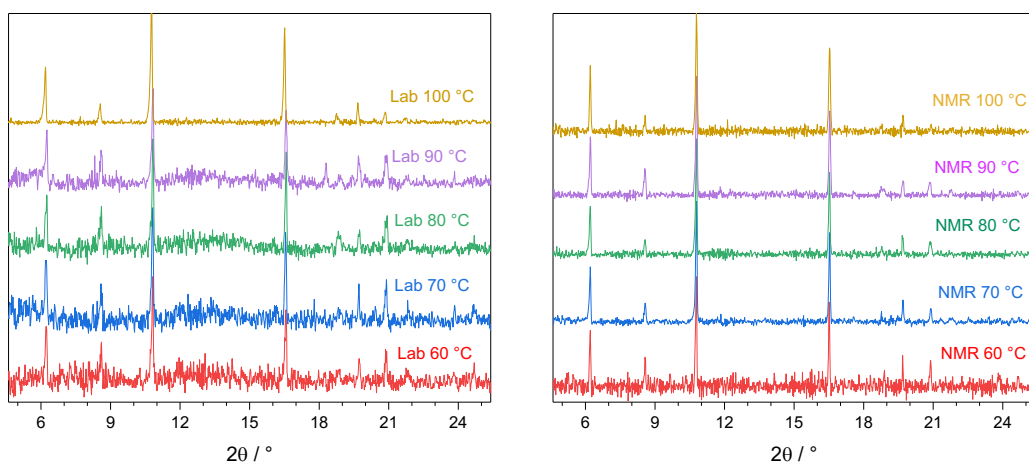


**Figure 2.16** Ex-situ PXRD patterns ( $\lambda = 1.54056 \text{ \AA}$ ) of phase-pure MFM-500(Ni) synthesised in both the in-situ laboratory scale (*left*) and CLASSIC NMR experiments (*right*).

To determine the phase behaviour of the material formed during the reaction, an in-situ XRD reaction was carried out on beamline I12 at Diamond Light Source by Dr Hamish Yeung (University of Oxford). The reaction was carried out using identical concentration of reactants and deuterated solvents as in the CLASSIC NMR experiment, but on a larger scale to monitor the formation of solid product. Figure 2.17 shows individual PXRD patterns recorded at varying time intervals; an initial period where no solid formation occurs can be seen from 0 – 80 minutes.

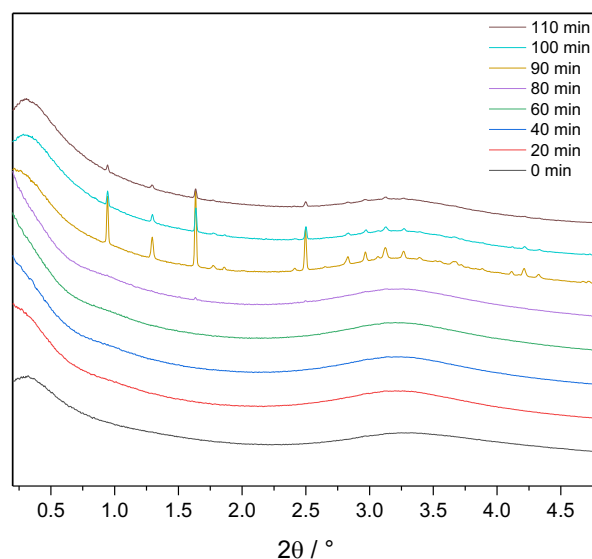


**Figure 2.17** Individual PXRD patterns taken from the in-situ XRD experiment ( $\lambda = 0.23417 \text{ \AA}$ ). The appearance of MFM-500(Ni) occurs between 80 – 90 minutes, with only one crystalline phase forming.

This is approximately 15 minutes longer than the initial period that is seen in the 90 °C in-situ NMR data (~65 minutes), which is ascribed to: i) the time needed for the larger system (vessel and contents) to reach the desired temperature; ii) the time taken to grow sufficiently large particles (several nanometres) that will be observable in the XRD measurement. The diffraction pattern confirms that the first appearance of any crystalline solid is MFM-500(Ni) and that no other crystalline phases were observed during the reaction.

The initial rise in appearance of MOF is consistent with the rate of loss of  $^1\text{H}$  signal corresponding to the BTPPA linker in the NMR data, but the reaction kinetics could not be definitively obtained from the diffraction experiment due to the high reactant concentration used. Once solid product begins to form, 'lumps' of crystallites (macro-scale aggregates) drop erratically out of the beamline measurement region. Figure 2.18 shows the unsuccessful attempt at the Gualtieri fit due to irregular drops in signal intensity as the material collected at the bottom of the sample tube.

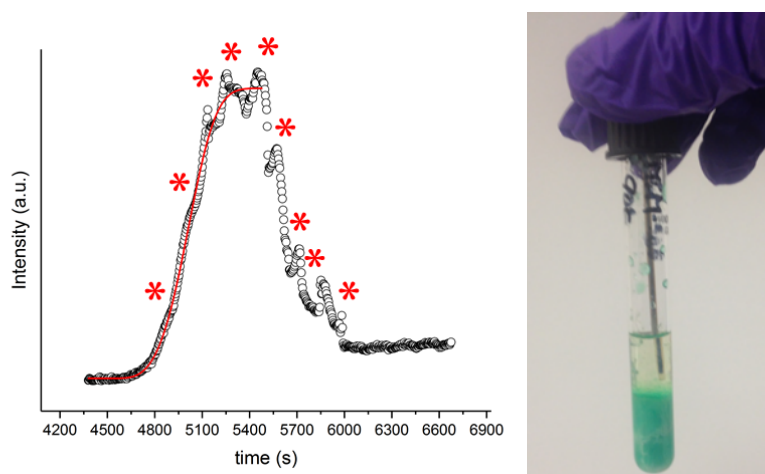


**Figure 2.18** Data points (*left*) were produced by Dr Yeung using a Pawley refinement on the in-situ XRD pattern collected at a given time and integrating the area under the diffraction peaks to give a combined "intensity", with the red trace showing the unsuccessful attempt at the Gualtieri fit. The red stars indicate where material is falling out of the beam path and MFM-500(Ni) collected at the bottom of the sample tube (*right*).

The measurement was not repeated at a lower concentration as recent evidence on other MOF syntheses has shown that concentration effects on MOF nucleation and growth can be very significant,<sup>42</sup> therefore making comparison with the NMR experiment unreliable. Nevertheless, the experiment confirmed the phase purity of

material and the reaction timescales of MFM-500(Ni) agree with the CLASSIC NMR experiment.

### 2.3.1.5 SAXS results

Smaller particulates of less than 21 nm are not observable by the CLASSIC NMR technique,<sup>28</sup> therefore preliminary small-angle X-ray scattering (SAXS) measurements were carried out to study the formation of these small crystallites during the early stage of the reaction. An ex-situ reaction was set up using the same conditions as the NMR experiment at 80 °C but on a larger scale. Sampling of the reaction solution was taken every 45 minutes for three hours, and then as small particulates (visible by eye) were observed forming the time between sampling was reduced to 30 minutes. After a total of four hours, when significant MFM-500(Ni) had begun to form, the measurements were ceased.

Figure 2.19 shows the evolution of the SAXS signal over time. This reaction was carried out alongside Dr Alison Paul (Cardiff University), who successfully fitted the data as described in the following paragraphs.

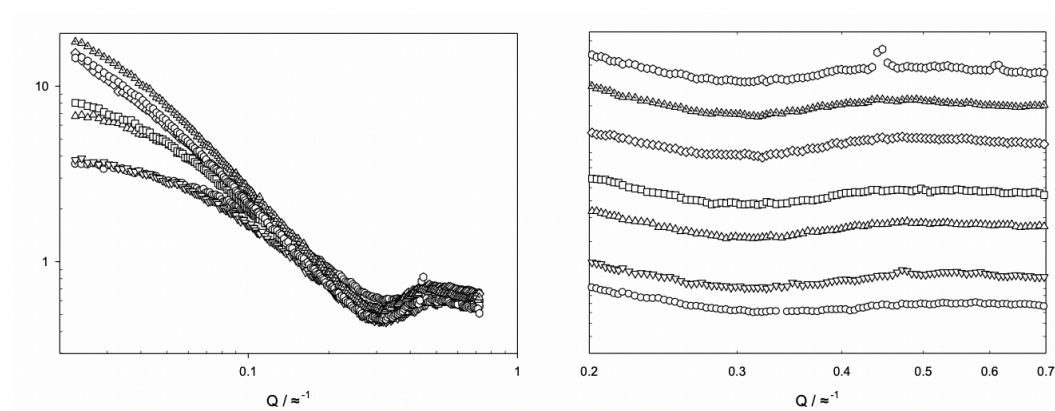


**Figure 2.19**  $I(Q)$  vs.  $Q$  plot for aliquots taken from 80 °C MFM-500(Ni) reaction solution over 4 hours (*left*) with an expansion of the high  $Q$  region, offset for clarity (*right*). This plot was produced by Dr Alison Paul.

Key: 0 min (before heating, circles); 45 min (inverted triangles); 90 min (triangles); 135 min (squares); 180 min (diamonds); 210 min (dotted triangles) and 240 min (hexagons).

In each sample, a broad peak around  $Q = 0.5 \text{ \AA}^{-1}$  is present, which corresponds to a length scale of *ca.* 6 Å ( $d = 2\pi/Q$ ). After 240 min, once the reaction was stopped, two peaks at  $Q = 0.61$  and  $0.45 \text{ \AA}^{-1}$  can be seen at high  $Q$  scattering angles which correspond to length scales of 10 Å and 14 Å respectively. The peak at  $0.45 \text{ \AA}^{-1}$  agrees

with the d-spacing of the first Bragg peak in the PXRD patterns that were discussed in Section 2.3.1.4. The measurements between 0 and 180 minutes follow a smooth decay between 0.02 and 0.25  $\text{\AA}^{-1}$  in the lower  $Q$  range. As the reaction time progresses, the shape of this decay becomes more linear adopting a  $Q^{-1.5}$  dependence after 180 min. The data was modelled by Dr Paul using SASView modelling suite version 4.1.2<sup>43</sup> using a least squares type analysis to refine model parameters to the data (Figure 2.20). The description of the fitting in the rest of this section is reproduced from the completed manuscript.

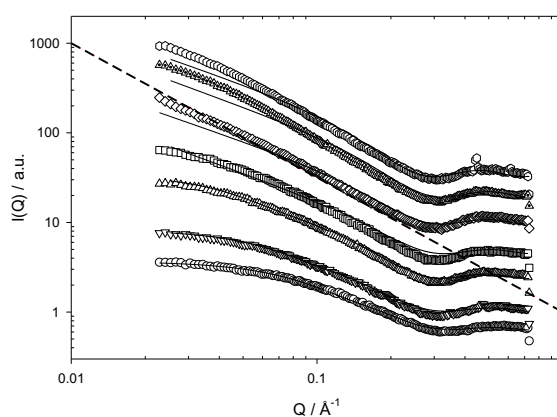


**Figure 2.20** The measured intensities have been scaled by factors of 1, 2, 4, 8, 16, 32 and 64 in intensity for presentation purposes. Solid lines represent fits to a core-shell rod model; dashed line corresponds to a power law of  $Q^{-1.5}$ . This plot was produced by Dr Alison Paul.

Key: 0 min (before heating, circles); 45 min (inverted triangles); 90 min (triangles); 135 min (squares); 180 min (diamonds); 210 min (dotted triangles) and 240 min (hexagons).

The data did not fit to a simple model for rods and the best fits were obtained using the form factor for a cylinder with core-shell morphology, which is parameterised as core radius, shell thickness and cylinder length. The fitted parameters were the core-radius and cylinder length. A shell thickness was included as the data did not fit to a model for a solid cylinder. The SAXS signal is heavily weighted to regions of high electron density, and hence reflects the regions occupied by the metal atoms. The shell thickness was therefore fixed at 1  $\text{\AA}$  to allow for the possibility of a thin region of very different scattering length density to the core. For all samples the radius of the cylinder was  $7 \pm 0.2 \text{\AA}$ . This radius, combined with the fixed shell width of 1  $\text{\AA}$ , is notably similar to the ligand stacks identified in the MFM-500(Ni) crystal structure, with the cylinder walls potentially corresponding to the columns of metal ions that surround the linkers.

At short reaction times, the cylinder model accounts reasonably well for the scattering, and fits are consistent with an elongation of these cylindrical rod-like structures:  $L = 52 \text{ \AA}$  at  $t = 0$ , increasing to  $L = 73 \text{ \AA}$  at 45 min and  $L = 118 \text{ \AA}$  at 90 min, rising dramatically to  $880 \text{ \AA}$  at 135 min. After this time, the model fails to fit the low  $Q$  data satisfactorily. The length scales present are above that accessible at the measurement  $Q$  range, and measurements over the available  $Q$  range become insensitive to the length of the cylinder used once greater than  $900 \text{ \AA}$ , with any larger value of  $L$  giving an equally poor representation of the low  $Q$  data.

As the SAXS experiment follows the formation of crystals of MFM-500(Ni) that eventually separate out under gravity, it is reasonable to assume that at any given time a distribution of structures is present (some with length scales outside the range accessible by SAXS and some with smaller structures that remain readily dispersed). To probe this issue further, SAXS data were recorded for a sample containing the supernatant taken from 240 min sample after separation under gravity. The data showed the same type of scattering profile as seen immediately after sampling, and was best accounted for by a cylinder model of radius  $7 \pm 0.2 \text{ \AA}$ , shell thickness  $1 \text{ \AA}$  and now a length of  $90 \pm 5 \text{ \AA}$ . This is consistent with the  $90 \text{ \AA}$  cylindrical rods remaining in suspension, with larger species precipitating out on standing.

The data shows the presence of short cylinders, immediately upon mixing at the  $t = 0$  measurement, which suggests that structural evolution begins rapidly. A degree of elongation of the structures occurs up to 90 minutes when heated at  $80 \text{ }^\circ\text{C}$ , after which time the structures become more complex but retain the characteristic short length-scales that were established at the start of the reaction. This correlates with the suggestion of small-scale aggregates forming in solution (between 90 – 135 minutes) prior to MOF formation and the timescales seen in the CLASSIC NMR experiments.

### 2.3.1.6 Summary

We have synthesised phase-pure MFM-500(Ni) at five different temperatures which can successfully be monitored using an in-situ NMR technique. The time-evolution of both the liquid and solid-state of the reaction could be obtained for the entire reaction, and the kinetic parameters for nucleation and growth were calculated by modelling the  $^1\text{H}$  liquid-state data to a Gualtieri model. From these rate constants, the activation energies for both processes were found to be similar in value at  $61$  and  $72 \text{ kJ mol}^{-1}$

respectively. The in-situ XRD experiment agreed with ex-situ PXRD patterns confirming that there is only the one crystalline phase of MFM-500(Ni) present throughout the entire reaction, and the timescale of the experiment corresponded to the data obtained from the CLASSIC NMR experiments. Finally, SAXS measurements performed on samples from an ex-situ reaction confirmed the hypothesis of aggregation prior to complexation.

In these experiments, while the solid-state  $^{31}\text{P}$  spectra were consistent with the rest of the data, the broad, weak peaks were largely uninformative. We therefore decided to try a different system containing phosphorus nuclei in order to test the technique with an alternative material.

### 2.3.2 AIPO-5

AIPO-5 is part of the zeolitic aluminophosphate series, which are classed as microporous crystals consisting of  $\text{AlO}_4$  and  $\text{PO}_4$  tetrahedra, and have been synthesised since the early 1980s (Figure 2.21).<sup>30</sup> Studies have shown that they possess zeolite-like properties and have potential for applications such as adsorbents for molecular separations and as catalysts.<sup>44</sup> In 2012, it was discovered that AIPO-5 can be synthesised with tetrapropylammonium hydroxide (TPAOH) at the relatively low temperature of 120 °C, which falls within the upper limit of the temperature range available on the solid-state NMR spectrometer.

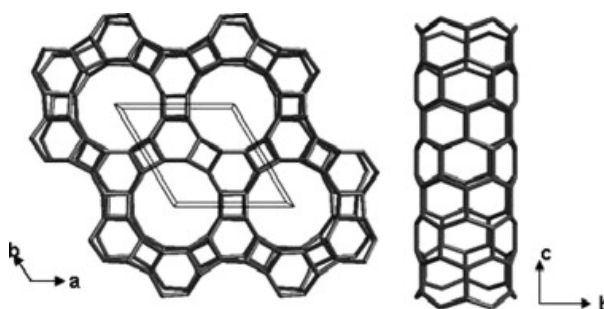


Figure 2.21 Crystal structure of AIPO-5. Reproduced from reference 30.

#### 2.3.2.1 Synthesis

A gel precursor was formed ex-situ by stirring a mixture of  $\text{Al}_2\text{O}_3$  and phosphoric acid for 24 hours, before adding TPAOH and stirring for a further 24 hours. The gel was

transferred to a Kel-F tube and sealed in a rotor and increased to 120 °C. The reported synthesis states that the reaction was to be heated for 48 hours, but due to the limited timeframe to use the high-field spectrometer we were only able to monitor the in-situ reaction for *ca.* 21 hours.

### 2.3.2.2 CLASSIC NMR of AlPO-5

The sequence of NMR spectra recorded were the same as in the MFM-500(Ni) in-situ reaction (Section 2.3.1.2) giving a time resolution of 7.1 minutes between sequential measurements (comparable to the MFM-500(Ni) experiment). Unfortunately, due to the long timescales needed for this reaction the in-situ experiment could only be attempted once.

#### 2.3.2.2.1 <sup>1</sup>H data

The <sup>1</sup>H liquid-phase data from the CLASSIC NMR experiment is shown in Figure 2.22 in which four distinct signals at 0.5, 1.1, 2.7 and 4.0 ppm can be seen in the 2D spectrum.

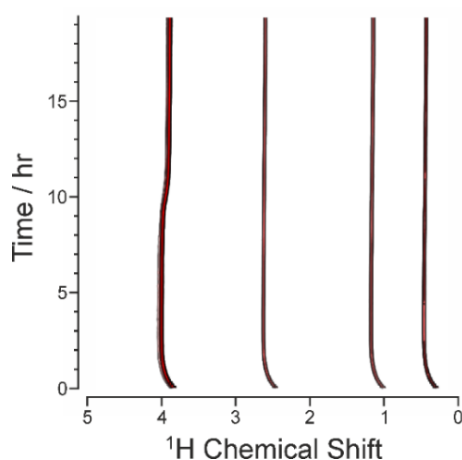


**Figure 2.22** 2D <sup>1</sup>H direct excitation spectra from the in-situ AlPO-5 experiment. This plot was produced by Dr Colan Hughes.

The three upfield peaks do not show much movement during the experiment (after the initial shift as the temperature of the shim coils stabilise). However, the most downfield peak at 4.0 ppm shifts around 10 hours, moving by 0.05 ppm to a lower chemical shift and then remaining at *ca.* 3.9 ppm for the remainder of the experiment.

### 2.3.2.2.2 $^{31}\text{P}$ data

In the  $^{31}\text{P}$  direct excitation NMR spectra four peaks, labelled in Figure 2.23, are seen. All of these peaks are significantly sharper than the  $^{31}\text{P}$  peaks seen in the MFM-500(Ni) experiments discussed above. Peak 1, the first peak observed, is the broadest  $^{31}\text{P}$  peak seen in the experiment (*ca.* 10 ppm), indicative of the precursor gel. Around 10 hours into the experiment, peak 1 shifts upfield and becomes sharper as the solution becomes less viscous, which we attribute to more rapid tumbling as the gel-state is lost. The appearance of the solid-state peak 2, 3 and 4 occurs after 6.0, 6.5 and 8.4 hours respectively, while peak 5 is a shoulder of peak 2 which appears around 10.7 hours; there is very little peak shift seen once these peaks have appeared. The chemical shift of peak 3 at *ca.* -30 ppm is found to be in good agreement with the reported chemical shift for AlPO-5.<sup>45</sup>

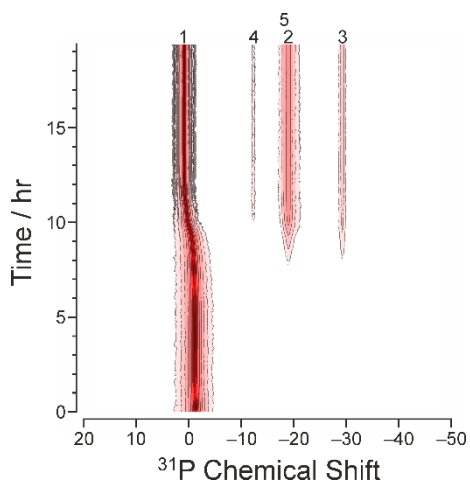


**Figure 2.23** 2D  $^{31}\text{P}$  direct excitation NMR spectrum from in-situ formation of AlPO-5, in which four species are present during the reaction. This plot was produced by Dr Colan Hughes.

Unfortunately, after cutting open the Kel-F tube post-reaction, there was not enough solid material to analyse by PXRD. However, the remaining pre-cursor gel that had not been used in the CLASSIC NMR experiment was heated in a Parr bomb for 24 hours at 120 °C in an oven. A small amount of solid was recovered and the PXRD pattern is shown in Figure 2.24. Some peaks correspond to the reported powder pattern,<sup>30</sup> but as the reaction was not left for the full 48 hour duration it is possible that the final phase pure product has not formed.

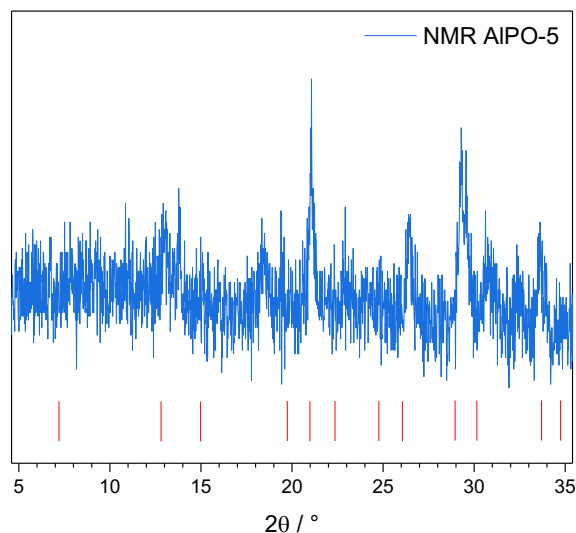


**Figure 2.24** PXRD pattern of the ex-situ AlPO-5 product formed after 24 hours of heating at 120 °C, compared with the literature reported pattern (*red lines*) after 48 hours.

### 2.3.2.3 Summary

The multi-nuclear CLASSIC NMR experiment has been used to study the formation of AlPO-5, however due to time constraints the reaction could not be run for the full duration. Both the  $^1\text{H}$  and  $^{31}\text{P}$  spectra collected show very few changes during the pre-nucleation stage, which was unsurprising when monitoring a gel matrix due to the slow diffusion in the system. We were able to see that some product appears around the 10-hour mark, but we were unable to see if the rest of the peaks change in intensity and position as the reaction was stopped after only 24 hours, meaning that analysis of transient phases in the reaction could not be achieved. An insufficient quantity of product was synthesised meaning that it was not possible to fully characterise the material post-synthesis.

We have successfully shown that the CLASSIC NMR approach can be used to study systems containing  $^{31}\text{P}$  nuclei, with the AlPO-5 results giving sharp peaks compared to those seen in the MFM-500(Ni) experiment. The  $^{31}\text{P}$  spectra showed that a previously unobserved phase(s) forms during the AlPO-5 synthesis. Further work is required to characterise these new species which may be either kinetic products or intermediates formed on the way to the final AlPO-5 product.

### 2.3.3 Lithium-tartrate MOFs

MFM-500(Ni) and AlPO-5 are examples of reactions that form a final single product phase, but the identification of multiple phases that form in MOF syntheses is very important and key to understanding the driving forces controlling crystallisation. The crystallisation of a series of lithium tartrate MOFs has been reported by Yeung *et al.* in which synchrotron in-situ PXRD was used to monitor the reaction of lithium acetate and *meso*-tartaric acid in a water/ethanol mixture between 40 – 125 °C, with product formation occurring on timescales ranging from minutes to hours.<sup>31</sup> They found that the reaction progresses by dissolution and recrystallisation of two phases to form a third, thermodynamically stable MOF product; this makes the reaction suitable for testing the capability of the CLASSIC NMR methodology to provide insight into such complicated multi-phase MOF reactions. Figure 2.25 shows the two intermediates that are seen at lower temperatures (**1** and **2a**), however the formation of phase **2b** is not seen until the temperature is increased above 104 °C.<sup>31</sup>

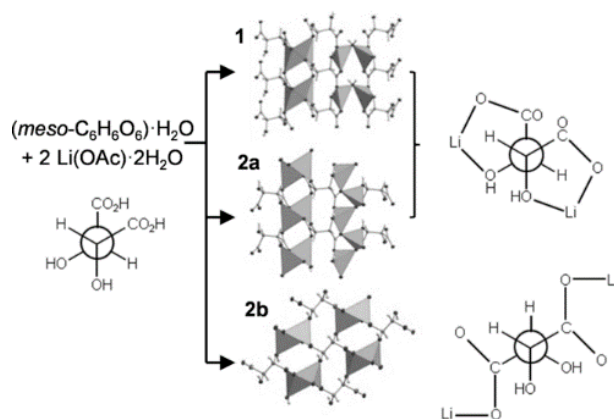


**Figure 2.25** Multiple phases form during the lithium-tartrate MOF reaction. Reproduced from reference 31.

#### 2.3.3.1 Synthesis

To monitor the synthesis using the CLASSIC NMR experiment the literature procedure was adapted to use a more concentrated solution of lithium acetate and *meso*-tartaric acid in deuterated solvents ( $\text{D}_2\text{O}/d_6\text{-EtOD}$ ).

A set of ex-situ experiments were also performed in which larger scale samples were prepared in both deuterated (D) and non-deuterated (H) solvents at the increased

concentration, and each sample was individually heated to one of three temperatures (40, 80 or 105 °C) for 24 hours. The mixtures were cooled, and the white solid was pipetted from the solutions and transferred to a petri dish to air dry in order to record the solid-state  $^{13}\text{C}$  NMR spectra.

### 2.3.3.2 CLASSIC NMR of lithium-tartrate MOF

For the in-situ experiment, 20  $\mu\text{L}$  of reaction mixture was transferred to a Kel-F tube and inserted into a rotor and sealed with a drive tip. During the experiment the rotor was heated to 40 °C for 2 hours, then increased to 80 °C for 12 hours and then a final increase to 105 °C for 4 hours. Three sets of spectra were recorded:  $^1\text{H}$  direct excitation,  $^{13}\text{C}$  cross-polarisation (CP) and  $^{13}\text{C}$  high-power decoupling (HPDEC) spectra. This gave a hypothetical time resolution for the NMR experiment of approximately 14 minutes. This time resolution is increased (compared to the MFM-500(Ni) and AlPO-5 experiments) due to the increased time to record a  $^{13}\text{C}$  spectrum as a result of the low abundance of the nuclei.

#### 2.3.3.2.1 $^1\text{H}$ results

Unlike the changes in the  $^1\text{H}$  liquid-state spectra from the CLASSIC NMR experiment of MFM-500(Ni) formation, there were very few significant changes seen in the in-situ lithium-tartrate MOF experiment. Figure 2.26 shows the  $^1\text{H}$  direct excitation spectra collected over the course of the experiment at the three different temperatures.

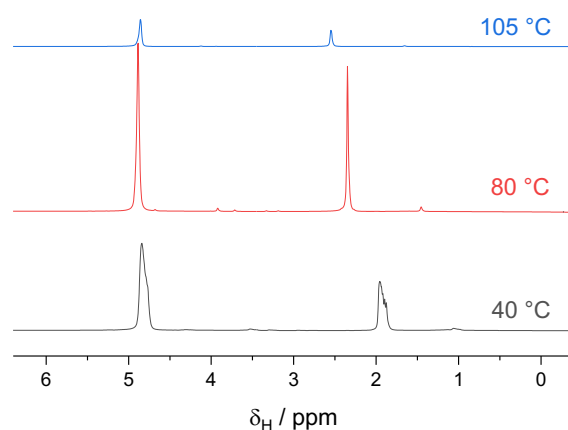


**Figure 2.26**  $^1\text{H}$  spectra from the in-situ NMR experiment in which the rotor was heated at three different temperatures over the course of 18 hours (the individual spectra collected at 80 and 105 °C have been summed).

There was initial drifting of the peaks at 40 °C due to the shim coil temperature increasing, therefore the spectrum presented in Figure 2.26 is the last spectrum recorded after 2 hours before the probe temperature was increased to 80 °C. Dr Colan Hughes has summed the individual spectra recorded at 80 and 105 °C as no evolution of the peaks were observed after the initial drifting due to the shim coils (seen at 40 °C), therefore resulting in spectra with a better signal-to-noise ratio. The peak at *ca.* 4.9 ppm corresponds to the central carbon atoms in the meso-tartaric acid and shows very little movement over the course of the reaction as the temperature is increased. The peak at 1.9 ppm corresponds to the methyl group of the lithium acetate. As the temperature increases, the peak shifts downfield to around 2.5 ppm, suggesting formation of the acetate as the Li<sup>+</sup> reacts with the meso-tartaric acid.

#### 2.3.3.2.2 <sup>13</sup>C results

As with the <sup>1</sup>H data in Section 2.3.3.2.1, the individual HPDEC <sup>13</sup>C spectra recorded during the in-situ reaction were summed by Dr Hughes as there were very little movement of the peak positions during the time held at each of the three temperatures. Figure 2.27 shows the four distinct peaks seen in the HPDEC spectra, as well as two broad intense peaks at 105 and 115 ppm due to the Kel-F insert.

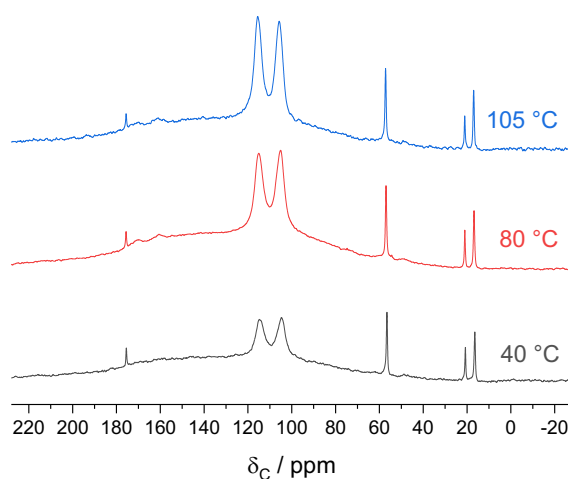


**Figure 2.27** <sup>13</sup>C HPDEC summed spectra from the in-situ CLASSIC NMR experiment at 40, 80 and 105 °C.

The peaks at *ca.* 15 and 56 ppm are from the ethanol in the reaction solution. The peak at 21 ppm is assigned as the signal from the methyl group in lithium acetate, which remains consistent throughout the experiment. Only one carboxyl resonance is seen at 175 ppm which is present at all temperatures.

The summation of the individual solid-state  $^{13}\text{C}$  data showed the most significant changes over the three temperatures during the in-situ experiment are shown in Figure 2.28. The reaction mechanism for the different phases in the lithium-tartrate MOF reaction proceed from **1**→**2a**→**2b**; the structure becomes denser as the kinetic product changes from the chelated binding of lithium to the meso-tartaric acid (**2a**) to the thermodynamic product in which the lithium ions show monodentate binding (**2b**).<sup>31</sup> At 40 °C, **2a** is the final phase whereas it **2b** is seen at 80 °C and 105 °C.

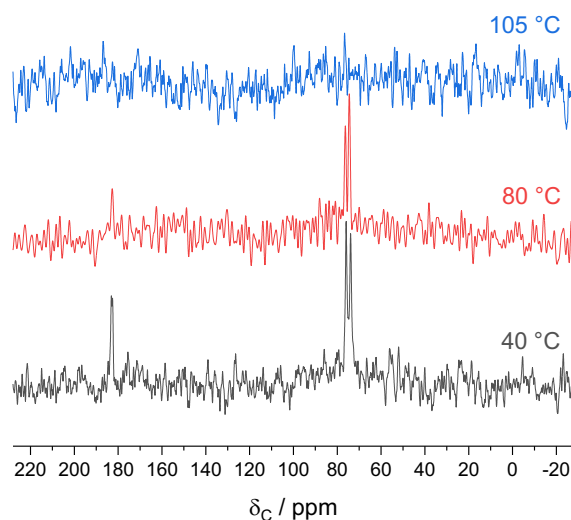


**Figure 2.28** Sum of  $^{13}\text{C}$  CP spectra from in-situ CLASSIC NMR experiment at 40, 80 and 105 °C.

At 40 °C a single peak around 182 ppm and two peaks at 75 ppm can be seen which are attributed to the carbon of the carboxylic acid and the carbon atoms of the central portion of the *meso*-tartaric acid respectively; the two peaks at 75 ppm could suggest that the coordination of the lithium ions results in asymmetric binding leading to two different environments. After heating the mixture at 80 °C, very little change occurred. Upon heating to 105 °C no peaks were seen in the spectrum, indicating that the relaxation delay was not long enough to obtain a signal. Peaks that would indicate the **2a** and **2b** phase of the framework are not observed and it is possible that the ratio of starting materials in the 20  $\mu\text{L}$  tube insert is inaccurate as they are not fully soluble in

the reaction solvents, therefore the sample under analysis was an inhomogeneous mixture.

The experimental procedure was modified as it was not possible to attempt the in-situ reaction again due to the limited time available on the high-field spectrometer. Six samples using both deuterated and non-deuterated solvents were prepared ex-situ to obtain the solid-state spectra of the products at the three different temperatures.

### 2.3.3.3 NMR of ex-situ lithium-tartrate MOF samples

For the ex-situ prepared samples, the white product was packed into a rotor and  $^{13}\text{C}$  CP spectra were recorded. Figure 2.29 shows the  $^{13}\text{C}$  CP spectra recorded at room temperature for the six solid samples: three prepared from deuterated and three from non-deuterated solvents.

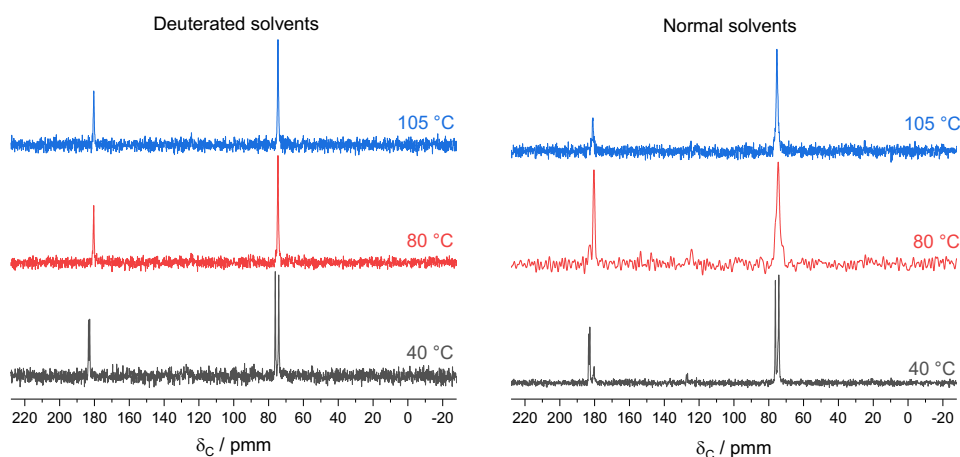


**Figure 2.29** Summed  $^{13}\text{C}$  CP spectra of lithium-tartrate MOFs at 40, 80 and 105 °C prepared ex-situ in deuterated (*left*) and non-deuterated (*right*) solvent mixtures.

In the solid-state spectra of the samples prepared with deuterated solvents at 40 and 80 °C, a 12 second delay was used. The 40 °C sample showed two peaks around 75 ppm and two peaks around 183 ppm. This corresponds to the **2a** phase as the central carbon atoms and two carbonyl groups will show different environments upon chelation of lithium ions. The 80 °C sample showed only one peak at 75 ppm and a peak at 180 ppm indicating the **2b** phases in which the alkyl and carbonyl environments are now equivalent when the lithium is only monodentate bound to the tartaric acid. To ensure a spectrum was obtained for the 105 °C sample (unlike in in-situ experiment), a longer relaxation delay of 30 seconds was required between scans to ensure sufficient signal. One peak at 75 ppm and 180 ppm was seen, which

was identical to the equivalent 80 °C reaction, which matches the literature in that **2b** is the final phase at higher temperatures.

Some unusual results are seen in the  $^{13}\text{C}$  CP spectra of the samples prepared with non-deuterated solvents (Figure 2.29), as there is a mixture of **2a** and **2b** phases present at 40 °C and 80 °C suggesting that the reaction progresses at a different speed in normal solvents compared to the deuterated solvents. For the 40 °C sample, the same peaks were observed at both 75 and 183 ppm (**2a**), however an additional small peak at 180 ppm is present which corresponds with the single peak seen at 80 °C for the **2b** phase in both the deuterated and non-deuterated samples. In the 80 °C sample, the same major peaks are observed as in the deuterated sample, but there is a small broad peak at 183 ppm which corresponds to the **2a** peak in the 40 °C samples. This can be seen in closer detail in Figure 2.30.

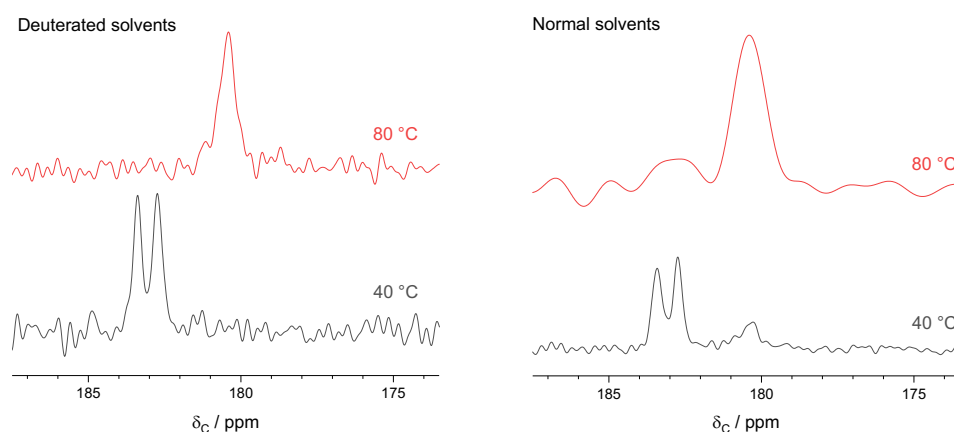


**Figure 2.30** Expanded high ppm region of  $^{13}\text{C}$  CP spectra for the deuterated sample (*left*) and non-deuterated samples (*right*).

Yeung *et al.* reported that upon forming the **2a** phase at 40 °C, the **2b** phase then forms as the temperature is increased to 80 °C, which then converts back to **2a** before finally reforming **2b** at 105 °C. The ex-situ samples were heated at the three temperatures for 24 hours before the reaction was stopped, which is a much longer timescale than the reactions were performed for during in-situ XRD experiment. Therefore, it is possible that the reaction in the non-deuterated solvents is faster which is why we see both phases in the NMR spectra; at 40 °C some **2a**→**2b** conversion is seen and then **2b**→**2a** conversion at 80 °C due to the length of time the ex-situ experiment was ran for.

The  $^{13}\text{C}$  CP measurement was repeated for the two samples synthesised at  $105\text{ }^\circ\text{C}$ , but after heating the sample at  $105\text{ }^\circ\text{C}$  and cooling back to room temperature. Figure 2.31 shows that spectrum is the same as that recorded at room temperature for both the non-deuterated and deuterated sample. The peaks in the normal sample are slightly broader at room temperature suggesting the sample was still slightly wet, but the peaks then appear even broader and less intense when the spectrum is recorded at high temperature. This may be a likely reason for why no signal was obtained at  $105\text{ }^\circ\text{C}$  during the in-situ reaction in Section 2.3.3.2.

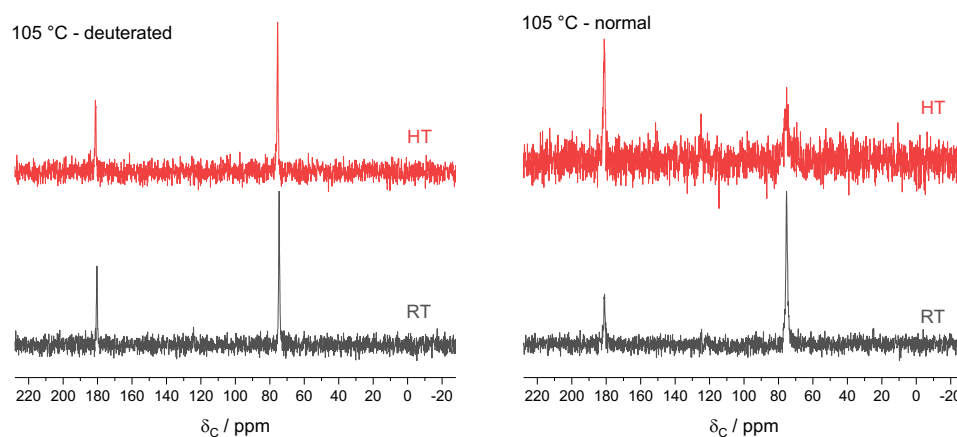


**Figure 2.31**  $^{13}\text{C}$  CP spectra recorded at room temperature (RT) and high temperature (HT) of lithium-tartrate samples prepared at  $105\text{ }^\circ\text{C}$  in both deuterated (*left*) and (*right*) normal solvents.

#### 2.3.3.4 Ex-situ and in-situ PXRD results

Characterisation of the solid reaction products were carried out by PXRD. After the in-situ NMR experiment was completed, the sample was recovered from the tube insert and post-reaction diffraction patterns were obtained. Figure 2.32 shows the diffraction pattern of the in-situ sample compared with the ex-situ sample prepared in deuterated solvents at  $105\text{ }^\circ\text{C}$ . The signal-to-noise ratio is poor due to the small quantity of material, but the more intense peaks broadly correspond with the ex-situ pattern confirming that the **2b** phase is the final product of the reaction.

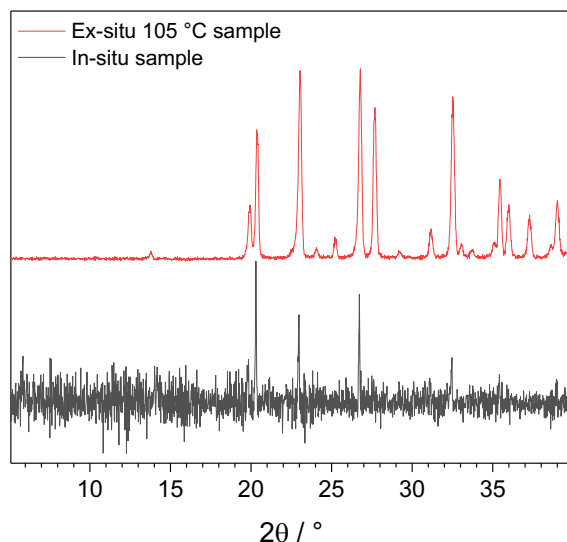


**Figure 2.32** PXRD pattern of the solid prepared in the in-situ reaction (background has been corrected).

The diffraction patterns of the six ex-situ samples are shown in Figure 2.33, strongly agreeing with the reported data by Yeung *et al.* in which phase **2a** should be present at 40 °C, while phase **2b** is formed at 80 °C and 105 °C.

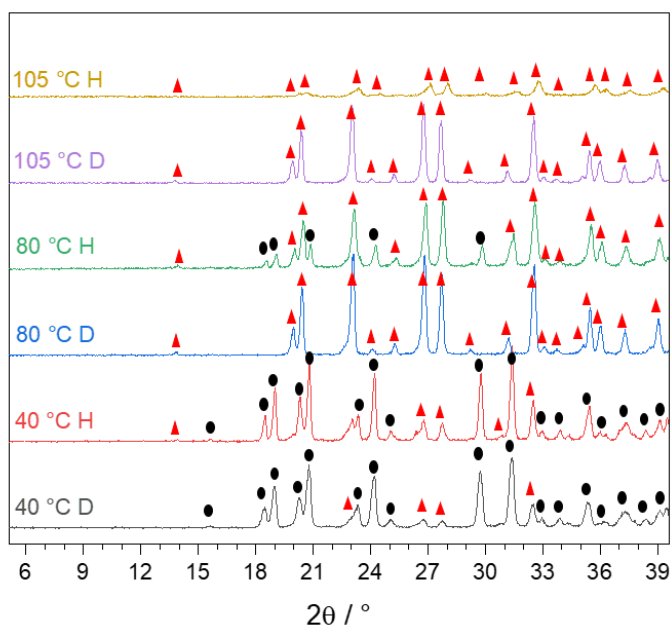


**Figure 2.33** PXRD patterns of lithium-tartrate MOFs formed at 40, 80 and 105 °C prepared in non-deuterated (H) and deuterated (D) solvent mixtures. The two phases **2a** (black circles) and **2b** (red triangles) are indicated.

In deuterated solvents, this is evident and at each reaction stage the solid produced is phase pure and this corroborates the NMR results in Section 2.3.3.3; the 40 °C product has a few peaks associated with **2b** present, but at a very low proportion. The reactions

carried out in non-deuterated solvents show some interesting results. At 40 °C and 80 °C both phases are observed agreeing with the NMR data, again strengthening the suggestion for the reaction progressing at a faster rate in non-deuterated solvents.

### 2.3.3.5 Summary

The formation of a lithium-tartrate MOF has been monitored using the CLASSIC NMR approach. The liquid phase spectra showed the starting materials were present at all temperatures throughout the experiment but did not provide any kinetic information. Heating at three discrete temperatures, rather than covering a range may have led to the transitions being missed by NMR and the small quantity of material produced resulted in very weak  $^1\text{H}$  and  $^{13}\text{C}$  spectra. However, ex-situ syntheses of larger-scale samples ex-situ allowed for collection of the  $^{13}\text{C}$  solid-state spectra. This yielded interesting results as we were able to distinguish between the **2a** and **2b** phases in the NMR data when comparing alongside the reported PXRD patterns. The experiments were carried out in both deuterated and non-deuterated solvents and the NMR spectra provided insight into the H/D kinetics of the reaction as the reaction appeared to progress faster in non-deuterated solvents resulting in a mixture of phases at the lower temperature range.

As the NMR approach has successfully highlighted the difference between multiple phases, the technique was applied to one of the most well-known MOFs syntheses with interesting phase behaviour in the following section.

### 2.3.4 MOF-5

MOF-5 is the archetypal framework – mentioned briefly in Chapter 1 – renowned for its exceptionally high porosity and stability (Figure 2.34).<sup>32</sup> However, unlike the multiple phases that form with lithium tartrate MOFs, the solvothermal synthesis of MOF-5 using zinc nitrate and terephthalic acid in DMF at temperatures around 120 °C often forms unwanted side products in the form of phases that are impossible to separate.<sup>46</sup> Diffraction studies have been used to understand the growth of these by-products, but the mechanisms are still unclear. It was hoped that the CLASSIC NMR experiment would provide an orthogonal study whereby the formation of MOF-5 can be monitored using variations of both reactant concentration and reaction temperatures, providing an insight into the complicated pathways to formation of the phases that form when performing scale-ups of this reaction. Recently, it has been found that MOF-5 can be formed from conversion of MOF-2/MOF-2-DMF, with the interconversion readily occurring upon removal and addition of water molecules.<sup>47</sup>

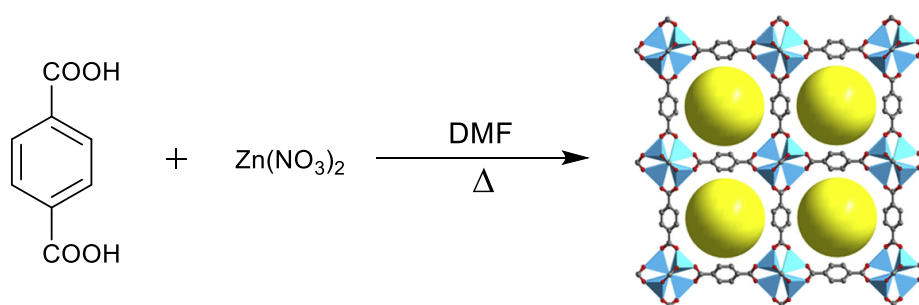


**Figure 2.34** Synthesis of MOF-5. Adapted from reference 32.

#### 2.3.4.1 Synthesis

The synthesis of phase-pure MOF-5 had previously been optimised by MChem student Amy Mathias, under the supervision of the thesis author. It had been found that adding specific mmol quantities of water to a mixture of  $\text{ZnNO}_3$  and BDC in DMF, followed by solvent exchange of the white product, a phase-pure material could be obtained. For the in-situ NMR experiment, the concentration of the reactants was increased five-fold and deuterated  $d_7$ -DMF was used as the solvent.

### 2.3.4.2 CLASSIC NMR of MOF-5

The reaction solution was added to a 20  $\mu\text{L}$  Kel-F tube which was inserted into a rotor and the reaction was monitored in-situ at 120  $^{\circ}\text{C}$  for approximately 45 hours, in which the acquisitions and time resolution were the same for the lithium-tartrate MOF reaction (Section 2.3.3). Due to the extended time scales needed for this reaction, only a single reaction was performed on the high-field spectrometer.

#### 2.3.4.2.1 $^1\text{H}$ results

Figure 2.35 shows the  $^1\text{H}$  liquid-phase 2D spectra during the in-situ reaction at 120  $^{\circ}\text{C}$ . There is an initial shift of all peaks of *ca.* 1 ppm downfield to a higher ppm during the first 2 hours of the reaction; this is a result of the increased temperature as the shim coils warmed up. Only one peak at *ca.* 9 ppm associated with the terephthalic acid linker is present which remains throughout the duration of the synthesis. A large broad peak at *ca.* 7 ppm can also be seen (like in the MFM-500(Ni) reaction) which does not begin to shift until 22 hours into the reaction. It moves downfield, moving past the sharp peak of the aromatic linker, to approximately 9 ppm. The signals for the DMF are present, but weak and do not shift during the course of the reaction. At around 27 hours, there is a loss in signal due to tuning problems, resulting in the following spectra having weaker intensities. After 33 hours, no signal is seen but the reaction was continued for a further 10 hours.

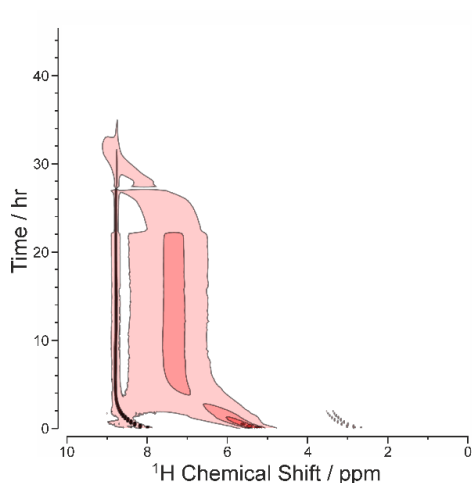


**Figure 2.35** 2D  $^1\text{H}$  NMR spectrum for in-situ MOF-5 reaction. This plot was produced by Dr Colan Hughes.

### 2.3.4.2.2 $^{13}\text{C}$ results

The  $^{13}\text{C}$  HPDEC spectra show both the liquid and solid phases of the reaction (Figure 2.36). As with the  $^1\text{H}$  2D spectra, the signals show a slight shift to higher ppm as the shim coil temperature increases. The two large peaks at 116 and 107 ppm are the signal from the Kel-F tube and remain present throughout the reaction. The peaks attributed to the terephthalic acid linker are present at *ca.* 130 and 138 ppm and at 170 ppm which are from the two aromatic environments and the carbonyl environment respectively. The peaks at 138 and 170 ppm become weaker around 22 hours (the same time as which the broad peak in the  $^1\text{H}$  spectra begin to shift) and the peak at 130 ppm remains prominent until approximately 27 hours. There is a loss of signal in the contour plot at 27 hours into the reaction due to a problem with the tuning, and when the signal is regained the spectrum intensity is slightly weaker. The two peaks between 30 – 40 ppm and peak at 165 ppm can be assigned to the two methyl groups and aldehyde group of DMF respectively, and these remain present until *ca.* 33 hours after which they disappear. However, there are no additional peaks present that can be assigned to the formation of MOF-5. The  $^{13}\text{C}$  CP solid-state spectrum is not shown as no signal was observed during the in-situ measurement.

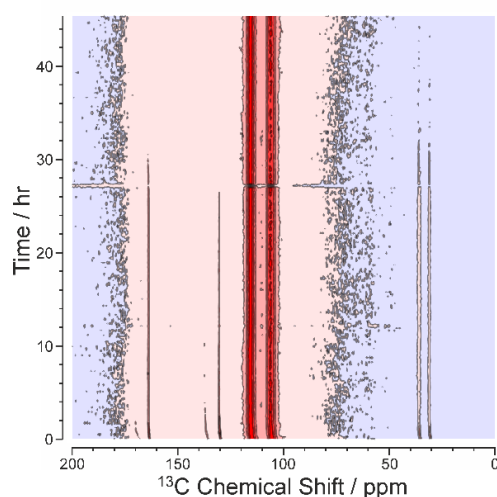


**Figure 2.36** 2D  $^{13}\text{C}$  HPDEC spectra during in-situ MOF-5 reaction. This plot was produced by Dr Colan Hughes.

### 2.3.4.3 PXRD results

The rotor contained a small quantity of white solid post-reaction which was analysed by PXRD (Figure 2.37). It can be seen that phase-pure MOF-5 was not synthesised, however some peaks do correspond to the simulated MOF-2-DMF pattern.<sup>48</sup> This suggests that the unknown amounts of water present from the deuterated solvent is affecting the final reaction product.

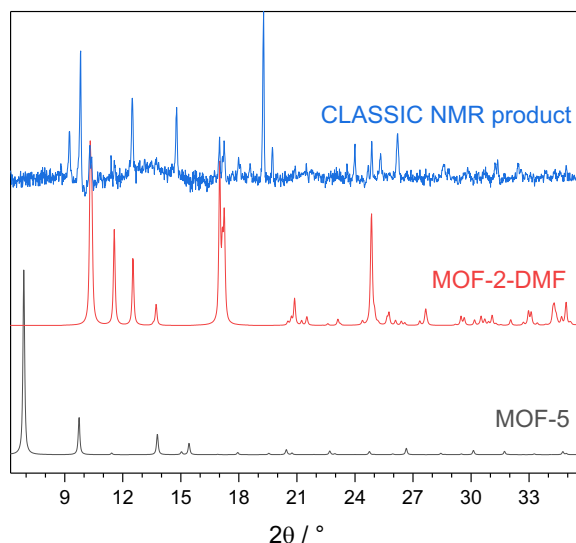


**Figure 2.37** PXRD comparison of simulated MOF-5 (black), MOF-2-DMF (red) and the product synthesised during the CLASSIC NMR experiment (blue).

### 2.3.4.3 Summary

The in-situ NMR approach was used to study the formation of MOF-5, allowing us to monitor the changes in the  $^1\text{H}$  and  $^{13}\text{C}$  spectra. Unfortunately, only signals from the starting reagents were observed suggesting that the reaction concentration was too weak to detect any signal as a result of product formation. While the approach allowed us to record in-situ measurements with a reasonable time resolution, we were unable to obtain the nucleation and growth parameters for the process as the long duration experiment could not be conducted at multiple temperatures due to time constraints. Analysis of the in-situ reaction product formed by PXRD concluded that an additional crystalline phase (that was neither MOF-5 or MOF-2-DMF) had formed, which is yet to be identified, suggesting that the use of deuterated solvents and excess water is influencing the synthesis. The MOF-5 reaction is well-known for its synthetic complications; it would be necessary to undertake further laboratory syntheses in order

to optimise the reaction conditions needed to obtain phase-pure material during the in-situ NMR experiment. Although more information can be extracted, it is beyond the scope of this thesis.

In the final section of this chapter, a novel photoactive MOF was studied in the hope that the NMR data will provide a more complete picture of the unknown formation process.

### 2.3.5 Spiropyran-MOFs

Spiropyran-based MOFs show potential as interesting class of photoresponsive materials, in which the spiro-containing component of the framework can undergo a structural change upon irradiation with UV light, only coming to light in the last few years. A novel spiro- based MOF was synthesised in 2016 by Dr Magdalene Chong, supervised by Prof. Martin Schröder and Dr Timothy Easun at the University of Nottingham, and the synthesis has been found to form multiple phases.<sup>33</sup> Figure 2.38 shows the reaction of zinc nitrate, 1',3',3'-trimethylspiro[chromene-2,2'-indoline]-5',6-dicarboxylic acid and *N*<sup>1</sup>,*N*<sup>4</sup>-di(pyridine-4-yl)-terephthalamide in DMF and ethanol. The reaction yields two crystalline phases (shown) and an amorphous phase. They have yet to be isolated phase pure, and by monitoring the reaction by NMR may shed light onto the way crystallisation process can be controlled.

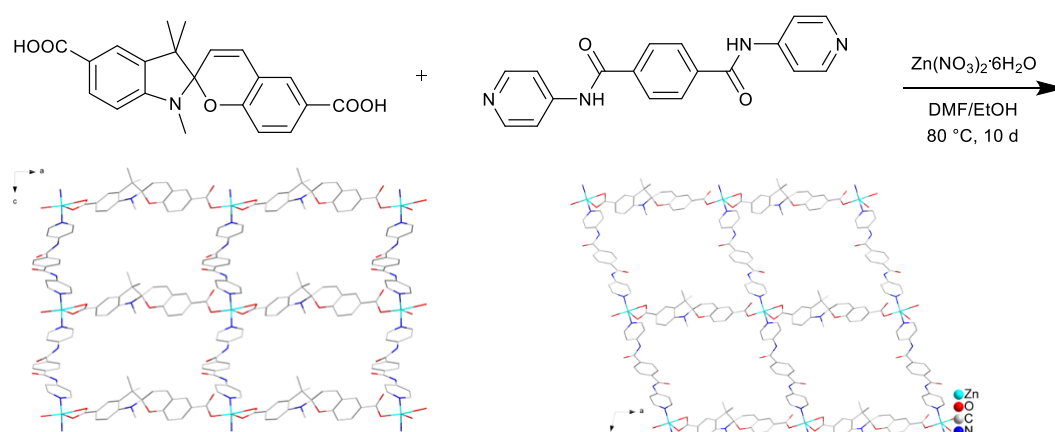


**Figure 2.38** Reaction of zinc nitrate, L = 1',3',3'-trimethylspiro[chromene-2,2'-indoline]-5',6-dicarboxylic acid and P = *N*<sup>1</sup>,*N*<sup>4</sup>-di(pyridine-4-yl)-terephthalamide in DMF/EtOH producing colourless crystals of {Zn(L<sub>3</sub>)(*syn*-P)·(DMF)<sub>3</sub>(H<sub>2</sub>O)}<sub>n</sub> (left) and {Zn(L<sub>3</sub>)(*anti*-P)·(DMF)<sub>3.5</sub>(H<sub>2</sub>O)<sub>1.5</sub>}<sub>n</sub> (right).

### 2.3.5.1 Synthesis

In order to study the several phases by NMR, the conditions were altered to have an increased reactant concentration and to use deuterated solvents. Due to the small quantity of material produced and the long timescales for the syntheses, the in-situ CLASSIC NMR experiment was not attempted. Instead, multiple parallel reactions were performed in the laboratory and stopped at different time points, sampled and the  $^1\text{H}$  and  $^{13}\text{C}$  spectra were recorded on the 850 MHz spectrometer at University of Warwick.

In a first set of experiments, multiple reactions at the original and an increased concentration were carried out ex-situ and each reaction was stopped after heating at 80 °C for 1 day, 2 days *etc.* up to 10 days. The liquid and solid-state NMR spectra of the resulting mixtures of reaction solution and phase-impure products were obtained.

In a second set of experiments, only four reactions at the increased concentration were carried out ex-situ in which the reactions were stopped after 1, 4, 7 and 10 days at 80 °C. The solid material was separated from the solution, and the pink product was left to dry in air. Previous experiments have shown the crystalline products to be air stable for prolonged periods of time, which have been confirmed via PXRD taken after a 5-month interval showing no changes to the diffraction peaks.

### 2.3.5.2 NMR of ex-situ spiropyran-MOF samples

For the first set of experiments, a mixture of the solid products and reaction solution were inserted into a 20  $\mu\text{L}$  Kel-F tube and sealed in a rotor.  $^1\text{H}$  and  $^{13}\text{C}$  CP and  $^{13}\text{C}$  HPDEC spectra were recorded, with a recycle delay of 5 seconds for the  $^1\text{H}$  measurement and 3 seconds for both  $^{13}\text{C}$  measurements at room temperature on the 3-day and 8-day reaction samples.

In the second experiment attempts, the pink solid product only was inserted into a rotor and the  $^{13}\text{C}$  CP spectra were recorded (with a recycle delay of 6 s) for the 1, 4, 7- and 10-day reaction samples.

### 2.3.5.2.1 $^1\text{H}$ results

Figure 2.39 shows the  $^1\text{H}$  spectrum of the spiro-MOF reaction solution and solid products after heating at 80 °C for 8 days. The original reaction concentration was too weak meaning that a poor spectrum was recorded. The increased concentration gave a better spectrum, however there are many peaks attributed to the spiropyran molecule and  $N^l, N^l$ -di(pyridine-4-yl)-terephthalamide dissolved in the deuterated DMF/ethanol mixture. This makes it very hard to characterise peaks that may be associated with solid formation during the reaction and the spectra are hence unassigned.

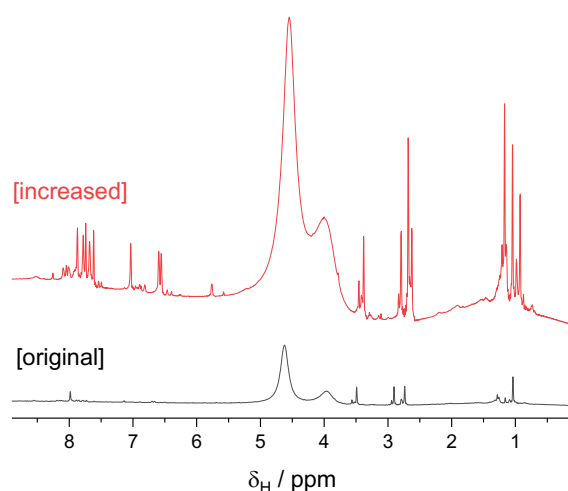


**Figure 2.39**  $^1\text{H}$  spectra of spiro-MOF 8-day reaction sample at the original concentration (black) and increased concentration (red).

### 2.3.5.3.2 $^{13}\text{C}$ results

From first set of experiments, it was difficult to obtain adequate signal in both the liquid and solid-state spectra, even after 64 and 1024 scans respectively (Figure 2.40 – black and red trace), at both the original and increased reactant concentrations. This was due to two possible causes: the small amount of product in the reaction solution in the 20  $\mu\text{L}$  tube insert and insufficient relaxation delay. To eliminate the possibility of relaxation delay, a  $^{13}\text{C}$  CP spectrum of the spiro-MOF precursor was obtained with a delay of 6 seconds (blue).

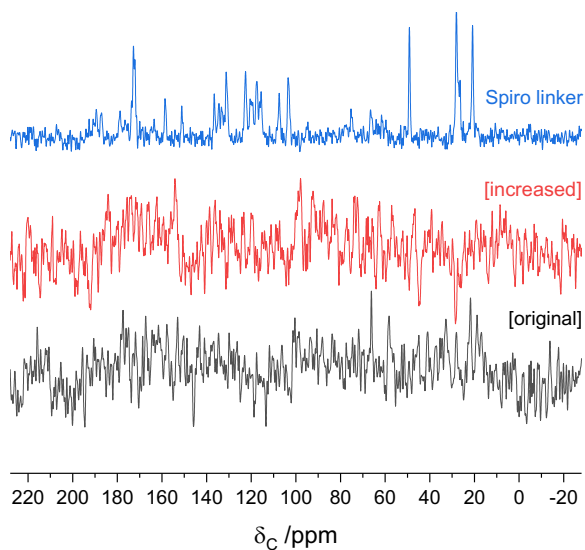


**Figure 2.40**  $^{13}\text{C}$  CP spectra of spiropyran-MOF 8-day reaction sample at the original concentration (black) and increased concentration (red) compared with the solid-state spectrum of the spiropyran linker only (blue).

This led to reduction of the decoupling power and increasing the number of acquisitions, but as neither of these factors increased the signal intensity it was concluded that there was not enough solid material present in the sample.

After revising the experimental procedure for the second set of the experiments using an increased reactant concentration, the solid products were filtered from the reaction solvents and dried before collecting the solid-state spectra. Weak  $^{13}\text{C}$  CP spectra were obtained after varying numerous parameters such as the number of acquisitions and the relaxation delay. The solid-state spectra of the 1, 4, 7 and 10-day samples were acquired with 512 scans and a 6 second delay (Figure 2.41). The  $^{13}\text{C}$  spectrum of the spiropyran linker is also shown for comparison. The poor signal-to-noise ratio indicate the number of scans were not sufficient, but it was not possible to repeat due to the time constraints on the high-field spectrometer.

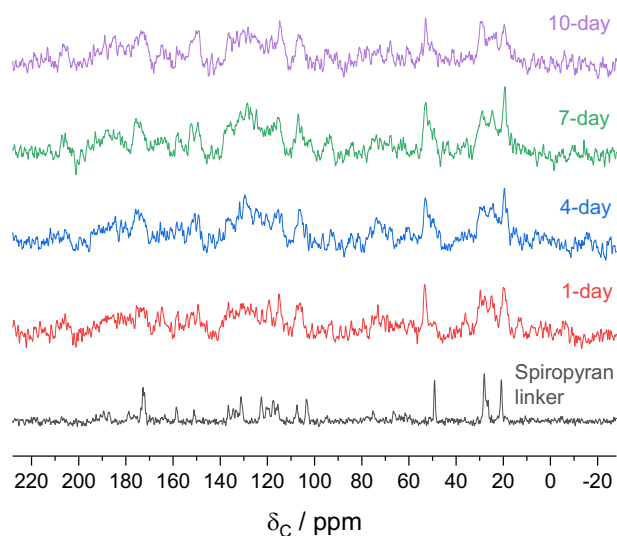


**Figure 2.41**  $^{13}\text{C}$  CP spectra of timed spiropyran-MOF syntheses (coloured traces) compared with the spiropyran linker (black trace).

The solid reaction products produce very different solid-state spectra to the spiropyran linker clearly indicating that reactions have occurred, even after only 1 day of heating. Changes of peaks at *ca.* 20, 30, 50, 105, 150 and 175 ppm occur as the reaction time increases, which could initially be a result of nucleation of small complexes at early timescales before growth of the framework. It is difficult to conclude any further detail of these results from the NMR spectra.

### 2.3.5.3 PXRD results

Post-NMR, the solid samples from the second set of experiments were analysed by PXRD and the patterns are shown in Figure 2.42. The patterns are weak, have insufficient well-defined peaks to index and show the presence of amorphous material, but they can be compared to the patterns to the simulated PXRD patterns of the two known crystalline phases of the spiropyran-based MOF.

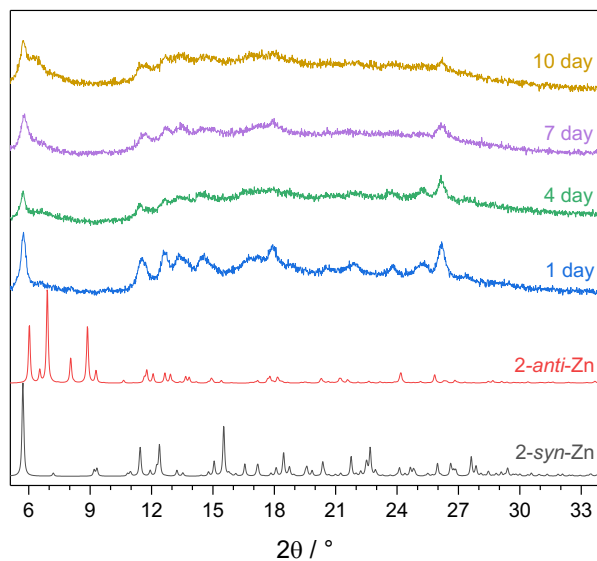


**Figure 2.42** PXRD patterns of the spiropyran-MOFs synthesised using the adapted method compared with the simulated patterns for the known *syn*- and *anti*- crystalline phases.

The appearance of the *syn*-conformation can be seen after only one day ( $\sim 5.74^\circ 2\theta$ ) suggesting that this is the first crystalline phase that forms and is still present after heating the reagents for 10 days. As reaction time progress, the peaks become broader suggesting that the amorphous phase forms at longer reaction timescales.

#### 2.3.5.4 Summary

Using the 850 MHz spectrometer, we were able to obtain solid-state  $^{13}\text{C}$  data of a novel spiropyran-based MOF synthesised for varying reaction times. Unfortunately, due to the phase impurity of the material, it was impossible to assign the peaks seen in each spectrum. However, PXRD data showed that the *syn*-phase of the MOF formed after only one day yielding some insight into the reaction pathway. This suggests that a lower yield is obtained at decreased reaction time, but perhaps phase-pure material could possibly be extracted after 1 day. The long timescales and small amounts of material produced make this reaction difficult to study by in-situ NMR but using these new insights it may be possible upon further increasing the reactant concentrations to study the initial phase formation during the first 24 hours of the reaction.

## 2.4 Conclusions

This chapter has demonstrated that the CLASSIC NMR technique can be used to study the formation of a wide variety of MOFs. Entire reactions of well-published and novel material have been monitored from start to finish, providing complementary information on the time-evolution of the liquid and solid-state of the reaction simultaneously. A mixture of outcomes were achieved upon studying the five different frameworks described in the previous sections.

Due to the limited time availability of the three visits to the NMR facility, we were unable to obtain a clear picture of the crystallisation of AlPO-5 and MOF-5. The experiments were less successful due to problems associated with the synthesis of the material and the small quantity of product formed to be detected by NMR. The results of the spiropyran-MOFs also did not achieve all the objectives set out however we have been able to monitor the changes in crystallinity leading us to adapt the reaction parameters to obtain phase pure material in the future.

Studying the formation of a lithium-tartrate MOF by NMR proved to be very informative. Not only could the different phases be distinguished, the H/D effects when the framework was synthesised in non-deuterated and deuterated solvents could be observed.

For the MFM-500(Ni) system, it was possible to meet all the objectives set out at the beginning of this section. Qualitative data was obtained from the  $^1\text{H}$  spectra on the solution-phase processes at five different temperature and therefore quantitative information to model the kinetic parameters of crystallisation using a Gualtieri fit.

## 2.5 Experimental

All chemicals were of reagent-grade quality and used as received. Nickel nitrate hexahydrate, zinc nitrate hexahydrate, terephthalic acid, triisopropylphosphite, phosphoric acid, aluminium oxide (20% in water colloidal dispersion) and tetrapropylammonium hydroxide were purchased from Alfa Aesar. *Meso*-tartaric acid and 1,3,5-tris(*p*-bromophenyl)benzene were purchased from TCI UK Ltd. Lithium acetate was purchased from Fluorochem and commercial solvents were bought from Fisher Scientific. Deuterated DMF and ethanol were purchased from Goss Scientific and D<sub>2</sub>O from Sigma Aldrich.

CLASSIC NMR measurements were performed on a Bruker Avance III spectrometer at the UK 850 MHz Solid-State NMR Facility, University of Warwick (<sup>1</sup>H Larmor frequency, 850 MHz; <sup>31</sup>P Larmor frequency, 344 MHz; <sup>13</sup>C Larmor frequency, 214 MHz; 4 mm HXY probe in double-resonance mode). In all CLASSIC NMR syntheses, the sample rotor was inserted into the spectrometer, spun at a MAS frequency of 12 kHz and the temperature (internally calibrated against lead nitrate<sup>28</sup>) was increased to the required value, taking into account the heating effect due to the spinning (12 kHz MAS corresponds to a temperature increase of 13 °C).<sup>29</sup>

Liquid-state <sup>1</sup>H, <sup>13</sup>C and <sup>31</sup>P NMR measurements were performed at Cardiff University on a Bruker Avance II 400 or Bruker Ascend 500 MHz spectrometer.

FT-IR spectra were recorded using a SHIMADZU IRAffinit-1S spectrometer embedded with an ATR attachment.

PXRD patterns of all synthesised materials were obtained with a Bruker D8 Diffractometer (Ge-monochromated CuK $\alpha_1$  radiation) operating in transmission mode with a Vântec detector using Cu/Mo radiation ( $\lambda = 1.54056 \text{ \AA}$ ) at 21 °C scanning a range of  $2\theta = 4^\circ - 50^\circ$  or an PANalytical X'Pert PRO Chiller 59 using a Ni-filtered CuK $\alpha$  radiation source ( $\lambda = 1.5418 \text{ \AA}$ ) scanning a range of  $2\theta = 4 - 50^\circ$ .

SAXS measurements were recorded using a Xenocs Xeuss 2.0 laboratory beamline equipped with a Cu microfocus source ( $\lambda = 1.54056 \text{ \AA}$ ). A sample-to-detector distance of 550 mm, giving scattering vector ( $Q$ ) in the range  $0.02 - 0.72 \text{ \AA}^{-1}$  where  $Q = 4\pi/\lambda \sin(\theta/2)$ .

In-situ XRD data was recorded on beamline I12<sup>49</sup> at Diamond Light Source, Harwell Science and Innovation Campus, UK, using monochromatic X-rays ( $\lambda = 0.23417 \text{ \AA}$ ). Data processing was performed using DAWN<sup>50</sup> and batch Pawley refinements were performed in Topas-Academic V6.<sup>51</sup> Kinetics were modelled in OriginPro 2017, attempting to use the Gualtieri model,<sup>36</sup> fitted to the total integrated diffraction peak area extracted from the Pawley refinements.

### 2.5.1 MFM-500(Ni)

**Synthesis of BTPPA.** Benzene-1,3,5-*p*-phenylphosphonic acid was synthesized following a literature procedure.<sup>34</sup> A suspension of 1,3,5-tris(*p*-bromophenyl)benzene (2.0 g, 3.68 mmol), triisopropyl phosphite (12.0 mL, 52.3 mmol), and Pd(PPh<sub>3</sub>)<sub>4</sub> (20 mg, 0.02 mmol) was heated at 120 °C for 3 hours. After 3 h, additional triisopropyl phosphite (3.0 mL, 13.10 mmol) and Pd(PPh<sub>3</sub>)<sub>4</sub> (20 mg, 0.02 mmol) were added. The mixture was heated to 205 °C for 2-3 days. Upon cooling, the crude product crystallised, was filtered and washed with hexane (60 mL) to give 1,3,5-[*p*-C<sub>6</sub>H<sub>4</sub>P(O)(O*i*-Pr)<sub>2</sub>]<sub>3</sub>C<sub>6</sub>H<sub>3</sub>. This was then solubilised in HCl/H<sub>2</sub>O (*v/v* = 2:1) and refluxed for 2 days. Upon cooling, a viscous oil formed. The solution was decanted, and the product was recrystallized from MeOH. Yield: 92.8 %. **<sup>1</sup>H NMR** (500 MHz, *d*<sub>6</sub>-DMSO):  $\delta_{\text{H}} = 8.01$  (s, 3H), 7.99 (dd, 6H, *J* = 8.3, 3.2 Hz), 7.81 (dd, 6H, *J* = 12.6, 8.3 Hz). **<sup>31</sup>P NMR** (202 MHz, *d*<sub>6</sub>-DMSO):  $\delta_{\text{P}} = 12.59$  (s). **HRMS** (ES<sup>-</sup>): *m/z* = 545.0343; calculated 545.0320 for [C<sub>24</sub>H<sub>20</sub>O<sub>9</sub>P<sub>3</sub>]<sup>-</sup>. **IR:**  $\nu_{\text{max}}/\text{cm}^{-1} = 1596, 1387, 1139, 999, 923, 818, 691, 535$ .

**Laboratory control synthesis.** BTPPA (156 mg, 0.25 mmol) and Ni(NO<sub>3</sub>)<sub>2</sub>·6H<sub>2</sub>O (165 mg, 0.50 mmol) were dissolved in D<sub>2</sub>O/*d*<sub>7</sub>-DMF (0.5 mL, *v/v* = 1.5:2) at room temperature. The clear green solution was sealed in a vial and heated on an aluminium heating block at 60, 70, 80 or 90 °C until solid formed. The green crystalline product was removed from solution and air dried. Yield: 290 mg. **IR:**  $\nu_{\text{max}}/\text{cm}^{-1} = 3366, 2359, 2077, 1620, 1406, 1331, 1258, 1136, 1042, 934, 899, 820, 691$ .

**CLASSIC NMR experiment.** BTPPA (25 mg, 0.046 mmol) and Ni(NO<sub>3</sub>)<sub>2</sub>·6H<sub>2</sub>O (26.5 mg, 0.091 mmol) were dissolved in D<sub>2</sub>O and *d*<sub>7</sub>-DMF (80  $\mu\text{L}$ , *v/v* = 1.5:2) at room temperature. 20  $\mu\text{L}$  of clear green solution was transferred to a Kel-F tube, which

was inserted into a zirconia rotor and sealed with an insert tightened by a screw, followed by a drive tip. Three types of NMR spectrum were acquired in a cycle:  $^1\text{H}$  direct excitation (liquid phase only),  $^{31}\text{P}$  direct excitation without  $^1\text{H}$  decoupling (liquid-phase only) and  $^{31}\text{P}$  direct excitation with  $^1\text{H}$  decoupling (liquid and solid-phase). The acquisition of one cycle of three spectra took 7.1 minutes setting the time resolution for the experiment. The recycle delay was 3 seconds for all measurements. Green crystalline material was formed in all reactions.

**In-situ XRD experiment.** BTPPA (624 mg, 1.14 mmol) and  $\text{Ni}(\text{NO}_3)_2 \cdot 6\text{H}_2\text{O}$  (660 mg, 2.28 mmol) were dissolved in  $d_7$ -DMF (1.14 mL) and  $\text{D}_2\text{O}$  (0.86 mL) respectively, the former requiring mild heating to accelerate dissolution. The solutions were combined at room temperature in a borosilicate glass vial (5 mL), which was placed within the in-situ SynRAC cell<sup>52</sup> and heated to 90 °C. Over the course of the reaction, diffraction data were recorded at intervals of 4 s on a Thales Pixium RF4343 area detector with  $430 \times 430 \text{ mm}^2$  active area and a detector distance of 2.402 m.

**Small-angle X-ray scattering experiment.** BTPPA (312 mg, 0.57 mmol) and  $\text{Ni}(\text{NO}_3)_2 \cdot 6\text{H}_2\text{O}$  (330 mg, 1.14 mmol) were dissolved in  $\text{D}_2\text{O}$  and  $d_7$ -DMF (1 mL,  $v/v = 1.5:2$ ) at room temperature. The clear green solution was sealed in a vial and heated on an aluminium heating block at 80 °C. The solution was sampled during the reaction (0, 45, 90, 135, 180, 210 and 240 minutes; 0 minutes = after mixing, before heating); aliquots were taken until green crystals of MFM-500(Ni) were visible by the naked eye. These aliquots were sealed in quartz capillaries and stored at room temperature for a maximum of 2 hr before measurement of the SAXS data. Data were averaged over three consecutive 600 s runs.

## 2.5.2 AIPO-5

A mixture of  $\text{Al}_2\text{O}_3$  (8.9 g, 0.087 mol) and phosphoric acid (85% in soln.) (10 mL, 0.17 mol) were stirred overnight for 24 hours. Tetrapropylammonium hydroxide (40% aq. soln.) (54 mL, 0.26 mol) was then added to the mixture and stirred for a further 24 h. The resulting gel was then used for the in-situ NMR experiment.

**CLASSIC NMR experiment.** 20  $\mu\text{L}$  of the gel was transferred to a Kel-F tube, which was inserted into a zirconia rotor and sealed with an insert tightened by a screw, followed by a drive tip. The temperature was increased to 120  $^{\circ}\text{C}$  for 21 hours.  $^1\text{H}$  direct excitation,  $^{31}\text{P}$  direct excitation *without*  $^1\text{H}$  decoupling and  $^{31}\text{P}$  direct excitation *with*  $^1\text{H}$  decoupling spectra were recorded and the acquisition of one cycle of three spectra took 7.1 minutes setting the time resolution for the experiment. The recycle delay was 3 seconds for all the measurements. The rotor was then cooled, and spectra were acquired at 100, 80, 60, 40 and 20  $^{\circ}\text{C}$ . Due to the small quantity of white material produced, PXRD characterisation could not be performed.

### 2.5.3 Lithium-tartrate MOFs

**CLASSIC NMR experiment.** Lithium acetate (6.6 mg, 0.10 mmol) and *meso*-tartaric acid (8.4 mg, 0.05 mmol) were added to  $d_6$ -ethanol (73  $\mu\text{L}$ ) and  $\text{D}_2\text{O}$  (27  $\mu\text{L}$ ). The suspension was sonicated and 20  $\mu\text{L}$  was transferred to a Kel-F tube, which was inserted into a zirconia rotor and sealed with an insert tightened by a screw, followed by a drive tip. The mixture was heated to 40  $^{\circ}\text{C}$  for 2 h, then heated to 80  $^{\circ}\text{C}$  for 12 h before finally heating to 105  $^{\circ}\text{C}$  for 4 h.  $^1\text{H}$  direct excitation,  $^{13}\text{C}$  CP and  $^{13}\text{C}$  HPDEC spectra were recorded, therefore the effective time resolution for the NMR experiment was approximately 14 minutes. The recycle delay was 5 s for  $^1\text{H}$  measurement and 6 s for  $^{13}\text{C}$  HPDEC and CP measurements. The rotor was then cooled to room temperature and a small quantity of white solid had formed which was analysed by PXRD.

**Ex-situ reactions.** 24 h prior to conducting 850 MHz NMR studies, lithium acetate (66 mg, 1.0 mmol) and *meso*-tartaric acid (84 mg, 0.5 mmol) were added to  $d_6$ -ethanol (0.73 mL) and  $\text{D}_2\text{O}$  (0.27 mL) in three Wheaton vials and all were individually heated at 40, 80 and 105  $^{\circ}\text{C}$ . Lithium acetate (198 mg, 3 mmol) and *meso*-tartaric acid (252 mg, 1.5 mmol) were added to non-deuterated solvents, ethanol (2.2 mL) and water (0.8 mL), in three Wheaton vials and again heated at 40, 80 and 105  $^{\circ}\text{C}$ . After 24 hours the reactions were cooled to room temperature and the white solid material was removed from solution and dried in air for *ca.* 2-3 hours, before being packed into rotors.  $^{13}\text{C}$  CP NMR spectra were recorded for the six samples and the recycle delay was 12 s for each measurement. **Yields:** 50 mg, 54 mg and 52 mg for the *deuterated* samples at 40, 80 and 105  $^{\circ}\text{C}$  respectively. For the *non-deuterated* samples, 207 mg, 202 mg and 157 mg at 40, 80 and 105  $^{\circ}\text{C}$  respectively.

**IR:**  $\nu_{\max}/\text{cm}^{-1} = \underline{40\text{ }^{\circ}\text{C D}}$  2361, 2318, 1595, 1578, 1456, 1429, 1348, 1335, 1302, 1236, 1115, 885, 856, 777, 691, 664;

80 °C D 2365, 1586, 1559, 1541, 1506, 1337, 1240, 1082, 1026, 941, 791, 685;

105 °C D 3177, 2367, 1586, 1541, 1423, 1337, 1240, 1082, 1026, 941, 797, 683;

40 °C H 3096, 2853, 27626, 2689, 1595, 1406, 1323, 1300, 1269, 1234, 1223, 1097, 966, 891, 858, 783, 760, 719, 692, 657;

80 °C H 3165, 2959, 2855, 2361, 1586, 1558, 1418, 1300, 1223, 1111, 1082, 945, 799, 687;

105 °C H 3165, 2961, 2853, 2363, 1558, 1410, 1323, 1298, 1283, 1223, 1111, 1082, 1022, 943, 889, 797, 681, 956.

#### 2.5.4 MOF-5

**CLASSIC NMR experiment.** Zinc nitrate (anhydrous, 16.5 mg, 0.09 mmol) and terephthalic acid (6.9 mg, 0.04 mmol) were dissolved in  $d_7$ -DMF (100  $\mu\text{L}$ ), before 20  $\mu\text{L}$  was transferred to a Kel-F tube, which was inserted into a zirconia rotor and sealed with an insert tightened by a screw, followed by a drive tip. The sample was heated to 120  $^{\circ}\text{C}$  and was monitored for *ca.* 45 hours.  $^1\text{H}$  direct excitation,  $^{13}\text{C}$  CP and  $^{13}\text{C}$  HPDEC spectra were recorded, therefore the effective time resolution for the NMR experiment was approximately 14 minutes. The recycle delay was 5 s for  $^1\text{H}$  measurement and 6 s for  $^{13}\text{C}$  HPDEC and CP measurements. The rotor was then cooled to room temperature and a small quantity of white solid had formed which was analysed by PXRD.

#### 2.5.5 Spiropyran-MOFs

The MOF synthesis in this section was *previously described* in Dr Magdalene Chong's thesis.<sup>33</sup> The procedure has been reproduced/adapted for the NMR experiments described in this chapter.

**Ex-situ reactions.** Prior to conducting 850 MHz NMR studies, multiple reactions were performed over different time periods to study the differences in the materials formed with variation of time. Zinc nitrate hexahydrate (2 mg, 0.007 mmol), 1',3',3'-trimethylspiro[chromene-2,2'-indoline]-5',6-dicarboxylic acid (2.5 mg, 0.007 mmol) and *N*<sup>l</sup>,*N*<sup>4</sup>-di(pyridin-4-yl)terephthalamide (1 mg, 0.003 mmol) were added to *d*<sub>7</sub>-DMF (80 μL) and *d*<sub>6</sub>-ethanol (40 μL) in 10 Wheaton vials, which were all heated to 80 °C. Each day, for 10 days, one vial was removed from the heat and left to cool. A parallel reaction was also carried out in which the concentration of the reaction solution was increased. Zinc nitrate hexahydrate (2 mg, 0.007 mmol), 1',3',3'-trimethylspiro[chromene-2,2'-indoline]-5',6-dicarboxylic acid (2.5 mg, 0.007 mmol) and the *N*<sup>l</sup>,*N*<sup>4</sup>-di(pyridin-4-yl)terephthalamide (1 mg, 0.003 mmol) were added to *d*<sub>7</sub>-DMF (40 μL) and *d*<sub>6</sub>-ethanol (20 μL). The temperature and duration of the experiment was performed identically as described above. 20 μL of the product and reaction solution was transferred to a Kel-F tube, which was inserted into a zirconia rotor and sealed with an insert tightened by a screw, followed by a drive tip. <sup>1</sup>H and <sup>13</sup>C CP and <sup>13</sup>C HPDEC spectra were recorded on selected samples, with a recycle delay of 5 s for each <sup>1</sup>H measurement and 3 s for both <sup>13</sup>C measurements. No spectra with good signal were obtained.

The second set of experiments were carried out at the increased concentration as described in the section above, however this time the vials were removed after 1, 4, 7 and 10 days. The solutions were centrifuged, and the pink solid material was left to air dry. The solids were inserted into a 20 μL capacity tube insert which was then inserted into the rotor. <sup>13</sup>C CP spectra were recorded on these samples, with a recycle delay of 6 s for each measurement. **Yields:** 4.1 mg, 3.7 mg, 3.6 mg and 3.2 mg for the 1, 4, 7 and 10-day synthesis respectively.

## 2.6 References

- 1 N. Stock and S. Biswas, *Chem. Rev.*, 2012, **112**, 933–969.
- 2 A. Rabenau, *Angew. Chemie Int. Ed. English*, 1985, **24**, 1026–1040.
- 3 J. Klinowski, F. A. Almeida Paz, P. Silva and J. Rocha, *Dalton Trans.*, 2011, **40**, 321–330.
- 4 G. Férey, *Chem. Mater.*, 2001, **13**, 3084–3098.
- 5 O. Shekhah, H. Wang, D. Zacher, R. A. Fischer and C. Wöll, *Angew. Chemie Int. Ed.*, 2009, **48**, 5038–5041.
- 6 F. Millange, M. I. Medina, N. Guillou, G. Férey, K. M. Golden and R. I. Walton, *Angew. Chemie Int. Ed.*, 2010, **49**, 763–766.
- 7 F. Ragon, P. Horcajada, H. Chevreau, Y. K. Hwang, U.-H. Lee, S. R. Miller, T. Devic, J.-S. Chang and C. Serre, *Inorg. Chem.*, 2014, **53**, 2491–2500.
- 8 G. Zahn, P. Zerner, J. Lippke, F. L. Kempf, S. Lilienthal, C. A. Schröder, A. M. Schneider and P. Behrens, *CrystEngComm*, 2014, **16**, 9198–9207.
- 9 Y. Wu, M. I. Breeze, G. J. Clarkson, F. Millange, D. O’Hare and R. I. Walton, *Angew. Chemie Int. Ed.*, 2016, **55**, 4992–4996.
- 10 S. J. Moorhouse, Y. Wu, H. C. Buckley, D. O’Hare, R. Qi, R. Huang, X. Tang, C.-G. Duan, J. Chu, G. Howell, S. Davies, T. Hill, G. Wilkin, U. Pedersen, A. Foster, N. De Maio, M. Basham, F. Yuan and K. Wanelik, *Chem. Commun.*, 2016, **52**, 13865–13868.
- 11 Y. Wu, S. Henke, G. Kieslich, I. Schwedler, M. Yang, D. A. X. Fraser and D. O’Hare, *Angew. Chemie Int. Ed.*, 2016, **55**, 14081–14084.
- 12 Y. Wu, S. J. Moorhouse and D. O’Hare, *Chem. Mater.*, 2015, **27**, 7236–7239.
- 13 M. Kondo, Y. Takashima, J. Seo, S. Kitagawa and S. Furukawa, *CrystEngComm*, 2010, **12**, 1–11.
- 14 A. Polyzoidis, M. Etter, M. Herrmann, S. Loebbecke and R. E. Dinnebier, *Inorg. Chem.*, 2017, **56**, 5489–5492.
- 15 A. K. Cheetham, G. Kieslich and H. H.-M. Yeung, *Acc. Chem. Res.*, 2018, **51**, 659–667.
- 16 M. G. Goesten, E. Stavitski, J. Juan-Alcañiz, A. Martínez-Joaristi, A. V Petukhov, F. Kapteijn and J. Gascon, *Catal. Today*, 2013, **205**, 120–127.
- 17 E. Stavitski, M. Goesten, J. Juan-Alcañiz, A. Martínez-Joaristi, P. Serra-Crespo, A. V Petukhov, J. Gascon and F. Kapteijn, *Angew. Chemie Int. Ed.*, 2011, **50**, 9624–9628.
- 18 J. Cravillon, C. A. Schröder, R. Nayuk, J. Gummel, K. Huber and M. Wiebcke, *Angew. Chemie*, 2011, **123**, 8217–8221.
- 19 J. P. Patterson, P. Abellan, M. S. Denny, C. Park, N. D. Browning, S. M. Cohen, J. E.

- Evans and N. C. Gianneschi, *J. Am. Chem. Soc.*, 2015, **137**, 7322–7328.
- 20 Z. Öztürk, M. Filez and B. M. Weckhuysen, *Chem. - A Eur. J.*, 2017, **23**, 10915–10924.
- 21 G. Delen, Z. Ristanović, L. D. B. Mandemaker and B. M. Weckhuysen, *Chem. - A Eur. J.*, 2018, **24**, 187–195.
- 22 H. Hoffmann, M. Debowski, P. Müller, S. Paasch, I. Senkovska, S. Kaskel and E. Brunner, *Materials (Basel)*, 2012, **5**, 2537–2572.
- 23 T. L. Easun, F. Moreau, Y. Yan, S. Yang and M. Schröder, *Chem. Soc. Rev.*, 2017, **46**, 239–274.
- 24 X. Kong, E. Scott, W. Ding, J. A. Mason, J. R. Long and J. A. Reimer, *J. Am. Chem. Soc.*, 2012, **134**, 14341–14344.
- 25 L.-C. Lin, J. Kim, X. Kong, E. Scott, T. M. McDonald, J. R. Long, J. A. Reimer and B. Smit, *Angew. Chemie Int. Ed.*, 2013, **52**, 4410–4413.
- 26 F. Moreau, D. I. Kolokolov, A. G. Stepanov, T. L. Easun, A. Dailly, W. Lewis, A. J. Blake, H. Nowell, M. J. Lennox, E. Besley, S. Yang and M. Schröder, *Proc. Natl. Acad. Sci. U. S. A.*, 2017, **114**, 3056–3061.
- 27 C. E. Hughes, P. A. Williams and K. D. M. Harris, *Angew. Chemie - Int. Ed.*, 2014, **53**, 8939–8943.
- 28 C. E. Hughes, P. A. Williams, V. L. Keast, V. G. Charalampopoulos, G. R. Edwards-Gau and K. D. M. Harris, *Faraday Discuss.*, 2015, **179**, 115–140.
- 29 S. Pili, S. P. Argent, C. G. Morris, P. Rought, V. García-Sakai, I. P. Silverwood, T. L. Easun, M. Li, M. R. Warren, C. A. Murray, C. C. Tang, S. Yang and M. Schröder, *J. Am. Chem. Soc.*, 2016, **138**, 6352–6355.
- 30 S. Tanahashi, T. Moteki and T. Okubo, *Chem. Lett.*, 2012, **41**, 889–891.
- 31 H. H.-M. Yeung, Y. Wu, S. Henke, A. K. Cheetham, D. O’Hare and R. I. Walton, *Angew. Chemie Int. Ed.*, 2016, **55**, 2012–2016.
- 32 O. M. Yaghi, H. Li, M. Eddaoudi and M. O’Keeffe, *Nature*, 1999, **402**, 276–279.
- 33 M. Chong, University of Nottingham, 2016.
- 34 J. Beckmann, R. Rüttinger and T. Schwich, *Cryst. Growth Des.*, 2008, **8**, 3271–3276.
- 35 R. Kruszynski and T. Sierański, *Cryst. Growth Des.*, 2016, **16**, 587–595.
- 36 A. F. Gualtieri, *Phys. Chem. Miner.*, 2001, **28**, 719–728.
- 37 F. Millange, R. El Osta, M. E. Medina and R. I. Walton, *CrystEngComm*, 2011, **13**, 103–108.
- 38 J. Cravillon, C. A. Schröder, H. Bux, A. Rothkirch, J. Caro and M. Wiebcke, *CrystEngComm*, 2012, **14**, 492–498.
- 39 F. Niekpiel, M. Ackermann, P. Guerrier, A. Rothkirch and N. Stock, *Inorg. Chem.*, 2013, **52**, 8699–8705.

- 40 P. Y. Moh, M. Brenda, M. W. Anderson and M. P. Attfield, *CrystEngComm*, 2013, **15**, 9672–9678.
- 41 T. Rhauderwiek, N. Heidenreich, H. Reinsch, S. Øien-Ødegaard, K. A. Lomachenko, U. Rütt, A. V. Soldatov, K. P. Lillerud and N. Stock, *Cryst. Growth Des.*, 2017, **17**, 3462–3474.
- 42 H. H.-M. H.-M. Yeung, A. F. Sapnik, F. Massingberd-Mundy, M. W. Gaultois, Y. Wu, D. A. X. Fraser, S. Henke, R. Pallach, N. Heidenreich, O. V. Magdysyuk, N. T. Vo and A. L. Goodwin, *Angew. Chemie Int. Ed.*, 2019, **58**, 566–571.
- 43 M. Doucet, J. H. Cho, G. Alina, J. Bakker, W. Bouwman, P. Butler, K. Campbell, M. Gonzales, R. Heenan, A. Jackson, P. Juhas, S. King, P. Kienzle, J. Krzywon, A. Markvardsen, T. Nielsen, L. O’Driscoll, W. Potrzebowski, R. Ferraz Leal, T. Richter, P. Rozycko, T. Snow and A. Washington, , DOI:10.5281/ZENODO.825675.
- 44 P. Rungrojchaipon, X. Wang and A. J. Jacobson, *Microporous Mesoporous Mater.*, 2008, **109**, 478–484.
- 45 C. A. Fyfe, K. C. Wong-Moon and Y. Huang, *Zeolites*, 1996, **16**, 50–55.
- 46 C. McKinstry, E. J. Cussen, A. J. Fletcher, S. V Patwardhan and J. Sefcik, *Cryst. Growth Des.*, 2013, **13**, 5481–5486.
- 47 L. Schweighauser, K. Harano and E. Nakamura, *Inorg. Chem. Commun.*, 2017, **84**, 1–4.
- 48 S. M. Hawxwell, H. Adams and L. Brammer, *Acta Crystallogr. Sect. B Struct. Sci.*, 2006, **62**, 808–814.
- 49 M. Drakopoulos, T. Connolley, C. Reinhard, R. Atwood, O. Magdysyuk, N. Vo, M. Hart, L. Connor, B. Humphreys, G. Howell, S. Davies, T. Hill, G. Wilkin, U. Pedersen, A. Foster, N. De Maio, M. Basham, F. Yuan, K. Wanelik and IUCr, *J. Synchrotron Radiat.*, 2015, **22**, 828–838.
- 50 J. Filik, A. W. Ashton, P. C. Y. Chang, P. A. Chater, S. J. Day, M. Drakopoulos, M. W. Gerring, M. L. Hart, O. V. Magdysyuk, S. Michalik, A. Smith, C. C. Tang, N. J. Terrill, M. T. Wharmby, H. Wilhelm and IUCr, *J. Appl. Crystallogr.*, 2017, **50**, 959–966.
- 51 A. A. Coelho, *J. Appl. Crystallogr.*, 2018, **51**, 210–218.
- 52 N. Heidenreich, U. Rütt, M. Köppen, A. K. Inge, S. Beier, A.-C. Dippel, R. Suren and N. Stock, *Rev. Sci. Instrum.*, 2017, **88**, 104102.



---

## **Chapter 3**

### **Syntheses of benzimidazolone-based coordination polymers**

---

### 3 Syntheses of benzimidazolone-based coordination polymers

#### 3.1 Introduction

Since the late 1980's when Robson and Hoskins published ground-breaking research on the synthesis of infinite polymeric frameworks consisting of tetrahedral or octahedral metal centres linked by rod-like units,<sup>1,2</sup> there have been countless MOFs reported in the literature formed of metal nodes with *rigid* organic linkers. Examples include the extremely well-known frameworks such as MOF-5,<sup>3</sup> HKUST-1<sup>4</sup> and NOTT-10x series.<sup>5</sup> This chapter will explore unusual structural behaviour with the aim to synthesise materials with a more '*flexible*' linker.

Some of the first examples of flexible *frameworks* were reported in the early 2000s. A nanoporous interpenetrated iron framework by Halder *et al.*<sup>6</sup> and a zinc framework Dybtsev *et al.*<sup>7</sup> both demonstrated considerable flexibility as a result of guest-dependent interactions. Structurally dynamic MOFs have become more frequently reported in recent years, with a comprehensive summary produced in 2018 by Thallapally and co-workers, describing various frameworks that demonstrate flexibility.<sup>8–11</sup> Van Speybroeck and co-workers have also reported an extensive set of theoretical guidelines to computationally model the mechanical stability of flexible and rigid frameworks.<sup>12</sup> Dynamic frameworks often undergo a reversible “breathing motion,” and one of the most famous examples is the MIL-53 series (synthesised with a *rigid* linker). In the chromium analogue, the framework was found to open and shut (resulting in a dramatic change in pore dimensions) upon adsorption and desorption of water molecules (Figure 3.1).<sup>13</sup>

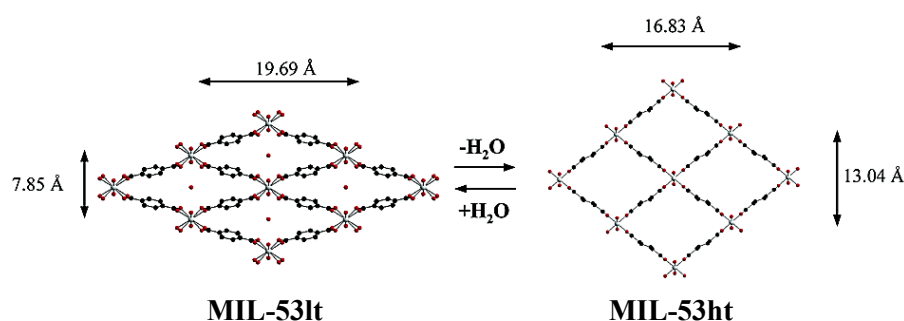
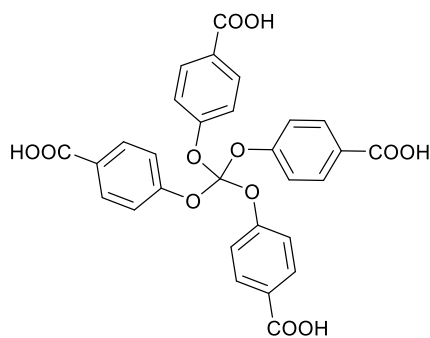


**Figure 3.1** The reversible transition between the hydrated phase (MIL-53lt) and the anhydrous phase (MIL-53ht) results in the pore dimension changing by more than 5 Å. Reproduced from reference 13.

As well as guest molecules inducing structural changes, other external stimuli can also influence the flexible nature of frameworks including which were introduced in Chapter 1 (Section 1.4).<sup>14–17</sup>

In recent years, many new MOFs have been reported that are synthesised with *flexible* linkers (FL-MOFs).<sup>18</sup> They define linkers to be flexible if there is rotation around a single bond with a  $sp^3$  hybrid C, N or O atom in the backbone. The structural diversity using a tetrakis[4-(carboxyphenyl)oxamethyl]methane acid linker (H<sub>4</sub>tcm) (Scheme 3.1) has been heavily explored,<sup>19–21</sup> as various conformations can be achieved due to the relative orientation of the four 4-methoxybenzoic acid arms around the -{O-CH<sub>2</sub>}- moieties.



**Scheme 3.1** Structure of tetrakis[4-(carboxyphenyl)oxamethyl]methane acid (H<sub>4</sub>tcm).

Another way of designing such MOFs is to use flexible peptide-based linkers. Several examples based on this phenomenon have been reported by Rosseinsky and co-workers (earlier examples were described in Chapter 1, Section 1.3). In their most recently published work, the group have used a tripeptide glycine–glycine–l-histidine (GGH) linker to produce a 3D chiral MOF, [ZnGGH-1·(DMF-H<sub>2</sub>O)].<sup>22</sup> Figure 3.2 shows the different torsional angles of the linker which influences the pore shape and internal surface chemistry. This allows the MOF to exhibit nine experimentally observed transformation states that have been found as a result of exchanging the solvent molecules that occupy the pores.

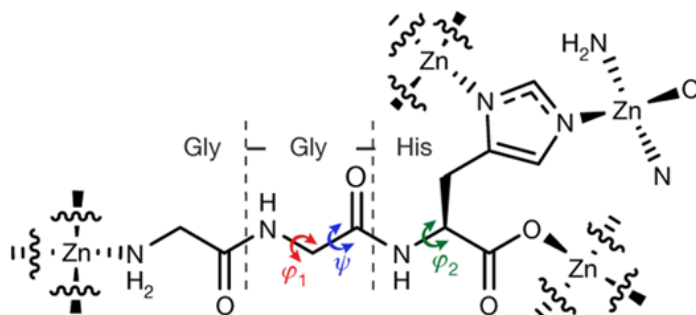


**Figure 3.2** The GGH linker is tetratopic and is connected to four different  $Zn^{2+}$  centres. Multiple conformations can be adopted due to three torsion angles ( $\varphi_1$ ,  $\psi$  and  $\varphi_2$ ). Reproduced from reference 22.

Compared to peptides, benzimidazolone diacetic acid is a molecule with limited conformational flexibility. There have been numerous reports of benzimidazolone-based derivatives published in the literature, in which one of the earliest halogenated examples found applications as fire-retardant monomers and fireproofing agents.<sup>23</sup> Over the last two decades, most studies containing benzimidazolone analogues have found uses in biological applications,<sup>24,25</sup> particularly as use for antiviral agents as inhibitors of HIV,<sup>26,27</sup> and some derivatives have also been assessed for their antifungal and antibacterial properties.<sup>28,29</sup> The molecules are perhaps underutilised as a heterocyclic scaffold, but more recently they have been attached to the *N*-terminus of flexible short peptides to induce self-assembly of the peptides into tuneable hydrogels for use in biomedical applications.<sup>30</sup> Prior to publication of the results discussed in this thesis, there were no reports of benzimidazolones being used as a linker in MOF syntheses.

Dr Adam Martin (UNSW, Australia) has experience working with benzimidazolone-based molecules for the biological hydrogel applications mentioned in the previous paragraph; it was of interest to determine the interaction of a derivative with biologically relevant metals. A copper-based coordination polymer was synthesised with benzimidazolone diacetic acid (Section 3.3.2.3), leading to a collaboration with Dr Timothy Easun and the thesis author to determine how this linker, which has limited flexibility, will react with other metal ions. The structural preferences were explored to define the coordination geometry around different metal nodes, leading to potential insight into the formation of these materials with metal ions concerned with the formation of plaques in the brain leading to neurological diseases.

As Group 2 metals do not display strong geometrical preferences and as the coordination number is primarily based on the size and charge of the ion,<sup>31</sup> it can be expected that strontium and barium structures will have larger coordination numbers than magnesium and calcium structures. Unlike group 2 metals, transition metals often exhibit strong geometrical preferences, dependent on the number of d-electrons, which will ultimately influence the coordination geometry and topology of the subsequent networks.<sup>32</sup>

### 3.2 Aim and objectives

In this chapter, the syntheses of coordination polymers using a flexible linker with a choice of different metals was explored to determine the geometrical preferences in the final structures. The objectives were to:

- i) Synthesise benzimidazolone diacetic acid as a flexible linker.

A three-step synthetic method was followed to produce a large quantity of linker for subsequent reactions.

- ii) Synthesise coordination polymers using group 2 and transition metal salts and characterise bulk samples using PXRD and thermogravimetric analysis (TGA).

A combinatorial approach was carried out by varying metal salts, modulators and reaction temperatures to produce crystalline material suitable for analysis.

- iii) Obtain crystallographic data using SCXRD to describe the structural outcomes.

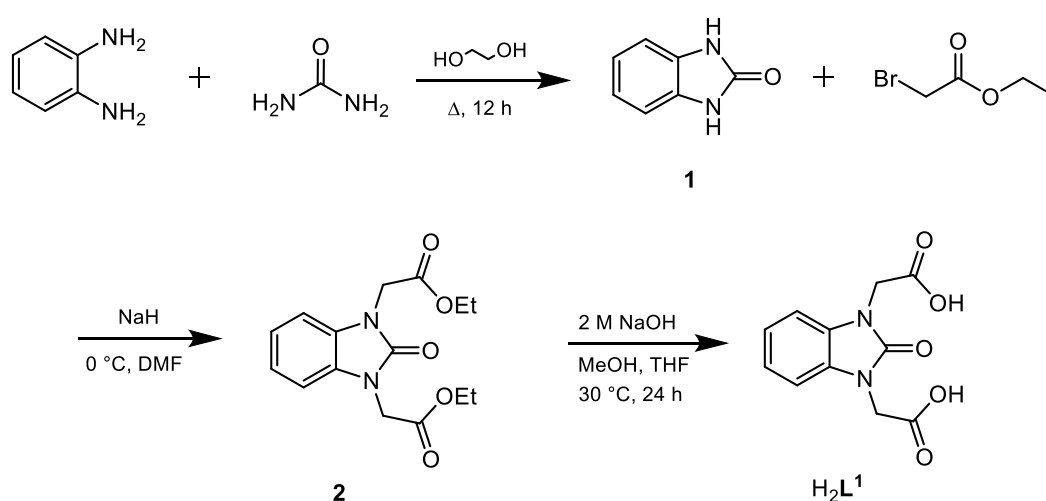
The crystals structures allowed determination of the coordination geometry for each product to assess if the geometry is linker- or metal-defined.

The following results in this chapter were published in 2017 in Royal Society Open Science (*Investigating the geometrical preferences of a flexible benzimidazolone-based linker in the synthesis of coordination polymers*).<sup>33</sup> The synthesis of benzimidazolone diacetic acid ( $H_2L^1$ ) was achieved using the procedure followed by Dr Adam Martin, and the linker was used to synthesise the copper-based coordination

polymer ( $\text{Cu}_3(\text{L}^1)_2$ ). This material was reproduced to obtain PXRD patterns and TGA data and all remaining syntheses of coordination polymers were carried out either by the thesis author or by BSc project student (Elizabeth Marsden), under the direct supervision of the thesis author. Crystal structure descriptions, bulk crystalline analysis and synthetic procedures are reproduced from the published work, of which the thesis author is first author.

### 3.3 Results and discussion

#### 3.3.1 Linker synthesis



**Scheme 3.2** Three-step synthesis of benzimidazolone diacetic acid ( $\text{H}_2\text{L}^1$ ).

Benzimidazolone diacetic acid ( $\text{H}_2\text{L}^1$ ) was first synthesised in 1985,<sup>34</sup> however in this work we used an adapted procedure (Scheme 3.2) which eliminated the use of solid sodium in the literature method. Phenylenediamine and urea were refluxed in ethylene glycol to give **1**,<sup>35</sup> which was alkylated using ethyl bromoacetate and sodium hydride to produce **2**. This was hydrolysed by stirring in sodium hydroxide, before acidification to precipitate the linker in a 56% yield.

#### 3.3.2 Benzimidazolone-based coordination polymer synthesis

$\text{H}_2\text{L}^1$  was used in a series of combinatorial reactions with various group 2 and transition metal nitrate salts and different modulators/co-solvents to yield crystals suitable for SCXRD. All the combinatorial syntheses as summarised in the Appendix

(Section 3.7, Table A.1). The successful reactions yielding the best quality crystals are described in the following sections, in which four group 2 and three transition-metal coordination polymers have been reported.

The following structures in Section 3.3.2.1 and 3.3.2.3 were solved either by Adam Nevin (Cardiff University), Benson Kariuki (Cardiff University) or Mohan Bhadbhade (UNSW) and the descriptions are taken from the published work.<sup>33</sup> The crystallographic tables are detailed in the Appendix (Section 3.7, Table A.2 – A.8).

### 3.3.2.1 Crystal structures of group 2 coordination polymers

**Magnesium nitrate** and  $\text{H}_2\text{L}^1$  were dissolved in DMF with a small quantity of ethanol and water, and heated at 80 °C for 2 days to give colourless crystals of  $\{\text{MgL}^1(\text{H}_2\text{O})(\text{DMF})_{0.75}\}_\infty$  (**MgL<sup>1</sup>**) which crystallises in the triclinic space group *P*-1 (Table A.2). The asymmetric unit contains one  $\text{Mg}^{2+}$  ion, one  $\text{L}^1$  molecule, one coordinated water molecule and one coordinated DMF molecule (Figure 3.3). Only one type of magnesium ion is present in the structure, in which each metal centre is octahedrally coordinated to six oxygen atoms. O(1) is from a water molecule, O(2) is from a DMF molecule and O(3) is the ketone oxygen from  $\text{L}^1$ . O(4), O(5) and O(6) are carboxylate oxygens from three different  $\text{L}^1$  molecules. The linker bridges between chains of magnesium ions running along the *a*-axis, where it binds with the carboxylic acids in a *trans*-conformation on opposite sides of the plane of the central rings. Due to the ketone binding to magnesium ions, the crystal structure exhibits a staggered ladder motif whereby a screw axis relates the chains; the staggered chains run along the *b*-axis. The 2D sheets are perpendicular to the *c*-axis.

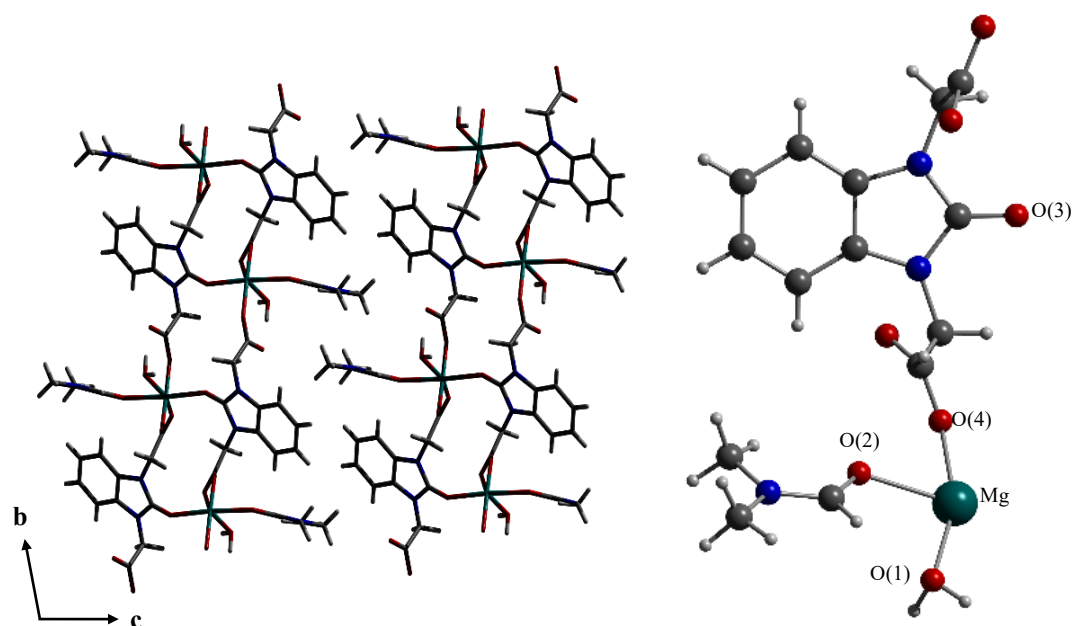


**Figure 3.3** Crystal structure of  $\text{MgL}^1$  showing the asymmetric unit (*right*) and the view along the *a*-axis (*left*). Structure solving and refinement was carried out by Adam Nevin.

**Calcium nitrate** and  $\text{H}_2\text{L}^1$  were dissolved in DMF and formic acid was added before heating to 100 °C for 24 hours, producing colourless crystals of  $\{\text{CaL}^1(\text{DMF})_2\}_\infty$  ( $\text{CaL}^1$ ) which crystallise in the triclinic space group *P*-1 (Table A.3). The asymmetric unit contains one  $\text{Ca}^{2+}$  ion, one  $\text{L}^1$  molecule and two coordinated dimethylformamide molecules (Figure 3.4). There is only one type of calcium ion present throughout the crystal structure, in which each metal centre is octahedrally coordinated. The 1D chain of metal ions extends along the *a*-axis, while the linkers connecting the metal chains propagate along the *b*-axis. The 2D sheets formed are hence perpendicular to the *c*-axis. Six oxygen atoms surround each calcium ion, whereby O(1) and O(2) come from the coordinated DMF molecules that bind in the axial positions. O(3) – O(6) are in the equatorial positions and each come from carboxylate groups of four different  $\text{L}^1$  molecules. The other oxygen of each carboxylate binds to the next calcium ion along in the chain. The linker exists throughout the structure with the carboxylic acids oriented in a *trans*-conformation with respect to the plane of the central rings, in which one carboxylate group binds to two  $\text{Ca}^{2+}$  ions in one chain, while the other carboxylate group only binds to one  $\text{Ca}^{2+}$  ion in an adjacent chain.

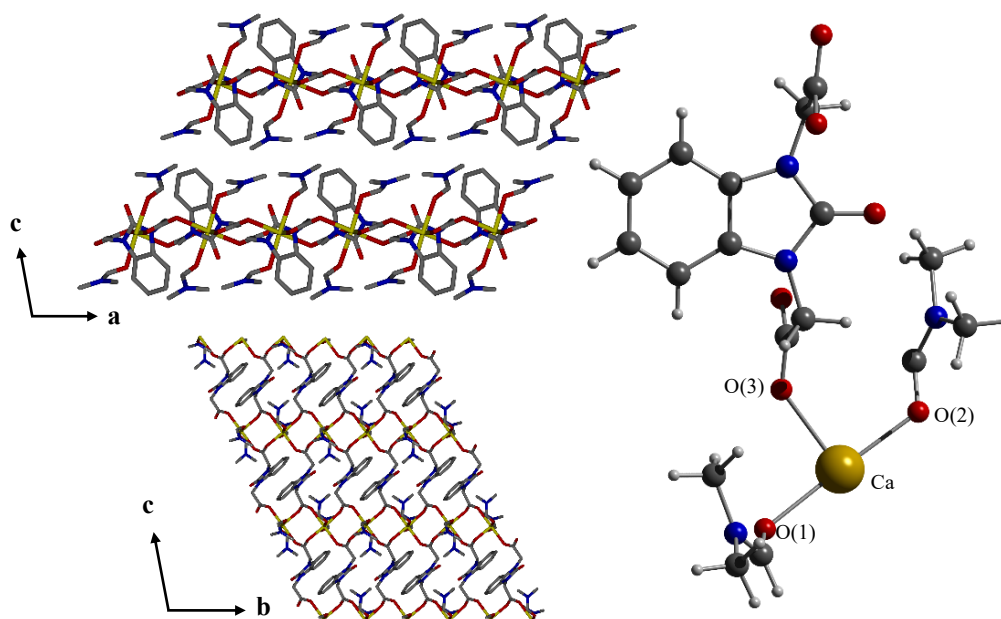


**Figure 3.4** Crystal structure of  $\text{CaL}^1$  showing the asymmetric unit (*right*), the view along the  $b$ -axis showing the metal chain (*top left*) and the view along the  $a$ -axis in which the H-atoms have been omitted (*bottom left*). Structure solving and refinement was carried out by Benson Kariuki.

**Strontium nitrate** and  $\text{H}_2\text{L}^1$  were dissolved in DMF and dilute HCl was added to the solution and heated at  $80\text{ }^\circ\text{C}$  for 24 hours, yielding colourless crystals of  $\{\text{SrL}^1(\text{H}_2\text{O})_{0.5}\}_\infty$  ( $\text{SrL}^1$ ) which crystallise in the monoclinic space group  $I2/a$  (Table A.4). The asymmetric unit contains one  $\text{Sr}^{2+}$  ion, one  $\text{L}^1$  molecule and one bridging water molecule on a special position (Figure 3.5). The interaction between metal cations and  $\text{L}^1$  anions gives rise to a structure consisting of 2D sheets which are perpendicular to the  $c$ -axis. There is only one type of strontium ion in the structure, however they are in a staggered conformation whereby four different orientations propagate along the  $a$ -axis. The symmetry operation relating the strontium ions involves a rotation of  $180^\circ$  followed by a reflection ( $\perp$  to  $a$ -axis) to move between Sr(1) and Sr(2). This is then followed by an inversion (between two Sr atoms), followed by a  $90^\circ$  rotation to move from Sr(2) to Sr(3). Sr(3) to Sr(4) requires a  $180^\circ$  rotation followed by reflection and Sr(4) to another Sr(1) requires inversion at  $90^\circ$  rotation. These operations can then be repeated to move along the staggered formation of strontium ions extending in the plane of the  $a$ -axis, while identical chains of strontium ions extend along the  $b$ -axis. Each strontium ion is 6-coordinate. O(1) is the ketone oxygen from  $\text{L}^1$ , while O(2) is a carboxylate oxygen binding only to Sr(1). O(3) is an oxygen atom from a bridging water molecule. O(4) is a different carboxylate

group binding to Sr(1). O(5) and O(6) are both from further different carboxylate oxygens from two more linkers each binding to Sr(1) and the identical Sr(1) in an adjacent chain. The linker differs from the magnesium structure in that it crystallises with the carboxylate groups in a *cis*-conformation with respect to the plane of the central rings. The ketone oxygen binds to Sr(1) in an adjacent chain giving rise to the 2D sheets, while one carboxylate group binds solely to Sr(1). The one oxygen atom of the other carboxylate group binds to Sr(1), whilst the remaining oxygen atom binds to Sr(2) and Sr(2) in an adjacent chain. The bridging oxygen atom links Sr(2) and Sr(3).

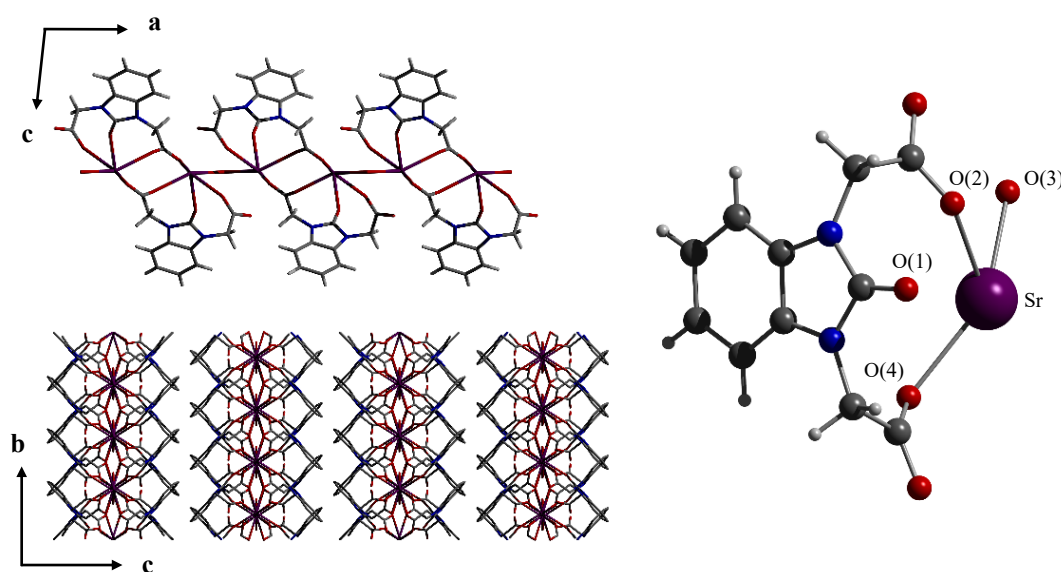


**Figure 3.5** Crystal structure of  $\text{SrL}^1$  showing the asymmetric unit (*right*), the view along the *b*-axis showing the metal chain (*top left*) and the view along the *a*-axis in which the H-atoms have been omitted (*bottom left*). Structure solving and refinement was carried out by Adam Nevin.

**Barium nitrate** and  $\text{H}_2\text{L}^1$  were dissolved in DMF and dilute HCl was added to the solution and heated at 80 °C for 24 hours, yielding colourless crystals of  $\{\text{BaL}^1(\text{H}_2\text{O})_{0.5}\}_\infty$  ( $\text{BaL}^1$ ), which crystallise in the monoclinic space group  $I2/a$  (Table A.5). The asymmetric unit contains one  $\text{Ba}^{2+}$  ion, one  $\text{L}^1$  molecule and one bridging  $\text{H}_2\text{O}$  molecule on a special position (Figure 3.6). The structure consists of 2D sheets that are perpendicular to the *b*-axis. Staggered chains of barium ions run along the *c*-axis, while identical chains of barium ions extend along the *b*-axis. The symmetry elements that relate the barium ions in four different orientations are the same as in

**SrL<sup>1</sup>**. The coordination of the linker in the *cis*-conformational binding to the metal cations is isostructural to **SrL<sup>1</sup>**.

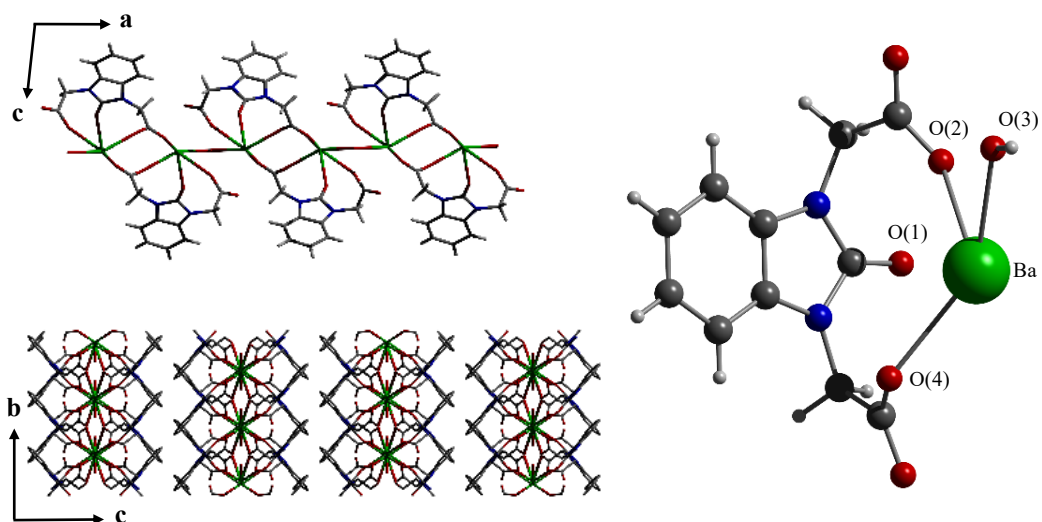


**Figure 3.6** Crystal structure of **BaL<sup>1</sup>** showing the asymmetric unit (*right*), the view along the *b*-axis showing the metal chain (*top left*) and the view along the *a*-axis in which the H-atoms have been omitted (*bottom left*). Structure solving and refinement was carried out by Adam Nevin.

### 3.3.2.2 Group 2 coordination polymers structural discussion

The four coordination polymers discussed in Section 3.3.2.1 all formed 2D sheets and contain exclusively 6-coordinate metal centres (Figure 3.7).

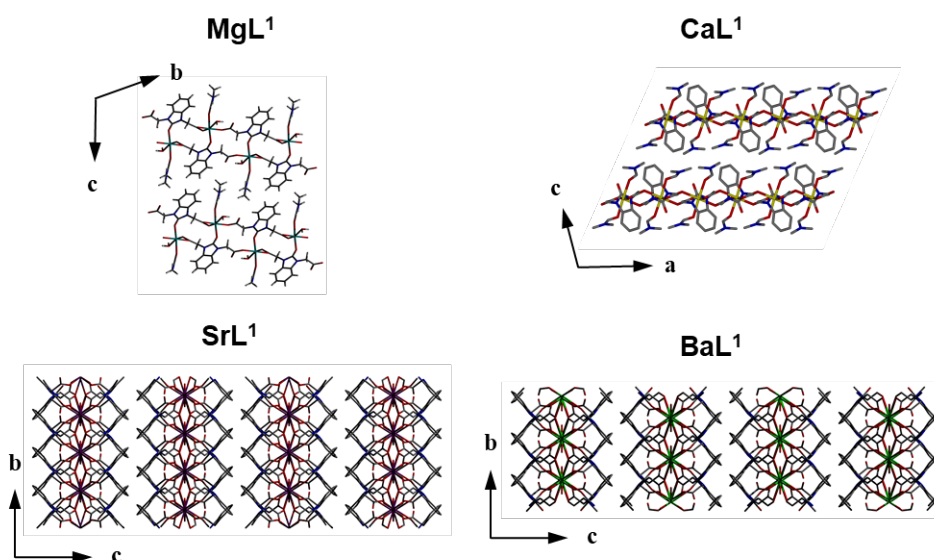


**Figure 3.7** 2D layers are present in the four group 2 metal coordination polymers.

The ionic radii of six-coordinate  $\text{Mg}^{2+}$ ,  $\text{Ca}^{2+}$ ,  $\text{Sr}^{2+}$  and  $\text{Ba}^{2+}$  increase from 72, 100, 118 to 135 pm respectively upon descending the group.<sup>36</sup> The observed coordination number of 6 was expected for the magnesium and calcium framework, but unexpected for strontium and barium due to their larger ionic radii which commonly results in a coordination number greater than six.<sup>37–39</sup>

The main difference in the crystal structures is the way in which the linker binds to the metal centres. The  $-\{\text{CH}_2\}$ - spacer between the aromatic rings and the carboxylate group can adopt either a *cis* or *trans* configuration with respect to the planar central part of the molecule, which is shown schematically in Figure 3.8. The linker carboxylate groups adopt a *trans* configuration in  $\text{MgL}^1$  and  $\text{CaL}^1$  in which each group binds to a different metal centre, but in  $\text{SrL}^1$  and  $\text{BaL}^1$  a *cis* configuration is adopted and the two carboxylate groups of the linker both bind to the same metal ion.

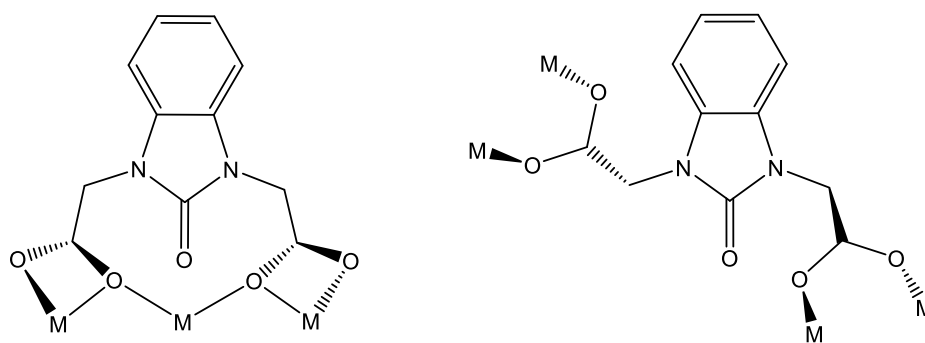


**Figure 3.8** The limited flexibility of  $\text{L}^1$  allows for binding to a metal centre in either a *cis* (left) or *trans* configuration (right).

It is proposed that the linker can adopt the more ‘constrained’ *cis* configuration in  $\text{SrL}^1$  and  $\text{BaL}^1$  structures due to the larger cation size upon descending group 2 allowing for chelate binding. The resulting coordination polymers then form a tighter mesh due to the both carboxylate groups of one  $\text{L}^1$  molecule binding to the same metal node. The  $\text{MgL}^1$  and  $\text{CaL}^1$  structures contain much smaller metal ions centres so even though the arms of the linker are flexible, they cannot be brought close enough together for the metal to be coordinated in the *cis* configuration and therefore the bridging *trans* configuration is observed.

This study with group 2 metals has revealed the complex relationship between the linker flexibility and the metal ion used in the reaction synthesis. This led to a curiosity-driven investigation to consider the linker flexibility in structures formed

with other metal ions, particularly those with geometrical coordination preferences. Combinatorial reactions with  $\text{Cr}^{2+}$ ,  $\text{Mn}^{2+}$ ,  $\text{Fe}^{2+}$ ,  $\text{Co}^{2+}$ ,  $\text{Ni}^{2+}$ ,  $\text{Cu}^{2+}$ ,  $\text{Zn}^{2+}$ ,  $\text{Al}^{3+}$  and  $\text{In}^{3+}$  were attempted and the syntheses are briefly outlined in the Appendix (Section 3.7, Table A.1). The successful syntheses of three new transition metal coordination polymers with  $\text{H}_2\text{L}^1$  were achieved with  $\text{Mn}^{2+}$ ,  $\text{Cu}^{2+}$  and  $\text{Zn}^{2+}$ , and the results are discussed in the next section.

### 3.3.2.3 Crystal structures of transition metal coordination polymers

**Manganese nitrate** and  $\text{H}_2\text{L}^1$  were dissolved in DMF and dilute HCl was added to the solution and heated at 80 °C for two days, yielding colourless crystals of  $\{\text{MnL}^1(\text{DMF})(\text{H}_2\text{O})_{3.33}\}_\infty$  (**MnL<sup>1</sup>**), which crystallise in the monoclinic space group  $P2_1/n$  (Table A.6). The asymmetric unit contains one  $\text{Mn}^{2+}$  ion, one  $\text{L}^1$  molecule, two water molecules and one coordinated DMF molecule (the methyl groups are disordered over two positions) (Figure 3.9). One of the water molecules hydrogen-bonds to the ketone oxygen of  $\text{L}^1$ . The crystal structure consists of 2D sheets that are perpendicular to the  $b$ -axis and contains identical manganese ions that have a slight distorted octahedral geometry. In the equatorial plane, there are two water molecules in a *cis*-arrangement (O(1) and O(2)), a DMF molecule (O(3)) and an oxygen atom from the carboxylate group (O(4)) of  $\text{L}^1$ . Two linker molecules bind to the manganese ion in the axial positions through an oxygen of the carboxylate group. The other carboxylate groups bind to adjacent  $\text{Mn}^{2+}$  ions in the neighbouring chains, therefore linking the chains running along the  $a$ -axis.

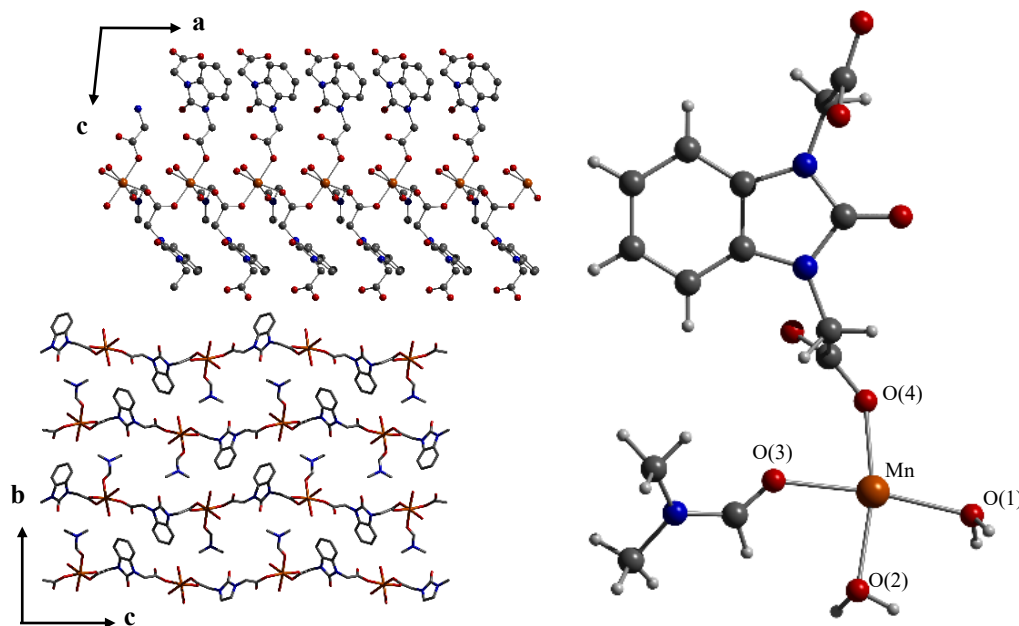


**Figure 3.9** Crystal structure of  $\text{MnL}^1$  showing the asymmetric unit (*right*), view along the *b*-axis (*top left*) and the view along the *a*-axis in which the H-atoms have been omitted (*bottom left*). Structure solving and refinement was carried out by Adam Nevin.

**Copper nitrate** and  $\text{H}_2\text{L}^1$  were dissolved in DMF and formic acid was added to the solution before heating to 90 °C for 24 hours, producing green crystals of  $\{\text{Cu}_3(\text{L}^1)_2(\text{DMF})_2(\text{CHO}_2)_2\}_\infty (\text{Cu}_3(\text{L}^1)_2)$ , which crystallises in the triclinic space group *P*-1 (Table A.7). The asymmetric unit contains three  $\text{Cu}^{2+}$  ions, two  $\text{L}^1$  molecules, two coordinated DMF molecules and two molecules of formic acid (Figure 3.10). There are three types of copper centres present in the coordination polymer. Cu(1) is square planar whereby two oxygen atoms come from the carboxylate groups of two different linker molecules and the other two are from DMF molecules coordinated *trans* to each other. Cu(2) and Cu(3) form a distorted paddlewheel, whereby two oxygen atoms are from carboxylate groups of two different  $\text{L}^1$  molecules and the other two points of extension *trans* to each other are formic acid molecules. The axial substituent on the bottom of the paddlewheel is a carboxylate from  $\text{L}^1$ , which binds through one oxygen atom to Cu(2), while the other binds to the square planar Cu(1) centre, thus bridging the two Cu environments and forming a staggered chain. Cu(3) forms the top half of the paddlewheel in which  $\text{L}^1$  binds through the carboxylate group in the axial position. The alternating square planar Cu(1), and Cu(2)/Cu(3) paddlewheel sequence extends along the *a*-axis, giving rise to 2D sheets that intersect the *b*- and *c*-axis. There are also two linker binding motifs throughout the crystal structure, both in the *trans*-

conformation. In the first motif, the linker binds to Cu(2) and Cu(3) in a distorted paddlewheel through both oxygen atoms of one carboxylate group, while the other carboxylate on the same linker binds to a square planar Cu(1) site via one oxygen atom, and the axial site of Cu(2) on a different paddlewheel through the other. The second motif also involves one carboxylate binding to a distorted paddlewheel and the other bridging Cu(3) on a paddlewheel and the square planar Cu(1) site, however the latter is achieved through only one oxygen atom on the carboxylate, leaving the other oxygen atom free.

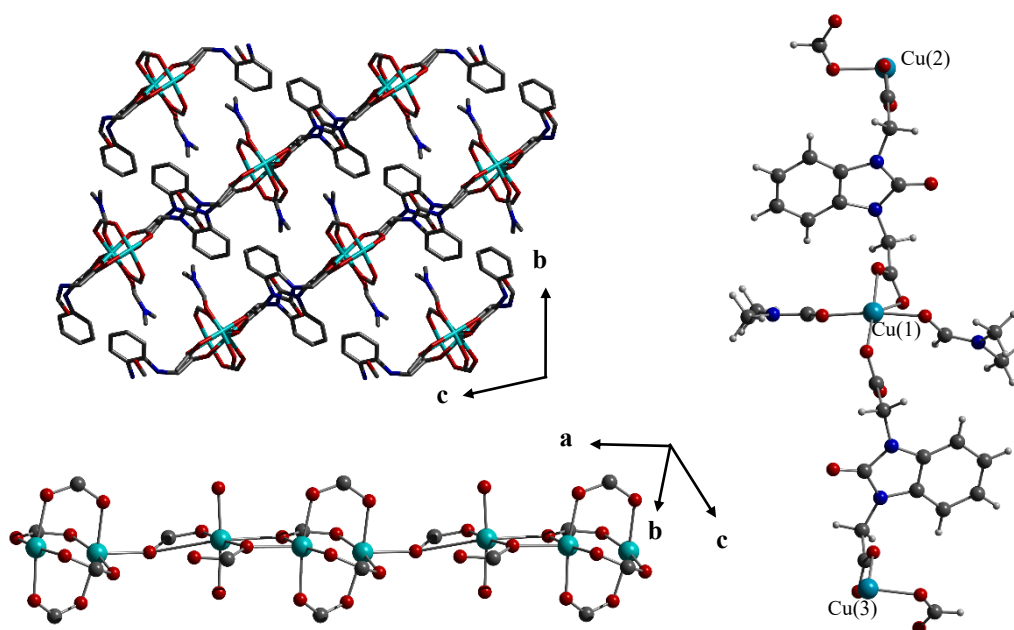


**Figure 3.10** Crystal structure of  $\text{Cu}_3(\text{L}^1)_2$  showing the asymmetric unit (*right*), view along the *a*-axis (*top left*) and the copper chain running throughout the coordination polymer, in which the linker has been omitted (*bottom left*). Structure solving and refinement was carried out by Mohan Bhadbhade.

**Zinc nitrate** and  $\text{H}_2\text{L}^1$  were dissolved in DMF and formic acid was added to the solution before heating to 100 °C for 24 hours, producing colourless crystals of  $\{\text{ZnL}^1(\text{DMF})\}_\infty$  ( $\text{ZnL}^1$ ) which crystallise in the monoclinic space group  $P2_1$  (Table A.8). The crystal structure was collected, solved and refined by Benson Kariuki. The asymmetric unit contains one  $\text{Zn}^{2+}$  ion, one  $\text{L}^1$  molecule and one coordinated DMF molecule (Figure 3.11). The structure exists as 2D sheets that are perpendicular to the *c*-axis. 1D chains of zinc ions propagate along the *a*-axis, while the linker molecules extend along the *b*-axis. Only one type of  $\text{Zn}^{2+}$  centre is seen in the coordination polymer; two different orientations are present, related by a 180°

rotation, thereby leading to formation of a zig-zag 2D sheet. Each metal centre is 4-coordinate, in which four oxygen atoms are bound. O(1) is coordinated DMF, while O(2) – O(4) are oxygen atoms from carboxylate groups of three different linker molecules. As seen in **MnL<sup>1</sup>**, the linker carboxylate groups adopt a *trans*-conformation throughout the structure. One carboxylate group of **L<sup>1</sup>** bridges between two Zn<sup>2+</sup> ions in a chain, while the other carboxylate group binds to a zinc ion in an adjacent chain.

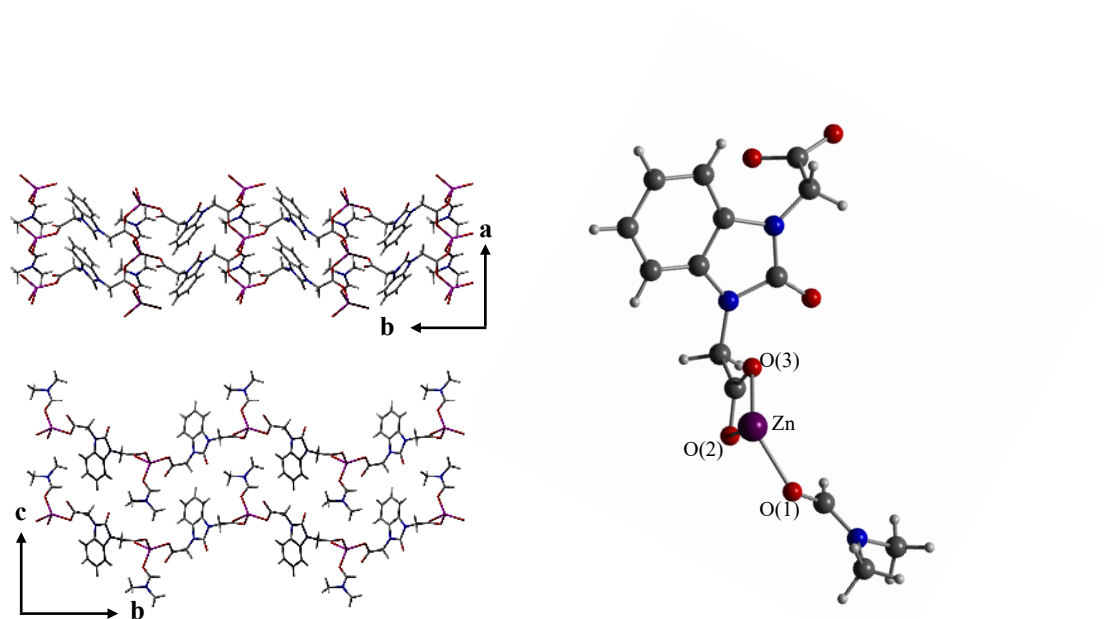


**Figure 3.11** Crystal structure of **ZnL<sup>1</sup>** showing the asymmetric unit (*right*) view along the *c*-axis (*top left*) and the view along the *a*-axis (*bottom left*). Structure solving and refinement was carried out by Benson Kariuki.

### 3.3.2.4 Transition metal coordination polymers structural discussion

The three successful syntheses formed coordination polymers with 2D sheets, however the coordination geometry is more complex than that observed in the group 2 structures in the previous section. **MnL<sup>1</sup>** has 6-coordinate distorted octahedral metal centres, whilst **ZnL<sup>1</sup>** contains tetrahedrally coordinated metal centres. Both of these coordination geometries are the most common for the metals in the +2 oxidation state.<sup>40–43</sup>

Of the seven materials formed,  $\text{Cu}_3(\text{L}^1)_2$  alone displays two different types of coordination geometries in a single network. Typically, Cu-based MOFs with carboxylate linkers coordinate in a ‘paddlewheel’ unit,<sup>44</sup> whilst in  $\text{Cu}^{2+}$  transition metal complexes the preferred coordination geometry is 4-coordinate square planar.<sup>45</sup> However, in  $\text{Cu}_3\text{L}_2$  a combination of geometries is seen, with both distorted paddlewheels and square planar coordination modes present, making it the most unusual structure.

The ionic radii of 6-coordinate  $\text{Mn}^{2+}$ , 4-coordinate square planar  $\text{Cu}^{2+}$ , 6-coordinate octahedral  $\text{Cu}^{2+}$  and 4-coordinate tetrahedral  $\text{Zn}^{2+}$  ions are 83, 57, 73 and 60 pm respectively.<sup>36</sup> In the three transition-metal based materials the linker adopts the *trans* configuration, confirming that the smaller ionic radii seem to prefer this particular binding mode.

### 3.3.3 Group 2 vs. transition metal coordination polymer comparison

Comparing the structures described in Sections 3.3.2.1 and 3.3.2.3, the empirical formulae show that each coordination polymer contains a 1:1 linker-to-metal ratio with only one type of metal centre observed, with the only exception of  $\text{Cu}_3(\text{L}^1)_2$  where the ratio is 2:3. All of the coordination polymers contain no solvent accessible volume calculated by PLATON SOLV,<sup>46</sup> which is a consequence of the tight meshes formed due to the small size of the linker.

The other difference in the structures is that the linker can exhibit two different binding modes. The *cis* configuration is only seen in  $\text{SrL}^1$  and  $\text{BaL}^1$ , whereas the *trans* configuration is adopted in all three transition metal structures and the smaller group 2 metal coordination polymers. Table 3.1 compares the size of the metal ions with the linker configuration observed in the final structures. The most obvious difference is the size of the metal ions and we observe that the *cis* configuration only occurs with metal ions with ionic radii greater than 118 pm. In  $\text{SrL}^1$  and  $\text{BaL}^1$  we observe the largest of the M-O bond distance compared with the other five structures, and they also contain bridging oxygen atoms from water molecules between the chain of metal centres. This suggests that distance is adequate for metal-oxygen-metal bonding; this is not seen in the coordination polymers with smaller metal ionic radii.

Metal	Ionic radius / pm	M-O bond lengths / Å	Configuration of L <sup>1</sup>	Metal	Ionic radius / pm	M-O bond lengths / Å	Configuration of L <sup>1</sup>
Mg <sup>2+</sup>	72	1.988(5) – 2.259(6)	trans	Mn <sup>2+</sup>	83	2.135(3) – 2.255(4)	trans
Ca <sup>2+</sup>	100	2.281(2) – 2.385(2)	trans	Cu <sup>2+</sup>	57 (SP), 73 (O <sub>h</sub> )	1.943(2) – 2.373(2)	trans
Sr <sup>2+</sup>	118	2.548(3) – 2.823(3)	cis	Zn <sup>2+</sup>	60	1.937(14) – 2.483(19)	trans
Ba <sup>2+</sup>	135	2.749(11) – 2.917(10)	cis				

**Table 3.1** Summary of ionic radii of the metal ions in the +2 oxidation state and their metal oxide bond lengths vs. the configuration of L<sup>1</sup> in the corresponding benzimidazolone-based coordination polymer.

### 3.3.4 Bulk characterisation of coordination polymers

Obtaining suitable quality crystals for SCXRD was the main objective for this chapter, however analysing the bulk crystallinity of each material was also important. In the following two sections, the PXRD and TGA results are discussed for the seven benzimidazolone-based coordination polymers.

#### 3.3.4.1 PXRD results

Figure 3.12 shows the simulated PXRD patterns, generated from the crystal structures in Section 3.3.2.1 and 3.3.2.3, compared with experimental patterns of the seven frameworks synthesised. The simulated vs. experimental patterns are all in good agreement. Pawley refinements were performed on each pattern, with the exception of **Cu<sub>3</sub>(L<sup>1</sup>)<sub>2</sub>** and **ZnL<sup>1</sup>**, to give a reliable goodness of fit ( $\chi^2 < 4$ ). The bulk crystallinity of the **ZnL<sup>1</sup>** sample shows phase impurity, as the peaks at 15.17°, 20.63° and 21.63° 2 $\theta$  can tentatively be assigned for the presence of zinc formate. In the experimental PXRD pattern for **Cu<sub>3</sub>(L<sup>1</sup>)<sub>2</sub>**, copper oxide peaks are clearly seen at 36.45° and 42.38° 2 $\theta$ , which is a result of heating the copper nitrate at elevated temperatures.

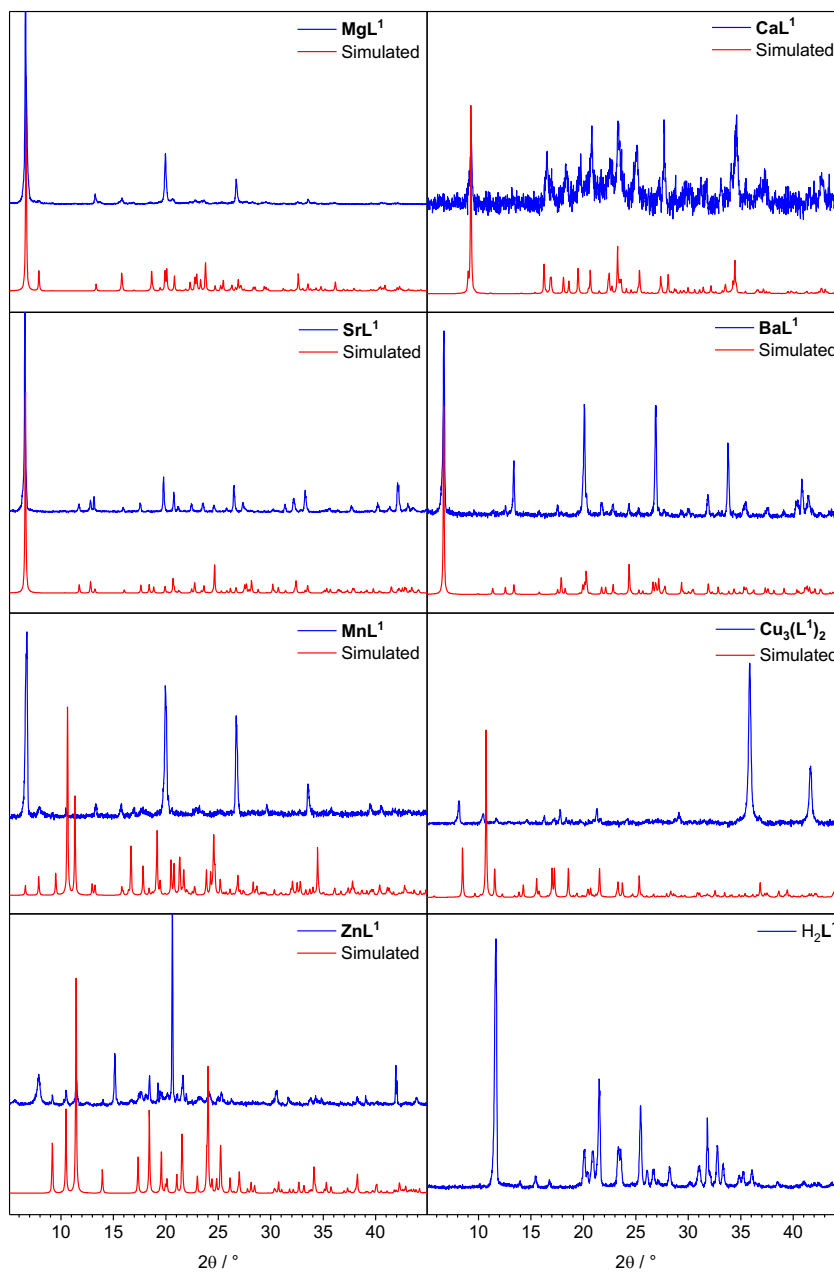


**Figure 3.12** PXRD patterns of the synthesised seven coordination polymers and  $H_2L^1$  (blue traces) compared with the simulated patterns from SCXRD (red traces). The powder patterns for synthesised  $CaL^1$  and  $Cu_3(L^1)_2$  have been background corrected.

### 3.3.4.2 TGA results

Figure 3.13 shows the TGA plots for thermal decomposition of the seven benzimidazolone-based coordination polymers and  $\text{H}_2\text{L}^1$  in air upon heating to 600 °C.

For  $\text{H}_2\text{L}^1$ , the first step at 95 °C corresponds to the loss of water and the second step at 300 °C can be attributed to the loss of both  $-\{\text{CH}_2\text{CO}_2\text{H}\}-$  flexible arms from the molecule. Upon heating the coordination polymers, all seven materials showed a mass loss around 150 – 200 °C, which is more than 100 °C less than the temperature at which the ligand begins to decompose, that is tentatively ascribed to loss of coordinated solvents (water and DMF).

The subsequent mass losses at increased temperatures could be consistent with decarboxylation, as one or two  $\text{CO}_2$  molecules are lost from each linker. The exact mechanism of thermal decarboxylation is not well-known in this case, and it was not the objective for this particular study, but is not uncommon for metal-coordinated carboxylates.<sup>47</sup> At higher temperatures, group 2 metal coordination polymers have been found to decompose to a mixture of metal oxides and metal nitrides.<sup>48</sup>

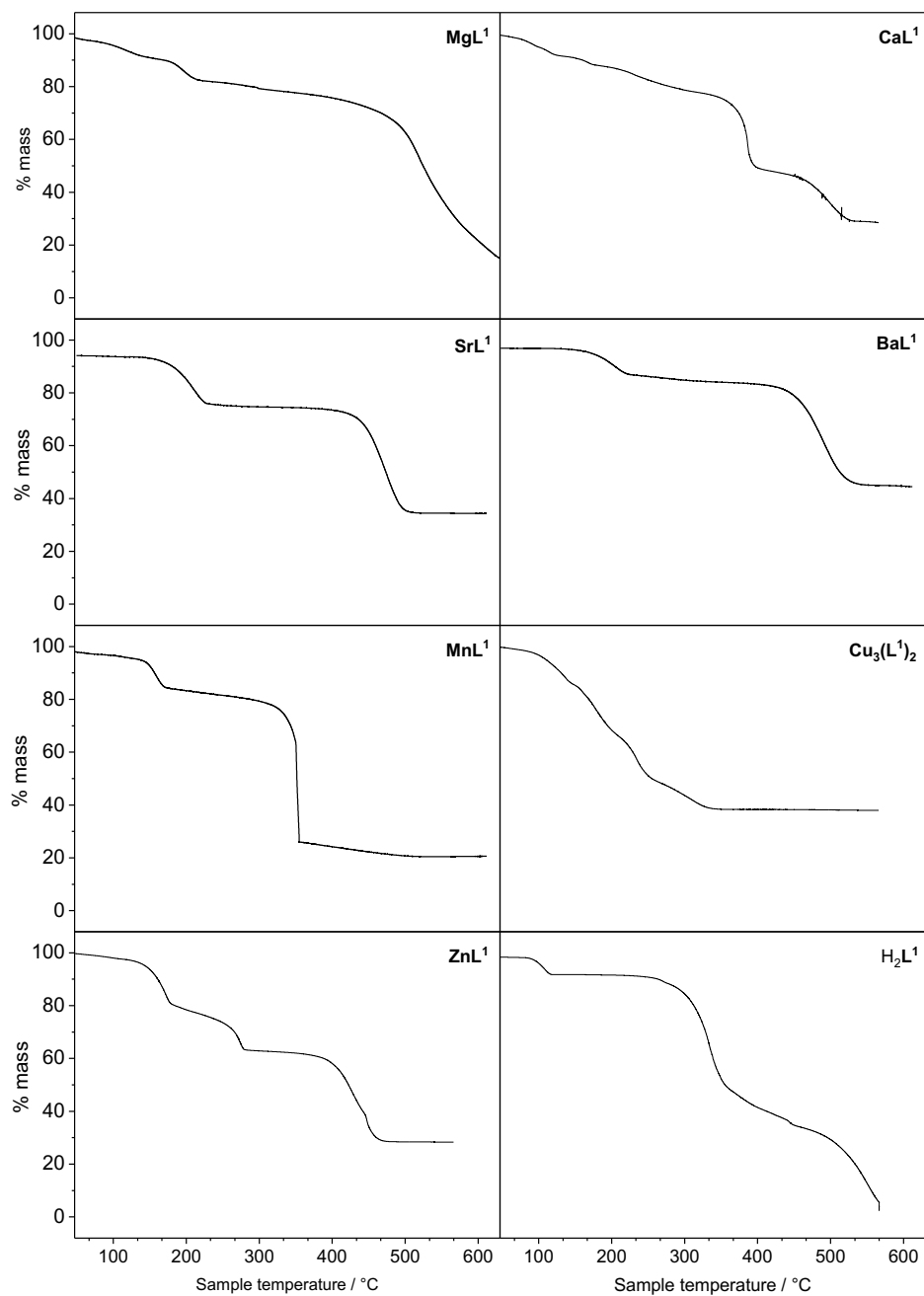


**Figure 3.13** TGA data of the seven coordination polymers and  $H_2L^1$ .

### 3.4 Conclusions

To summarise, a benzimidazolone diacetic acid linker (with limited flexibility) was prepared and used in combinatorial syntheses with group 2 and first-row transition metal salts to form seven novel coordination polymers: **MgL<sup>1</sup>**, **CaL<sup>1</sup>**, **SrL<sup>1</sup>**, **BaL<sup>1</sup>**, **MnL<sup>1</sup>**, **ZnL<sup>1</sup>** and **Cu<sub>3</sub>(L<sup>1</sup>)<sub>2</sub>**. The synthetic conditions were optimised to achieve suitable crystals for SCXRD. The bulk materials were characterised by PXRD and TGA and the porosity was calculated to be low due to the tight network formed by the small linker.

SCXRD data showed that all the materials formed structures containing 2D sheets. **MgL<sup>1</sup>**, **CaL<sup>1</sup>**, **SrL<sup>1</sup>**, **BaL<sup>1</sup>** and **MnL<sup>1</sup>** contained six-coordinate octahedral metal centres, however **ZnL<sup>1</sup>** and **Cu<sub>3</sub>(L<sup>1</sup>)<sub>2</sub>** were different. The zinc coordination polymer exhibited 4-coordinate tetrahedral coordination and, most interestingly, the copper-based material contained a different linker-to-metal ratio, with two distinct copper nodes coordinated in either 6-coordinate distorted paddlewheels or a 4-coordinate square planar geometry.

The most interesting feature of the structures was the way in which the benzimidazolone diacetic acid was bound to the metal ions. Due to the linker possessing a -{CH<sub>2</sub>}- spacer connecting the planar benzimidazolone component to the carboxylate groups on either arm, two discrete modes of binding were seen. A *cis* or *trans* configuration of the arms relative to the planar central portion of the molecule could be adopted, with the *cis* configuration only seen in **SrL<sup>1</sup>** and **BaL<sup>1</sup>** and the *trans* configuration seen in the other five coordination polymers. It can be presumed that the *cis* configuration is favoured when the metal ion size is large, and bridging water molecules were also only observed in the strontium and barium coordination polymers as the metal ions were a sufficient distance apart for this coordination to occur.

The synthetic outcomes of this study have showed that the structures formed are an interplay of both the linker and metal geometry preferences. The flexibility observed in crystal structures is difficult to predict, even when a linker can only adopt a limited number of conformations. This work leads on to the final chapter in this thesis which will focus on a moiety that can not only act as a flexible linker but can also undergo a light-induced structural change.

### 3.5 Experimental

All chemicals were of reagent-grade quality and used as received. 1,2-Phenylenediamine and sodium hydride were purchased from Sigma Aldrich. Ethyl bromoacetate was purchased from Acros Organics. Ethylene glycol and other commercial solvents from Fisher Scientific. Metal salts were bought from Alfa Aesar.

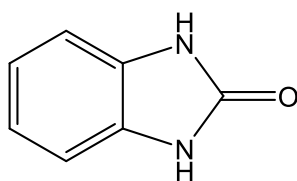
$^1\text{H}$  and  $^{13}\text{C}$  nuclear magnetic resonance (NMR) spectra were recorded on a Bruker 400 UltraShield<sup>TM</sup> spectrometer. The obtained chemical shifts ( $\delta$ ) are reported in ppm and are referenced to the residual solvent signal. Spin-spin coupling constants ( $J$ ) are given in Hz. A SHIMADZU IRAffinit-1S spectrometer was used to collect IR data, scanning between 500 – 4000  $\text{cm}^{-1}$  and averaging 16 scans.

PXRD was collected at room temperature on a X'Pert PRO PANalytical Chiller 59 diffractometer using  $\text{CuK}\alpha$  radiation. The samples were loaded onto zero-background silicon wafers directly from the reaction solution. The experimental PXRD patterns (excluding  $\text{Cu}_3(\text{L}^1)_2$  and  $\text{ZnL}^1$ ) were refined using a Pawley fit based on the simulated unit cell and space group<sup>49</sup> to a reliable goodness of fit ( $\chi^2 < 4$ ).

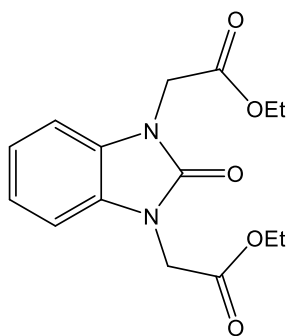
TGA was performed using a PerkinElmer Pyris 1 thermogravimetric analyser. The samples were heated from 25 °C to 600 °C under a flow of air (20 mL/min) using a heating rate of 5 °C/min.

Single crystal X-ray diffraction data for the group 2, manganese and zinc networks were collected on an Agilent SuperNova Dual Atlas four-circle diffractometer with either a Cu source ( $\lambda = 1.5418 \text{ \AA}$  for  $\text{SrL}^1$  and  $\text{BaL}^1$ ) or a Mo source ( $\lambda = 0.7107 \text{ \AA}$  for  $\text{MgL}^1$ ,  $\text{CaL}^1$ ,  $\text{MnL}^1$  and  $\text{ZnL}^1$ ) and CCD detector. For  $\text{Cu}_3(\text{L}^1)_2$ , data was collected on a Bruker Apex II with a Mo source and CCD detector. Data integration and reduction was performed by the CrysAlisPro system software. All structures were solved by direct methods using Olex2,<sup>50</sup> with the ShelXT and ShelXS structure solution program<sup>51,52</sup> refined with the ShelXL refinement package using least squares minimisation.<sup>53</sup> The H atoms on water molecules could not be located, but are stated in the formula sums.

### 3.5.1 Synthesis of benzimidazolone diacetic acid ( $H_2L^1$ )

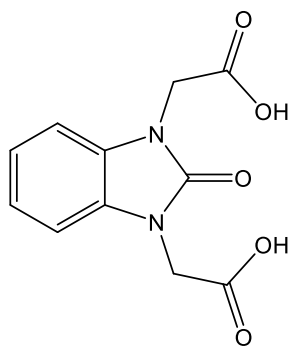


**Benzimidazolone (1).** 1,2-phenylenediamine (5.4 g, 50 mmol), urea (3.4 g, 57 mmol) and ethylene glycol (25 mL) were stirred at 135 °C for 1 hour; a colour change from orange to red-orange was seen. The solution was stirred overnight (18 hours) at 170 °C. The dark red solution was cooled down to 40-50 °C before the addition of 95% ethanol (5 mL, 0.08 mol) which was stirred for 10 minutes and then distilled water (20 mL) was added. The brown precipitate was washed with successive batches of water and 95% ethanol (~ 1 L), before drying under vacuum to give benzimidazolone as a pale brown solid (3.54 g, 60%).  **$^1H$  NMR** (400 MHz, DMSO):  $\delta_H = 10.56$  (s, 2H), 6.91 (s, 4H).  **$^{13}C\{^1H\}$  NMR** (101 MHz, DMSO):  $\delta_C = 155.2, 129.6, 120.37, 108.4$ . **IR:**  $\nu_{max}/cm^{-1} = 2895, 1630, 1360, 1196, 725, 714, 590$ . **HRMS (ES $^+$ ):**  $m/z = 134.0479$ ; calculated 134.0480 for  $[C_7H_6N_2O]^+$ .



**Benzimidazolone diethyl acetate ester (2).** Sodium hydride (60% in mineral oil) (0.75 g, 12.4 mmol) was added to hexane (20 mL) under  $N_2$ . After stirring for a few minutes, excess hexane was removed, before repeating. Anhydrous DMF (50 mL) was added and the brown solution stirred for 2 minutes. Benzimidazolone (1 g, 7.5 mmol) was added slowly and stirred for 30 minutes to form a grey cloudy solution. After cooling to 0 °C, ethyl bromoacetate (1.8 mL, 16.4 mmol) was added dropwise, resulting in a brown solution, which was stirred for a further 90 minutes. Keeping the reaction mixture at 0 °C, methanol was added to quench the reaction giving a yellow

solution. The addition of water (150 mL) formed a white precipitate. The white solid was extracted into ethyl acetate (150 mL), washed with water (3 x 100 mL) and dried to give benzimidazolone diethyl acetate ester as an off-white solid (1.51 g, 66%). The solid was purified by column chromatography (3:2 hexane:ethyl acetate).  $^1\text{H NMR}$  (400 MHz,  $\text{CDCl}_3$ ):  $\delta_{\text{H}} = 7.11$  (dd, 2H,  $J = 5.80, 3.20$  Hz), 6.91 (dd, 2H,  $J = 5.70, 3.20$  Hz), 4.64 (s, 4H), 4.23 (q, 4H,  $J = 7.1$  Hz), 1.27 (t, 6H,  $J = 7.1$  Hz).  $^{13}\text{C}\{^1\text{H}\}$  NMR (101 MHz,  $\text{CDCl}_3$ ):  $\delta_{\text{C}} = 167.8, 154.1, 129.3, 122.1, 108.0, 62.0, 42.6, 14.3$ . **IR**:  $\nu_{\text{max}}/\text{cm}^{-1} = 1724, 1429, 1372, 1210, 750$ . **HRMS (ES<sup>+</sup>)**:  $m/z = 307.1285$ ; calculated 307.1294 for  $[\text{C}_{15}\text{H}_{18}\text{N}_2\text{O}_5]^+$ .



**Benzimidazolone diacetic acid (H<sub>2</sub>L<sup>1</sup>).** Benzimidazolone diethyl acetate ester (1.25 g, 4.1 mmol) was dissolved in methanol (50 mL) and THF (50 mL). 2 M NaOH (50 mL, 100 mmol) was added and the solution was stirred at 30 °C for 24 hours. The solvents were removed under reduced pressure, before water was added (20 mL) and the yellow solution was acidified with 6 M HCl (aq). The solution turned colourless at approximately pH 6, and a white precipitate formed at pH 2. The precipitate was filtered to give benzimidazolone diacetic acid as a white solid (0.57 g, 56%).  $^1\text{H NMR}$  (400 MHz, DMSO):  $\delta_{\text{H}} = 7.16$  (dd, 2H,  $J = 5.80, 3.20$  Hz), 7.06 (dd, 2H,  $J = 5.80, 3.20$  Hz), 4.62 (s, 4H).  $^{13}\text{C}\{^1\text{H}\}$  NMR (101 MHz, DMSO):  $\delta_{\text{C}} = 169.5, 153.5, 129.1, 121.2, 108.3, 42.0$ . **IR**:  $\nu_{\text{max}}/\text{cm}^{-1} = 3343, 1676, 1437, 1265, 750, 598$ . **HRMS (ES<sup>+</sup>)**:  $m/z = 251.0677$ ; calculated 251.0668 for  $[\text{C}_{11}\text{H}_{10}\text{N}_2\text{O}_5]^+$ .

### 3.5.2 Single crystal syntheses of coordination polymers

**MgL<sup>1</sup>.** Mg(NO<sub>3</sub>)<sub>2</sub>·6H<sub>2</sub>O (31 mg, 0.12 mmol) and H<sub>2</sub>L<sup>1</sup> (10 mg, 0.04 mmol) were dissolved in DMF (2 mL) in an 8 mL Wheaton vial. Ethanol (0.5 mL) and water (0.2 mL) were added to the solution which was then sealed and heated at 80 °C for 2 days to give colourless crystals. The crystals were used to seed a second reaction, under the same conditions, yielding larger colourless crystals. **IR:**  $\nu_{\max}/\text{cm}^{-1} = 3211, 2160, 1709, 1651, 1585, 1495, 1447, 1387, 1342, 1312, 1207, 1184, 1057, 1011, 928, 854, 754, 704, 655.$

**CaL<sup>1</sup>.** Ca(NO<sub>3</sub>)<sub>2</sub>·4H<sub>2</sub>O (71 mg, 0.30 mmol) and H<sub>2</sub>L<sup>1</sup> (25 mg, 0.10 mmol) were dissolved in DMF (2.5 mL) in an 8 mL Wheaton vial. Formic acid (11  $\mu$ L) was added to the solution which was then sealed and heated at 100 °C for 24 h yielding colourless crystals. **IR:**  $\nu_{\max}/\text{cm}^{-1} = 3450, 2300, 1757, 1689, 1667, 1593, 1495, 1439, 1387, 1315, 1300, 1207, 1182, 1045, 1012, 935, 914, 818, 739, 704, 662.$

**SrL<sup>1</sup>.** Sr(NO<sub>3</sub>)<sub>2</sub> (25 mg, 0.12 mmol) and H<sub>2</sub>L<sup>1</sup> (10 mg, 0.04 mmol) were dissolved in DMF (2.5 mL) in an 8 mL Wheaton vial. 0.4 M HCl (1 mL) was added to the solution which was then sealed and heated at 80 °C for 24 h yielding colourless crystals. **IR:**  $\nu_{\max}/\text{cm}^{-1} = 3356, 3000, 2910, 2790, 1694, 1585, 1497, 1437, 1404, 1379, 1312, 1202, 1171, 1063, 1011, 912, 833, 791, 706, 652.$

**BaL<sup>1</sup>.** Ba(NO<sub>3</sub>)<sub>2</sub> (31 mg, 0.12 mmol) and H<sub>2</sub>L<sup>1</sup> (10 mg, 0.04 mmol) were dissolved in DMF (2.5 mL) in an 8 mL Wheaton vial. 0.4 M HCl (1 mL) was added to the solution which was then sealed and heated at 80 °C for 24 h yielding colourless crystals. **IR:**  $\nu_{\max}/\text{cm}^{-1} = 3356, 2990, 2779, 1694, 1595, 1495, 1402, 1383, 1312, 1171, 1011, 787, 739, 706, 610.$

**MnL<sup>1</sup>.** Mn(NO<sub>3</sub>)<sub>2</sub>·4H<sub>2</sub>O (30 mg, 0.12 mmol) and H<sub>2</sub>L<sup>1</sup> (10 mg, 0.04 mmol) were dissolved in DMF (2.5 mL) in an 8 mL Wheaton vial. 0.2 M HCl (1 mL) was added to the solution which was then sealed and heated at 80 °C for 2 days yielding colourless crystals. **IR:**  $\nu_{\max}/\text{cm}^{-1} = 3410, 3085, 2990, 1667, 1574, 1495, 1445, 1383, 1304, 1206, 1188, 1011, 850, 748, 723, 658.$

**Cu<sub>3</sub>(L<sup>1</sup>)<sub>2</sub>.** Cu(NO<sub>3</sub>)<sub>2</sub>·3H<sub>2</sub>O (73 mg, 0.30 mmol) and H<sub>2</sub>L<sup>1</sup> (25 mg, 0.10 mmol) were dissolved in DMF (2.5 mL) in an 8 mL Wheaton vial. Formic acid (11  $\mu$ L) was added

to the solution which was then sealed and heated at 90 °C for 24 h yielding green crystals. **IR:**  $\nu_{\text{max}}/\text{cm}^{-1} = 3211, 2355, 2183, 2018, 1676, 1570, 1495, 1435, 1385, 1315, 1269, 1204, 1177, 1057, 1013, 918, 756, 710, 619.$

**ZnL<sup>1</sup>.** Zn(NO<sub>3</sub>)<sub>2</sub>·6H<sub>2</sub>O (90 mg, 0.30 mmol) and H<sub>2</sub>L<sup>1</sup> (25 mg, 0.10 mmol) were dissolved in DMF (2.5 mL) in an 8 mL Wheaton vial. Formic acid (11 μL) was added to the solution which was then sealed and heated at 80 °C for 24 h yielding colourless product. Single crystals were obtained by using the same conditions and heating the reaction to 100 °C for 24 h. **IR:**  $\nu_{\text{max}}/\text{cm}^{-1} = 3350, 2191, 2004, 1667, 1632, 1497, 1580, 1497, 1456, 1385, 1310, 1296, 1275, 1206, 1188, 1053, 1015, 924, 847, 773, 727, 712, 685, 664.$

### 3.6 References

- 1 B. F. Hoskins and R. Robson, *J. Am. Chem. Soc.*, 1989, **111**, 5962–5964.
- 2 B. F. Hoskins and R. Robson, *J. Am. Chem. Soc.*, 1990, **112**, 1546–1554.
- 3 O. M. Yaghi, H. Li, M. Eddaoudi and M. O’Keeffe, *Nature*, 1999, **402**, 276–279.
- 4 S. S.-Y. Chui, S. M.-F. Lo, J. P. H. Charmant, A. G. Orpen and I. D. Williams, *Science (80-. )*, 1999, **283**, 1148–1150.
- 5 X. Lin, I. Telepeni, A. J. Blake, A. Dailly, C. M. Brown, J. M. Simmons, M. Zoppi, G. S. Walker, K. M. Thomas, T. J. Mays, P. Hubberstey, N. R. Champness and M. Schröder, *J. Am. Chem. Soc.*, 2009, **131**, 2159–2171.
- 6 G. J. Halder, C. J. Kepert, B. Moubaraki, K. S. Murray and J. D. Cashion, *Science (80-. )*, 2002, **298**, 1762–1765.
- 7 D. N. Dybtsev, H. Chun and K. Kim, *Angew. Chemie Int. Ed.*, 2004, **43**, 5033–5036.
- 8 A. Schneemann, V. Bon, I. Schwedler, I. Senkovska, S. Kaskel and R. A. Fischer, *Chem. Soc. Rev.*, 2014, **43**, 6062–6096.
- 9 Z. Chang, D.-H. Yang, J. Xu, T.-L. Hu and X.-H. Bu, *Adv. Mater.*, 2015, **27**, 5432–5441.
- 10 T. D. Bennett, A. H. Fuchs, A. K. Cheetham and F.-X. Coudert, *Dalton Trans.*, 2016, **45**, 4058–4059.
- 11 S. K. Elsaïdi, M. H. Mohamed, D. Banerjee and P. K. Thallapally, *Coord. Chem. Rev.*, 2018, **358**, 125–152.
- 12 S. M. J. Rogge, M. Waroquier and V. Van Speybroeck, *Acc. Chem. Res.*, 2018, **51**, 138–148.
- 13 G. Marsolier, C. Serre, C. Thouvenot, M. Noguès, D. Louër, F. Millange and G. Férey, *J. Am. Chem. Soc.*, 2002, **124**, 13519–13526.
- 14 K. J. Gagnon, C. M. Beavers and A. Clearfield, *J. Am. Chem. Soc.*, 2013, **135**, 1252–1255.
- 15 E. C. Spencer, M. S. R. N. Kiran, W. Li, U. Ramamurty, N. L. Ross and A. K. Cheetham, *Angew. Chemie Int. Ed.*, 2014, **53**, 5583–5586.
- 16 L. D. DeVries, P. M. Barron, E. P. Hurley, C. Hu and W. Choe, *J. Am. Chem. Soc.*, 2011, **133**, 14848–14851.
- 17 F.-X. Coudert, *Chem. Mater.*, 2015, **27**, 1905–1916.
- 18 Z.-J. Lin, J. Lü, M. Hong and R. Cao, *Chem. Soc. Rev.*, 2014, **43**, 5867–5895.
- 19 T. F. Liu, J. Lü, X. Lin and R. Cao, *Chem. Commun.*, 2010, **46**, 8439–8441.
- 20 Z. Guo, R. Cao, X. Wang, H. Li, W. Yuan, G. Wang, H. Wu and J. Li, *J. Am. Chem. Soc.*, 2009, **131**, 6894–6895.

- 21 L. L. Liang, S. Bin Ren, J. Zhang, Y. Z. Li, H. Bin Du and X. Z. You, *Dalton Trans.*, 2010, **39**, 7723–7726.
- 22 A. P. Katsoulidis, D. Antypov, G. F. S. Whitehead, E. J. Carrington, D. J. Adams, N. G. Berry, G. R. Darling, M. S. Dyer and M. J. Rosseinsky, *Nature*, 2019, **565**, 213–217.
- 23 *Ger. Offen.*, 1975, 40 pp.
- 24 G. Dannhardt and B. K. Kohl, *Arch. Pharm. (Weinheim)*, 2000, **333**, 123–129.
- 25 Z. Zawahir, R. Dayam, J. Deng, C. Pereira and N. Neamati, *J. Med. Chem.*, 2009, **52**, 20–32.
- 26 P. Acharya, C. Dogo-Isonagie, J. M. LaLonde, S.-N. Lam, G. J. Leslie, M. K. Louder, L. L. Frye, A. K. Debnath, J. R. Greenwood, T. S. Luongo, L. Martin, K. S. Watts, J. A. Hoxie, J. R. Mascola, C. A. Bewley and P. D. Kwong, *ACS Chem. Biol.*, 2011, **6**, 1069–1077.
- 27 *PCT Int. Appl.*, 2016, 350 pp.
- 28 B. K. Karale, S. S. Rindhe and M. A. Rode, *Indian J. Pharm. Sci.*, 2015, **77**, 230–236.
- 29 N. Xu, C. Yang, X. Gan, S. Wei and Z. Ji, *Int. J. Mol. Sci.*, 2013, **14**, 6790–6804.
- 30 A. D. Martin, J. P. Wojciechowski, H. Warren, M. In Het Panhuis and P. Thordarson, *Soft Matter*, 2016, **12**, 2700–2707.
- 31 N. S. Poonia and A. V. Bajaj, *Chem. Rev.*, 1979, **79**, 389–445.
- 32 P. Atkins, T. Overton, J. Rourke, M. Weller and F. Armstrong, *Shriver & Atkins' Inorganic Chemistry*, Oxford University Press, 4th edn., 2006.
- 33 C. L. Jones, E. A. Marsden, A. C. Nevin, B. M. Kariuki, M. M. Bhadbhade, A. D. Martin and T. L. Easun, *R. Soc. Open Sci.*, 2017, **4**, 171064.
- 34 S. S. Khalikov, C. S. Kadyrov, A. T. Ayupova and L. V. Molchanov, *Chem. Heterocycl. Compd.*, 1985, **21**, 1251–1254.
- 35 J. L. Yao, X. Gao, W. Sun, S. Shi and T. M. Yao, *Dalton Trans.*, 2013, **42**, 5661–5672.
- 36 R. D. Shannon and IUCr, *Acta Crystallogr. Sect. A*, 1976, **32**, 751–767.
- 37 M. Usman, S. Mendiratta, S. Batjargal, G. Haider, M. Hayashi, N. Rao Gade, J.-W. Chen, Y.-F. Chen and K.-L. Lu, *ACS Appl. Mater. Interfaces*, 2015, **7**, 22767–22774.
- 38 R. Wang, X. Liu, A. Huang, W. Wang, Z. Xiao, L. Zhang, F. Dai and D. Sun, *Inorg. Chem.*, 2016, **55**, 1782–1787.
- 39 O. Just and W. S. Rees, *Phosphorus. Sulfur. Silicon Relat. Elem.*, 2001, **168**, 215–225.
- 40 I. Bertini, *Biological Inorganic Chemistry: Structure and Reactivity*, University Science Books, 1st edn., 2007.
- 41 L. Rulišek and J. Vondrášek, *J. Inorg. Biochem.*, 1998, **71**, 115–127.
- 42 T. Dudev and C. Lim, *J. Am. Chem. Soc.*, 2000, **122**, 11146–11153.

- 43 D. Venkataraman, Y. Du, S. R. Wilson, K. A. Hirsch, P. Zhang and J. S. Moore, *J. Chem. Educ.*, 1997, **74**, 915–918.
- 44 F. Dai, H. He, D. Gao, F. Ye, X. Qiu and D. Sun, *CrystEngComm*, 2009, **11**, 2516–2522.
- 45 W. Clegg, J. M. Holcroft and N. C. Martin, *CrystEngComm*, 2015, **17**, 2857–2871.
- 46 A. L. Spek, *Acta Crystallogr. Sect. D Biol. Crystallogr.*, 2009, **65**, 148–155.
- 47 R. Shang and L. Liu, *Sci. China Chem.*, 2011, **54**, 1670–1687.
- 48 G. Brauer, *Handbook of Preparative Inorganic Chemistry*, Academic Press, 2nd edn., 1963.
- 49 W. I. F. David, K. Shankland, J. Van De Streek, E. Pidcock, W. D. S. Motherwell and J. C. Cole, *J. Appl. Crystallogr.*, 2006, **39**, 910–915.
- 50 O. V Dolomanov, L. J. Bourhis, R. J. Gildea, J. A. K. Howard and H. Puschmann, *J. Appl. Crystallogr.*, 2009, **42**, 339–341.
- 51 G. M. Sheldrick, *Acta Crystallogr. Sect. A Found. Crystallogr.*, 2015, **71**, 3–8.
- 52 G. M. Sheldrick, *Acta Crystallogr. Sect. A*, 2008, **64**, 112–122.
- 53 G. M. Sheldrick, *Acta Crystallogr. Sect. C*, 2015, **71**, 3–8.

### 3.7 Appendix

**Table A.1** Combinatorial syntheses to form benzimidazolone-based coordination polymers. **Bold** outcome denotes sample from which crystal structure was obtained.

Metal salt	Mass of L / mg	Mass of M / mg	DMF / mL	Modulator / co-solvent	T / °C	Outcome
Mg(NO <sub>3</sub> ) <sub>2</sub> ·6H <sub>2</sub> O <i>(mmol)</i>	<i>(0.04)</i>	<i>(0.12)</i>	2.5	0.1 M HCl, 0.1 mL	90	White solid
				0.1 M HCl, 0.5 mL		White solid
				0.1 M HCl, 1 mL		No solid
				0.5 M HCl, 0.1 mL		White solid
				0.5 M HCl, 0.5 mL		White solid
				0.5 M HCl, 1 mL		No solid
				1 M HCl, 0.1 mL		White solid
				1 M HCl, 0.5 mL		White solid
				1 M HCl, 1 mL		No solid
				2 M HCl, 0.1 mL		White solid
				2 M HCl, 0.5 mL		White solid
				2 M HCl, 1 mL		No solid
				6 M HCl, 1 drop		No solid
				6 M HCl, 3 drops		No solid
				6 M HCl, 5 drops		No solid
				Formic acid, 5 µL		White solid
				Formic acid, 10 µL		No solid
				Formic acid, 15 µL		No solid
				Formic acid, 20 µL		No solid
				Formic acid, 25 µL		No solid
				Formic acid, 30 µL		No solid
				Formic acid, 35 µL		No solid
				Formic acid, 40 µL		No solid
				0.1 M HCl, 0.5 mL		<b>Solid</b>
				0.5 M HCl, 0.5 mL		<b>Solid</b>
				2 M HCl, 1 mL		<b>Solid</b>
				0.1 M HCl, 0.1 mL		No solid
				0.1 M HCl, 0.25 mL		No solid
				0.5 M HCl, 0.1 mL		No solid
				0.5 M HCl, 0.25 mL		No solid

Metal salt	Mass of L / mg	Mass of M / mg	DMF / mL	Modulator / co-solvent	T / °C	Outcome	
Mg(NO <sub>3</sub> ) <sub>2</sub> ·6H <sub>2</sub> O <i>(mmol)</i>	10 <i>(0.04)</i>	29 <i>(0.12)</i>	2.5	1 M HCl, 0.1 mL	80	No solid	
				1 M HCl, 0.25 mL		No solid	
				Formic acid, 5 µL		No solid	
				Formic acid, 10 µL		No solid	
				Formic acid, 15 µL		No solid	
				Formic acid, 20 µL		No solid	
	10 <i>(0.04)</i>	31 <i>(0.12)</i>	1	0.1 M HCl, 0.5 mL		No solid	
				Formic acid, 4.5 µL		No solid	
				2.5	-		No solid
				2	0.5 mL EtOH, 3 drops H <sub>2</sub> O		No solid
					0.6 mL EtOH, 0.1 mL H <sub>2</sub> O		Amorphous
					0.5 mL EtOH, 0.1 mL H <sub>2</sub> O		Amorphous
					0.4 mL EtOH, 0.1 mL H <sub>2</sub> O		Amorphous
					0.3 mL EtOH, 0.1 mL H <sub>2</sub> O		Solid
					0.5 mL EtOH		No solid
					0.5 mL EtOH, 0.05 mL H <sub>2</sub> O		Amorphous
					0.5 mL EtOH, 0.15 mL H <sub>2</sub> O		Amorphous
					<b>0.5 mL EtOH, 0.2 mL H<sub>2</sub>O</b>		<b>White solid</b>
	0.2 mL EtOH, 0.15 mL H <sub>2</sub> O		No solid				
<i>(mmol)</i>	25 <i>(0.10)</i>	78 <i>(0.30)</i>	2.5	Formic acid, 11 µL	80	Solid	
				Formic acid, 11 µL	90	Solid	
				Formic acid, 11 µL	100	Solid	
Ca(NO <sub>3</sub> ) <sub>2</sub> ·4H <sub>2</sub> O <i>(mmol)</i>	25 <i>(0.10)</i>	72 <i>(0.30)</i>	2.5	Formic acid, 11 µL	80	White solid	
				Formic acid, 11 µL	90	White solid	
				<b>Formic acid, 11 µL</b>	<b>100</b>	<b>White solid</b>	
Sr(NO <sub>3</sub> ) <sub>2</sub> <i>(mmol)</i>	10 <i>(0.04)</i>	25 <i>(0.12)</i>	2.5	0.1 M HCl, 0.1 mL	90	White solid	
				0.1 M HCl, 0.5 mL		White solid	
				0.1 M HCl, 1 mL		White solid	
				0.5 M HCl, 0.1 mL		White solid	
				0.5 M HCl, 0.5 mL		White solid	

Metal salt	Mass of L / mg	Mass of M / mg	DMF / mL	Modulator / co-solvent	T / °C	Outcome	
Sr(NO <sub>3</sub> ) <sub>2</sub> <i>(mmol)</i>	10 <i>(0.04)</i>	25 <i>(0.12)</i>	2.5	0.5 M HCl, 1 mL	90	White solid	
				1 M HCl, 0.1 mL		White solid	
				1 M HCl, 0.5 mL		White solid	
				1 M HCl, 1 mL		White solid	
				2 M HCl, 0.1 mL		White solid	
				2 M HCl, 0.5 mL		White solid	
				2 M HCl, 1 mL		White solid	
				6 M HCl, 1 drop		White solid	
				6 M HCl, 3 drops		White solid	
				6 M HCl, 5 drops		White solid	
				Formic acid, 5 µL		White solid	
				Formic acid, 10 µL		White solid	
				Formic acid, 15 µL		White solid	
				Formic acid, 20 µL		White solid	
				Formic acid, 25 µL		White solid	
				Formic acid, 30 µL		White solid	
				Formic acid, 35 µL		White solid	
				Formic acid, 40 µL		White solid	
				0.1 M HCl, 0.1 mL		80	White solid
				0.1 M HCl, 0.5 mL			White solid
				0.1 M HCl, 1 mL	White solid		
				0.5 M HCl, 0.1 mL	White solid		
				0.5 M HCl, 0.5 mL	White solid		
				0.5 M HCl, 1 mL	White solid		
				1 M HCl, 0.1 mL	White solid		
				1 M HCl, 0.5 mL	White solid		
				1 M HCl, 1 mL	White solid		
				2 M HCl, 0.1 mL	White solid		
				2 M HCl, 0.5 mL	White solid		
				2 M HCl, 1 mL	White solid		
				Formic acid, 5 µL	White solid		
				Formic acid, 10 µL	White solid		
				Formic acid, 15 µL	White solid		
				Formic acid, 20 µL	White solid		
				0.4 M HCl, 0.5 mL	White solid		
				0.4 M HCl, 0.75 mL	White solid		

<b>Metal salt</b>	<b>Mass of L / mg</b>	<b>Mass of M / mg</b>	<b>DMF / mL</b>	<b>Modulator / co-solvent</b>	<b>T / °C</b>	<b>Outcome</b>
Sr(NO <sub>3</sub> ) <sub>2</sub> <i>(mmol)</i>	10 <i>(0.04)</i>	25 <i>(0.12)</i>	2.5	<b>0.4 M HCl, 1 mL</b>	<b>80</b>	<b>White solid</b>
				0.4 M HCl, 1.25 mL		White solid
				0.5 M HCl, 0.5 mL		White solid
				0.5 M HCl, 0.75 mL		White solid
				0.5 M HCl, 1 mL		White solid
				0.5 M HCl, 1.25 mL		White solid
				0.6 M HCl, 0.5 mL		White solid
				0.6 M HCl, 0.75 mL		White solid
				0.6 M HCl, 1 mL		White solid
				0.6 M HCl, 1.25 mL		White solid
<i>(mmol)</i>	25 <i>(0.10)</i>	64 <i>(0.30)</i>	2.5	Formic acid, 11 μL	80	White solid
				Formic acid, 11 μL	90	White solid
				Formic acid, 11 μL	100	White solid
Ba(NO <sub>3</sub> ) <sub>2</sub> <i>(mmol)</i>	10 <i>(0.04)</i>	31 <i>(0.12)</i>	2.5	<b>0.4 M, 1 mL</b>	<b>80</b>	<b>White solid</b>
				0.5 M, 1.25 mL		White solid
				Formic acid, 11 μL	80	White solid
				Formic acid, 11 μL	90	White solid
<i>(mmol)</i>	25 <i>(0.10)</i>	79 <i>(0.30)</i>	2.5	Formic acid, 11 μL	100	White solid
				Formic acid, 11 μL		White solid
Cr(NO <sub>3</sub> ) <sub>2</sub> ·9H <sub>2</sub> O <i>(mmol)</i>	10 <i>(0.04)</i>	48 <i>(0.12)</i>	2.5	0.1 M HCl, 0.5 mL	80	No solid
				0.1 M HCl, 0.75 mL		No solid
				0.1 M HCl, 1 mL		No solid
			4	1 M HCl, 0.05 mL	120	Solid
				1 M HCl, 0.1 mL		Solid
			2.5	Formic acid, 5 μL	80	No solid
				Formic acid, 10 μL		No solid
				Formic acid, 15 μL		No solid
Mn(NO <sub>3</sub> ) <sub>2</sub> ·4H <sub>2</sub> O <i>(mmol)</i>	10 <i>(0.04)</i>	30 <i>(0.12)</i>	2.5	0.1 M HCl, 0.5 mL	80	White solid
				0.1 M HCl, 0.75 mL		White solid
				0.1 M HCl, 1 mL		White solid
				0.1 M HCl, 1.25 mL		White solid
				Formic acid, 5 μL		No solid
				Formic acid, 10 μL		No solid
				Formic acid, 15 μL		No solid
				Formic acid, 20 μL		No solid
0.5 M HCl, 1 mL		Solid				

Metal salt	Mass of L / mg	Mass of M / mg	DMF / mL	Modulator / co-solvent	T / °C	Outcome
Mn(NO <sub>3</sub> ) <sub>2</sub> ·4H <sub>2</sub> O <i>(mmol)</i>	10 <i>(0.04)</i>	30 <i>(0.12)</i>	2.5	1 M HCl, 0.05 mL	120	White solid
				1 M HCl, 0.1 mL		White solid
				<b>0.2 M HCl, 1 mL</b>	<b>80</b>	<b>White solid</b>
			2	0.5 mL EtOH, 0.2 mL H <sub>2</sub> O	80	White solid
Fe(NO <sub>3</sub> ) <sub>2</sub> ·9H <sub>2</sub> O <i>(mmol)</i>	10 <i>(0.04)</i>	49 <i>(0.12)</i>	2.5	0.1 M HCl, 0.5 mL	80	Brown solid
				0.1 M HCl, 0.75 mL		Brown solid
				0.1 M HCl, 1 mL		Brown solid
			4	1 M HCl, 0.05 mL	120	Brown solid
				1 M HCl, 0.1 mL		Brown solid
Co(NO <sub>3</sub> ) <sub>2</sub> ·6H <sub>2</sub> O <i>(mmol)</i>	10 <i>(0.04)</i>	35 <i>(0.12)</i>	2.5	0.1 M HCl, 0.5 mL	80	No solid
				0.1 M HCl, 0.75 mL		No solid
				0.1 M HCl, 1 mL		No solid
			4	1 M HCl, 0.05 mL	120	Solid
				1 M HCl, 0.1 mL		Solid
Ni(NO <sub>3</sub> ) <sub>2</sub> ·6H <sub>2</sub> O <i>(mmol)</i>	10 <i>(0.04)</i>	35 <i>(0.12)</i>	2.5	0.1 M HCl, 0.1 mL	90	Amorphous
				0.1 M HCl, 0.5 mL		Amorphous
				0.1 M HCl, 1 mL		No solid
				0.5 M HCl, 0.1 mL		Amorphous
				0.5 M HCl, 0.5 mL		Amorphous
				0.5 M HCl, 1 mL		No solid
				1 M HCl, 0.1 mL		Amorphous
				1 M HCl, 0.5 mL		Amorphous
				1 M HCl, 1 mL		No solid
				2 M HCl, 0.1 mL		Amorphous
				2 M HCl, 0.5 mL		No solid
				2 M HCl, 1 mL		No solid
				6 M HCl, 1 drop		No solid
				6 M HCl, 3 drops		No solid
				6 M HCl, 5 drops		No solid
4	1 M HCl, 0.05 mL	120	Solid			
	1 M HCl, 0.1 mL		Solid			
Cu(NO <sub>3</sub> ) <sub>2</sub> ·3H <sub>2</sub> O <i>(mmol)</i>	10 <i>(0.04)</i>	29 <i>(0.12)</i>	2.5	0.1 M HCl, 0.1 mL	90	Suspension
				0.1 M HCl, 0.5 mL		Solid
				0.1 M HCl, 1 mL		Green solid
				0.5 M HCl, 0.1 mL		Suspension

<b>Metal salt</b>	<b>Mass of L / mg</b>	<b>Mass of M / mg</b>	<b>DMF / mL</b>	<b>Modulator / co-solvent</b>	<b>T / °C</b>	<b>Outcome</b>
$\text{Cu}(\text{NO}_3)_2 \cdot 3\text{H}_2\text{O}$  <i>(mmol)</i>	10  <i>(0.04)</i>	29  <i>(0.12)</i>	2.5	0.5 M HCl, 0.5 mL	90	No solid
				0.5 M HCl, 1 mL		No solid
				1 M HCl, 0.1 mL		Green solid
				1 M HCl, 0.5 mL		Solid
				1 M HCl, 1 mL		No solid
				2 M HCl, 0.1 mL		No solid
				2 M HCl, 0.5 mL		No solid
				2 M HCl, 1 mL		No solid
				6 M HCl, 1 drop		Solid
				6 M HCl, 3 drops		No solid
6 M HCl, 5 drops		No solid				
<i>(mmol)</i>	25  <i>(0.10)</i>	73  <i>(0.30)</i>	2.5	Formic acid, 11 $\mu\text{L}$	80	Solid
				<b>Formic acid, 11 <math>\mu\text{L}</math></b>	<b>90</b>	<b>Solid</b>
				Formic acid, 11 $\mu\text{L}$	100	Solid
$\text{Zn}(\text{NO}_3)_2 \cdot 6\text{H}_2\text{O}$  <i>(mmol)</i>	25  <i>(0.10)</i>	90  <i>(0.30)</i>	2.5	<b>Formic acid, 11 <math>\mu\text{L}</math></b>	<b>80</b>	<b>Solid</b>
				Formic acid, 11 $\mu\text{L}$	90	Solid
				Formic acid, 11 $\mu\text{L}$	100	Solid
$\text{Al}(\text{NO}_3)_3 \cdot 9\text{H}_2\text{O}$  <i>(mmol)</i>	25  <i>(0.10)</i>	114  <i>(0.30)</i>	2.5	Formic acid, 11 $\mu\text{L}$	80	Solid
				Formic acid, 11 $\mu\text{L}$	90	Solid
				Formic acid, 11 $\mu\text{L}$	100	Solid
$\text{In}(\text{NO}_3)_3 \cdot \text{H}_2\text{O}$  <i>(mmol)</i>	25  <i>(0.10)</i>	97  <i>(0.30)</i>	2.5	Formic acid, 11 $\mu\text{L}$	80	Solid
				Formic acid, 11 $\mu\text{L}$	90	Solid
				Formic acid, 11 $\mu\text{L}$	100	Solid

**Table A.2** Summary of single crystal X-ray diffraction data for **MgL<sup>1</sup>**.

Chemical formula	(C <sub>53</sub> H <sub>61</sub> N <sub>11</sub> O <sub>27</sub> Mg <sub>4</sub> )
$M_r$ (g mol <sup>-1</sup> )	1381.36
Crystal system, space group	Triclinic, <i>P</i> -1
Temperature (K)	150
$a, b, c$ (Å)	4.8920(5), 11.6429(10), 13.6762(14)
$\alpha, \beta, \gamma$ (°)	101.100(8), 96.884(8), 100.184(8)
$V$ (Å <sup>3</sup> )	742.74(13)
$Z$	2
Radiation type	Mo $K\alpha$
$\mu$ (mm <sup>-1</sup> )	0.16
Crystal size (mm)	0.34 x 0.10 x 0.06
Absorption correction	Multi-scan
$T_{\min}, T_{\max}$	0.482, 1.000
No. of observed measured, independent and observed [ $I > 2\sigma(I)$ ] reflections	6310, 3459, 1975
$R_{\text{int}}$	0.050
( $\sin\theta/\lambda$ ) <sub>max</sub> (Å <sup>-1</sup> )	0.694
$R[F2 > 2\sigma(F2)], \omega R(F^2), S$	0.110, 0.342, 1.03
No. of reflections	3459
No. of parameters	218
H-atom treatment	H-atom parameters constrained
$\Delta\rho_{\text{max}}, \Delta\rho_{\text{min}}$ (e Å <sup>-3</sup> )	1.72, -0.75

**Table A.3** Summary of single crystal X-ray diffraction data for **CaL**<sup>1</sup>.

Chemical formula	(C <sub>17</sub> H <sub>22</sub> N <sub>4</sub> O <sub>7</sub> Ca)
$M_r$ (g mol <sup>-1</sup> )	434.46
Crystal system, space group	Triclinic, <i>P</i> -1
Temperature (K)	150
$a, b, c$ (Å)	9.3304(10), 11.2571(12), 11.4390(12)
$\alpha, \beta, \gamma$ (°)	108.146(9), 111.750(10), 103.744(9)
$V$ (Å <sup>3</sup> )	971.9(2)
$Z$	2
Radiation type	Mo $K\alpha$
$\mu$ (mm <sup>-1</sup> )	0.37
Crystal size (mm)	0.41 x 0.08 x 0.05
Absorption correction	Gaussian
$T_{\min}, T_{\max}$	0.985, 0.997
No. of observed measured, independent and observed [ $I > 2\sigma(I)$ ] reflections	7579, 4611, 2824
$R_{\text{int}}$	0.041
( $\sin\theta/\lambda$ ) <sub>max</sub> (Å <sup>-1</sup> )	0.698
$R[F_2 > 2\sigma(F_2)], \omega R(F^2), S$	0.064, 0.145, 1.06
No. of reflections	4611
No. of parameters	266
H-atom treatment	H-atom parameters constrained
$\Delta\rho_{\text{max}}, \Delta\rho_{\text{min}}$ (e Å <sup>-3</sup> )	0.37, -0.42

**Table A.4** Summary of single crystal X-ray diffraction data for **SrL<sup>1</sup>**.

Chemical formula	(C <sub>22</sub> H <sub>16</sub> N <sub>4</sub> O <sub>11</sub> Sr <sub>2</sub> )
$M_r$ (g mol <sup>-1</sup> )	687.62
Crystal system, space group	Monoclinic, <i>I2/a</i>
Temperature (K)	150
$a, b, c$ (Å)	17.1449(6), 4.8951(2), 26.8363(14)
$\beta$ (°)	95.495(4)
$V$ (Å <sup>3</sup> )	2241.93(18)
$Z$	8
Radiation type	Cu $K\alpha$
$\mu$ (mm <sup>-1</sup> )	6.96
Crystal size (mm)	0.14 x 0.05 x 0.02
Absorption correction	Gaussian
$T_{\min}, T_{\max}$	0.838, 1.000
No. of observed measured, independent and observed [ $I > 2\sigma(I)$ ] reflections	4021, 2192, 1849
$R_{\text{int}}$	0.049
$(\sin\theta/\lambda)_{\text{max}}$ (Å <sup>-1</sup> )	0.623
$R[F^2 > 2\sigma(F^2)], \omega R(F^2), S$	0.045, 0.114, 1.02
No. of reflections	2192
No. of parameters	169
H-atom treatment	H-atom parameters constrained
$\Delta\rho_{\text{max}}, \Delta\rho_{\text{min}}$ (e Å <sup>-3</sup> )	0.85, -1.30

**Table A.5** Summary of single crystal X-ray diffraction data for **BaL**<sup>1</sup>.

Chemical formula	(C <sub>22</sub> H <sub>16</sub> N <sub>4</sub> O <sub>11</sub> Ba <sub>2</sub> )
$M_r$ (g mol <sup>-1</sup> )	787.07
Crystal system, space group	Monoclinic, <i>I</i> 2/ <i>a</i>
Temperature (K)	150
$a, b, c$ (Å)	26.6103(14), 5.0441(2), 17.9012(9)
$\beta$ (°)	96.211(4)
$V$ (Å <sup>3</sup> )	2388.7(2)
$Z$	8
Radiation type	Cu $K\alpha$
$\mu$ (mm <sup>-1</sup> )	26.13
Crystal size (mm)	0.33 x 0.05 x 0.03
Absorption correction	Multi-scan
$T_{\min}, T_{\max}$	0.485, 1.000
No. of observed measured, independent and observed [ $I > 2\sigma(I)$ ] reflections	6650, 2392, 2054
$R_{\text{int}}$	0.071
( $\sin\theta/\lambda$ ) <sub>max</sub> (Å <sup>-1</sup> )	0.625
$R[F_2 > 2\sigma(F_2)], \omega R(F^2), S$	0.074, 0.217, 1.05
No. of reflections	2392
No. of parameters	130
H-atom treatment	H-atom parameters constrained
$\Delta\rho_{\text{max}}, \Delta\rho_{\text{min}}$ (e Å <sup>-3</sup> )	3.87, -2.37

**Table A.6** Summary of single crystal X-ray diffraction data for **MnL<sup>1</sup>**.

Chemical formula	(C <sub>42</sub> H <sub>65</sub> N <sub>9</sub> O <sub>28</sub> Mn <sub>3</sub> )
$M_r$ (g mol <sup>-1</sup> )	1308.82
Crystal system, space group	Monoclinic, $P2_1/n$
Temperature (K)	150
$a, b, c$ (Å)	4.8941(4), 16.6396(13), 22.4311(15)
$\beta$ (°)	92.215(7)
$V$ (Å <sup>3</sup> )	1825.3(2)
$Z$	4
Radiation type	Mo $K\alpha$
$\mu$ (mm <sup>-1</sup> )	0.78
Crystal size (mm)	0.28 x 0.06 x 0.05
Absorption correction	Gaussian
$T_{\min}, T_{\max}$	0.749, 1.000
No. of observed measured, independent and observed [ $I > 2\sigma(I)$ ] reflections	16555, 4474, 2856
$R_{\text{int}}$	0.086
$(\sin\theta/\lambda)_{\text{max}}$ (Å <sup>-1</sup> )	0.696
$R[F2 > 2\sigma(F2)], \omega R(F^2), S$	0.083, 0.204, 1.09
No. of reflections	4474
No. of parameters	284
H-atom treatment	H-atom parameters constrained
$\Delta\rho_{\text{max}}, \Delta\rho_{\text{min}}$ (e Å <sup>-3</sup> )	0.87, -0.88

**Table A.7** Summary of single crystal X-ray diffraction data for **Cu<sub>3</sub>(L<sup>1</sup>)<sub>2</sub>**.

Chemical formula	(C <sub>30</sub> H <sub>32</sub> N <sub>6</sub> O <sub>16</sub> Cu <sub>3</sub> )
$M_r$ (g mol <sup>-1</sup> )	923.23
Crystal system, space group	Triclinic, <i>P</i> -1
Temperature (K)	150
$a, b, c$ (Å)	9.7937(11), 12.2893(14), 15.9285(17)
$\alpha, \beta, \gamma$ (°)	100.636(7), 98.109(7), 107.225(6)
$V$ (Å <sup>3</sup> )	1760.1(3)
$Z$	2
Radiation type	Mo $K\alpha$
$\mu$ (mm <sup>-1</sup> )	1.88
Crystal size (mm)	0.1 x 0.08 x 0.06
Absorption correction	Multi-scan
$T_{\min}, T_{\max}$	0.662, 0.746
No. of observed measured, independent and observed [ $I > 2\sigma(I)$ ] reflections	29110, 7771, 5218
$R_{\text{int}}$	0.072
( $\sin\theta/\lambda$ ) <sub>max</sub> (Å <sup>-1</sup> )	0.643
$R[F^2 > 2\sigma(F^2)], \omega R(F^2), S$	0.046, 0.103, 1.03
No. of reflections	7771
No. of parameters	500
H-atom treatment	H-atom parameters constrained
$\Delta\rho_{\text{max}}, \Delta\rho_{\text{min}}$ (e Å <sup>-3</sup> )	0.84, -0.50

**Table A.8.** Summary of single crystal X-ray diffraction data for **ZnL<sup>1</sup>**.

Chemical formula	(C <sub>14</sub> H <sub>15</sub> N <sub>3</sub> O <sub>6</sub> Zn)
$M_r$ (g mol <sup>-1</sup> )	386.66
Crystal system, space group	Monoclinic, $P2_1$
Temperature (K)	283
$a, b, c$ (Å)	4.7261(7), 19.247(2), 8.7281(17)
$\beta$ (°)	104.839(17)
$V$ (Å <sup>3</sup> )	767.5(2)
$Z$	2
Radiation type	Mo $K\alpha$
$\mu$ (mm <sup>-1</sup> )	1.64
Crystal size (mm)	0.35 x 0.10 x 0.02
Absorption correction	Gaussian
$T_{\min}, T_{\max}$	0.986, 0.999
No. of observed measured, independent and observed [ $I > 2\sigma(I)$ ] reflections	4685, 2563, 1681
$R_{\text{int}}$	0.096
$(\sin\theta/\lambda)_{\text{max}}$ (Å <sup>-1</sup> )	0.589
$R[F2 > 2\sigma(F2)], \omega R(F^2), S$	0.092, 0.257, 1.000
No. of reflections	2563
No. of parameters	207
H-atom treatment	H-atom parameters constrained
$\Delta\rho_{\text{max}}, \Delta\rho_{\text{min}}$ (e Å <sup>-3</sup> )	092, -0.85



---

## **Chapter 4**

# **Spiropyran-incorporated metal-organic frameworks**

---

## 4 Spiropyran-incorporated metal-organic frameworks

---

### 4.1 Introduction

In the previous chapters of this thesis structural control in MOFs has been discussed in detail. Looking at the literature from the last decade we can see that design and synthesis are both very important, and we have looked at the way in which these syntheses can be monitored in Chapter 2. Linker flexibility has also been considered in Chapter 3, in which the coordination geometry in the frameworks formed with a benzimidazolone-based linker of limited flexibility was found to be an interplay of the linker and metal geometric preferences. Flexibility in MOFs can also be induced via applied stimuli, which is the focus of this final chapter. Spiroyrans (introduced in Chapter 1) fall into a class of photoactive molecules that can undergo a reversible structural conversion upon exposure to UV and visible light. The following sections describe attempts to form frameworks containing these highly flexible stimuli-responsive molecules.

The properties of spiroyrans have begun to be exploited in MOF research in recent years. The spiroyrans moiety was first introduced into the building blocks of the MOF structure in 2016 when D'Alessandro and co-workers reported a two-step procedure for the PSM of the Zr-oxo nodes in MOF-808.<sup>1</sup> In 2017, Schwartz *et al.* showed how spiroyrans were successfully loaded into the pores of three well-known MOFs by a vapour-phase process, whereby the embedded guests showed photo-switching and optical absorption properties similar to those in solutions leading to the frameworks being considered as “*solid solvents*”.<sup>2</sup> Heinke and co-workers also used the embedding method to improve the conductance of UiO-67 MOF films.<sup>3</sup>

More recently, the spiroyrans component has been used by Williams *et al.* as a pendent in the organic linker to form novel zinc frameworks by solvothermal syntheses; the reversible photoinduced isomerisation was observed at a rate that mimicked solution behaviour (Figure 4.1).<sup>4</sup> The spiroyrans in this structure are covalently part of the framework linkers but their structural change does not affect the MOF struts directly.

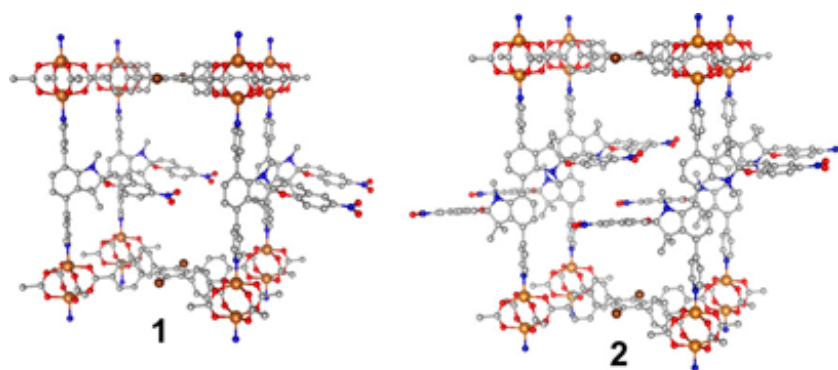
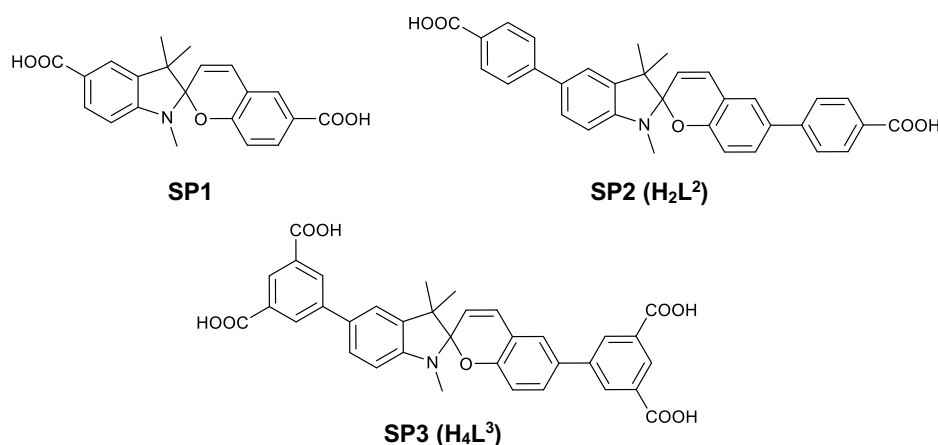


**Figure 4.1** Single-crystal structures of  $[Zn_2(DBTD)(TNDS)]$  (1) and  $[Zn_2(DBTD)(HDDB)]$  (2) with the simulated location of the spiroopyran moieties in the pores of the framework. Adapted from reference 4.

While there are only a handful of examples of spiroopyran-containing MOFs reported in literature to date, the incorporation of these molecules into the struts of metal-organic frameworks was the subject of an as-yet unpublished investigation by the thesis author's supervisor at the University of Nottingham. A series of carboxylic acid functionalised spiroopyrans (SP1 – 3) were synthesised by Dr Magdalene Chong in 2016 (Scheme 4.1) under the supervision of Prof. Martin Schröder and Dr Timothy Easun.



**Scheme 4.1** Structures of three functionalised spiroopyran-based linkers synthesised by Dr Magdalene Chong in 2016.

The photochemical and electrochemical properties of the three molecules have also been investigated, before initial combinatorial screening reactions were carried out in an attempt to synthesise MOF products suitable for crystallographic analysis by Dr Chong.<sup>5</sup> No promising materials were formed using SP2 and SP3, however the first

MOF incorporating the photoactive spiropyran moiety into the strut of the framework was achieved using SP1.

The zinc framework was formed by solvothermal reaction of zinc nitrate, SP1 and *N',N'*-di(pyridine-4-yl)-terephthalamide in DMF and ethanol, in which two different crystallographic phases were observed. These two MOF phases were first introduced in Chapter 2 (Section 2.3.5), and the synthesis was investigated by NMR as part of this thesis. Upon irradiation of any MOF material containing the spiropyran moiety a large structural change may be expected, therefore the method of employing a co-linker<sup>6</sup> was attempted to provide stability and rigidity to the framework. Initially intending to form a layer-pillar framework, Dr Chong incorporated *N',N'*-di(pyridine-4-yl)-terephthalamide into the synthetic procedure which unexpectedly acted as a non-pillaring co-linker. The aim was to decrease the number of dimensions that were directly affected by the photo-isomerisation of SP1 and effectively reduce the inherent disorder in the structure. Solid-state UV-visible spectroscopy showed that the optical absorption associated with the spiropyran component was found to be unchanged, which suggested that coordination to the zinc ions did not alter the properties compared to the free molecule. Raman spectroscopy found that the crystalline phases were stable to UV irradiation by monitoring the decay of light-induced fluorescence over multiple points of a crystal; the closed form of the spiropyran was recovered at room temperature after 23 hours.

The preliminary work of Dr Chong formed the starting point for the work reported in the final chapter of this thesis, in which further solvothermal syntheses with SP2 ( $H_2L^2$ ) and SP3 ( $H_4L^3$ ) have been investigated to create a series of potential spiropyran-based MOFs. As it can be difficult to form ordered crystalline materials due to the multiple conformations in which the spiropyran-based linkers can exist and their fundamental asymmetry between the points of linker extension.<sup>7</sup> Two factors have been considered to reduce this problem: i) reactions can be carried out at elevated temperatures to ensure that any molecules in the open merocyanine (MC) form are converted to the closed (SP) form, and/or ii) the use of dark conditions for the same reason. An additional reason to avoid the MC form is to prevent the potential binding of metal ions in the centre of the linker, inhibiting MOF formation.<sup>8</sup>

## 4.2 Aims and objectives

In this chapter, attempts to synthesise novel frameworks containing flexible photo-switching linkers have been described. During the course of this research, the initial aim of making novel MOFs was only partially successful. It became clear that a better understanding of the nature of the linkers in the reaction solutions was needed to enable future success of making MOF crystals. Therefore, the objectives were to:

- i) Synthesise and characterise spiropyran molecules for use as linkers in MOFs.

Following the work from Magdalene Chong, the extended spiropyran-based carboxylate linkers ( $H_2L^2$  and  $H_4L^3$ ) were re-synthesised and the photophysical properties of these molecules were explored beyond her initial studies of UV-visible absorption/emission properties and quantum yields.

- ii) Optimise synthetic conditions to grow suitable quality crystals of novel photoactive MOFs.

Combinatorial syntheses were carried out to incorporate the spiropyran functionality of  $H_2L^2$  and  $H_4L^3$  into novel MOFs. The choice of metal is important, as seen in Chapter 3, to determine the linker- or metal-defined geometry in the material. The first-row transition metals were investigated (due to previous success of the first zinc spiropyran-based carboxylate containing MOF by Dr Chong) along with group 2 metal salts that display no geometrical preference. A co-linker approach was also investigated to determine structural stability. PXRD was used to characterise any promising crystalline materials, and SCXRD analysis of a spiropyran-containing copper-based framework is described.

- iii) To understand the behaviour of the linkers under reaction conditions so that successful MOF crystals can be synthesised.

The ring-opening effects of the spiropyran linkers in solution was investigated using UV-vis absorption spectroscopy to further understand the complex behaviour of the linker under MOF reaction conditions, enabling prediction of the outcomes in future combinatorial syntheses.

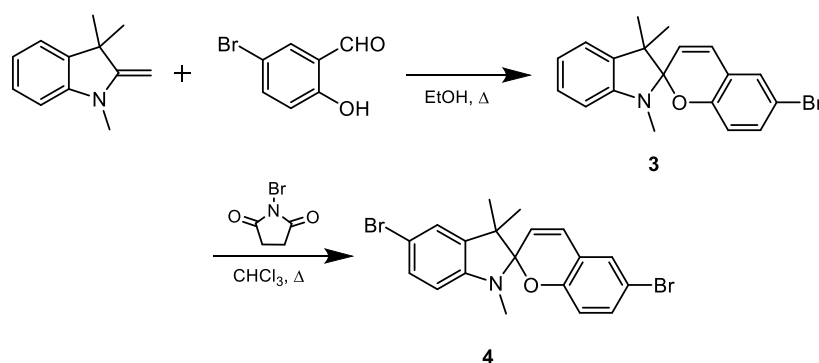
## 4.3 Results and discussion

### 4.3.1 Spiropyran-based carboxylate linkers for MOF synthesis

#### 4.3.1.1 Synthesis

This section describes the syntheses of two photoactive spiropyran-based linkers which follows the preparation method detailed in Dr Chong's thesis.<sup>5</sup>

5-bromosalicylaldehyde and 1,3,3-trimethyl-2-methyleneindoline were refluxed in a 1:1 ratio in ethanol to form the spiro-core of the molecules (**3**).<sup>9</sup> This reaction was followed by reflux with *N*-bromosuccinimide (NBS) in chloroform; the NBS undergoes electrophilic addition reaction at the 5' position of the aromatic ring to give the dibrominated spiropyran (**4**) in a 75% yield (Scheme 4.2).<sup>10</sup>



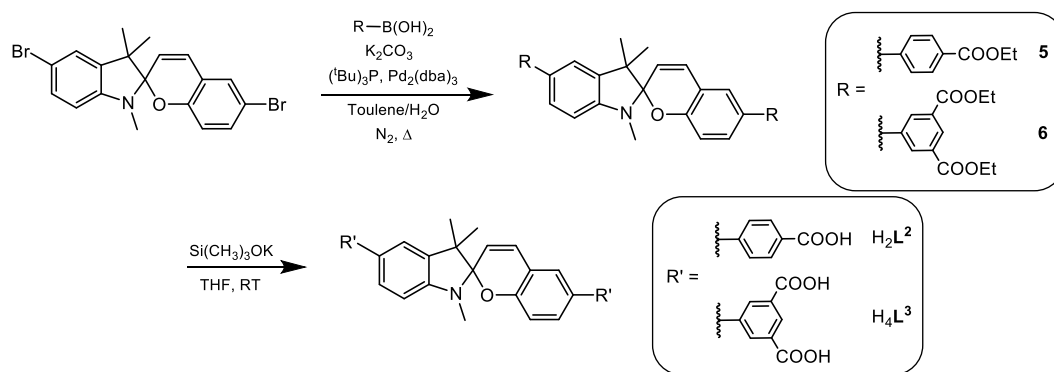
**Scheme 4.2** Synthesis of **3** to form the dibrominated spiropyran core **4**.

In order to synthesise the extended spiropyran-based linkers, **4** was used as a precursor. The bromine substituents allow for reaction with boronic acid-functionalised molecules (containing para-carboxylic ester and isophthalate carboxylate ester groups) in Suzuki-Miyaura cross-coupling reactions, which result in extended conjugated linkers. There are similar examples that have been reported in many previous MOF linker syntheses.<sup>11,12</sup>

Scheme 4.3 shows the reactions of (4-(ethoxycarbonyl)phenyl) boronic acid and 3,5-bis(ethoxycarbonyl)phenyl boronic acid with **4** to give the ethyl ester functionalised spiropyran, **5** and **6** respectively. The reactions were carried out in a mixture of toluene, water and potassium carbonate. Tris(dibenzylideneacetone)dipalladium(0) (Pd<sub>2</sub>(dba)<sub>3</sub>) was found to be a suitable

catalyst choice as the palladium centre is already in the reduced state and tri-*tert*-butylphosphine was used in order to activate the catalyst efficiently.

In the final step of the synthesis, the ethyl ester protecting groups of **5** and **6** were hydrolysed using potassium trimethylsilanolate in THF. Dr Chong investigated the use of stronger bases such as NaOH, however it was found to cleave the molecules at the spiro-centre, therefore highlighting the necessity for a mild base. The carboxylic acid products were precipitated by acidification with HCl to give bright red gelatinous solid which were collected by filtration and left to dry in air. The final products, H<sub>2</sub>L<sup>2</sup> and H<sub>4</sub>L<sup>3</sup>, were characterised by NMR and mass spectroscopy. The free carboxylic acids allowed the molecule to be used as a linker in MOF synthesis reactions in the attempt to form promising novel MOF structures.



**Scheme 4.3** Suzuki-Miyaura cross-coupling of the dibrominated spiroopyran with ethyl ester functionalised boronic acids to give **5** and **6**, followed by the subsequent hydrolysis with a mild base to give H<sub>2</sub>L<sup>2</sup> and H<sub>4</sub>L<sup>3</sup> respectively.

#### 4.3.1.2 Photophysical characterisation

The UV-visible absorption and emission properties of H<sub>2</sub>L<sup>2</sup> and H<sub>4</sub>L<sup>3</sup> were previously reported by Dr Chong, which found that the Stokes shift of H<sub>4</sub>L<sup>3</sup> was larger as a result of the electronic effects of the isophthalate groups.<sup>5</sup> The UV-visible spectra of both linkers in ethanol (0.02 mM) were re-recorded for the purpose of this thesis and are noted in the Experimental (Section 4.5). Instead, this section focuses on further photochemical characterisation which specifically look at the processes which induce the SP→MC ring opening. This is of particular importance to determine whether there is a small percentage of the open form of the linkers present in solution, as this may be affecting the outcome of combinatorial reactions for MOF formation.

#### 4.3.1.2.1 Dissolution in polar solvents

Not only does irradiation induce the ring-opening reversible transformation in spiropyran molecules, but dissolution in polar solvents can also cause this effect,<sup>13</sup> with the MC form having been found to be stabilised in more polar environments.<sup>14</sup>

The intense colour change has been observed upon dissolution of  $H_2L^2$  and  $H_4L^3$  in solvents such as DMF and DMSO for MOF combinatorial syntheses, indicating ring opening to the merocyanine form, before the colour reverts back to a paler solution (closed form) after several minutes. To investigate this process, the dissolution of  $H_2L^2$  in DMSO was monitored by UV-vis spectroscopy (the concentration of the final solution was 0.08 mM) by recording the absorption spectrum every five seconds immediately after dissolving the spiropyran. This work was carried out as part of an MChem project for James Down, supervised by the thesis author. Figure 4.2 shows the UV-vis spectra with two distinct peaks present.

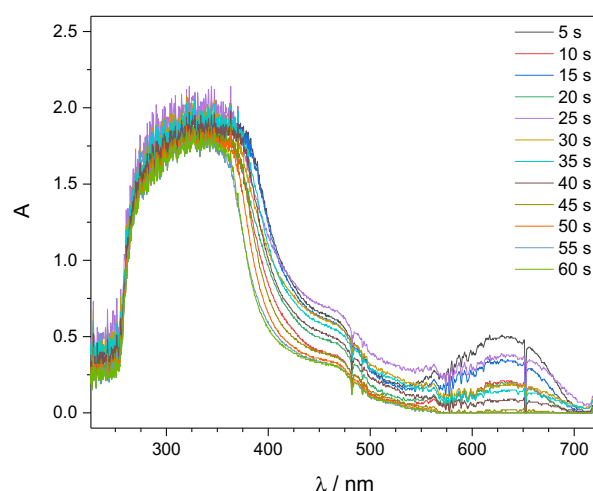


**Figure 4.2** UV-vis spectra monitoring the MC→SP conversion of  $H_2L^2$  in DMSO (0.08 mM) at room temperature over one minute.

The region below 400 nm is saturated meaning that the changes of the closed SP form cannot readily be observed due to the high concentration of the solution. Frustratingly, the peak at 625 nm which is attributed to the merocyanine form<sup>15</sup> could not readily be observed when the experiment was repeated at lower concentrations. The merocyanine form must therefore form a very small proportion of the solutions at concentrations below 0.08 mM since it cannot be observed by UV-vis spectroscopy, despite the typically high extinction coefficients of this form. At 0.08 mM, the peak at 625 nm is

present immediately upon dissolving  $\text{H}_2\text{L}^2$  in DMSO. After 60 seconds the peak has disappeared suggesting the conversion to the closed spiropyran is rapid, even at room temperature.

From this experiment it can be concluded that the order that components are added in a MOF synthesis is crucial. If metal salts are added at the same time as the linker, or immediately after, it is highly likely that coordination to the MC form will occur via the phenolate oxygen, particularly as di- or trivalent metals affect the SP→MC equilibrium.<sup>16</sup> This may have a significant impact on the formation of disordered crystalline materials if multiple conformations of the linker are present during syntheses.

#### 4.3.1.2.2 pH dependence

Spiropyran are also known to be acidochromic,<sup>13,17,18</sup> with cleaving of the spiro-centre to give the MC form at low pH, therefore it is necessary to model how changing the pH of a solution affects the form of the spiropyran linkers.

##### *Acidic effects*

Firstly, a decreasing pH was monitored using UV-vis spectroscopy. Aliquots of 0.1 M HCl were added to 1 mL solution of  $\text{H}_4\text{L}^3$  in ethanol, giving total concentrations of acid between 0.005 – 0.023 M to span the pH range between 1 – 7. Figure 4.3 shows three UV-vis absorption spectra of the varying concentration solutions recorded upon immediate addition of the acid ( $t = 0$ ) and after one hour and 24 hours of equilibration.

At  $t = 0$ , the absorbance of the 301 nm peak is seen decreasing upon increasing the acid concentration in solution. After allowing the spiropyran-containing solutions to equilibrate for one hour, the spectra were recorded again. There appears to be some recovery of the absorbance intensity of the peak at 301 nm and a small feature at *ca.* 450 nm begins to appear. After 24 hours, the broad peak at 450 nm is low intensity at the low concentrations and much more prominent in the solutions of increased [HCl] suggesting the presence of a new species.

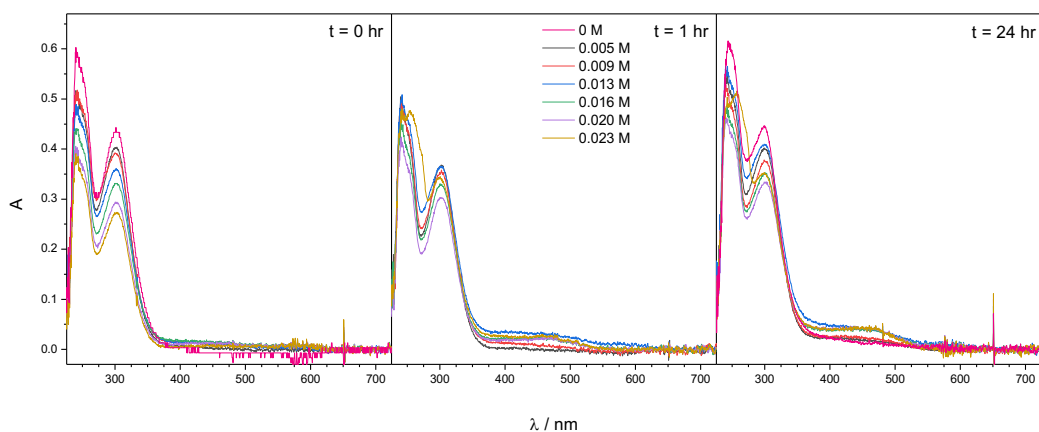


**Figure 4.3** UV-vis spectra showing the pH dependence of  $H_4L^3$  in ethanol upon addition of various concentrations of HCl covering a pH range from 1 – 7. Spectra were recorded at  $t = 0, 1$  and 24 hr.

During this experiment, it is important to note that the total concentration of the spiropyran in solution changes from 0.02 mM with no acid present to 0.0154 mM for the highest concentration of HCl as a result of the dilution with acid. Figure 4.4 shows change in extinction coefficient ( $\epsilon$ ) for the various solutions recorded when corrected for the decreasing spiropyran concentration.

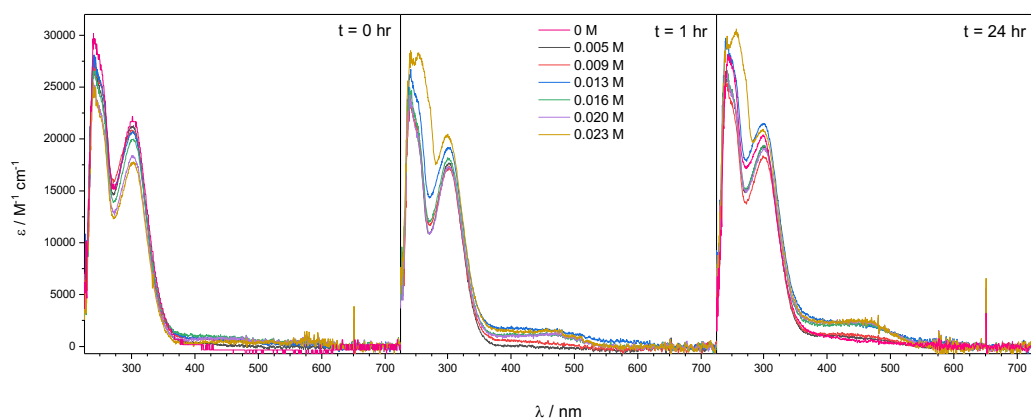


**Figure 4.4** UV-vis spectra of extinction coefficient vs. wavelength as the concentration of the spiropyran in ethanol changes upon addition of HCl. Spectra were recorded at  $t = 0, 1$  and 24 hr.

The spectra in Figure 4.4 show that the extinction coefficient at 301 nm peak decreases as the acid concentration increases, therefore confirming that the changes we observe are a result of the addition of HCl, not just a simple concentration effect. Section 1.4 introduced the many conformations of the spiropyran molecule that can exist due to the ring-opening process and there are also further studies in the literature showing the effect of adding acid or base to a solution.<sup>8,18</sup> Figure 4.5 shows that the addition of acid

can form a protonated spiropyran species (SPH<sup>+</sup>), as well as inducing ring-opening to the protonated merocyanine form (MCH<sup>+</sup>). The absorption peak associated with the SP form is typically observed around 300 nm, whilst the MC peak appears at wavelengths greater than 500 nm. There are many studies of the MCH<sup>+</sup> form typically observed around 400 – 450 nm,<sup>8,19–21</sup> which corroborates strongly with the new peak evolved in our pH experiment.

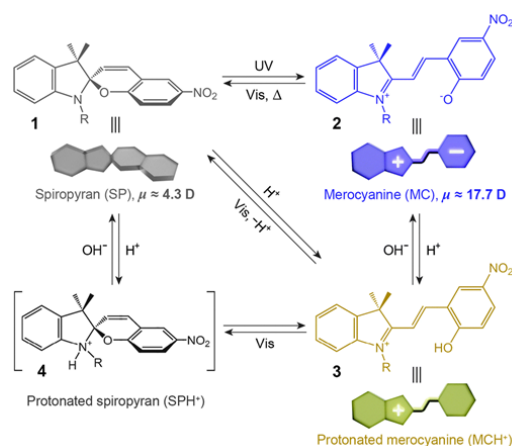


**Figure 4.5** The reversible transitions between four different species of a spiropyran as a result of irradiation and acidochromism. Reproduced from reference 8.

In order to observe the changes in the peak at 301 nm associated with the spiropyran form, the apparent  $\epsilon$  for the seven different acid concentrations were plotted at  $t = 0, 1$  and 24 hours (Figure 4.6).

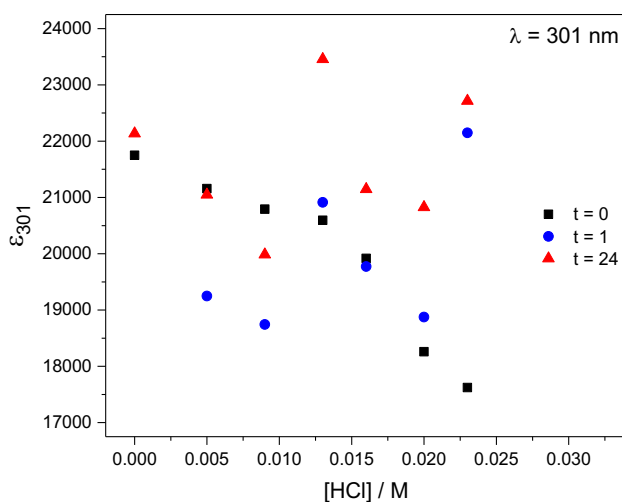


**Figure 4.6** Changes in the extinction coefficient of the 301 nm peak upon addition of HCl to H<sub>4</sub>L<sup>3</sup> in ethanol at  $t = 0, 1$  and 24 hours.

It can be clearly seen that at  $t = 0$  there is a decrease in the SP form upon acidification of the  $\text{H}_4\text{L}^3$  ethanol solution to the  $\text{SPH}^+$  form. Disregarding some obvious anomalies, after leaving the solutions to equilibrate when the spectra are re-recorded at  $t = 1$  and 24 hours, we begin to see apparent recovery of the peak, possibly indicating the reverse process  $\text{SPH}^+ \rightarrow \text{SP}$  form, although this is counterintuitive particularly at the higher concentrations of acid. Alternatively, the observed rise in the 301 nm peak may be due to an overlapping new band of higher extinction coefficient arising from one of the MC forms.

For the peak at 450 nm we are unable to plot the extinction coefficient as it is impossible to know the exact concentration of the open MC form, so a corrected absorbance value was used to account for the decreasing SP concentration as increased aliquots of acid were added (Figure 4.7).

The equation used was:  $A_{\text{corr}} = A \times [\text{H}_4\text{L}^3]_{\text{initial}} / [\text{H}_4\text{L}^3]_{\text{actual}}$

$[\text{H}_4\text{L}^3]_{\text{initial}}$  = the initial concentration of  $\text{H}_4\text{L}^3$  in ethanol (0.02 mM)

$[\text{H}_4\text{L}^3]_{\text{actual}}$  = the concentration of  $\text{H}_4\text{L}^3$  upon addition of aqueous HCl (or later NaOH)

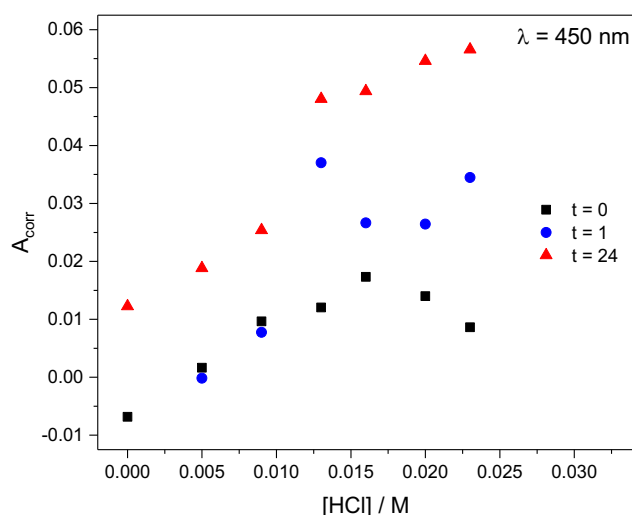


**Figure 4.7** Corrected absorbance values of the 450 nm peak with increasing acid concentration at  $t = 0$ , 1 and 24 hours.

Upon immediate addition of HCl, the absorbance of the peak increases as the concentration increases confirming the ring-opening to the protonated MC form. After 1 and 24 hours the absorbance has increased across the different concentrations of

HCl, however at the higher [HCl] values there is a more significant increase suggesting there is greater conversion, albeit slow, to the MCH<sup>+</sup> form over time.

The absorption difference spectra between the initial spectra with no acid and the two highest concentration solutions (0.020 and 0.023 M HCl) have been plotted (Figure 4.8).

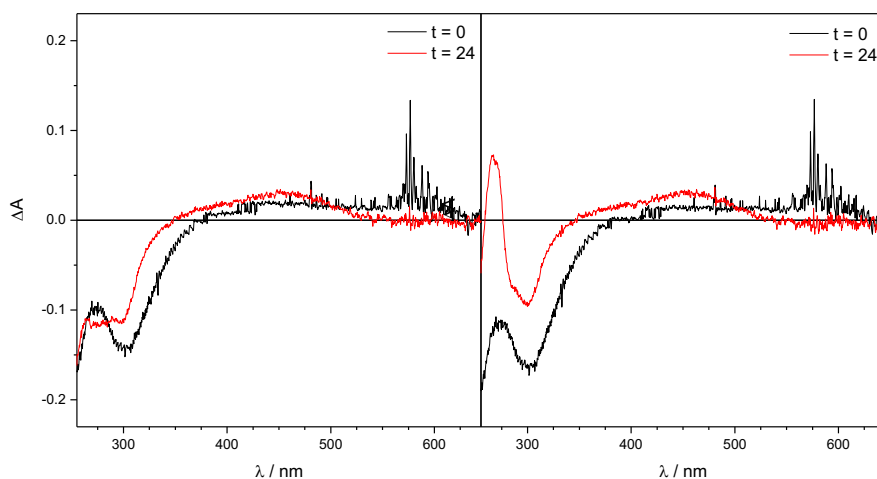


**Figure 4.8** Absorption difference spectra at  $t = 0$  and 24 hr for the 0.020 M HCl (*left*) and 0.023 M HCl solutions (*right*).

Both plots clearly show the growth of the peak in the 400 nm region, confirming that the addition of acid to the spiropyran-containing solutions is inducing the ring opening effect when left to equilibrate. Recovery of the 301 nm peak is observed at both concentrations; it cannot be attributed to recovery of the SP form *only* as it is possible there is an overlap with the growing MC region. Further deconvolution of the peaks is required in future and out of the scope of this thesis.

### *Basic effects*

In order to investigate the consequences of adding a base to a solution of H<sub>4</sub>L<sup>3</sup> in ethanol, the same experiment was repeated with additions of 0.01 M aqueous NaOH to give final concentrations between 0.0005 – 0.0023 M spanning the equivalent pH range between 7 – 14. Figure 4.9 shows the absorbance spectra after measuring the samples immediately after the addition of sodium hydroxide, 1 hour and 24 hours later.

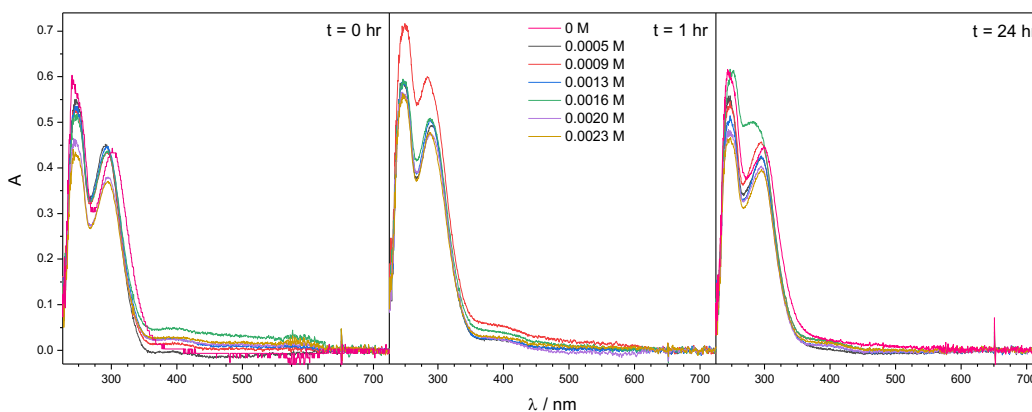


**Figure 4.9** UV-vis spectra showing the pH dependence of  $H_4L^3$  upon addition of various concentrations of NaOH covering an equivalent pH range from 7 – 14. Spectra were recorded at  $t = 0, 1$  and 24 hr.

After 1 hour, there is the appearance of a small feature at *ca.* 400 nm at all concentrations, which then reduces in intensity after leaving the solutions to equilibrate for 24 hours. As mentioned in the previous section upon addition of acid, the corrected absorbance ( $A_{\text{corr}}$ ) values for the changing  $H_4L^3$  concentration have been plotted for the SP peak (this varies from 285 – 301 nm) and the 400 nm peak. Figure 4.10 shows the changes in the peak values of the closed form of  $H_4L^3$ .

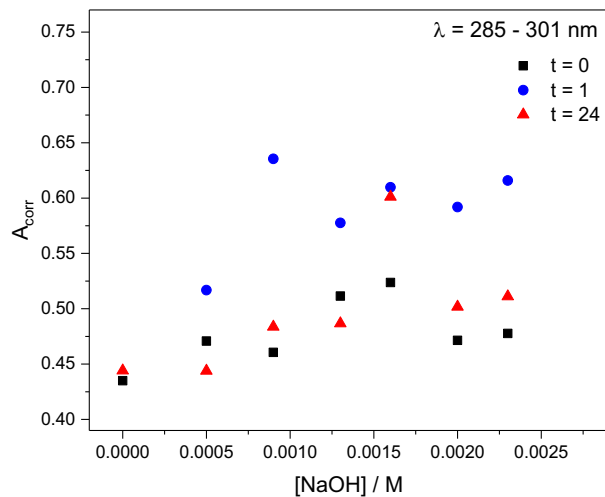


**Figure 4.10** Corrected absorbance values of the SP peak with increasing  $[NaOH]$  after  $t = 0, 1$  and 24 hours.

There is a clear increase in the absorbance values after immediate addition of base to the time the measurements are re-recorded after 1 hour at all concentrations. Upon leaving the solutions to equilibrate for 24 hours the absorbance values appear to recover. Figure 4.11 shows the corrected absorbance values for the 400 nm peak that

appears at the higher NaOH concentrations. There is initially a very small increase in the absorbance values after 1 hour, which then decrease after leaving the solutions to stand for 24 hours.

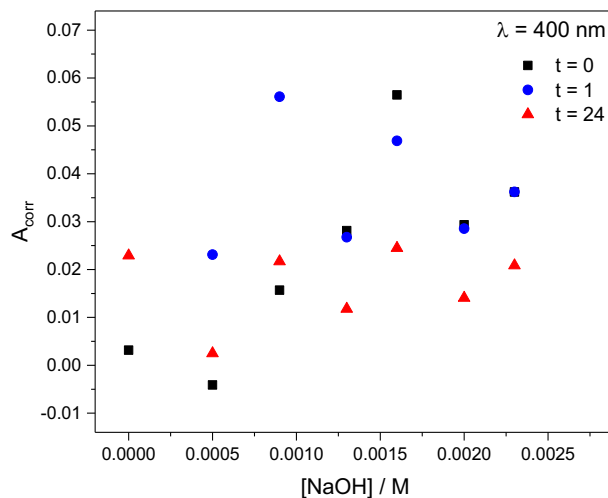


**Figure 4.11** Corrected absorbance values of the 400 nm peak with increasing [NaOH] after  $t = 0, 1$  and 24 hours.

Like for the HCl solutions, the absorption difference spectra between the initial spectra with no base and the two highest concentration solutions (0.0020 and 0.0023 M NaOH) have been plotted (Figure 4.12).

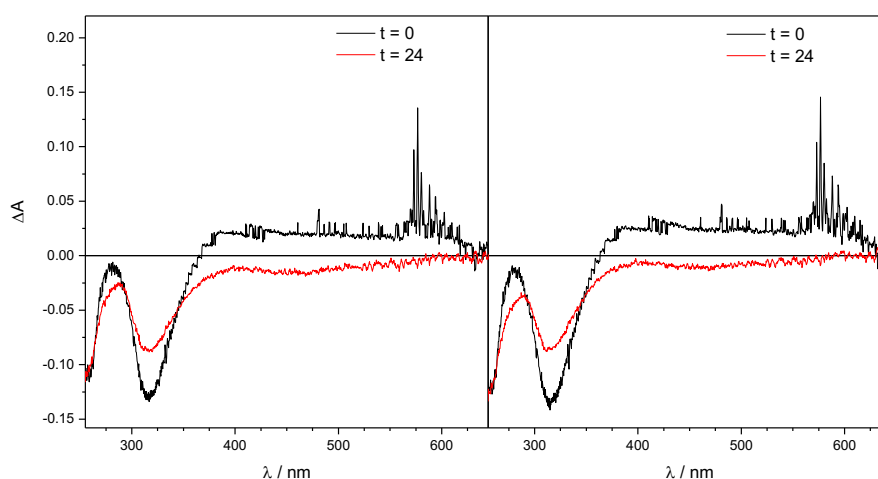


**Figure 4.12** Absorption difference spectra at  $t = 0$  and 24 hr upon addition of 0.0020 M NaOH (*left*) and 0.0023 M NaOH (*right*) solutions.

At both concentrations, the 300 nm peak recovers after 24 hours while the broad peak at 400 nm diminishes. It is possible that upon the addition of base there is

deprotonation of  $\text{-COOH}$  groups  $\text{H}_4\text{L}^3$  causing the initial changes in the absorption spectra. Over time there are potentially excess  $\text{Na}^+$  ions in solutions which can bind to the linker to form the sodium carboxylate salt. It is unknown how similar the absorption spectra of these species are therefore, further work would be required to understand this process.

#### 4.3.1.2.3 Irradiation

To investigate the ring-opening of spiropyrans under UV light, 0.1 mM solutions of  $\text{H}_2\text{L}^2$  and  $\text{H}_4\text{L}^3$  in ethanol were irradiated under a short wavelength TLC lamp ( $\lambda = 254 \text{ nm}$ ) for various time periods. The concentrations were chosen due to previous success with similar experiments on other spiropyran-based linkers carried prior to this work in this thesis.

Figure 4.13 shows the absorption spectra of  $\text{H}_2\text{L}^2$  after irradiation for 4 and 24 hours. While there is very little change to the peaks at 264 and 316 nm associated with the SP form, we observe the  $\text{MCH}^+$  peak appearing at 464 nm after 24 hours; this is seen in the difference spectra.

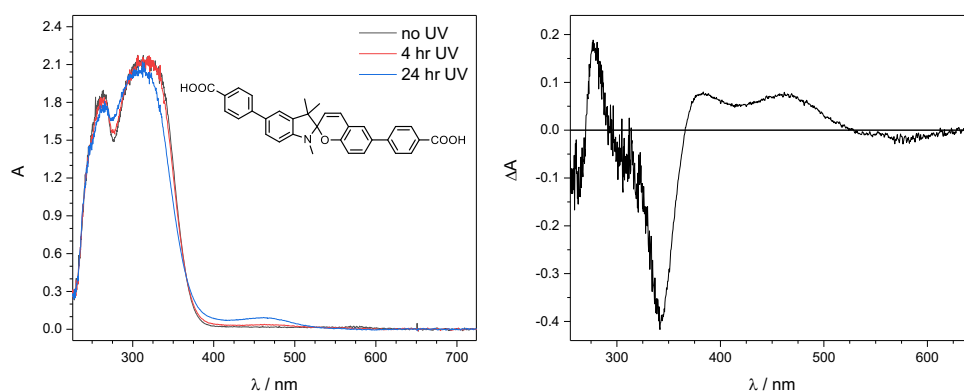


**Figure 4.13** UV-vis spectra of  $\text{H}_2\text{L}^2$  after a total of 4 and 24 hours of irradiation (*left*) and the difference spectra after 24 hours (*right*).

The spectral changes upon irradiation of  $\text{H}_4\text{L}^3$  were also monitored, with the appearance of the  $\text{MCH}^+$  peak at 454 nm appearing much earlier after 4 hours (Figure 4.14). Unfortunately, the experiment needed to be stopped meaning the sample was refrigerated overnight. The UV-vis absorption spectrum was collected the following morning, and the 454 nm peak was still present although there appeared to be some slightly recovery to the closed form due to the intensity decrease. The sample

was irradiated again for 1 hour (5 hr total) and 4 hours (9 hr total), with the 454 nm peak still present. After leaving the solution to be irradiated overnight, the spiropyran was found to breakdown suggesting the molecule was unstable to prolonged irradiation.

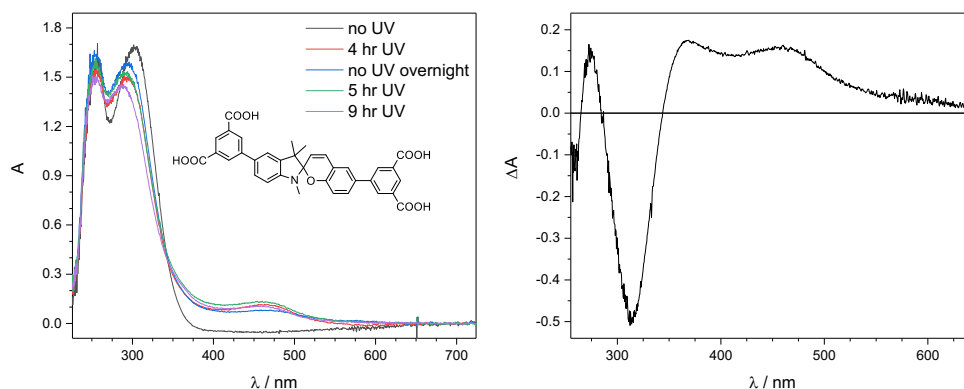
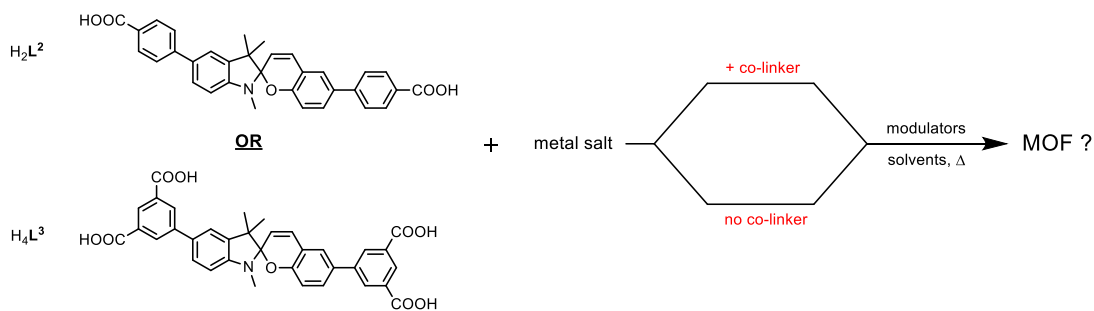


**Figure 4.14** UV-vis spectra of  $H_4L^3$  after a total of 4, 5 and 9 hours of irradiation (*left*) and the difference spectra after 9 hours (*right*).

The increasing intensity of the  $MCH^+$  peak is surprising as no acid is present in the solution. Polar solvent environments are well-known to stabilise the MC form, and it has even been reported that the  $SP \rightarrow MC$  transition can occur spontaneously (without irradiation with UV light) under dark conditions.<sup>8</sup> As the linkers were dissolved in EtOH for the measurements it is possible that there is self-protonation of the MC form from the excess protons in solutions from the solvent. This information is crucial to determine the factors that can influence the formation of ordered frameworks using these molecules.

### 4.3.2 Photoactive MOF syntheses

A combinatorial approach with  $H_2L^2$  or  $H_4L^3$  with metal salts was used to synthesise novel photoactive MOFs by varying the solvents, modulators and reaction temperature. Two different approaches in the syntheses were used: *with* and *without* a co-linker present in the reactions (Scheme 4.4). All combinatorial reactions attempted with the product outcomes are detailed in the Appendix (Section 4.7, Table A.9).



**Scheme 4.4** Schematic representation of combinatorial syntheses with either  $H_2L^2$  or  $H_4L^3$  using two different approaches (*with* and *without* a co-linker) under various reaction conditions.

Colourless metal salts, such as group 2 ions and  $Zn^{2+}$  and  $Mn^{2+}$ , were initially chosen so that any colour observed in solid products could be attributed to the spiropyran-based linkers. These metals also gave very interesting results in Chapter 3 of this thesis, thereby forming the starting point to synthesise a series of structures using the more flexible spiropyran linkers. Cu(II), Al(III), In(III), Zr(IV) and Sc(III) ions were also used in later reactions to attempt to synthesise suitable quality MOF crystals. The linkers showed excellent solubility in DMF therefore it was used in all combinatorial reactions, with the addition of other polar solvents such as EtOH, MeOH and  $H_2O$  in some cases.

Due to Dr Chong's success of using  $N^1, N^4$ -di(pyridin-4-yl)terephthalamide in the synthesis of the first spiropyran-containing framework with SP1 and  $Zn^{2+}$  ions,<sup>5</sup> the same co-linker was also used in the combinatorial reactions described in this thesis with  $H_2L^2$  and  $H_4L^3$ . The use of a shorter, dipyridyl co-linker was primarily investigated in the combinatorial reactions.

The modulators used in some reactions were aqueous acids (including hydrochloric acid, formic acid, nitric acid and acetic acid), benzoic acid or ammonium acetate. Modulators were briefly introduced at the beginning of this thesis in Section 1.1. The role of HCl has been explored in the syntheses of zirconium MOFs (UiO series) where Forgan, Farha and Serre (and co-workers) suggested that the acid can: i) condition the DMF reaction solvent by neutralising basic amine impurities; ii) improve the crystallinity of the final product and/or iii) aid with the formation of  $Zr_6$  clusters.<sup>22–24</sup> The addition of acid to our spiropyran-based MOF reactions was intended to allow the thermodynamically stable product to form, however there may be some unfavourable effects on the spiropyran linker with formation of the  $MCH^+$  form.

Reactions were carried out at elevated temperatures to ensure the linker was in the closed SP form, which reportedly favours the MC→SP equilibrium process.<sup>25</sup> A range of temperatures from 65 – 210 °C were initially attempted in the syntheses, but ultimately lower temperatures (65 – 100 °C) were eventually favoured based on the success of previous spiropyran-MOF formation by Dr Chong, and also the benzimidazolone-based coordination polymers that were discussed earlier in this thesis.

Analysis of any solid materials formed was first undertaken using PXRD to determine the crystallinity of each sample (Section 4.3.2.2). MChem student Joe Alemzadeh assisted the thesis author with the setting up of combinatorial reactions and loading of samples for PXRD analysis. In cases where crystals appeared of suitable quality for SCXRD, they were firstly analysed in-house and when good quality data was difficult to obtain the samples were sent to the National Crystallography Service (Section 4.3.2.3). All solid products were produced in very low yields due to the small scale of combinatorial reactions performed.

#### 4.3.2.1 PXRD results

The formation of ordered, crystalline frameworks was anticipated to be challenging due to the disorder that could arise from the spiropyran linkers. In those reactions where solid was observed to form, the majority did not produce crystals large enough for SCXRD and were therefore analysed using PXRD.

As the air stability of the materials produced was not known, all of the powder patterns were obtained by directly loading the samples from the reaction solution onto zero-background silicon wafers. Some powder patterns were therefore found to contain a large broad peak at higher angles ( $20 - 30^\circ 2\theta$ ) due to excess DMF that had not evaporated.

Upon analysis of the PXRD patterns, any diffraction peaks below  $10^\circ 2\theta$  were considered promising as this corresponds to a d-spacing (interplanar distance) greater than 8 Å. The lengths of H<sub>2</sub>L<sup>2</sup> and H<sub>4</sub>L<sup>3</sup> are very similar at *ca.* 16.9 and 16.7 Å respectively (calculated using Chem3D measuring the atom-atom distance from the

carboxylate oxygens at either ends of the molecules), therefore a large d-spacing between repeating metal centres in a crystalline MOF would suggest incorporation of the spiropyran linker into the lattice.

#### 4.3.2.1.1 Syntheses with $H_4L^2$ and $H_4L^3$ in *absence* of co-linker

Many combinatorial reactions were performed with no co-linker present that yielded unsuccessful results. However, two powder diffraction patterns from different samples using  $H_4L^3$  showed promise of spiropyran incorporation into a framework; one with magnesium and the other with calcium.

Magnesium and calcium acetate were each reacted with  $H_4L^3$  in a 10:1 ratio at 75 °C. For the magnesium acetate reaction, a solvent system of DMF/EtOH was used, whereas DMF/EtOH/H<sub>2</sub>O was used for the calcium acetate reaction. The PXRD patterns are shown in Figure 4.15. Both patterns contain a large broad peak due to excess solvent, however there are weak Bragg peaks that are observed at low  $2\theta$  values. In the solid obtained with magnesium, the first peak corresponds to a d-spacing of 11.5 Å, while for the calcium material the d-spacing value of the lowest angle peak is 16.7 Å.

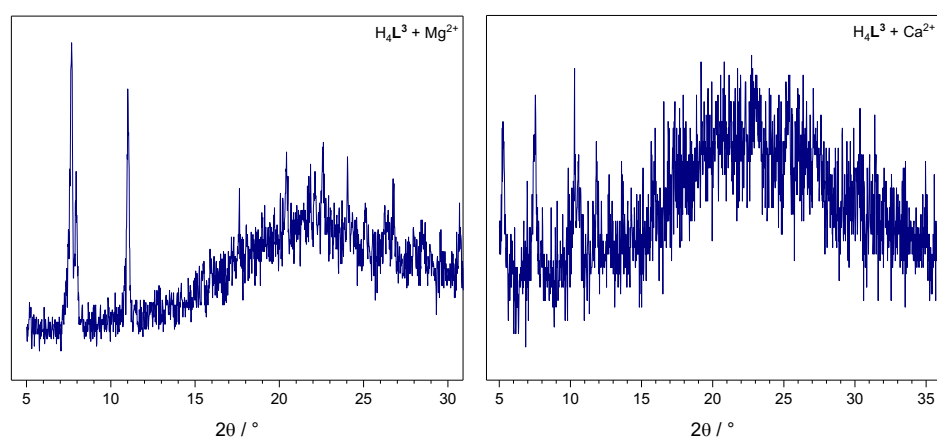


**Figure 4.15** PXRD patterns obtained from initial combinatorial syntheses with  $H_4L^3$  and group 2 metal salts – magnesium (II) (*left*) and calcium (II) (*right*).

As both patterns show diffraction peaks at low  $2\theta$  values potentially indicating spiropyran incorporation into a framework, the next step was to improve both the product yield and the crystallite size to enable characterisation and structural analysis by SCXRD. The addition of a co-linker in the combinatorial reactions was attempted.

#### 4.3.2.1.2 Syntheses with $H_2L^2$ and co-linker

The combinatorial syntheses with a co-linker present in the  $H_2L^2$  reaction solution were first attempted using  $N^1, N^4$ -di(pyridine-4-yl)terephthalamide. Unfortunately, the PXRD patterns of any products yielded did not contain crystalline peaks. Due to the flexibility exhibited by the extended spiropyran ( $H_2L^2$ ), along with the flexibility of the co-linker, it was possible that only disordered material was yielded. The synthetic procedure was therefore adapted to use a shorter, rigid molecule (4,4'-dipyridyl) as a co-linker to increase the likelihood of forming ordered framework materials. Unfortunately, syntheses with group 2 or copper metal salts, 4,4'-dipyridyl and  $H_2L^2$  did not yield crystalline products with low angle Bragg peaks to suggest spiropyran incorporation.

The synthesis was also attempted with zinc acetate (due to previous success of using Zn(II) ions by Dr Chong) in a solvent mixture of DMF/MeOH at 65 °C. Pleasingly, small crystallites ( $Zn-L^2$ ) were formed in the reaction and the PXRD pattern gave a very promising result (Figure 4.16, *black trace*). The PXRD patterns of the zinc acetate and also  $H_2L^2$  are shown for comparison confirming that the metal salt or linker has not simply been recrystallised during the reaction. The reaction was also repeated in the absence of the metal salt yielding no solid product, as the linker and co-linker remained soluble in the reaction solvent.

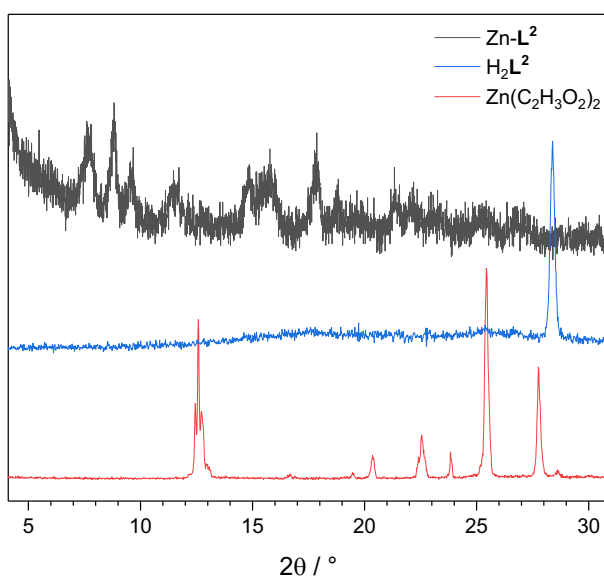


**Figure 4.16** PXRD pattern of  $Zn-L^2$ . The powder diffraction pattern of  $H_2L^2$  and zinc acetate are shown for comparison.

The peaks observed confirm the crystallinity of the sample, albeit the peaks are very weak small due to the small amount of solid material produced. The first peak in the pattern appears at  $7.69^\circ 2\theta$  which corresponds to a d-spacing of *ca.* 11.6 Å, consistent with the possibility of a spiropyran-containing MOF structure. Interestingly, the first Bragg peak of Zn-L<sup>2</sup> is in a very similar position to the product of the reaction with H<sub>4</sub>L<sup>3</sup> and magnesium acetate in the previous section (possibly due to the similar linker size), the rest of the peaks are different. The broadness of the peaks in the PXRD pattern of Zn-L<sup>2</sup> is due to the small quantity of material produced and potentially also suggests that there is also some amorphous material present alongside the crystallites. This can be expected due to the multiple conformations that H<sub>2</sub>L<sup>2</sup> can exhibit, and this was also observed in all of Dr Chong's MOF syntheses where an amorphous solid was formed alongside the crystalline framework (first mentioned in Chapter 2). The solid also appears to be stable upon exposure to air, as the powder pattern were the same after an initial 10 min scan followed by the 30 min scan shown in Figure 4.17. The only difference was the large, broad peak due to residual DMF has reduced as the sample dried on the silicon wafer.

These initial results are very promising for the incorporation of a spiropyran into a metal-organic framework that shows some degree of air stability. Unfortunately, due to the small quantity of solid produced in each combinatorial reaction the only characterisation that could be performed was PXRD to indicate the crystallinity of the samples. For continuation of this project, large crystals are ideally needed for SCXRD and more product needs to be produced either by performing multiple parallel reactions that can be combined or repeating the same synthesis on a larger scale. This will enable further characterisation of the product by FTIR, CHN and NMR digestion to provide further evidence of spiropyran incorporation into a MOF.

#### 4.3.2.1.3 Syntheses with H<sub>4</sub>L<sup>3</sup> and co-linker

The promising PXRD pattern of Zn-L<sup>2</sup> prompted further investigation using the co-linker approach with the isophthalate spiropyran linker, H<sub>4</sub>L<sup>3</sup>. The group 2, copper, and zinc salts were again used due to previous successful reactions.

### Group 2 materials

Four promising diffraction patterns were obtained from four out of over eighty syntheses involving  $H_4L^3$  and 4,4'-dipyridyl with group 2 metal salts; these were the only four to produce crystalline products.  $Ca-L^3$  and  $Sr-L^3$  were synthesised at 65 °C in a solvent mixture of DMF/MeOH/ $H_2O$ , whilst  $Mg-L^3$  and  $Ba-L^3$  were synthesised at 80 °C in DMF with a concentrated HCl as a modulator.

The PXRD patterns obtained are all different (Figure 4.17). In all four patterns, peaks are observed below  $10^\circ 2\theta$ , with the first Bragg peaks corresponding to d-spacings of 11.48, 16.46, 16.46 and 13.25 Å for  $Mg-L^3$ ,  $Ca-L^3$ ,  $Sr-L^3$  and  $Ba-L^3$  respectively. The diffractions peaks for  $Mg-L^3$ ,  $Ca-L^3$  and  $Ba-L^3$  are weak due to the small amount of material present.

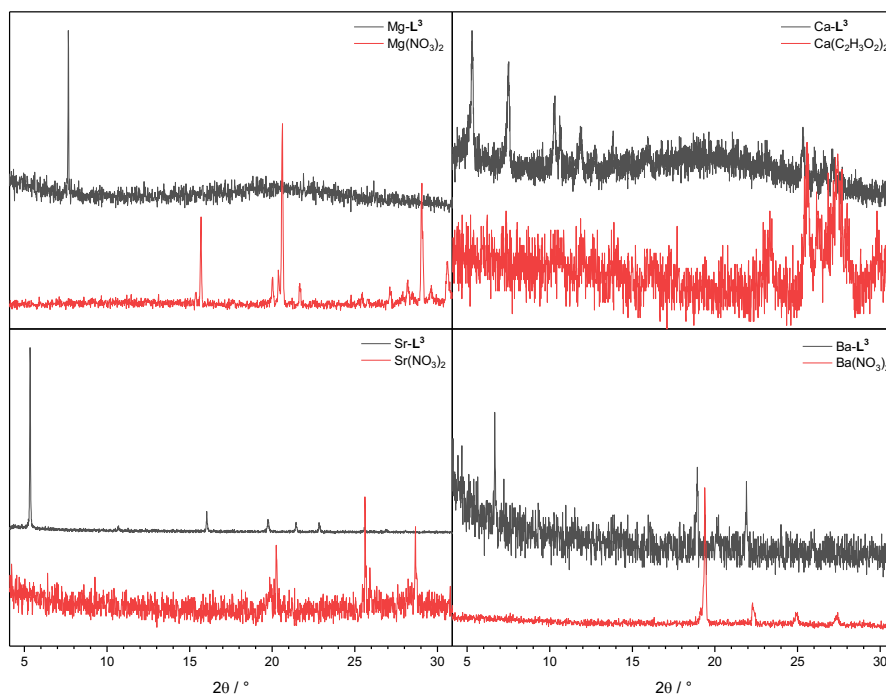


**Figure 4.17** PXRD patterns of four crystalline products obtained from combinatorial syntheses with  $H_4L^3$ , 4,4'-dipyridyl and group 2 metal salts. The PXRD patterns of the metal salts are shown (*red trace*).

The powder pattern of  $Ca-L^3$  was the only pattern which enough peaks present to initially index. The result gave a monoclinic unit cell where  $a = 17.0966$ ,  $b = 7.4119$  and  $c = 12.0677$  Å,  $\beta = 104.7450^\circ$  and  $V = 1478.84$  Å<sup>3</sup>. The unit cell is large enough

to be consistent with metal-linker-metal distances, providing further evidence of incorporation of  $\text{H}_4\text{L}^3$  into a calcium framework.

Interestingly, the diffraction patterns for  $\text{Mg-L}^3$  and  $\text{Ca-L}^3$  are almost identical to the two patterns obtained in Section 4.3.2.1.2 when a co-linker was not present in the syntheses (Figure 4.18). This suggests that the 4,4'-dipyridyl co-linker does not form part of the final structure, but in some way assists with the formation of the more crystalline material.

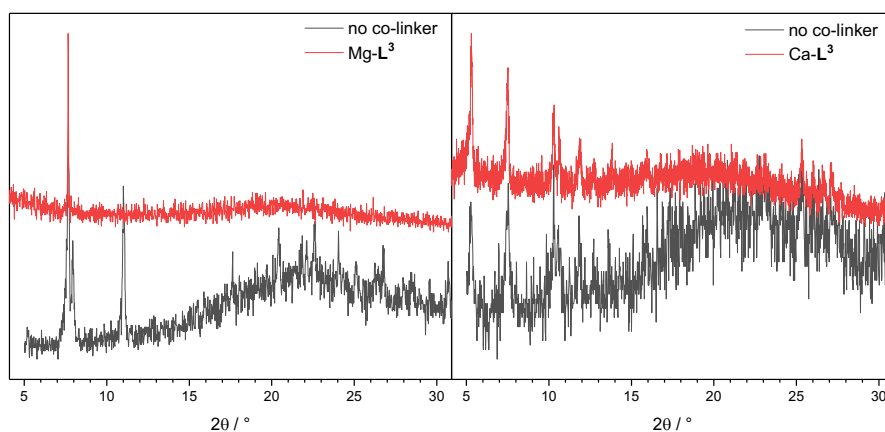


**Figure 4.18** PXR D comparison of crystalline material formed with magnesium or calcium (II) ions and  $\text{H}_4\text{L}^3$ , *with* and *without* a co-linker present in the reaction solution.

$\text{Sr-L}^3$  was the only sample in which the crystallites looked promising for SCXRD analysis. Data collection for the sample was first attempted in-house and proved unsuccessful. The sample was therefore sent to the National Crystallography Service for further analysis, but unfortunately no data could be obtained.

The results in this section are extremely promising and show the reaction between spiropyran molecule with group 2 metals to form crystalline materials. As in the previous section with  $\text{Zn-L}^2$ , only small quantities of the four solid products were produced meaning that PXR D was the only characterisation method to be performed. Scale-up would need to be achieved in the future to fully characterise these materials. Concurrently with the group 2 combinatorial syntheses, reactions with  $\text{H}_4\text{L}^3$  and transition metals were also being performed and the results are discussed in the subsequent section.

### Transition metal materials

The co-linker approach was used with  $H_4L^3$  and Cu(II) or Zn(II) nitrate. The reactions were both carried out at 65 °C (due to the partial success of forming crystalline material with the group 2 metals) in either DMF/MeOH/H<sub>2</sub>O or DMF/H<sub>2</sub>O to form Cu-L<sup>3</sup> and Zn-L<sup>3</sup> respectively. Figure 4.19 shows the PXRD patterns of the solid products obtained during the reactions.

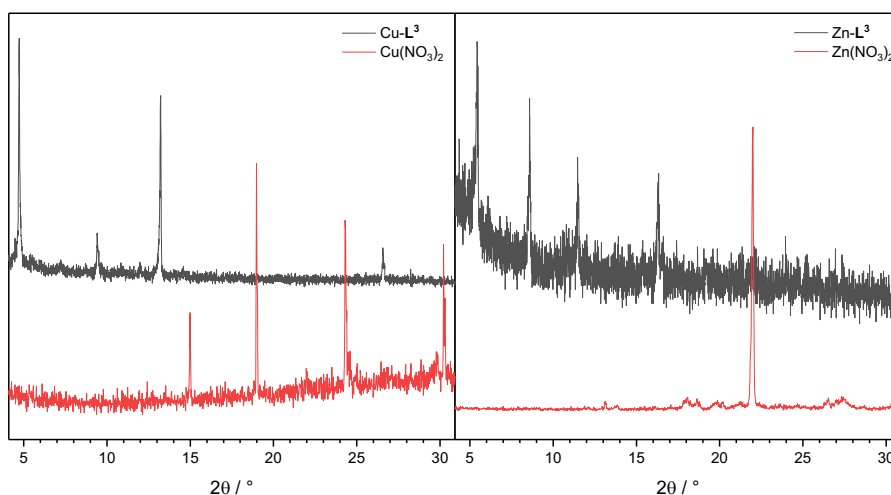


**Figure 4.19** PXRD patterns of two crystalline products obtained from combinatorial syntheses with  $H_4L^3$ , 4,4'-dipyridyl and first row transition metal salts. The PXRD patterns of the metal salts are also shown.

Cu-L<sup>3</sup> appears to be very crystalline with strong Bragg peaks observed in the pattern. The first peak appears at 4.78°  $2\theta$ , which corresponds to the largest d-spacing seen in the materials that have been mentioned in this section (18.46 Å). Zn-L<sup>3</sup> has promising Bragg peaks at low angles, however the pattern is very weak due to the small quantity of material used to obtain the pattern. The first peak in the pattern at 5.50°  $2\theta$  corresponds to a d-spacing of 16.06 Å.

Unfortunately, there are not enough peaks in both PXRD pattern to successfully index the patterns and obtain the unit cell information. However, the crystallites of Cu-L<sup>3</sup> did appear to be of suitable quality for SCXRD analysis and are discussed further in the next section of this thesis.

### *Comparison between group 2 and transition metal materials*

All six materials discussed in this section appear to be air stable upon solvent evaporation as multiple PXRD scans were performed over the course of a several hours with no apparent change in their diffraction patterns. The promising PXRD patterns have provided encouraging evidence of probable spiropyran-incorporation into MOFs. The structure series of coordination polymers reported in Chapter 3 showed that there can often be similarities in the PXRD pattern when the same linker is reacted with different metals. The results in this section are quite different, particularly as the only similarities in PXRD patterns are that the first low angle peak for Ca-L<sup>3</sup>, Sr-L<sup>3</sup> and Zn-L<sup>3</sup> are at approximately the same 2θ positions resulting in similar d-spacing values. Unfortunately, the products of Mg-L<sup>3</sup>, Ca-L<sup>3</sup>, Sr-L<sup>3</sup>, Ba-L<sup>3</sup> and Zn-L<sup>3</sup> were all microcrystalline powders which were unsuitable for SCXRD. Further refinement of conditions will be required in the future to produce large single crystals for structural characterisation, and scale-up will also be necessary to provide large enough quantities for full characterisation by other methods discussed earlier in this section.

#### **4.3.2.2 Cu-L<sup>3</sup> SCXRD results**

Cu-L<sup>3</sup> was crystalline by PXRD and the small crystals were potentially suitable for SCXRD analysis. After first attempting data collection in-house in which it was difficult to obtain good quality data, the sample was sent to the National Crystallography Service. Data collection was obtained but have proved challenging to interpret. Solving and refinement of the crystal structure by Dr Stephen Argent (University of Nottingham) is underway – the description in this section is of the partially completed structure (Figure 4.22).

The linker H<sub>4</sub>L<sup>3</sup> can be considered as two isophthalate groups either side of a bent molecular core. This general motif is well-known in the MOF community, and often forms copper-based frameworks that contain broadly square-planar paddlewheels with two copper ions and four carboxylates. As a consequence of the isophthalate geometry these paddlewheels can join up to form Kagomé lattices. There are many reported examples of networks with a Kagomé lattice.<sup>26–30</sup> In 2011 Zaworotko and co-workers reacted a 5-substituted-1,3-BDC linker with CuCl<sub>2</sub> to form the structure shown in Figure 4.20.<sup>31</sup> The linkers can be described as “partially flexible” due to the position

of the two isophthalate carboxylate groups that extend at  $120^\circ$  to each other, allowing for twisting or bending with respect to the plane of the benzene ring. This favours the formation of Kagomé networks with square paddlewheel nodes when DEF is used as the solvent.

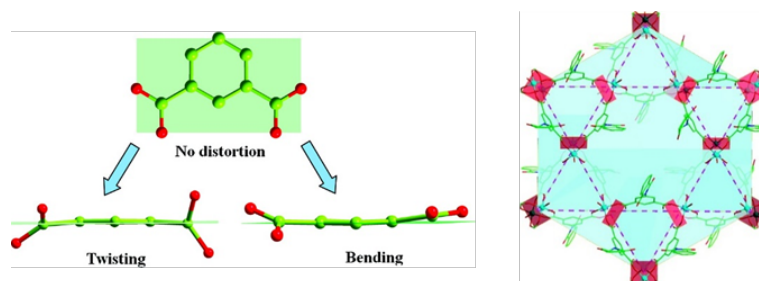


**Figure 4.20** 1,3-BDC-based linkers can exhibit partial flexibility by twisting and bending (*left*) which when reacted with  $\text{Cu}^{2+}$  ions results in the formation of a Kagomé lattice (*2D layer shown right*). Adapted from reference 31.

In a similar manner, our partial structure  $\text{Cu-L}^3$  also contains square planar copper paddlewheels (Figure 4.22). Each paddlewheel similarly binds to four different carboxylate groups from the isophthalate groups of four different linkers forming a Kagomé lattice motif in the  $ab$  plane. The isophthalate groups are reasonably readily identified in the structure but the spirocyan cores are heavily disordered and cannot reliably be located. The distance between the isophthalate groups is sufficient to accommodate the disordered cores. Disorder is unsurprising since there is a chiral centre at the spiro carbon, and the linker can bind at any given paddlewheel with either of its isophthalate groups. This combination means that any one linker has four possible orientations in the structure, and an attempt to model this is shown in Figure 4.21 (see experimental for details).

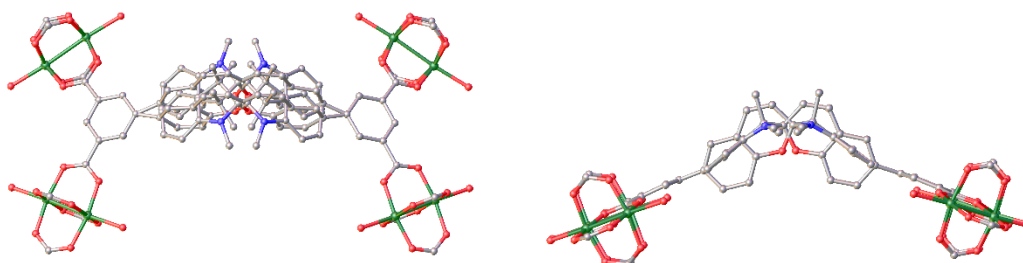


**Figure 4.21** Modelling of the possible four-way disorder of the spirocyan core in  $\text{Cu-L}^3$ .

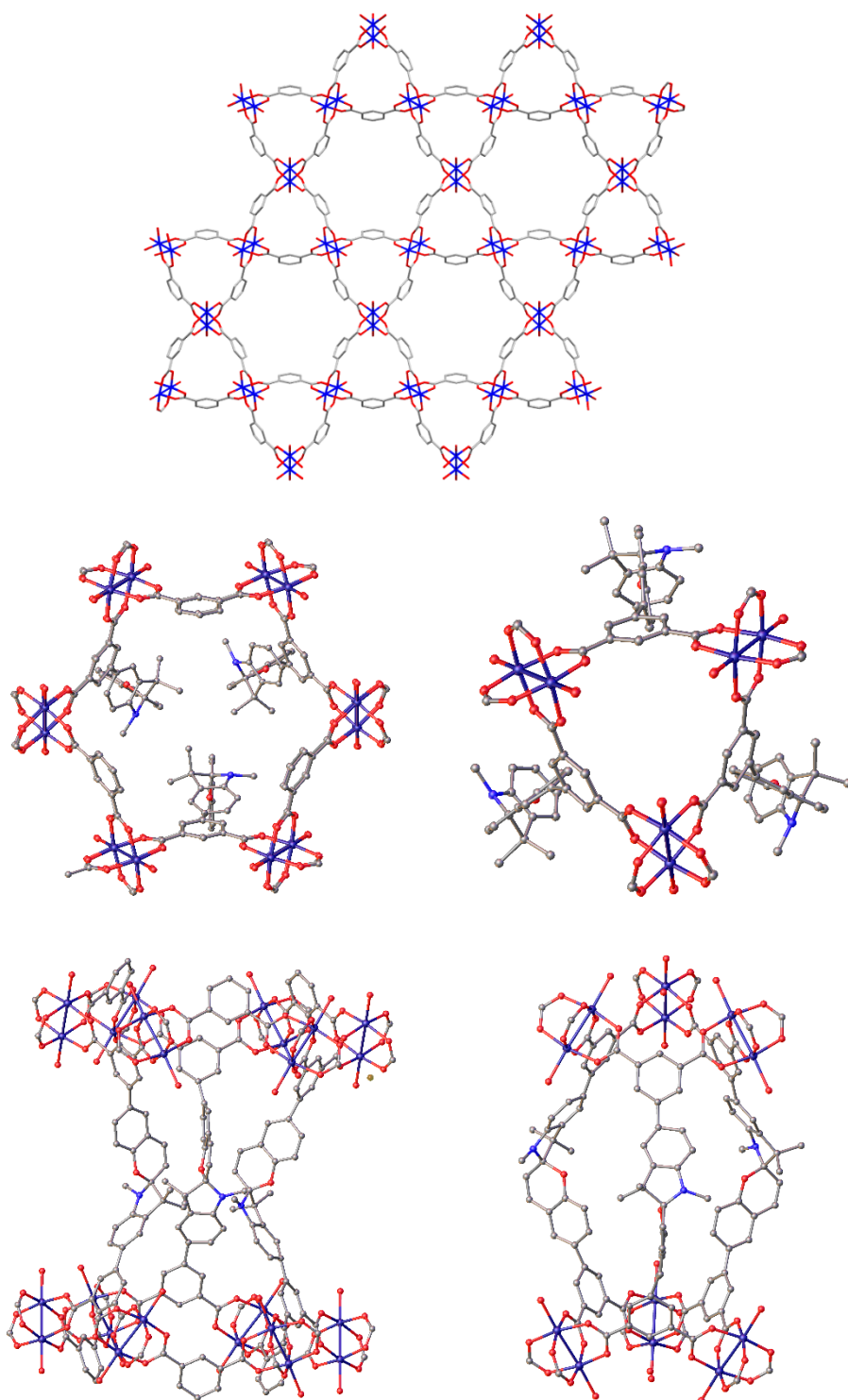


**Figure 4.22** Proposed structure of  $\text{Cu-L}^3$ . *Top*: Kagomé layers in  $ab$  plane – the disordered spirocyan core has been removed from the image for clarity. *Left (middle and bottom)*: View of hexagonal channel in which the linkers can be seen bending towards the centre. *Right (middle and bottom)*: View of triangular channel in which the linkers can be seen bending away from the centre of the pore forming a capsule. The disorder around the spirocyan cores is not shown in order to clearly display the proposed network connectivity.

Despite the structure of Cu-L<sup>3</sup> being incomplete due to the challenges of high disorder around the spiropyran core, the simulated powder pattern can be generated from the partially completed structure (Figure 4.23). When compared with the experimental powder pattern, there is very good agreement of the low-angle peaks, particularly the first peak at 4.78° 2θ. The simulated pattern of copper oxide is also shown and is not observed in the product diffraction pattern of Cu-L<sup>3</sup>. However, given that the single crystal structure is still incomplete, we cannot definitively say that the bulk powder is phase pure.

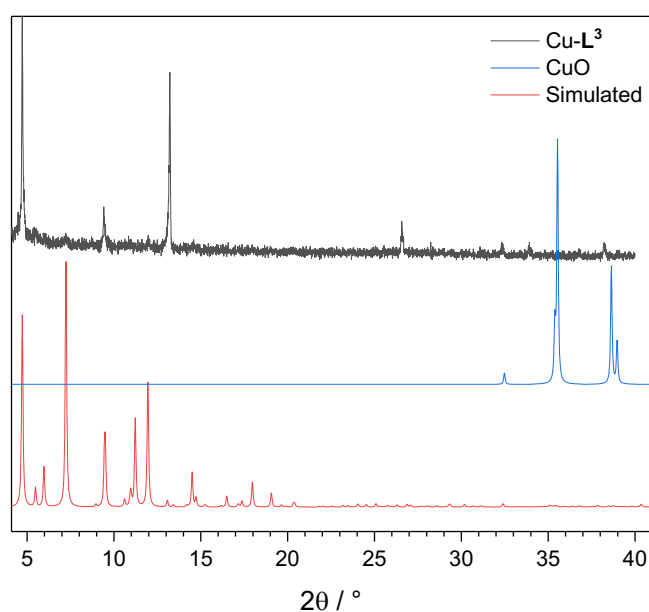


**Figure 4.23** Simulated and experimental PXRD patterns of Cu-L<sup>3</sup>; the powder pattern of copper oxide is also shown.

Interestingly, 4,4'-dipyridyl is not apparently present in the crystal structure of the final product despite it being present in the synthesis; whether the molecule acts as a modulator is unknown, but the role it and the other reaction components play in these syntheses is explored further in the next section.

#### 4.3.2.3 UV-vis absorption spectra of “MOF condition” solutions

The results described in the previous sections in this chapter have showed that formation of large MOF crystals for SCXRD is somewhat challenging. Rather than continuing the trial and error method of combinatorial synthesis, we decided to focus

our efforts on understanding what is happening during the reactions and under what conditions crystalline materials form. Specifically, we are interested in the SP/MC ratio in solution; the various ways in which the SP→MC transition can be induced were discussed earlier in this chapter. Variable temperature (VT) UV-vis absorption spectroscopy was used to investigate the state of H<sub>4</sub>L<sup>3</sup> in a range of the MOF conditions.

Due to the high concentration of H<sub>4</sub>L<sup>3</sup> used for combinatorial reactions, the concentration was diluted 10-fold for the purpose of this series of experiments. The first caveat is therefore that we assume at the lower concentration, the amount of aggregation (if any) of the molecules in solution does not change and also that the ratio of SP/MC is the same at both the higher and lower concentration. In order to minimise the reduction in concentration needed to allow measurements to be taken, a shorter pathlength quartz cell (2 mm) was also used for the measurements. The second caveat is that the metal salts have been excluded in this set of reactions to determine the changes observed due to the effect of the reaction solvents/modulators and temperature, however it is very possible that metal ions may change the SP/MC state of the linker.

There were a large number of variables, therefore a vast number of possible combinations. A small subset of twenty different reaction conditions with H<sub>4</sub>L<sup>3</sup> were prepared (Table 4.1) in order to sample a range of different variables that are listed below:

- solvent mix – DMF only, DMF/MeOH, DMF/H<sub>2</sub>O/MeOH, DMF/H<sub>2</sub>O, DMF/EtOH or DMF/H<sub>2</sub>O/EtOH
- modulators – hydrochloric, nitric, formic or acetic acid
- absence/presence of a co-linker - 4,4'-dipyridyl (abbreviated to 4,4'-DP in Table 4.1)

The samples were prepared prior to the experiments and left to equilibrate for three weeks in dark conditions. The vials were checked after 48 hours and the colour difference from immediate preparation to two days later is shown in Figure 4.24.

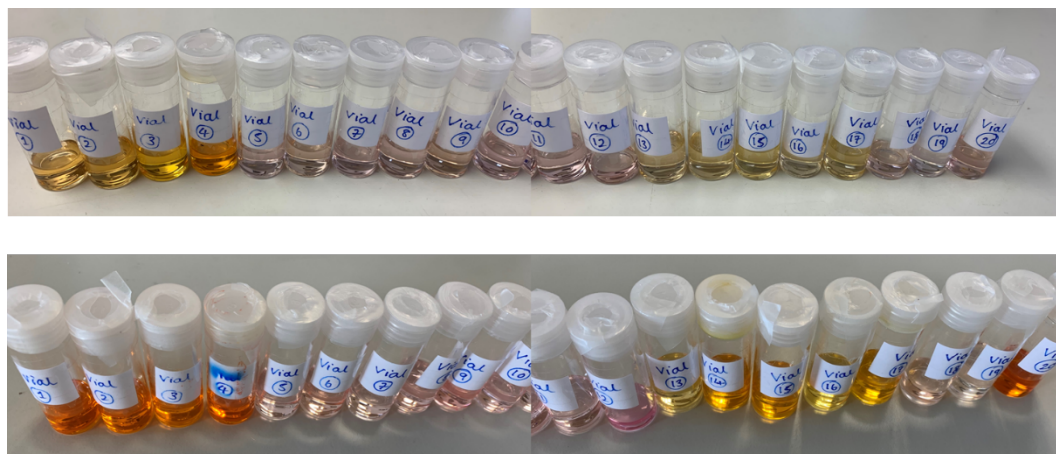


**Figure 4.24** Samples of  $H_4L^3$  spanning a wide range of “MOF reaction conditions” (see Table 4.1) in the absence of metal ions prepared for UV-vis spectroscopy, shown immediately after preparation (*top*) and after leaving to equilibrate for 48 hours (*bottom*).

The yellow-orange coloured solutions are those containing small quantities of acid; the colour change from pink to yellow has previously been observed from *ca.* pH 5 to lower pH values in solutions of spiropyrans.<sup>32</sup> On leaving in the dark, the colours intensified significantly suggesting that there is a further shift in SP-MC equilibrium; this could also be a result of less exposure to light from ambient sources due to the glass vials. After the three-week equilibration period, VT UV-visible absorption spectra were collected at 20, 45 and 65 °C; the maximum temperature was chosen due to the success of the promising crystalline materials synthesised at 65 °C described earlier in this chapter.

Vial	H <sub>4</sub> L <sup>3</sup> / mg	Co-linker	Co-linker / mg	Ratio (L: P)	Solvent mixture	Total solvent volume / mL	Modulator
1	1				DMF	2	1 M HCl (0.1 mL)
2	1				DMF	2	1 M HCl (0.25 mL)
3	1				DMF	2	1 M HCl (0.5 mL)
4	1				DMF	2	Conc. HCl (2 drops)
5	1				DMF : EtOH : H <sub>2</sub> O (1 : 0.25 : 0.05)	2.6	
6	1				DMF : EtOH : H <sub>2</sub> O (1 : 0.15 : 0.25)	2.8	
7	1				DMF	2	
8	1				DMF : EtOH : H <sub>2</sub> O (1 : 0.25 : 0.2)	2.9	
9	1				DMF : H <sub>2</sub> O (1 : 0.25)	2.5	
10	1				DMF : EtOH : H <sub>2</sub> O (1 : 0.09 : 0.075)	2.33	
11	1				DMF : EtOH (1 : 0.25)	2.5	
12	0.5	4,4'-DP	1.3	1 : 1	DMF : MeOH (1 : 1)	1	
13	0.5	4,4'-DP	1.3	1 : 1	DMF : MeOH : H <sub>2</sub> O (1 : 0.5 : 0.5)	3	
14	0.5	4,4'-DP	1.3	1 : 1	DMF : MeOH : H <sub>2</sub> O (1 : 0.5 : 0.5)	3	Conc. HCl (1 μL)
15	0.5	4,4'-DP	1.3	1 : 1	DMF : MeOH : H <sub>2</sub> O (1 : 0.5 : 0.5)	3	Conc. HNO <sub>3</sub> (1 μL)
16	0.5	4,4'-DP	1.3	1 : 1	DMF : MeOH : H <sub>2</sub> O (1 : 0.5 : 0.5)	3	Conc. acetic acid (1 μL)
17	05	4,4'-DP	1.3	1 : 1	DMF : MeOH : H <sub>2</sub> O (1 : 0.5 : 0.5)	3	Conc. formic acid (1 μL)
18	0.5	4,4'-DP	1.3	1 : 1	DMF : MeOH : H <sub>2</sub> O (1 : 0.5 : 0.5)	1	
19	0.5	4,4'-DP	1.3	1 : 1	DMF : MeOH : H <sub>2</sub> O (1 : 0.5 : 0.5)	2.5	
20	1	4,4'-DP	1.9	1 : 1.5	DMF	2.5	Conc. HCl (0.3 μL)

**Table 4.1** Quantities per vial of “MOF reaction conditions” for UV-vis absorption analysis.

The UV-vis spectra for vials 1- 20 at the three temperatures are shown in Figure 4.25 and 4.26. The SP peak at 311 nm is present in all spectra, with absorption bands also present in most spectra at *ca.* 455 and/or 573 nm associated with the MCH<sup>+</sup> and MC forms respectively. The absorption maxima at each of these wavelengths are reported in Tables 4.2 and 4.3.

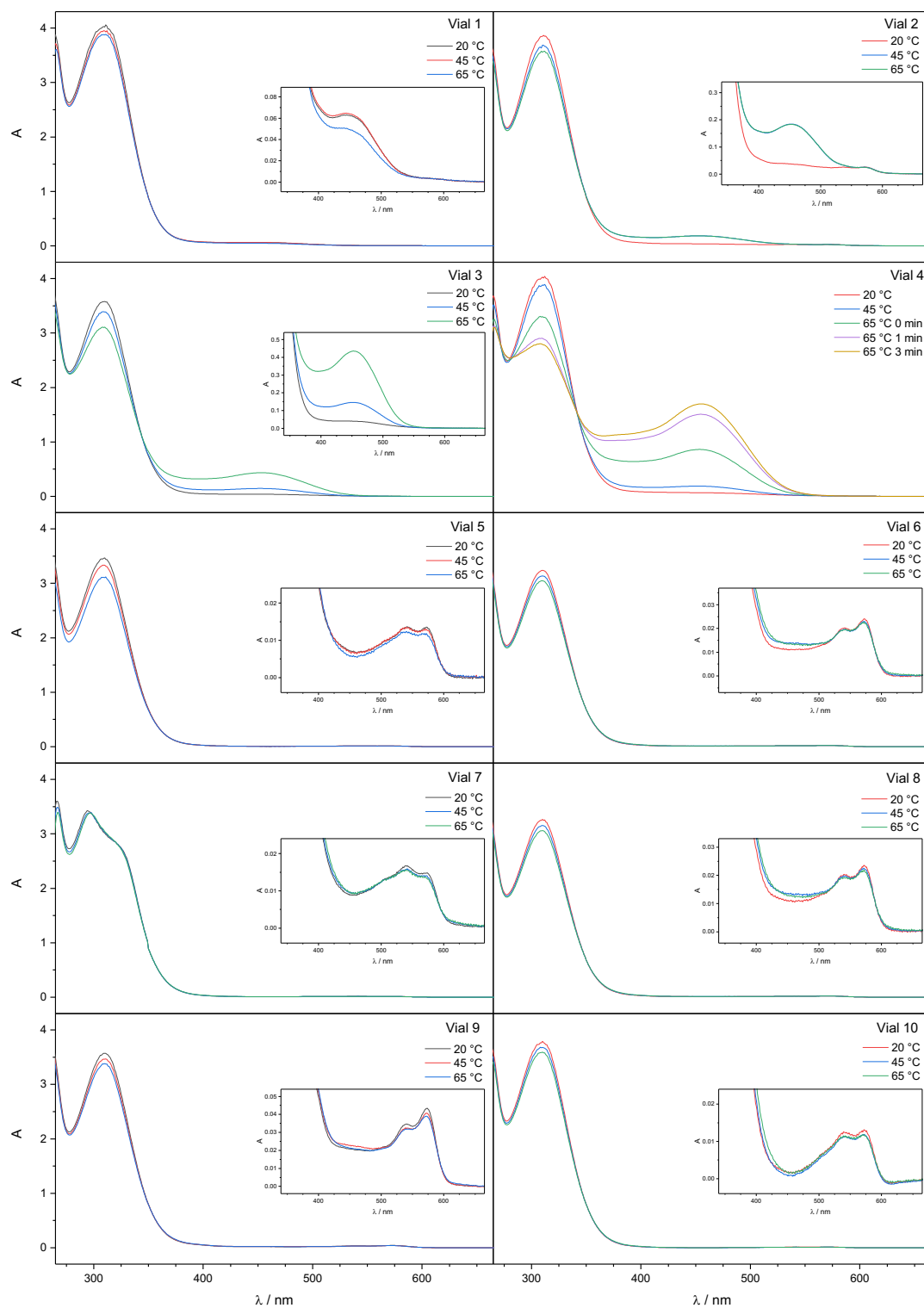


**Figure 4.25** VT UV-vis absorption spectra of vials 1 – 10; expanded region of low intensity showing weak peaks at 450 and 550 nm (*inset*).

Vial	T / °C	A (311 nm)	A (455 nm)	A (573 nm)
1	20	4.05933	0.06157	0.0039
1	45	3.92696	0.06322	0.00378
1	65	3.88384	0.04834	0.00365
-----				
2	20	3.8642	0.03661	0.02549
2	45	3.68196	0.18428	0.02519
2	65	3.57006	0.18334	0.02453
-----				
3	20	3.56848	0.03998	0.00314
3	45	3.38841	0.14539	0.00218
3	65	3.09077	0.43455	0.00374
-----				
4	20	4.01016	0.06783	0.00957
4	45	3.87287	0.18790	0.00926
4	65 (0 min)	3.2897	0.86210	0.01012
4	65 (1 min)	2.88903	1.50781	0.01221
4	65 (3 min)	2.7836	1.69791	0.01315
-----				
5	20	3.44108	0.00704	0.01356
5	45	3.31665	0.00693	0.01277
5	65	3.1193	0.00581	0.0117
-----				
6	20	3.2321	0.01115	0.0240
6	45	3.1302	0.01390	0.02278
6	65	3.04094	0.01366	0.02214
-----				
7	20	2.98933	0.00883	0.01479
7	45	3.00351	0.00943	0.01404
7	65	3.02361	0.00951	0.01339
-----				
8	20	3.24802	0.01118	0.02342
8	45	3.15006	0.01371	0.02221
8	65	3.05598	0.01290	0.02155
-----				
9	20	3.56918	0.02062	0.04331
9	45	3.46698	0.02265	0.04056
9	65	3.37391	0.02105	0.03899
-----				
10	20	3.76787	0.00180	0.01298
10	45	3.67096	0.00096	0.01184
10	65	3.57695	0.00173	0.01150

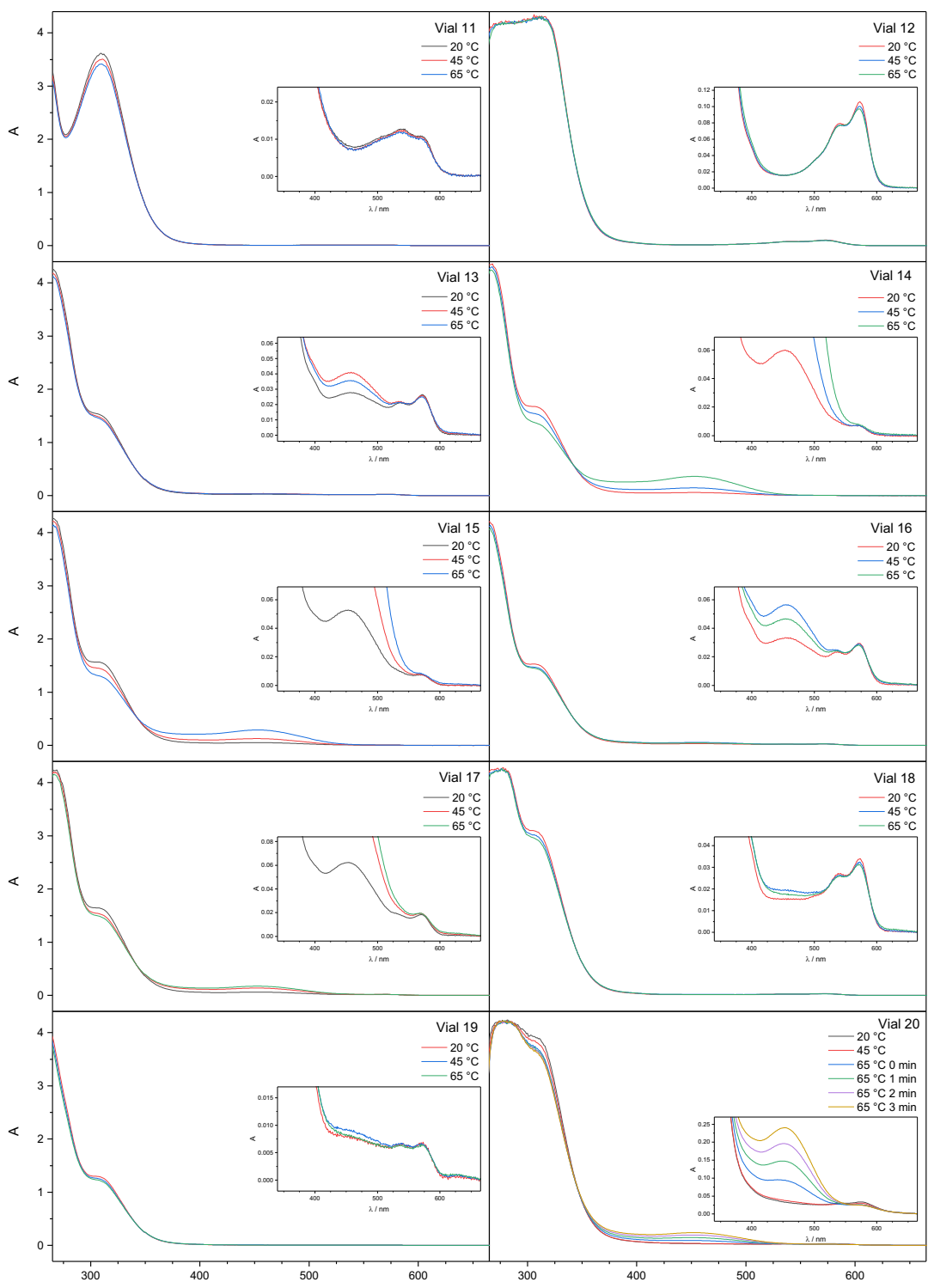
**Table 4.2** Absorbance maxima for the SP (311 nm), MCH<sup>+</sup> (455 nm) and MC (573 nm) peaks from the VT UV-vis spectra for vials 1 – 10 for H<sub>4</sub>L<sup>3</sup> under different “MOF conditions”.

Figure 4.25 and Table 4.2 show that in all solutions from vials 1 – 10 the predominant species present is the SP form at 311 nm. Vials 1 – 3 contain increasing quantities of 1 M HCl as a modulator, and the MCH<sup>+</sup> peak at 455 nm is present in all spectra at the three different temperatures. For vial 1, the MCH<sup>+</sup> peak decreases as the temperature increases which agrees with the prevailing literature observations of the MC→SP

conversion increasing with increasing heat. Vials 2 and 3 (containing greater amount of aqueous acid) show an interesting and opposing result as the peak at 450 nm is quite weak at 20 °C, but then increases in intensity upon heating the solution to 45 and 60 °C. For Vial 2 only there is also a weak peak at 570 nm at all three temperatures confirming presence of the MC form; it is possible there is not enough acid present to fully protonate all of the MC species. The spectra for Vial 3 contain the highest absorbance values for  $\lambda_{450}$  which would be expected for the largest volume of 1 M HCl in the solution.

Vial 4 contains a few drops of concentrated HCl as a modulator, with the spectra showing the largest MCH<sup>+</sup> peaks at the three temperatures. As with vials 2 and 3, the percentage of protonated merocyanine form of H<sub>4</sub>L<sup>3</sup> increases significantly from 20 °C to 65 °C as the absorbance of the SP form decreases. Three 65 °C spectra were recorded over a period of three minutes once the sample stage reached temperature; an evolution of 450 nm peak is observed. There is a clear isosbestic point at *ca.* 342 nm in which the conversion from the SP to MCH<sup>+</sup> species can be seen as the temperature increases. The linker is not behaving as expected with increasing temperature, as we would expect the equilibrium to be shifted towards the SP form at higher temperatures (in the absence of acid). This provides evidence that the effect of the acid on the spiropyran is greater than the increased temperature on effecting the SP-MC equilibrium in solution, as the MCH<sup>+</sup> form is clearly soluble in the polar solvents. The control experiment without acid present, Vial 7, shows no evidence of the MCH<sup>+</sup> species.

Vials 5 – 10 contain H<sub>4</sub>L<sup>3</sup> (with no co-linker or acid) in DMF with either H<sub>2</sub>O, EtOH or both; vial 7 contains DMF only. All absorption spectra recorded show two very weak peaks in the MC region around 550 – 570 nm. As the temperature is increased there is no significant change in that region. This shows that the polar nature of the solvents is clearly affecting the SP-MC equilibrium, potentially stabilising the presence of a small percentage of the open MC form.



**Figure 4.26** VT UV-vis absorption spectra of vials 11 – 20; expanded region of low intensity showing weak peaks at 450 and 550 nm (*inset*).

Vial	T / °C	A (311 nm)	A (455 nm)	A (573 nm)
11	20	3.58898	0.0082	0.01054
11	45	3.50817	0.00756	0.01024
11	65	3.40751	0.00759	0.00974
-----				
12	20	4.31633	0.01550	0.10603
12	45	4.28466	0.01565	0.10052
12	65	4.29041	0.01562	0.09712
-----				
13	20	1.49438	0.02776	0.02632
13	45	1.44304	0.04071	0.02591
13	65	1.41571	0.03553	0.02514
-----				
14	20	1.64837	0.05956	0.00685
14	45	1.51501	0.14627	0.00706
14	65	1.34139	0.36220	0.00764
-----				
15	20	1.54790	0.05247	0.00731
15	45	1.42790	0.12793	0.00718
15	65	1.28538	0.29031	0.00784
-----				
16	20	1.50867	0.03328	0.02945
16	45	1.44771	0.05659	0.02869
16	65	1.42345	0.04665	0.02779
-----				
17	20	1.62371	0.06232	0.01790
17	45	1.51307	0.13827	0.01873
17	65	1.46369	0.17428	0.01869
-----				
18	20	3.04581	0.01549	0.03389
18	45	2.95798	0.01936	0.03244
18	65	2.89628	0.01763	0.03106
-----				
19	20	1.27114	0.00790	0.00690
19	45	1.22977	0.00917	0.00653
19	65	1.19707	0.00825	0.00628
-----				
20	20	3.89093	0.03262	0.03354
20	45	3.77405	0.03725	0.03029
20	65 (0 min)	3.66786	0.09328	0.02620
20	65 (1 min)	3.63675	0.14671	0.02538
20	65 (2 min)	3.60886	0.19556	0.02526
20	65 (3 min)	3.56935	0.23996	0.02495

**Table 4.3** Absorbance values for the SP (310 nm), MCH<sup>+</sup> (450 nm) and MC form (550 nm) of H<sub>4</sub>L<sup>3</sup> under different “MOF conditions”.

Figure 4.26 and Table 4.3 show the absorbance spectra for vials 11 – 20. Vial 11 has two very weak peaks in the MC region around 550 – 570 nm, in addition to the predominant SP peak at 311 nm. As with vials 5 – 10, there is no significant change to the MC peak with increasing temperature.

Vial 12 contains  $H_4L^3$  and 4,4'-dipyridyl as a co-linker in a solvent mix of DMF/MeOH. The solution is very concentrated, hence the saturation in the SP region, but two very distinct peaks are observed in the MC region around 550 – 570 nm. Like with vials 5 – 11, the presence of a polar solvent such as EtOH or MeOH are altering the SP-MC equilibrium by potentially stabilising the presence of a small proportion of the open MC form in the solution, with little conversion back to the closed SP form upon heating to 65 °C.

Vials 13, 18 and 19 contain  $H_4L^3$  and 4,4'-dipyridyl as a co-linker in a solvent mix of DMF/MeOH/H<sub>2</sub>O. The total solvent volume differs resulting in a change of concentration of the spiropyran in solution. Vial 13 is the most concentrated of the three samples and the spectra show that the SP peak at 310 nm has drastically decreased (compared with vials 1 – 12), whilst peaks in the  $MCH^+$  and MC region are observed. As the temperature is increased there is little change in the SP and MC region, however the  $MCH^+$  peak (455 nm) increases in intensity as the temperature is increased above 20 °C. The evolution of this peak associated with the protonated species was observed above in vials 1 – 4 when acid was present. Vials 18 and 19 contain a more dilute solution of  $H_4L^3$  and 4,4'-dipyridyl in DMF/MeOH/H<sub>2</sub>O and, as with vial 13, the absorbance of the SP peak is lower than vials 1 - 12. Two weak peaks are observed in the MC region for both solutions, but also a very broad peak in the  $MCH^+$  region (this also has a small evolution as the temperature is increased). Methanol can be considered more acidic than ethanol,<sup>33</sup> therefore this could explain the appearance of the  $MCH^+$  peak in vials 13, 18 and 19 compared with vials 5 – 11.

Vials 14 – 17 contain  $H_4L^3$  and 4,4'-dipyridyl in DMF/MeOH/H<sub>2</sub>O with only a small amount of various concentrated acidic modulators. In the four spectra, the SP peak absorbance maxima is lower compared to vials 1 – 4. As the temperature increases, there is a slight decrease in the 310 nm peak. For all the four solutions there is an absorbance at 450 nm due to the presence of the  $MCH^+$  form, which is now expected when acid is present. There is also a small peak/s associated with the MC form present in all the spectra at *ca.* 573 nm. As the temperature is increased from 20 to 65 °C, the 450 nm peak increases in intensity for each solution which corresponds with the observations of the  $MCH^+$  peak described earlier. It can also be noted that the  $MCH^+$  peak intensities decrease for vials 14 > 15 > 17 > 16 corresponding to the increase of

the pKa of the acid modulator present in the solution (hydrochloric,  $\sim -7 < \text{nitric} \sim -3 < \text{formic}, \sim 3.75 < \text{acetic}, \sim 4.75$ ); this suggests that stronger acids can protonate the open form MC more easily. Vial 14 and 15 contain the two strongest acids, HCl and HNO<sub>3</sub> respectively, and in both sets of spectra the ratio of MCH<sup>+</sup> to MC is greater. Vial 17 also contains more MCH<sup>+</sup> (but at a lower intensity than vials 14 and 15), again with only a small proportion of MC present. Vial 16 contains the weakest acid (acetic) and the absorbance peaks of the MCH<sup>+</sup> and MC are of very similar intensity compared to the other solutions.

Finally, vial 20 contains H<sub>4</sub>L<sup>3</sup> and 4,4'-dipyridyl in DMF only, along with the lowest volume of concentrated HCl (compared with vials 4 and 14). The SP peak is saturated, however clear peaks can be seen at *ca.* 455 nm due to the MCH<sup>+</sup> form, and also weak peaks due to the MC form, at all three temperatures. Again, there is clear evolution of the MCH<sup>+</sup> peak as it increases in intensity as the temperature increases to 65 °C; the absorbance increases when the temperature is held at 65 °C for 3 minutes. Simultaneously, the MC peak decreases as more of the MCH<sup>+</sup> species forms upon heating, confirming that acid is the dominant culprit for the formation of MCH<sup>+</sup> in solution. As with vial 4, there is an isosbestic point at *ca.* 342 nm, whereby the intensity decrease of the SP form corresponds to the MCH<sup>+</sup> species increasing in intensity.

Interestingly the pKa of a pyridinium cation is *ca.* 5.25,<sup>34,35</sup> suggesting that the 4,4'-dipyridyl co-linker is protonated under the MOF reaction conditions when acid is present as modulator. Protonation could be occurring before the spiropyran opens to the MC form meaning that the co-linker does not take part in binding to the metal centres; this could be a possible explanation as to why the co-linker is not present in the final structure of Cu-L<sup>3</sup> described earlier (Section 4.3.2.2).

Two conclusions can be made from the results observed in this section. In the absence of acid, the SP form of H<sub>4</sub>L<sup>3</sup> is favoured in solution with only a small peak associated with the open MC form present. The temperature has little effect in *this range* as no change in the peak ratios were observed upon heating to 65 °C. However, in the presence of acid (*with* or *without* a co-linker present in solution), the equilibrium moves towards formation of the MCH<sup>+</sup> species as temperature increases to 65 °C. At

20 °C, the predominant species is still the closed SP form, although some MC peaks are observed.

To conclude this section, the absorbance maxima of the three peaks observed in the UV-vis spectra at 65 °C for vials 1 – 20 (Table 4.2 and 4.3) were used to calculate the ratios of the absorbances of peaks assigned to SP (311 nm), MC (573 nm) and MCH<sup>+</sup> (455 nm) species. These absorbance ratios, SP/MC, MCH<sup>+</sup>/MC and SP/MCH<sup>+</sup>, are not direct measures of concentration ratios of any two species as their extinction coefficients differ, but they do inform on the changes in relative concentration. The highest temperature (65 °C) data were used in each case as they were most representative of the solutions in the combinatorial reactions. The ratios have been plotted against the product outcomes (detailed in the Appendix, Table A.10) that were observed for each vial in the combinatorial syntheses. From the many combinatorial reactions carried out as part of this thesis, four qualitatively different outcomes have been noted. We can assign a number to each of these outcomes in order to construct the plot: 1 = no solid formed, 2 = amorphous product only, 3 = mixture of amorphous/crystalline and 4 = crystalline product only. The plot provides an indication of how the metal ions are affecting the position of equilibrium between the three forms of H<sub>4</sub>L<sup>3</sup> in solution. This cannot be done experimentally; as soon as metal ions are introduced to the solutions the SP-MC equilibrium may already have shifted before spectra can be recorded.

Figure 4.27 shows the ratio of the SP/MC peaks at 65 °C; the vials have also been categorised based on the presence (triangles) or absence (circles) of co-linker in the solutions. The data points are coloured based on the outcome with a particular metal salt; the counterions on the metal salt have not been accounted for.

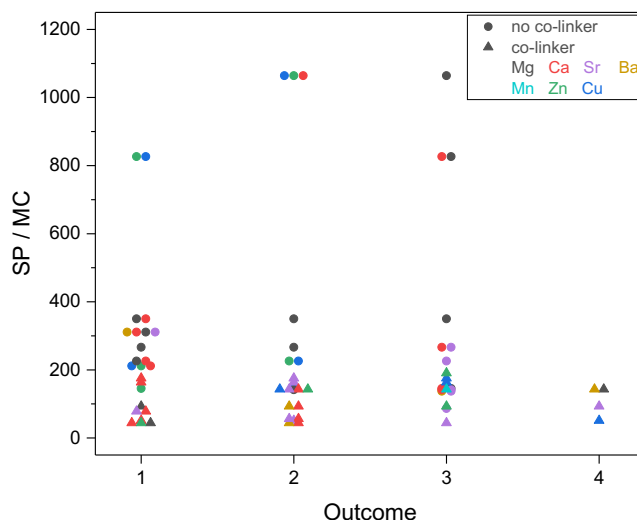


**Figure 4.27** Plot of SP/MC ratio against the observed outcome in the combinatorial reactions using the conditions from vials 1 – 20.

There are two very distinct regions observed in the plot: i) predominantly SP form in the solution with very little MC form (Vials 1 – 12) or ii) a decrease in the SP form (Vials 13 – 20), which coincides with the presence of co-linker. There is a large range of outcomes when looking at the metal salts used. It can be noted that from the range of conditions sampled in vials 1 – 20, reactions with strontium seem to produce crystalline material more easily than magnesium and calcium for example.

The SP/MCH<sup>+</sup> ratio is shown in Figure 4.28, where again two very distinct regions are observed. Given the previous results in this section, it is unsurprising that the SP peak decreases when there is more of the MCH<sup>+</sup> form present. In the majority of reactions sampled, as the MCH<sup>+</sup> form either there is no solid product or amorphous material is formed. There is also more MCH<sup>+</sup> when the co-linker is present in the reaction solutions, further suggesting that the 4,4'-dipyridyl is having an impact on the reaction outcome, particularly as it can be seen that crystalline product is only being formed in the cases where the co-linker is present. Indeed, this particular outcome also indicates that the co-linker cannot only be acting as a simple base and reducing the proton concentration since that would *reduce* the relative presence of MCH<sup>+</sup>. To better understand the role of the co-linker, control experiments should be performed in future using a simpler monodentate analogue of 4,4'-dipyridyl (*e.g.* pyridine) that cannot act as a bridging linker.

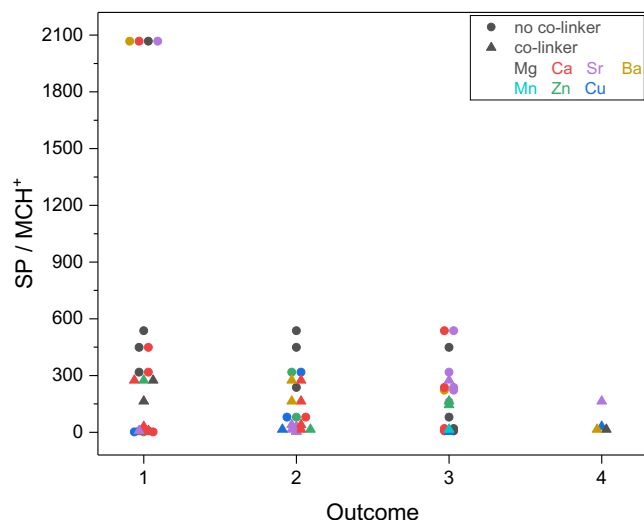


**Figure 4.28** Plot of  $SP/MCH^+$  ratio against the observed outcome in the combinatorial reactions using the conditions from vials 1 – 20.

Finally, Figure 4.29 shows the  $MCH^+/MC$  ratio against the observed outcomes. The plot again confirms that the co-linker is influencing the  $SP-MCH^+-MC$  equilibrium, in which more of the  $MCH^+$  form is present. The spread of outcomes across the different metal ions indicates that it is difficult to predict the equilibrium of  $H_4L^3$  in solution under the range of conditions.

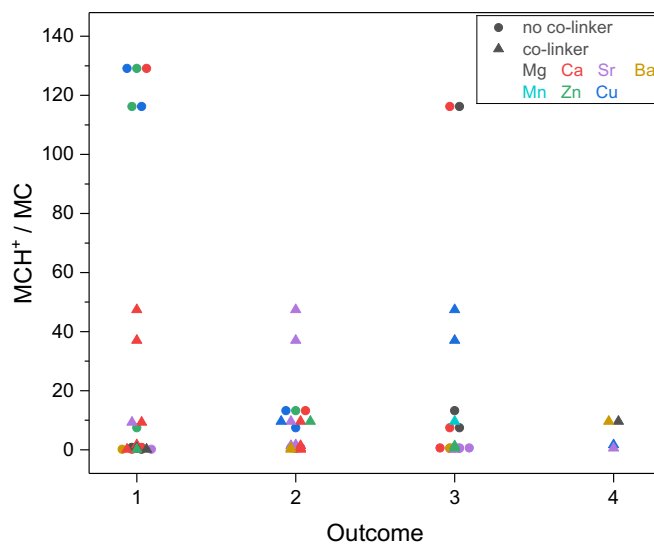


**Figure 4.29** Plot of  $MCH^+/MC$  ratio against the observed outcome in the combinatorial reactions using the conditions from vials 1 – 20.

The results obtained from the VT UV-vis experiments show that the temperature, in the range studied, does not have as much of an effect on the  $SP-MC-MCH^+$

equilibrium as previously expected. Notably, in the presence of acid (and/or possibly a co-linker) an increase in temperature favours the protonated  $\text{MCH}^+$  form. This suggests that in order to avoid the  $\text{MCH}^+$  form, MOF reactions should be carried out at low temperatures for a longer time period. Further VT UV-vis measurements will need to be performed in future to determine if higher temperatures (ideally  $>60\text{ }^\circ\text{C}$ ) have a greater effect on the  $\text{SP/MCH}^+/\text{MC}$  equilibrium.

#### 4.4 Conclusions

The final section of this thesis has focussed on the attempts to synthesise photoactive metal-organic frameworks using large flexible photoactive linkers. Spiropyran-based linkers,  $\text{H}_2\text{L}^2$  and  $\text{H}_4\text{L}^3$ , were synthesised using previously reported synthetic procedures developed by Dr Chong, a previous student supervised by Dr Timothy Easun. The  $\text{SP-MC-MCH}^+$  equilibria of the two molecules were investigated by UV-visible absorption spectroscopy; the dissolution of  $\text{H}_2\text{L}^2$  in a polar solvent, the pH effects on a solution of  $\text{H}_4\text{L}^3$  and the irradiation of both  $\text{H}_2\text{L}^2$  and  $\text{H}_4\text{L}^3$  with UV light were all monitored. In all experiments, small absorption peaks of either the open merocyanine or the protonated merocyanine form were observed, clearly showing the nature of the solution affects the state of the linker.

Both  $\text{H}_2\text{L}^2$  and  $\text{H}_4\text{L}^3$  were used in combinatorial reactions covering a range of conditions in attempts to synthesise crystalline materials for full structural analysis. Due to the small scale of the reactions, any solid formed was produced in only small quantities. PXRD was initially used to assess the crystallinity of each material. Unfortunately, many reactions were unsuccessful, yielding either amorphous material or no solid at all. A co-linker (4,4'-dipyridyl) was introduced to the combinatorial syntheses with the aim of improving the crystallinity of any materials formed. Seven promising materials were obtained ( $\text{Zn-L}^2$ ,  $\text{Mg-L}^3$ ,  $\text{Ca-L}^3$ ,  $\text{Sr-L}^3$ ,  $\text{Ba-L}^3$ ,  $\text{Zn-L}^3$  and  $\text{Cu-L}^3$ ) with the PXRD patterns showing low angle Bragg peaks indicative of spiropyran incorporation into a framework. Unlike the results in Chapter 3 of this thesis, when these highly flexible molecules are used as linkers in the MOF synthesis the PXRD results are very different.

Cu-L<sup>3</sup> was the only product that yielded single crystals suitable for single crystal XRD analysis. The spiropyran linker appears to have been incorporated into a 3D framework in which the copper paddlewheels are bridged in 2D layers by the isophthalate groups of H<sub>4</sub>L<sup>3</sup>, resulting in a Kagomé lattice motif. The framework shows sufficient stability upon exposure to air for SCXRD and PXRD analysis to be performed without crystal degradation. Due to the small amount of crystals yielded in the reaction, further characterisation has yet to be performed.

The work in this final chapter has shown that it can be very difficult to predict the synthetic outcomes when working with such flexible and stimuli responsive linkers. In order to better understand the conformational changes that occur in solution under MOF reaction conditions, twenty different solutions of H<sub>4</sub>L<sup>3</sup> were prepared and left in the dark to equilibrate for three weeks. Variable temperature UV-visible absorption spectra were recorded, with room temperature data showing that the SP form is predominant in all cases, with a small ratio of the MCH<sup>+</sup> and MC states of the linker present. Increasing temperature did not strongly influence the equilibrium in the absence of acid, however when the solutions are acidified, higher temperatures favour the MCH<sup>+</sup> form in both the absence and presence of a co-linker. Purely crystalline product was only formed in the presence of the co-linker, and interestingly when the ratio of SP/MC form was lower rather than higher (*i.e.* some MC form was clearly present).

To conclude, the work described in this thesis has shown that structural control in metal-organic frameworks is a very challenging area. It is difficult to predict the linker- or metal-directing effects in a series of materials, particularly when highly flexible linkers are used. Further research will be required to optimise the reaction conditions of the seven promising spiropyran-based crystalline materials described in this final chapter, to gain full structural characterisation before exploring the photoswitching effects of light on the structures. The use of the CLASSIC NMR technique in Chapter 2 will be extremely beneficial to overcoming these synthetic challenges in the future production of new photoresponsive MOFs.

## 4.5 Experimental

All chemicals were of reagent-grade quality and used as received. Tri-*tert*-butylphosphine, potassium trimethylsilanolate, *N*-bromosuccinimide and 1,3,3-trimethyl-2-methyleneindoline were purchased from Sigma Aldrich. 5-bromosalicylaldehyde was purchased from Acros Organics and tris(dibenzylideneacetone)dipalladium(0) from Fluorochem. Potassium carbonate and metal salts were bought from Alfa Aesar and commercial solvents from Fisher Scientific.

<sup>1</sup>H and <sup>13</sup>C nuclear magnetic resonance (NMR) spectra were recorded on either a Bruker 300 Fourier, Bruker 400 UltraShield™ or a Bruker 500 MHz Avance NMR spectrometer. The obtained chemical shifts ( $\delta$ ) are reported in ppm and are referenced to the residual solvent signal. Spin-spin coupling constants ( $J$ ) are given in Hz. A SHIMADZU IRAffinit-1S spectrometer was used to collect IR data, scanning between 500 – 4000 cm<sup>-1</sup> and averaging 16 scans. Mass spectra were obtained by Analytical Services using a Xevo G2-XS QToF Quadrupole Time-of-Flight Mass Spectrometer.

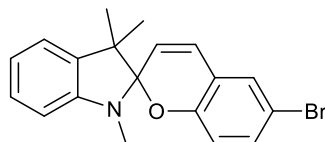
UV-Vis studies of the “MOF conditions” were performed on an Agilent Cary 5000 UV-Vis spectrophotometer (with VT stage) using quartz cells with path length of 0.2 cm. All other UV-vis spectra were acquired using an Optics USB2000+UV-VIS-ES spectrometer using a DT-MINI-2-GS light source; solution state UV-vis spectra were obtained in a quartz cuvette (path length 1.0 cm) placed in a CUV 1 cm cuvette holder with P200-2 transmission fibre optic and recorded in absorbance ( $A$ ) mode.

PXRD patterns of all synthesised materials were obtained using a PANalytical X'Pert PRO Chiller 59 using a Ni-filtered CuK $\alpha$  radiation source ( $\lambda = 1.5419 \text{ \AA}$ ) scanning a range of  $2\theta = 4^\circ - 50^\circ$ . Samples were loaded onto zero-background silicon wafers directly from the reaction solution.

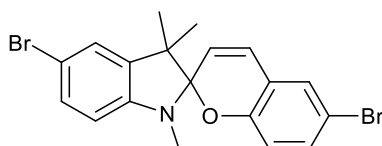
Data collection for Cu-L<sup>3</sup> was performed at the National Crystallography Service, University of Southampton. X-ray diffraction data was obtained using a Rigaku 007HF equipped with Varimax confocal mirrors and an AFC11 goniometer and HyPix 6000 detector (CuK $\alpha$ ,  $\lambda = 1.5419 \text{ nm}$ ). Further information in Section 4.5.2.3.

#### 4.5.1 Synthesis of spiropyran-based linkers

The syntheses in this section were *previously described* in Dr Magdalene Chong's thesis.<sup>5</sup> The synthetic protocols described herein are specifically as performed by the thesis author and contain minor variations in quantities, durations and workup.

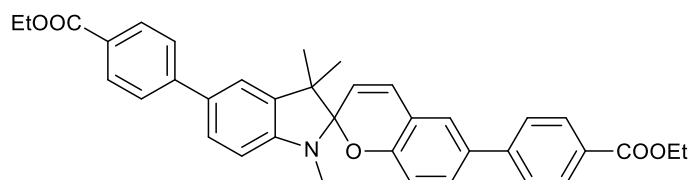


**6-Bromo-1',3',3'-trimethylspiro[chromene-2,2'-indoline] (3).** 1,3,3-trimethyl-2-methyleneindoline (7.5 ml, 0.042 mol) was added to ethanol (125 ml). The addition of 5-bromosalicylaldehyde (8.5 g, 0.042 mol) gave a deep purple solution, which was heated to reflux for approximately 60 hours. The solution was then cooled and left in an ice bath at 0°C, before being left in a freezer over the weekend. Solid precipitate was present in solution, which was filtered and washed with cold ethanol (350 ml) to afford **3** as a pale pink solid. Yield: 10.42 g (69 %). <sup>1</sup>H NMR (300 MHz, CDCl<sub>3</sub>): δ<sub>H</sub> = 1.18 (s, 3H), 1.31 (s, 3H), 2.74 (s, 3H), 5.75 (d, 1H, *J* = 10.2 Hz), 6.55 (d, 1H, *J* = 7.8 Hz), 6.62 (d, 1H, *J* = 9.3 Hz), 6.81 (d, 1H, *J* = 10.5 Hz), 6.87 (t, 1H, *J* = 7.4 Hz), 7.09 (d, 1H, *J* = 7.2 Hz), 7.16 – 7.22 (m, 3H).

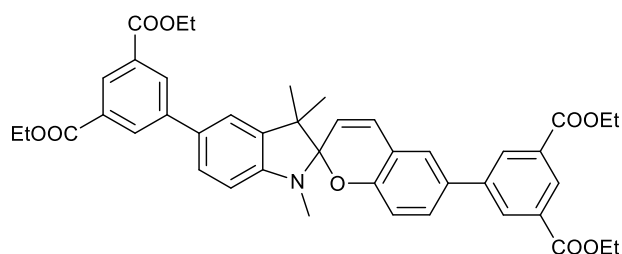


**5,6-Dibromo-1',3',3'-trimethylspiro[chromene-2,2'-indoline] (4).** A solution of **3** (10.4 g, 29.19 mmol) in chloroform (80 ml) was heated to reflux to give a dark brown solution. *N*-bromosuccinimide (5.20 g, 29.19 mmol) was dissolved in chloroform (300 ml) and added dropwise to the solution slowly over an hour giving a darker solution, which was then heated at reflux for a further 30 minutes. Upon cooling, a bright orange solid crashed out in the solution, which was filtered and washed with chloroform. The organic filtrate was washed with water (2 x 300 ml), dried over anhydrous magnesium sulphate and the solvent was removed under vacuum to give an oily solid. Recrystallisation from ethanol gave **4** as a pale-yellow solid. Yield: 9.50 g (75 %). <sup>1</sup>H NMR (300 MHz, CDCl<sub>3</sub>): δ<sub>H</sub> = 1.13 (s, 3H), 1.24 (s, 3H),

2.66 (s, 3H), 5.67 (d, 1H,  $J = 10.5$  Hz), 6.37 (d, 1H,  $J = 8.1$  Hz), 6.57 (d, 1H,  $J = 9.3$  Hz), 6.77 (d, 1H,  $J = 10.2$  Hz), 7.07 – 7.28 (m, 4H). **LRMS (ES<sup>+</sup>):**  $m/z = 436.01$  [M+H]<sup>+</sup>. **IR:**  $\nu_{max} / \text{cm}^{-1} = 1597, 1475, 1359, 1255, 1176, 1097, 1017, 948, 924, 876, 833, 820, 806, 770, 714, 679, 646, 586$ .

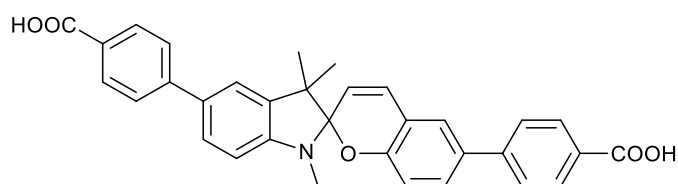


**Diethyl 4,4'-(1',3',3'-trimethylspiro[chromene-2,2'-indoline]-5',6-diyl)-dibenzoate (5).** A peach suspension of **4** (1 g, 2.3 mmol), (4-(ethoxycarbonyl)phenyl) boronic acid (1.07 g, 5.5 mmol) and potassium carbonate (1.53 g, 11.0 mmol) in toluene (100 ml) and water (25 ml) was heated to 60 °C and degassed with N<sub>2</sub> for 15 minutes. Tri-*tert*-butylphosphine (1.1 ml, 4.4 mmol, commercial 1 M solution in toluene) was added, followed by tris(dibenzylideneacetone)dipalladium(0) (0.41 g, 0.4 mmol) giving a dark mixture. The reaction was heated to 80 °C overnight. The yellow/brown mixture was filtered, and the resulting solid was further washed with DCM. The filtrate was added to water (*ca.* 150 mL) and extracted with DCM. The organic phase was dried over anhydrous magnesium sulphate, filtered and evaporated *in vacuo* to give a brown oil. Recrystallisation from dichloromethane and methanol produced **5** as pale-yellow solid. Yield: 0.99 g (75 %). **<sup>1</sup>H NMR** (500 MHz, CDCl<sub>3</sub>):  $\delta_{\text{H}} = 1.24$  (s, 3H), 1.45 – 1.36 (m, 9H), 2.81 (s, 3H), 4.40 (q, 4H,  $J = 7.1$  Hz), 5.77 (d, 1H,  $J = 10.2$  Hz), 6.62 (d, 1H,  $J = 7.8$  Hz), 6.83 (d, 1H,  $J = 8.7$  Hz), 6.96 (d, 1H,  $J = 10.4$  Hz), 7.37 (dd, 3H,  $J = 22.0, 9.4$  Hz), 7.49 (d, 1H,  $J = 8.1$  Hz), 7.60 (d, 2H,  $J = 8.1$  Hz), 7.65 (d, 2H,  $J = 7.9$  Hz), 8.08 (d, 4H,  $J = 8.0$  Hz).

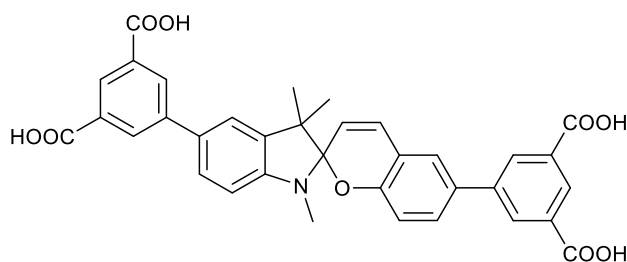


**Tetraethyl-5,5'-(1',3',3'-trimethylspiro[chromene-2,2'-indoline]-5',6-diyl) diisophthalate (6).** A peach suspension of **4** (1 g, 2.3 mmol), 3,5-bis(ethoxycarbonyl)phenyl boronic acid (1.47 g, 5.5 mmol) and potassium

carbonate (1.53 g, 11.0 mmol) in toluene (100 ml) and water (25 ml) was heated to 60 °C and degassed with N<sub>2</sub> for 15 minutes. Tri-*tert*-butylphosphine (1.1 ml, 4.4 mmol, commercial 1 M solution in toluene) was added, followed by tris(dibenzylideneacetone)dipalladium(0) (0.41 g, 0.4 mmol) giving a dark mixture. The reaction was heated to 80 °C overnight. The yellow/brown mixture was filtered, and the resulting solid was further washed with DCM. The filtrate was added to water (*ca.* 150 mL) and extracted with DCM. The organic phase was dried over anhydrous magnesium sulphate, filtered and evaporated *in vacuo* to give a brown oil. Recrystallisation from dichloromethane and methanol produced **6** as a pale-yellow solid. Yield: 1.22 g (74 %). <sup>1</sup>H NMR (400 MHz, CDCl<sub>3</sub>): δ<sub>H</sub> = 1.24 (s, 3H), 1.39 - 1.45 (m, 15 H), 2.80 (s, 3H), 4.38 – 4.46 (m, 8H), 5.77 (d, 1H, *J* = 10.4 Hz), 6.62 (d, 1H, *J* = 8 Hz), 6.83 (d, 1H, *J* = 8.4 Hz), 6.96 (d, 1H, *J* = 10.4 Hz), 7.39 – 7.42 (m, 3H), 7.50 (dd, 1H, *J* = 8.2, 1.8 Hz), 8.38 (d, 2H, *J* = 1.6 Hz), 8.43 (d, 2H, *J* = 1.6 Hz), 8.54 – 8.59 (m, 2H). HRMS (ES<sup>+</sup>): *m/z* = 718.3024 [M+H]<sup>+</sup>. IR: ν<sub>max</sub>/cm<sup>-1</sup> = 1717, 1497, 1369, 1333, 1234, 1105, 1076, 1049, 1028, 1015, 962, 812, 750, 723, 685, 669, 613.



**4,4'-(1',3',3'-Trimethylspiro[chromene-2,2'-indoline]-5',6-diyl)dibenzoic acid (H<sub>2</sub>L<sup>2</sup>).** Potassium trimethylsilanolate (0.33 g, 2.6 mmol) and **5** (0.05 g, 0.9 mmol) were added to anhydrous tetrahydrofuran (15 ml) and the yellow solution stirred at room temperature overnight and monitored by TLC. The mixture was evaporated to dryness to give a pale-yellow solid. Upon addition of water (15 ml), the dark purple solution was acidified to pH 3 using hydrochloric acid (1 M). The red precipitate was filtered, washed with water and left to dry in air. Yield: 0.03 g (66 %). <sup>1</sup>H NMR (400 MHz, (CD<sub>3</sub>)<sub>2</sub>SO): δ<sub>H</sub> = 1.18 (s, 3H), 1.32 (s, 3H), 2.74 (s, 3H), 5.88 (d, 1H, *J* = 10.2 Hz), 6.71 (d, 1H, *J* = 8.6 Hz), 6.82 (d, 1H, *J* = 8.6 Hz), 7.15 (d, 1H, *J* = 10.3 Hz), 7.56 – 7.46 (m, 3H), 7.64 (s, 1H), 7.78 – 7.71 (m, 4H), 7.97 (dd, 4H, *J* = 8.3, 1.9 Hz). HRMS (ES<sup>+</sup>): *m/z* = 518.1970 [M+H]<sup>+</sup>. UV-Vis: λ<sub>max</sub> (EtOH) / nm = 243 (ε / dm<sup>3</sup> mol<sup>-1</sup> cm<sup>-1</sup> 22500), 261 (27590), 315 (36245).



**Tetraethyl-5,5'-(1',3',3'-trimethylspiro[chromene-2,2'-indoline]-5',6-diyl) diisophthalic acid ( $H_4L^3$ ).** Potassium trimethylsilanolate (0.42 g, 3.3 mmol) and **6** (0.4 g, 0.6 mmol) were added to anhydrous tetrahydrofuran (30 ml) and the orange solution stirred at room temperature overnight and monitored by TLC. The mixture was evaporated to dryness to give a pale-yellow solid. Upon addition of water (20 ml), the dark purple solution was acidified to pH 3 using hydrochloric acid (1 M). The resulting red solid was filtered, washed with water and left to dry in air. Yield: 0.26 g (77 %).  **$^1H$  NMR** (400 MHz,  $(CD_3)_2SO$ ):  $\delta_H$  = 1.20 (s, 3H), 1.35 (s, 3H), 2.76 (s, 3H), 5.89 (d, 1H,  $J$  = 10 Hz), 6.74 (d, 1H,  $J$  = 8.8 Hz), 6.84 (d, 1H,  $J$  = 8.4 Hz), 7.22 (d, 1H,  $J$  = 10.4 Hz), 7.50 – 7.56 (m, 3H), 7.69 (d, 1H,  $J$  = 2.4 Hz), 8.34 – 8.39 (m, 5H), 8.40 (t, 1H,  $J$  = 1.6 Hz). **HRMS ( $ES^+$ ):**  $m/z$  = 606.1762  $[M+H]^+$ . **IR:**  $\nu_{max}$  /  $cm^{-1}$  = 1709, 1591, 1535, 1371, 1306, 1233, 1105, 1069, 1022, 999, 959, 812, 756, 714, 669, 642. **UV-Vis:**  $\lambda_{max}$  (EtOH) / nm = 241 ( $\epsilon$  /  $dm^3 mol^{-1} cm^{-1}$  30000), 253sh (27000), 301 (22000).

#### 4.5.2 Synthesis of spiropyran-based MOFs

The reactions described in the next two sections are the most successful novel combinatorial synthesis yielding crystalline products and were performed by the thesis author. Due to the scale of the reactions there was only a small quantity of solid product formed allowing to PXRD or SCXRD characterisation only; other characterisation data such as IR or CHN was unable to be obtained.

##### 4.5.2.1 Crystalline products with $H_2L^2$

**Zn- $L^2$ .** Zinc acetate dihydrate (8.5 mg, 39  $\mu$ L),  $H_2L^2$  (5 mg, 9.7  $\mu$ L) and 4,4'-dipyridyl (1.5 mg, 9.7  $\mu$ mol) were dissolved in DMF/MeOH (1:1 v/v, 1 mL) and sealed in a

Wheaton vial. The reaction solution was heated to 65 °C for 4 days yielding pale pink crystallites in a clear solution.

#### 4.5.2.2 Crystalline products with H<sub>4</sub>L<sup>3</sup>

**Mg-L<sup>3</sup>.** Magnesium nitrate hexahydrate (17 mg, 66 μmol) and H<sub>4</sub>L<sup>3</sup> (5 mg, 8.3 μmol) and 4,4'-dipyridyl (1.9 mg, 12.5 μmol) were dissolved in DMF (2.5 mL), with the addition of conc. HCl (0.3 μL) and sealed in a Wheaton vial. The reaction solution was heated to 80 °C for 8 days, forming small crystallites in a deep red solution.

**Ca-L<sup>3</sup>.** Calcium acetate hydrate (6 mg, 33 μmol) and H<sub>4</sub>L<sup>3</sup> (5 mg, 8.3 μmol) and 4,4'-dipyridyl (1.3 mg, 8.3 μmol) were dissolved in DMF/methanol/water (2:1:1 v/v/v, 0.5 mL) and sealed in a Wheaton vial. The reaction solution was heated to 65 °C for 3 days. Small pale crystallites were formed from the yellow/orange solution.

**Sr-L<sup>3</sup>.** Strontium nitrate (7 mg, 33 μmol) and H<sub>4</sub>L<sup>3</sup> (5 mg, 8.3 μmol) and 4,4'-dipyridyl (1.3 mg, 8.3 μmol) were dissolved in DMF/methanol/water (2:1:1 v/v/v, 0.5 mL) and sealed in a Wheaton vial. The reaction solution was heated to 65 °C for 3 days yielding small purple crystallites from the red solution.

**Ba-L<sup>3</sup>.** Barium nitrate (17 mg, 66 μmol) and H<sub>4</sub>L<sup>3</sup> (5 mg, 8.3 μmol) and 4,4'-dipyridyl (1.9 mg, 12.5 μmol) were dissolved in DMF (2.5 mL), with the addition of conc. HCl (0.3 μL) and sealed in a Wheaton vial. The reaction solution was heated to 80 °C for 8 days. Small crystallites were formed amongst amorphous material.

**Cu-L<sup>3</sup>.** Copper nitrate trihydrate (8 mg, 33 μmol) and H<sub>4</sub>L<sup>3</sup> (5 mg, 8.3 μmol) and 4,4'-dipyridyl (1.3 mg, 8.3 μmol) were dissolved in DMF/methanol/water (2:1:1 v/v/v, 2 mL) and sealed in a Wheaton vial. The reaction solution was heated to 65 °C for 4 days. Small dark blue/purple crystallites formed as the solution turned clear; the material was sent to the National Crystallography Service for SCXRD analysis.

**Zn-L<sup>3</sup>.** Zinc nitrate hexahydrate (10 mg, 33 μmol) and H<sub>4</sub>L<sup>3</sup> (5 mg, 8.3 μmol) and 4,4'-dipyridyl (1.3 mg, 8.3 μmol) were dissolved in DMF/water (1:1 v/v, 1 mL) and sealed in a Wheaton vial. The reaction solution was heated to 65 °C for 4 days yielding a mixture of red crystals amongst amorphous material. This is analogous to the results of the Zn-MOF synthesised by Dr Chong, first introduced and subsequently studied by NMR in Chapter 2 of this thesis.

#### 4.5.2.3 Crystal structure details of Cu-L<sup>3</sup>

*The description in this section was kindly provided by Dr Stephen Argent (University of Nottingham), based on the data collected at the National Crystallography Service; Dr Argent is still working on completing this structure.*

Diffraction data measured for the crystal was very weak with a resolution limit of 2 Å. Indexing indicates the crystal system is hexagonal with unit cell dimensions:  $a = b = 18.605(1)$  Å and  $c = 37.414(5)$  Å. Attempts at solving the structure using dual space methods (SHELXT) give plausible solutions for copper centres coordinated to isophthalate groups of H<sub>4</sub>L<sup>3</sup> in space groups P6<sub>3</sub>/mmc (centrosymmetric) and P6<sub>3</sub>/mc (polar). In both cases the solvated copper-isophthalate moieties are organised into Kagomé layers with a separation of 18.7 Å between planes. No further atom positions can be developed from the electron density map.

Inspection of the layered structures indicates that the distance and angle between isophthalate moieties opposite each other are a suitable match to be connected by a spiropyran moiety. Atom coordinates for a rigid spiropyran fragment were created using a mixture of information from CSD and DFT methods (Grade Web Server). The rigid fragment was introduced to the structure solutions in the two space groups and refined to examine the possible fit between the Kagomé layers.

In the case of centrosymmetric space group P6<sub>3</sub>/mmc the spiropyran fragment exhibits four-fold symmetry disorder: both head to tail and mirror images (*e.g.* R and S) of the fragment are overlaid. In the case of polar space group P6<sub>3</sub>/mc only two-fold symmetry disorder of the spiropyran fragment occurs: the mirror images. In the polar structure there is no head to tail disorder and all spiropyran moieties in the structure are oriented in the same direction with respect to the layers.

Without further evidence to support the polar space group the solution in the centrosymmetric space group was developed further. The rigid spiropyran moiety showed poor alignment where it met the isophthalate moieties. The rigidity constraint on the spiropyran fragment was removed and replaced with a large array of geometric restraints (DFIX, DANG and FLAT) which were also created by Grade Web Server. Further geometric restraints were applied to the isophthalate moiety and bonds between the two moieties. Only the copper centres were refined with anisotropic

displacement parameters, all other atoms were refined isotropically. The isotropic displacement parameters of the spiropyran moieties were all fixed at values of 0.1.

The refinement of the heavily restrained spiropyran moiety does not result in an improvement of the R1 value over the empty structure where no bridging moiety is modelled. Furthermore, the 2Fo-Fc electron density map only confirms positions of atoms in the copper paddle wheel Kagomé layers. The presence and orientation of the spiropyran linkers is supported only by the geometric complementarity they show for the parts of the structure which are determined by the electron density map.

### 4.5.3 Photophysical characterisation experiments

#### 4.5.3.1 Dissolution of H<sub>2</sub>L<sup>2</sup> in DMSO

A cuvette containing DMSO (3 mL) was set-up in the sample holder of the UV-vis spectrometer. H<sub>2</sub>L<sup>2</sup> (1.2 mg, 2.4 μmol) was added to a cuvette, which would result in a final concentration of 0.08 mM. A time series was started to collect spectra every five seconds immediately upon dissolution of the linker; the measurements were stopped after one minute when no further changes were observed. A colour change from dark blue to orange-brown was noted.

#### 4.5.3.2 pH study of H<sub>4</sub>L<sup>3</sup>

To study the pH effects, 0.1 M HCl and 0.01 M NaOH were added to 1 ml samples of 0.02 mM H<sub>4</sub>L<sup>3</sup> in ethanol. The aliquots of acid and alkali added were 0.05, 0.1, 0.15, 0.2, 0.25 and 0.3 mL to give a full pH range from 1 to 14. The concentration was chosen to match initial photophysical characterisation studies by Dr Chong.<sup>5</sup> The UV-vis spectra of the samples were recorded immediately upon addition of acid or base (t = 0) and were recorded again after allowing the solutions to equilibrate for 1 and 24 hours. Spectra were baselined between 675 – 725 nm and absorbance maximum values were average over 10 points.

#### 4.5.3.3 Irradiation of H<sub>2</sub>L<sup>2</sup> and H<sub>4</sub>L<sup>3</sup>

0.1 mM solutions of H<sub>2</sub>L<sup>2</sup> and H<sub>4</sub>L<sup>3</sup> in ethanol were prepared and *ca.* 2 mL of each solution were irradiated in a quartz cuvette with a TLC lamp ( $\lambda_{UV} = 254$  nm). UV-vis spectra were recorded at t = 0, 4 and 24 hr for H<sub>2</sub>L<sup>2</sup> and t = 0, 4, 5 and 9 hr for H<sub>4</sub>L<sup>3</sup>.

The increased concentration of the solutions was required in order to monitor any peak changes at higher wavelengths, due to the small absorption values of the MC form. Spectra were baselined between 675 – 725 nm.

#### **4.5.3.4 UV-vis spectra of ‘MOF’ condition samples**

Twenty different MOF conditions were chosen from reactions with  $H_4L^3$ , different modulators, solvent ratios and with/without a co-linker (4,4'-dipyridyl). The solutions were prepared in the absence of the metal salts and the amount of  $H_4L^3$  was diluted 10-fold. Table 4.1 details the reagent quantities used for the experiment in Section 4.3.2.3. The solutions were left for 3 weeks to equilibrate before the UV-vis spectra were collected at three different temperatures: 20, 45 and 65 °C. The spectra were baselined between 675 – 725 nm.

## 4.6 References

- 1 K. Healey, W. Liang, P. D. Southon, T. L. Church and D. M. D'Alessandro, *J. Mater. Chem. A*, 2016, **4**, 10816–10819.
- 2 H. A. Schwartz, S. Olthof, D. Schaniel, K. Meerholz and U. Ruschewitz, *Inorg. Chem.*, 2017, **56**, 13100–13110.
- 3 S. Garg, H. Schwartz, M. Kozłowska, A. B. Kanj, K. Müller, W. Wenzel, U. Ruschewitz and L. Heinke, *Angew. Chemie Int. Ed.*, 2019, **58**, 1193–1197.
- 4 D. E. Williams, C. R. Martin, E. A. Dolgoplova, A. Swifton, D. C. Godfrey, O. A. Ejegbavwo, P. J. Pellechia, M. D. Smith and N. B. Shustova, *J. Am. Chem. Soc.*, 2018, **140**, 7611–7622.
- 5 M. Chong, University of Nottingham, 2016.
- 6 Y.-X. Tan, Y.-P. He and J. Zhang, *Inorg. Chem.*, 2012, **51**, 9649–9654.
- 7 P. B. Markworth, B. D. Adamson, N. J. A. Coughlan, L. Goerigk and E. J. Bieske, *Phys. Chem. Chem. Phys.*, 2015, **17**, 25676–25688.
- 8 R. Klajn, *Chem. Soc. Rev.*, 2014, **43**, 148–184.
- 9 T. R. Silvia, V. S. L. Ana and E. A. S. González, *Synth. Commun.*, 1995, **25**, 105–110.
- 10 K. Wagner, M. Zanoni, A. B. S. Elliott, P. Wagner, R. Byrne, L. E. Florea, D. Diamond, K. C. Gordon, G. G. Wallace and D. L. Officer, *J. Mater. Chem. C*, 2013, **1**, 3913–3916.
- 11 N. Miyaura and A. Suzuki, *Chem. Rev.*, 1995, **95**, 2457–2483.
- 12 X. Lin, I. Telepeni, A. J. Blake, A. Dailly, C. M. Brown, J. M. Simmons, M. Zoppi, G. S. Walker, K. M. Thomas, T. J. Mays, P. Hubberstey, N. R. Champness and M. Schröder, *J. Am. Chem. Soc.*, 2009, **131**, 2159–2171.
- 13 B. S. Lukyanov and M. B. Lukyanova, *Chem. Heterocycl. Compd.*, 2005, **41**, 281–311.
- 14 W. Tian and J. Tian, *Dye. Pigment.*, 2014, **105**, 66–74.
- 15 F. Krohm, J. Kind, R. Savka, M. Alcaraz Janßen, D. Herold, H. Plenio, C. M. Thiele and A. Andrieu-Brunsen, *J. Mater. Chem. C*, 2016, **4**, 4067–4076.
- 16 S. V. Paramonov, V. Lokshin and O. A. Fedorova, *J. Photochem. Photobiol. C Photochem. Rev.*, 2011, **12**, 209–236.
- 17 Y. Hirshberg, E. B. Knott and E. Fischer, *J. Chem. Soc.*, 1955, 3313–3321.
- 18 J. T. C. Wojtyk, A. Wasey, N.-N. Xiao, P. M. Kazmaier, S. Hoz, C. Yu, R. P. Lemieux and E. Buncel, *J. Phys. Chem. A*, 2007, **111**, 2511–2516.
- 19 L. Kortekaas, J. Chen, D. Jacquemin and W. R. Browne, *J. Phys. Chem. B*, 2018, **122**, 6423–6430.

- 20 B. Ziółkowski, L. Florea, J. Theobald, F. Benito-Lopez and D. Diamond, *Soft Matter*, 2013, **9**, 8754–8760.
- 21 J. E. Stumpel, B. Ziółkowski, L. Florea, D. Diamond, D. J. Broer and A. P. H. J. Schenning, *ACS Appl. Mater. Interfaces*, 2014, **6**, 7268–7274.
- 22 R. J. Marshall, C. L. Hobday, C. F. Murphie, S. L. Griffin, C. A. Morrison, S. A. Moggach and R. S. Forgan, *J. Mater. Chem. A*, 2016, **4**, 6955–6963.
- 23 M. J. Katz, Z. J. Brown, Y. J. Colón, P. W. Siu, K. A. Scheidt, R. Q. Snurr, J. T. Hupp and O. K. Farha, *Chem. Commun.*, 2013, **49**, 9449–9451.
- 24 F. Ragon, P. Horcajada, H. Chevreau, Y. K. Hwang, U.-H. Lee, S. R. Miller, T. Devic, J.-S. Chang and C. Serre, *Inorg. Chem.*, 2014, **53**, 2491–2500.
- 25 M. Hammarson, J. R. Nilsson, S. Li, T. Beke-Somfai and J. Andréasson, *J. Phys. Chem. B*, 2013, **117**, 13561–13571.
- 26 B. Moulton, J. Lu, R. Hajndl, S. Hariharan and M. J. Zaworotko, *Angew. Chemie Int. Ed.*, 2002, **41**, 2821–2824.
- 27 P. Mahata, D. Sen and S. Natarajan, *Chem. Commun.*, 2008, **0**, 1278–1280.
- 28 M. G. Yamada, T. Soejima, N. Tsuji, D. Hirai, M. Dincă and H. Aoki, *Phys. Rev. B*, 2016, **94**, 081102.
- 29 S. Chen, J. Dai and X. C. Zeng, *Phys. Chem. Chem. Phys.*, 2015, **17**, 5954–5958.
- 30 J. Hungerford and K. S. Walton, *Inorg. Chem.*, 2019, **58**, 7690–7697.
- 31 Z. Zhang, L. Wojtas and M. J. Zaworotko, *Cryst. Growth Des.*, 2011, **11**, 1441–1445.
- 32 L. Cui, H. Zhang, G. Zhang, Y. Zhou, L. Fan, L. Shi, C. Zhang, S. Shuang and C. Dong, *Spectrochim. Acta Part A Mol. Biomol. Spectrosc.*, 2018, **202**, 13–17.
- 33 R. T. McIver, J. A. Scott and J. M. Riveros, *J. Am. Chem. Soc.*, 1973, **95**, 2706–2708.
- 34 R. G. Pearson and F. V. Williams, *J. Am. Chem. Soc.*, 1953, **75**, 3073–3075.
- 35 R. Linnell, *J. Org. Chem.*, 1960, **25**, 290–290.



## 4.7 Appendix

**Table A.9** Combinatorial data for photoactive MOF syntheses. **Bold** outcome denotes sample from which crystal structure was obtained.

Linker: Metal	Pillar	L:P:M ratio	Solvent ratio (v/v)	Total volume / mL	Modulator or co-solvent (mg, mL, v/v)	T / °C	Outcome
SP2 : Mg		1 : 0 : 5	DMF:EtOH (2:1)	1.5	-	80	no solid
SP2 : Mg		1 : 0 : 5	DMF:EtOH (2:1)	1.5	0.5 M HCl (100 $\mu$ L)	80	no solid
SP2 : Ca		1 : 0 : 5	DMF:EtOH (2:1)	1.5	-	80	amorphous
SP2 : Ca		1 : 0 : 5	DMF:EtOH (2:1)	1.5	0.5 M HCl (100 $\mu$ L)	80	amorphous
SP2 : Sr		1 : 0 : 5	DMF:EtOH (2:1)	1.5	-	80	amorphous
SP2 : Sr		1 : 0 : 5	DMF:EtOH (2:1)	1.5	0.5 M HCl (100 $\mu$ L)	80	no solid
SP2 : Ba		1 : 0 : 5	DMF:EtOH (2:1)	1.5	-	80	amorphous
SP2 : Ba		1 : 0 : 5	DMF:EtOH (2:1)	1.5	0.5 M HCl (100 $\mu$ L)	80	no solid
SP2 : Mn		1 : 0 : 5	DMF:EtOH (2:1)	1.5	-	80	amorphous
SP2 : Mn		1 : 0 : 5	DMF:EtOH (2:1)	1.5	0.5 M HCl (100 $\mu$ L)	80	no solid
SP2 : Zn		1 : 0 : 5	DMF:EtOH (2:1)	1.5	-	80	amorphous
SP2 : Zn		1 : 0 : 5	DMF:EtOH (2:1)	1.5	0.5 M HCl (100 $\mu$ L)	80	amorphous
SP2 : Mg		1 : 0 : 5	DMF	2	1M HCl (0.1 mL) / NH <sub>4</sub> CH <sub>3</sub> CO <sub>2</sub> (50 mg)	80	Amorphous
SP2 : Mg		1 : 0 : 5	DMF	2	NH <sub>4</sub> CH <sub>3</sub> CO <sub>2</sub> (50 mg)	80	Amorphous
SP2 : Mg		1 : 0 : 5	DMF	2	1M HCl (0.1 mL) / NH <sub>4</sub> CH <sub>3</sub> CO <sub>2</sub> (100 mg)	80	Amorphous

SP2 : Mg	1 : 0 : 5	DMF	2	NH <sub>4</sub> CH <sub>3</sub> CO <sub>2</sub> (100 mg)	80	Amorphous
SP2 : Ca	1 : 0 : 5	DMF	2	1M HCl (0.1 mL) / NH <sub>4</sub> CH <sub>3</sub> CO <sub>2</sub> (50 mg)	80	Amorphous
SP2 : Ca	1 : 0 : 5	DMF	2	NH <sub>4</sub> CH <sub>3</sub> CO <sub>2</sub> (50 mg)	80	Amorphous
SP2 : Ca	1 : 0 : 5	DMF	2	1M HCl (0.1 mL) / NH <sub>4</sub> CH <sub>3</sub> CO <sub>2</sub> (100 mg)	80	Amorphous
SP2 : Ca	1 : 0 : 5	DMF	2	NH <sub>4</sub> CH <sub>3</sub> CO <sub>2</sub> (100 mg)	80	Amorphous
SP2 : Cu	1 : 0 : 5	DMF	2	1M HCl (0.1 mL) / NH <sub>4</sub> CH <sub>3</sub> CO <sub>2</sub> (50 mg)	80	Amorphous
SP2 : Cu	1 : 0 : 5	DMF	2	NH <sub>4</sub> CH <sub>3</sub> CO <sub>2</sub> (50 mg)	80	Amorphous
SP2 : Cu	1 : 0 : 5	DMF	2	1M HCl (0.1 mL) / NH <sub>4</sub> CH <sub>3</sub> CO <sub>2</sub> (100 mg)	80	Amorphous
SP2 : Cu	1 : 0 : 5	DMF	2	NH <sub>4</sub> CH <sub>3</sub> CO <sub>2</sub> (100 mg)	80	Amorphous
SP2 : Zn	1 : 0 : 5	DMF	2	1M HCl (0.1 mL) / NH <sub>4</sub> CH <sub>3</sub> CO <sub>2</sub> (50 mg)	80	Amorphous
SP2 : Zn	1 : 0 : 5	DMF	2	NH <sub>4</sub> CH <sub>3</sub> CO <sub>2</sub> (50 mg)	80	Amorphous
SP2 : Zn	1 : 0 : 5	DMF	2	1M HCl (0.1 mL) / NH <sub>4</sub> CH <sub>3</sub> CO <sub>2</sub> (100 mg)	80	Amorphous
SP3 : Mg	1 : 0 : 10	DMF	2	1M HCl ( 0.1 mL)	80	amorphous + crystalline
SP3 : Mg	1 : 0 : 10	DMF	2	1M HCl (0.25 mL)	80	amorphous + crystalline
SP3 : Mg	1 : 0 : 10	DMF	2	1M HCl (0.5 mL)	80	amorphous + crystalline
SP3 : Ca	1 : 0 : 10	DMF	2	1M HCl ( 0.1 mL)	80	amorphous
SP3 : Ca	1 : 0 : 10	DMF	2	1M HCl (0.25 mL)	80	amorphous + crystalline
SP3 : Ca	1 : 0 : 10	DMF	2	1M HCl (0.5 mL)	80	amorphous + crystalline
SP3 : Ca	1 : 0 : 10	DMF	2	conc HCl (2 drops)	80	no solid
SP3 : Cu	1 : 0 : 10	DMF	2	1M HCl ( 0.1 mL)	80	amorphous

SP3 : Cu	1: 0 : 10	DMF	2	1M HCl (0.25 mL)	80	amorphous
SP3 : Cu	1: 0 : 10	DMF	2	1M HCl (0.5 mL)	80	no solid
SP3 : Cu	1: 0 : 10	DMF	2	conc HCl (2 drops)	80	no solid
SP3 : Zn	1: 0 : 10	DMF	2	1M HCl ( 0.1 mL)	80	amorphous
SP3 : Zn	1: 0 : 10	DMF	2	1M HCl (0.25 mL)	80	no solid
SP3 : Zn	1: 0 : 10	DMF	2	1M HCl (0.5 mL)	80	no solid
SP3 : Zn	1: 0 : 10	DMF	2	conc HCl (2 drops)	80	no solid
<hr/>						
SP3 : Mg	1: 0 : 8	DMF	2	EtOH/H <sub>2</sub> O (5:1 = 0.6 mL)	120	amorphous
SP3 : Ca	1: 0 : 8	DMF	2	EtOH/H <sub>2</sub> O (5:2 = 0.7 mL)	120	amorphous + crystalline
SP3 : Sr	1: 0 : 8	DMF	2	EtOH/H <sub>2</sub> O (3:5 = 0.8 mL)	120	amorphous + crystalline
SP3 : Ba	1: 0 : 8	DMF	2	EtOH/H <sub>2</sub> O (3:5 = 0.8 mL)	120	amorphous + crystalline
SP3 : Mg	1: 0 : 8	DEF	2	EtOH/H <sub>2</sub> O (5:1 = 0.6 mL)	120	amorphous
SP3: Ca	1: 0 : 8	DEF	2	EtOH/H <sub>2</sub> O (5:2 = 0.7 mL)	120	amorphous + crystalline
SP3: Sr	1: 0 : 8	DEF	2	EtOH/H <sub>2</sub> O (3:5 = 0.8 mL)	120	amorphous + crystalline
SP3: Ba	1: 0 : 8	DEF	2	EtOH/H <sub>2</sub> O (3:5 = 0.8 mL)	120	amorphous + crystalline
<hr/>						
SP3: Sr	1: 0 : 10	DMF	2		75	amorphous + crystalline
SP3: Sr	1: 0 : 10	DMF	2	EtOH/H <sub>2</sub> O (5:1 = 0.6 mL)	75	amorphous + crystalline
SP3: Sr	1: 0 : 10	DMF	2	EtOH/H <sub>2</sub> O (5:2 = 0.7 mL)	75	amorphous + crystalline
SP3: Sr	1: 0 : 10	DMF	2	EtOH/H <sub>2</sub> O (5:3 = 0.8 mL)	75	amorphous + crystalline
SP3: Sr	1: 0 : 10	DMF	2	EtOH/H <sub>2</sub> O (5:4 = 0.9 mL)	75	amorphous + crystalline
SP3: Sr	1: 0 : 10	DMF	2	EtOH/H <sub>2</sub> O (4:5 = 0.9 mL)	75	amorphous + crystalline
SP3: Sr	1: 0 : 10	DMF	2	EtOH/H <sub>2</sub> O (3:5 = 0.8 mL)	75	amorphous + crystalline

SP3 : Sr	1 : 0 : 10	DMF	2	EtOH/H <sub>2</sub> O (2:5 = 0.7 mL)	75	amorphous + crystalline
SP3 : Sr	1 : 0 : 10	DMF	2	EtOH/H <sub>2</sub> O (1:5 = 0.6 mL)	75	amorphous + crystalline
SP3 : Sr	1 : 0 : 10	DMF	2	H <sub>2</sub> O (0.5 mL)	75	amorphous + crystalline
SP3 : Mg	1 : 0 : 4	DMF	2	EtOH/H <sub>2</sub> O (1.2:1 = 0.33 mL)	75	No solid
SP3 : Mg	1 : 0 : 8	DMF	2	EtOH/H <sub>2</sub> O (1.2:1 = 0.33 mL)	75	No solid
SP3 : Mg	1 : 0 : 4	DMF	2	EtOH/H <sub>2</sub> O (1.2:1 = 0.33 mL)	75	No solid
SP3 : Mg	1 : 0 : 8	DMF	2	EtOH/H <sub>2</sub> O (1.2:1 = 0.33 mL)	75	No solid
SP3 : Ca	1 : 0 : 5	DMF	2	EtOH/H <sub>2</sub> O (1.2:1 = 0.33 mL)	75	No solid
SP3 : Ca	1 : 0 : 10	DMF	2	EtOH/H <sub>2</sub> O (1.2:1 = 0.33 mL)	75	No solid
SP3 : Ca	1 : 0 : 5	DMF	2	EtOH/H <sub>2</sub> O (1.2:1 = 0.33 mL)	75	No solid
SP3 : Ca	1 : 0 : 10	DMF	2	EtOH/H <sub>2</sub> O (1.2:1 = 0.33 mL)	75	No solid
SP3 : Sr	1 : 0 : 5	DMF	2	EtOH/H <sub>2</sub> O (1.2:1 = 0.33 mL)	75	No solid
SP3 : Sr	1 : 0 : 10	DMF	2	EtOH/H <sub>2</sub> O (1.2:1 = 0.33 mL)	75	No solid
SP3 : Sr	1 : 0 : 5	DMF	2	EtOH/H <sub>2</sub> O (1.2:1 = 0.33 mL)	75	No solid
SP3 : Sr	1 : 0 : 10	DMF	2	EtOH/H <sub>2</sub> O (1.2:1 = 0.33 mL)	75	No solid
SP3 : Ba	1 : 0 : 3	DMF	2	EtOH/H <sub>2</sub> O (1.2:1 = 0.33 mL)	75	No solid
SP3 : Ba	1 : 0 : 6	DMF	2	EtOH/H <sub>2</sub> O (1.2:1 = 0.33 mL)	75	No solid
SP3 : Ba	1 : 0 : 3	DMF	2	EtOH/H <sub>2</sub> O (1.2:1 = 0.33 mL)	75	No solid
SP3 : Ba	1 : 0 : 6	DMF	2	EtOH/H <sub>2</sub> O (1.2:1 = 0.33 mL)	75	No solid
SP3 : Ca	1 : 0 : 9	DMF	2		75	no solid
SP3 : Ca	1 : 0 : 9	DMF	2	EtOH/H <sub>2</sub> O (5:1 = 0.6 mL)	75	amorphous + crystalline
SP3 : Ca	1 : 0 : 9	DMF	2	EtOH/H <sub>2</sub> O (5:2 = 0.7 mL)	75	amorphous + crystalline
SP3 : Ca	1 : 0 : 9	DMF	2	EtOH/H <sub>2</sub> O (5:3 = 0.8 mL)	75	amorphous + crystalline

SP3 : Ca	1 : 0 : 9	DMF	2	EtOH/H <sub>2</sub> O (5:4 = 0.9 mL)	75	amorphous + crystalline
SP3 : Ca	1 : 0 : 9	DMF	2	EtOH (0.5 mL)	75	no solid
SP3 : Ca	1 : 0 : 9	DMF	2	EtOH (0.4 mL)	75	no solid
SP3 : Ca	1 : 0 : 9	DMF	2	EtOH (0.3 mL)	75	no solid
SP3 : Ca	1 : 0 : 9	DMF	2	EtOH (0.2 mL)	75	no solid
SP3 : Ca	1 : 0 : 9	DMF	2	EtOH (0.1 mL)	75	no solid
SP3 : Mg	1 : 0 : 9	DMF	2		75	no solid
SP3 : Mg	1 : 0 : 9	DMF	2	EtOH/H <sub>2</sub> O (5:1 = 0.6 mL)	75	no solid
SP3 : Mg	1 : 0 : 9	DMF	2	EtOH/H <sub>2</sub> O (5:2 = 0.7 mL)	75	no solid
SP3 : Mg	1 : 0 : 9	DMF	2	EtOH/H <sub>2</sub> O (5:3 = 0.8 mL)	75	amorphous
SP3 : Mg	1 : 0 : 9	DMF	2	EtOH/H <sub>2</sub> O (5:4 = 0.9 mL)	75	amorphous
SP3 : Mg	1 : 0 : 9	DMF	2	EtOH (0.5 mL)	75	no solid
SP3 : Mg	1 : 0 : 9	DMF	2	EtOH (0.4 mL)	75	no solid
SP3 : Mg	1 : 0 : 9	DMF	2	EtOH (0.3 mL)	75	no solid
SP3 : Mg	1 : 0 : 9	DMF	2	EtOH (0.2 mL)	75	no solid
SP3 : Mg	1 : 0 : 9	DMF	2	EtOH (0.1 mL)	75	no solid
SP3 : Mg	1 : 0 : 5	DMF	2	EtOH (0.5 mL)	75	amorphous + crystalline
SP3 : Mg	1 : 0 : 10	DMF	2	EtOH (0.5 mL)	75	amorphous + crystalline
SP3 : Mg	1 : 0 : 5	DMF	2	EtOH (0.5 mL)	85	amorphous
SP3 : Mg	1 : 0 : 10	DMF	2	EtOH (0.5 mL)	85	amorphous + crystalline
SP3 : Mg	1 : 0 : 5	DMF	2	EtOH (0.5 mL)	95	amorphous
SP3 : Mg	1 : 0 : 10	DMF	2	EtOH (0.5 mL)	95	amorphous + crystalline
SP3 : Ca	1 : 0 : 5	DMF	2	EtOH/H <sub>2</sub> O (3:2 = 0.5 mL)	75	amorphous

SP3 : Ca	1 : 0 : 10	DMF	2	EtOH/H <sub>2</sub> O (3:2 = 0.5 mL)	75	amorphous + crystalline
SP3 : Ca	1 : 0 : 5	DMF	2	EtOH/H <sub>2</sub> O (3:2 = 0.5 mL)	85	amorphous
SP3 : Ca	1 : 0 : 10	DMF	2	EtOH/H <sub>2</sub> O (3:2 = 0.5 mL)	85	amorphous
SP3 : Ca	1 : 0 : 5	DMF	2	EtOH/H <sub>2</sub> O (3:2 = 0.5 mL)	95	amorphous
SP3 : Ca	1 : 0 : 10	DMF	2	EtOH/H <sub>2</sub> O (3:2 = 0.5 mL)	95	amorphous + crystalline
SP3 : Sr	1 : 0 : 5	DMF	2	EtOH/H <sub>2</sub> O (5:3 = 0.8 mL)	75	amorphous
SP3 : Sr	1 : 0 : 10	DMF	2	EtOH/H <sub>2</sub> O (5:3 = 0.8 mL)	75	amorphous + crystalline
SP3 : Sr	1 : 0 : 5	DMF	2	EtOH/H <sub>2</sub> O (5:3 = 0.8 mL)	85	amorphous + crystalline
SP3 : Sr	1 : 0 : 10	DMF	2	EtOH/H <sub>2</sub> O (5:3 = 0.8 mL)	85	amorphous + crystalline
SP3 : Sr	1 : 0 : 5	DMF	2	EtOH/H <sub>2</sub> O (5:3 = 0.8 mL)	95	amorphous + crystalline
SP3 : Sr	1 : 0 : 10	DMF	2	EtOH/H <sub>2</sub> O (5:3 = 0.8 mL)	95	amorphous + crystalline
SP3 : Ba	1 : 0 : 5	DMF	2	EtOH/H <sub>2</sub> O (5:3 = 0.8 mL)	75	amorphous + crystalline
SP3 : Ba	1 : 0 : 10	DMF	2	EtOH/H <sub>2</sub> O (5:3 = 0.8 mL)	75	amorphous + crystalline
SP3 : Ba	1 : 0 : 5	DMF	2	EtOH/H <sub>2</sub> O (5:3 = 0.8 mL)	85	amorphous + crystalline
SP3 : Ba	1 : 0 : 10	DMF	2	EtOH/H <sub>2</sub> O (5:3 = 0.8 mL)	85	amorphous + crystalline
SP3 : Ba	1 : 0 : 5	DMF	2	EtOH/H <sub>2</sub> O (5:3 = 0.8 mL)	95	amorphous + crystalline
SP3 : Ba	1 : 0 : 10	DMF	2	EtOH/H <sub>2</sub> O (5:3 = 0.8 mL)	95	amorphous + crystalline
SP3 : Cu	1 : 0 : 3	DMF	2		85	Amorphous
SP3 : Cu	1 : 0 : 5	DMF	2		85	Amorphous
SP3 : Zn	1 : 0 : 3	DMF	2		85	Amorphous
SP3 : Zn	1 : 0 : 5	DMF	2		85	Amorphous
SP3 : Zr	1 : 0 : 4	DMF	3	Benzoic acid	120	Amorphous
SP3 : In	1 : 0 : 1.5	DMF/MeCN (2:1)	3		80	Amorphous

SP3 : Mg		1 : 0 : 10	DMF	2	EtOH (0.5 mL)	75	Amorphous
SP3 : Ca		1 : 0 : 10	DMF	2	EtOH/H <sub>2</sub> O (3:2 = 0.5 mL)	75	amorphous + crystalline
SP3 : Sr		1 : 0 : 10	DMF	2	EtOH/H <sub>2</sub> O (5:3 = 0.8 mL)	75	amorphous + crystalline
SP3 : Ba		1 : 0 : 10	DMF	2	EtOH/H <sub>2</sub> O (5:3 = 0.8 mL)	75	amorphous + crystalline
SP3 : Cu		1 : 0 : 10	DMF	2	EtOH/H <sub>2</sub> O (1:1 = 0.6 mL)	75	Amorphous
SP3 : Zn		1 : 0 : 10	DMF	2	EtOH/H <sub>2</sub> O (1:1 = 0.6 mL)	75	Amorphous
SP2 : Mg	<i>N</i> <sup>1</sup> , <i>N</i> <sup>4</sup> -di(pyridin-4-yl)terephthalamide	1 : 1 : 2	DMF : EtOH (2:1)	0.75		80	no solid
SP2 : Mg	<i>N</i> <sup>1</sup> , <i>N</i> <sup>4</sup> -di(pyridin-4-yl)terephthalamide	1 : 1 : 2	DMF : EtOH (2:1)	0.75		80	no solid
SP2 : Mg	<i>N</i> <sup>1</sup> , <i>N</i> <sup>4</sup> -di(pyridin-4-yl)terephthalamide	2 : 1 : 2	DEF : EtOH (2:1)	0.75		80	amorphous
SP2 : Mg	<i>N</i> <sup>1</sup> , <i>N</i> <sup>4</sup> -di(pyridin-4-yl)terephthalamide	2 : 1 : 2	DEF : EtOH (2:1)	0.75		80	amorphous
SP2 : Ca	<i>N</i> <sup>1</sup> , <i>N</i> <sup>4</sup> -di(pyridin-4-yl)terephthalamide	1 : 1 : 2	DMF : EtOH (2:1)	0.75		80	amorphous
SP2 : Ca	<i>N</i> <sup>1</sup> , <i>N</i> <sup>4</sup> -di(pyridin-4-yl)terephthalamide	1 : 1 : 2	DMF : EtOH (2:1)	0.75		80	amorphous
SP2 : Ca	<i>N</i> <sup>1</sup> , <i>N</i> <sup>4</sup> -di(pyridin-4-yl)terephthalamide	2 : 1 : 2	DEF : EtOH (2:1)	0.75		80	amorphous
SP2 : Ca	<i>N</i> <sup>1</sup> , <i>N</i> <sup>4</sup> -di(pyridin-4-yl)terephthalamide	2 : 1 : 2	DEF : EtOH (2:1)	0.75		80	amorphous + crystalline
SP2 : Mn	<i>N</i> <sup>1</sup> , <i>N</i> <sup>4</sup> -di(pyridin-4-yl)terephthalamide	1 : 1 : 2	DMF : EtOH (2:1)	0.75		80	amorphous
SP2 : Mn	<i>N</i> <sup>1</sup> , <i>N</i> <sup>4</sup> -di(pyridin-4-yl)terephthalamide	1 : 1 : 2	DMF : EtOH (2:1)	0.75		80	amorphous
SP2 : Mn	<i>N</i> <sup>1</sup> , <i>N</i> <sup>4</sup> -di(pyridin-4-yl)terephthalamide	2 : 1 : 2	DEF : EtOH (2:1)	0.75		80	amorphous
SP2 : Mn	<i>N</i> <sup>1</sup> , <i>N</i> <sup>4</sup> -di(pyridin-4-yl)terephthalamide	2 : 1 : 2	DEF : EtOH (2:1)	0.75		80	amorphous
SP2 : Zn	<i>N</i> <sup>1</sup> , <i>N</i> <sup>4</sup> -di(pyridin-4-yl)terephthalamide	1 : 1 : 2	DMF : EtOH (2:1)	0.75		80	amorphous
SP2 : Zn	<i>N</i> <sup>1</sup> , <i>N</i> <sup>4</sup> -di(pyridin-4-yl)terephthalamide	1 : 1 : 2	DMF : EtOH (2:1)	0.75		80	amorphous
SP2 : Zn	<i>N</i> <sup>1</sup> , <i>N</i> <sup>4</sup> -di(pyridin-4-yl)terephthalamide	2 : 1 : 2	DEF : EtOH (2:1)	0.75		80	amorphous
SP2 : Zn	<i>N</i> <sup>1</sup> , <i>N</i> <sup>4</sup> -di(pyridin-4-yl)terephthalamide	2 : 1 : 2	DEF : EtOH (2:1)	0.75		80	amorphous
SP2 : Zn	<i>N</i> <sup>1</sup> , <i>N</i> <sup>4</sup> -di(pyridin-4-yl)terephthalamide	2 : 1 : 2	DMF : MeOH (1:1)	3		80	no solid

SP2 : Zn	<i>N</i> <sup>1</sup> , <i>N</i> <sup>4</sup> -di(pyridin-4-yl)terephthalamide	2 : 1 : 2	DMF : EtOH (1:1)	3	80	no solid
SP2 : Zn	<i>N</i> <sup>1</sup> , <i>N</i> <sup>4</sup> -di(pyridin-4-yl)terephthalamide	2 : 1 : 2	DMF : MeOH: DMSO (1:1:1)	3	80	amorphous
SP2 : Zn	<i>N</i> <sup>1</sup> , <i>N</i> <sup>4</sup> -di(pyridin-4-yl)terephthalamide	2 : 1 : 2	DMF : EtOH: DMSO (1:1:1)	3	80	amorphous
SP2 : Zn	4,4'-dipyridyl	2 : 1 : 2	DMF : MeOH (1:1)	1.5	80	amorphous
SP2 : Zn	4,4'-dipyridyl	2 : 1 : 2	DMF : EtOH (1:1)	1.5	80	amorphous + crystalline
SP2 : Zn	4,4'-dipyridyl	2 : 1 : 2	DMF : MeOH: DMSO (1:1:1)	1.5	80	amorphous
SP2 : Zn	4,4'-dipyridyl	2 : 1 : 2	DMF : EtOH: DMSO (1:1:1)	1.5	80	amorphous
SP2 : Zn	<i>N</i> <sup>1</sup> , <i>N</i> <sup>4</sup> -di(pyridin-4-yl)terephthalamide	02:02:01	DMF : EtOH (1:1)	0.5	100	no solid
SP2 : Zn	<i>N</i> <sup>1</sup> , <i>N</i> <sup>4</sup> -di(pyridin-4-yl)terephthalamide	02:02:01	DMF : MeOH (1:1)	0.5	100	no solid
SP2 : Zn	4,4'-dipyridyl	02:02:01	DMF : EtOH (1:1)	0.5	100	no solid
SP2 : Zn	4,4'-dipyridyl	02:02:01	DMF : MeOH (1:1)	0.5	100	no solid
SP2 : Zn	4,4'-dipyridyl	02:02:01	DMF : EtOH : DMSO (1:1:0.5)	0.63	100	no solid
SP2 : Zn	4,4'-dipyridyl	02:02:01	DMF : MeOH : DMSO (1:1:0.5)	0.63	100	no solid
SP2 : Ca	4,4'-dipyridyl	04:01:01	DMF : MeOH (1:1)	1	65	amorphous
SP2 : Ca	4,4'-dipyridyl	04:01:01	DMF : MeOH (1:1)	1	65	amorphous
SP2 : Sr	4,4'-dipyridyl	04:01:01	DMF : MeOH (1:1)	1	65	amorphous
SP2 : Ba	4,4'-dipyridyl	04:01:01	DMF : MeOH (1:1)	1	65	amorphous
SP2 : Cu	4,4'-dipyridyl	04:01:01	DMF : MeOH (1:1)	1	65	amorphous
SP2 : Cu	4,4'-dipyridyl	04:01:01	DMF : MeOH (1:1)	1	65	amorphous
SP2 : Zn	4,4'-dipyridyl	04:01:01	DMF : MeOH (1:1)	1	65	amorphous
<b>SP2 : Zn</b>	<b>4,4'-dipyridyl</b>	<b>04:01:01</b>	<b>DMF : MeOH (1:1)</b>	<b>1</b>	<b>65</b>	<b>Crystalline</b>
SP2 : Mg	4,4'-dipyridyl	04:01:01	DMF : MeOH (1:1)	1	65	amorphous
SP3 : Mg	4,4'-dipyridyl	1 : 1 : 2	DMF : MeOH (1:1)	0.5	65	no solid

SP3 : Mg	4,4'-dipyridyl	1 : 1 : 2	DMF : MeOH (1:1)	1	65	no solid
SP3 : Mg	4,4'-dipyridyl	1 : 1 : 2	DMF : MeOH (1:1)	0.5	65	no solid
SP3 : Mg	4,4'-dipyridyl	1 : 1 : 2	DMF : MeOH (1:1)	1	65	amorphous
SP3 : Ca	4,4'-dipyridyl	1 : 1 : 2	DMF : MeOH (1:1)	0.5	65	no solid
SP3 : Ca	4,4'-dipyridyl	1 : 1 : 2	DMF : MeOH (1:1)	1	65	amorphous
SP3 : Ca	4,4'-dipyridyl	1 : 1 : 2	DMF : MeOH (1:1)	0.5	65	amorphous
SP3 : Ca	4,4'-dipyridyl	1 : 1 : 2	DMF : MeOH (1:1)	1	65	amorphous
SP3 : Sr	4,4'-dipyridyl	1 : 1 : 2	DMF : MeOH (1:1)	0.5	65	amorphous + crystalline
SP3 : Sr	4,4'-dipyridyl	1 : 1 : 2	DMF : MeOH (1:1)	1	65	amorphous
SP3 : Ba	4,4'-dipyridyl	1 : 1 : 2	DMF : MeOH (1:1)	0.5	65	amorphous
SP3 : Ba	4,4'-dipyridyl	1 : 1 : 2	DMF : MeOH (1:1)	1	65	no solid
SP3 : Zn	4,4'-dipyridyl	1 : 1 : 2	DMF : MeOH (1:1)	0.5	65	no solid
SP3 : Zn	4,4'-dipyridyl	1 : 1 : 2	DMF : MeOH (1:1)	1	65	amorphous
SP3 : Zn	4,4'-dipyridyl	1 : 1 : 2	DMF : MeOH (1:1)	0.5	65	no solid
SP3 : Zn	4,4'-dipyridyl	1 : 1 : 2	DMF : MeOH (1:1)	1	65	no solid
SP3 : Ca	4,4'-dipyridyl	1 : 1 : 2	DMF:MeOH:H <sub>2</sub> O (1 : 0.5 : 0.5)	0.5	65	amorphous
<b>SP3 : Ca</b>	<b>4,4'-dipyridyl</b>	<b>1 : 1 : 4</b>	<b>DMF:MeOH:H<sub>2</sub>O (1 : 0.5 : 0.5)</b>	<b>0.5</b>	<b>65</b>	<b>crystalline</b>
SP3 : Ca	4,4'-dipyridyl	2 : 1 : 2	DMF:MeOH:H <sub>2</sub> O (1 : 0.5 : 0.5)	0.5	65	amorphous
SP3 : Ca	4,4'-dipyridyl	2 : 1 : 4	DMF:MeOH:H <sub>2</sub> O (1 : 0.5 : 0.5)	0.5	65	amorphous
SP3 : Ca	4,4'-dipyridyl	1 : 1 : 2	DMF:MeOH:H <sub>2</sub> O (1 : 1 : 0.5)	1	65	amorphous
SP3 : Ca	4,4'-dipyridyl	1 : 1 : 4	DMF:MeOH:H <sub>2</sub> O (1 : 1 : 0.5)	1	65	amorphous
SP3 : Ca	4,4'-dipyridyl	2 : 1 : 2	DMF:MeOH:H <sub>2</sub> O (1 : 1 : 0.5)	1	65	amorphous
SP3 : Ca	4,4'-dipyridyl	2 : 1 : 4	DMF:MeOH:H <sub>2</sub> O (1 : 1 : 0.5)	1	65	amorphous

SP3 : Ca	4,4'-dipyridyl	1 : 1 : 2	DMF:MeOH:H <sub>2</sub> O (6: 5 : 1)	1.5	65	no solid
SP3 : Ca	4,4'-dipyridyl	1 : 1 : 4	DMF:MeOH:H <sub>2</sub> O (6: 5 : 1)	1.5	65	amorphous
SP3 : Ca	4,4'-dipyridyl	2 : 1 : 2	DMF:MeOH:H <sub>2</sub> O (6: 5 : 1)	1.5	65	amorphous
SP3 : Ca	4,4'-dipyridyl	2 : 1 : 4	DMF:MeOH:H <sub>2</sub> O (6: 5 : 1)	1.5	65	amorphous
SP3 : Ca	4,4'-dipyridyl	1 : 1 : 2	DMF:MeOH:H <sub>2</sub> O (8 : 7 : 1)	2	65	amorphous
SP3 : Ca	4,4'-dipyridyl	1 : 1 : 4	DMF:MeOH:H <sub>2</sub> O (8 : 7 : 1)	2	65	amorphous
SP3 : Ca	4,4'-dipyridyl	2 : 1 : 2	DMF:MeOH:H <sub>2</sub> O (8 : 7 : 1)	2	65	amorphous
SP3 : Ca	4,4'-dipyridyl	2 : 1 : 4	DMF:MeOH:H <sub>2</sub> O (8 : 7 : 1)	2	65	amorphous
SP3 : Mg	4,4'-dipyridyl	1 : 1 : 4	DMF:MeOH:H <sub>2</sub> O (1 : 0.5 : 0.5)	0.5	65	no solid
SP3 : Mg	4,4'-dipyridyl	1 : 1 : 4	DMF:MeOH:H <sub>2</sub> O (1 : 0.5 : 0.5)	0.5	65	no solid
SP3 : Ca	4,4'-dipyridyl	1 : 1 : 4	DMF:MeOH:H <sub>2</sub> O (1 : 0.5 : 0.5)	0.5	65	no solid
SP3 : Ca	4,4'-dipyridyl	1 : 1 : 4	DMF:MeOH:H <sub>2</sub> O (1 : 0.5 : 0.5)	0.5	65	amorphous
<b>SP3 : Sr</b>	<b>4,4'-dipyridyl</b>	<b>1 : 1 : 4</b>	<b>DMF:MeOH:H<sub>2</sub>O (1 : 0.5 : 0.5)</b>	<b>0.5</b>	<b>65</b>	<b>crystalline</b>
SP3 : Sr	4,4'-dipyridyl	1 : 1 : 4	DMF:MeOH:H <sub>2</sub> O (1 : 0.5 : 0.5)	0.5	65	amorphous + crystalline
SP3 : Ba	4,4'-dipyridyl	1 : 1 : 4	DMF:MeOH:H <sub>2</sub> O (1 : 0.5 : 0.5)	0.5	65	amorphous + crystalline
SP3 : Ba	4,4'-dipyridyl	1 : 1 : 4	DMF:MeOH:H <sub>2</sub> O (1 : 0.5 : 0.5)	0.5	65	amorphous + crystalline
SP3 : Ca	4,4'-dipyridyl	1 : 1 : 4	DMF:MeOH:H <sub>2</sub> O (1 : 0.5 : 0.5)	0.5	65	amorphous
SP3 : Ca	4,4'-dipyridyl	1 : 1 : 4	DMF:MeOH:H <sub>2</sub> O (1 : 0.5 : 0.5)	1	65	amorphous
SP3 : Ca	4,4'-dipyridyl	1 : 1 : 4	DMF:MeOH:H <sub>2</sub> O (1 : 0.5 : 0.5)	2	65	amorphous
SP3 : Sr	4,4'-dipyridyl	1 : 1 : 4	DMF:MeOH:H <sub>2</sub> O (1 : 0.5 : 0.5)	0.5	65	no solid
SP3 : Sr	4,4'-dipyridyl	1 : 1 : 4	DMF:MeOH:H <sub>2</sub> O (1 : 0.5 : 0.5)	1	65	crystalline
SP3 : Sr	4,4'-dipyridyl	1 : 1 : 4	DMF:MeOH:H <sub>2</sub> O (1 : 0.5 : 0.5)	2	65	no solid
SP3 : Mg	4,4'-dipyridyl	1 : 1 : 4	DMF:MeOH:H <sub>2</sub> O (1 : 0.5 : 0.5)	0.5	65	no solid

SP3 : Mg	4,4'-dipyridyl	1 : 1 : 4	DMF:MeOH:H <sub>2</sub> O (1 : 0.5 : 0.5)	1	65	no solid
SP3 : Mg	4,4'-dipyridyl	1 : 1 : 4	DMF:MeOH:H <sub>2</sub> O (1 : 0.5 : 0.5)	2	65	no solid
SP3 : Ba	4,4'-dipyridyl	1 : 1 : 4	DMF:MeOH:H <sub>2</sub> O (1 : 0.5 : 0.5)	0.5	65	amorphous
SP3 : Ba	4,4'-dipyridyl	1 : 1 : 4	DMF:MeOH:H <sub>2</sub> O (1 : 0.5 : 0.5)	1	65	amorphous
SP3 : Ba	4,4'-dipyridyl	1 : 1 : 4	DMF:MeOH:H <sub>2</sub> O (1 : 0.5 : 0.5)	2	65	amorphous
SP3 : Ba	4,4'-dipyridyl	1 : 1 : 2	DMF:MeOH:H <sub>2</sub> O (1 : 0.5 : 0.5)	0.5	65	amorphous + crystalline
SP3 : Ba	4,4'-dipyridyl	1 : 1 : 4	DMF:MeOH:H <sub>2</sub> O (1 : 0.5 : 0.5)	0.5	65	amorphous + crystalline
SP3 : Ba	4,4'-dipyridyl	2 : 1 : 2	DMF:MeOH:H <sub>2</sub> O (1 : 0.5 : 0.5)	0.5	65	amorphous + crystalline
SP3 : Ba	4,4'-dipyridyl	2 : 1 : 4	DMF:MeOH:H <sub>2</sub> O (1 : 0.5 : 0.5)	0.5	65	amorphous + crystalline
SP3 : Ba	4,4'-dipyridyl	1 : 1 : 2	DMF:MeOH:H <sub>2</sub> O (1 : 0.5 : 0.5)	0.5	65	amorphous + crystalline
SP3 : Ba	4,4'-dipyridyl	1 : 1 : 4	DMF:MeOH:H <sub>2</sub> O (1 : 0.5 : 0.5)	0.5	65	amorphous + crystalline
SP3 : Ba	4,4'-dipyridyl	2 : 1 : 2	DMF:MeOH:H <sub>2</sub> O (1 : 0.5 : 0.5)	0.5	65	amorphous + crystalline
SP3 : Ba	4,4'-dipyridyl	2 : 1 : 4	DMF:MeOH:H <sub>2</sub> O (1 : 0.5 : 0.5)	0.5	65	amorphous + crystalline
SP3 : Ca	4,4'-dipyridyl	1 : 1 : 4	DMF:MeOH:H <sub>2</sub> O (1 : 0.5 : 0.5)	2	65	amorphous
SP3 : Ca	4,4'-dipyridyl	1 : 1 : 4	DMF:MeOH:H <sub>2</sub> O (1 : 0.5 : 0.5)	3	65	amorphous
SP3 : Ca	4,4'-dipyridyl	1 : 1 : 4	DMF:MeOH:H <sub>2</sub> O (1 : 0.5 : 0.5)	2	85	amorphous
SP3 : Ca	4,4'-dipyridyl	1 : 1 : 4	DMF:MeOH:H <sub>2</sub> O (1 : 0.5 : 0.5)	3	85	amorphous
SP3 : Sr	4,4'-dipyridyl	1 : 1 : 4	DMF:MeOH:H <sub>2</sub> O (1 : 0.5 : 0.5)	2	65	crystalline
SP3 : Sr	4,4'-dipyridyl	1 : 1 : 4	DMF:MeOH:H <sub>2</sub> O (1 : 0.5 : 0.5)	3	65	amorphous
SP3 : Sr	4,4'-dipyridyl	1 : 1 : 4	DMF:MeOH:H <sub>2</sub> O (1 : 0.5 : 0.5)	2	85	amorphous
SP3 : Sr	4,4'-dipyridyl	1 : 1 : 4	DMF:MeOH:H <sub>2</sub> O (1 : 0.5 : 0.5)	3	85	amorphous
<b>SP3 : Cu</b>	<b>4,4'-dipyridyl</b>	<b>1 : 1 : 4</b>	<b>DMF:MeOH:H<sub>2</sub>O (1 : 0.5 : 0.5)</b>	<b>2</b>	<b>65</b>	<b>Crystalline</b>
SP3 : Cu	4,4'-dipyridyl	1 : 1 : 4	DMF:MeOH:H <sub>2</sub> O (1 : 0.5 : 0.5)	2	65	Crystalline

SP3 : Cu	4,4'-dipyridyl	1 : 1 : 4	DMF:MeOH:H <sub>2</sub> O (1 : 0.5 : 0.5)	2		65	amorphous
SP3 : Zr	4,4'-dipyridyl	1 : 1 : 4	DMF:MeOH:H <sub>2</sub> O (1 : 0.5 : 0.5)	2		65	amorphous
SP3 : Mn	4,4'-dipyridyl	1 : 1 : 4	DMF:MeOH:H <sub>2</sub> O (1 : 0.5 : 0.5)	2		65	No solid
SP3 : Sc	4,4'-dipyridyl	1 : 1 : 4	DMF:MeOH:H <sub>2</sub> O (1 : 0.5 : 0.5)	2		65	Amorphous
SP3 : Sc	4,4'-dipyridyl	1 : 1 : 4	DMF:MeOH:H <sub>2</sub> O (1 : 0.5 : 0.5)	2		65	amorphous
SP3 : Mg	4,4'-dipyridyl	1 : 1 : 4	DMF:MeOH:H <sub>2</sub> O (1 : 0.5 : 0.5)	2		100	No solid
SP3 : Ca	4,4'-dipyridyl	1 : 1 : 4	DMF:MeOH:H <sub>2</sub> O (1 : 0.5 : 0.5)	2		100	No solid
SP3 : Sr	4,4'-dipyridyl	1 : 1 : 4	DMF:MeOH:H <sub>2</sub> O (1 : 0.5 : 0.5)	2		100	No solid
SP3 : Ba	4,4'-dipyridyl	1 : 1 : 4	DMF:MeOH:H <sub>2</sub> O (1 : 0.5 : 0.5)	2		100	No solid
SP3 : Mg	4,4'-dipyridyl	1 : 1 : 4	DMF:MeOH:H <sub>2</sub> O (1 : 0.5 : 0.5)	1		65	No solid
SP3 : Ca	4,4'-dipyridyl	1 : 1 : 4	DMF:MeOH:H <sub>2</sub> O (1 : 0.5 : 0.5)	1		65	No solid
SP3 : Ca	4,4'-dipyridyl	1 : 1 : 4	DMF:MeOH:H <sub>2</sub> O (1 : 0.5 : 0.5)	1		65	amorphous
SP3 : Sr	4,4'-dipyridyl	1 : 1 : 4	DMF:MeOH:H <sub>2</sub> O (1 : 0.5 : 0.5)	1		65	amorphous
SP3 : Ba	4,4'-dipyridyl	1 : 1 : 4	DMF:MeOH:H <sub>2</sub> O (1 : 0.5 : 0.5)	1		65	amorphous
SP3 : Ca	4,4'-dipyridyl	1 : 1 : 4	DMF:MeOH:H <sub>2</sub> O (1 : 0.5 : 0.5)	3	HCl	65	No solid
SP3 : Ca	4,4'-dipyridyl	1 : 1 : 4	DMF:MeOH:H <sub>2</sub> O (1 : 0.5 : 0.5)	3	HNO <sub>3</sub>	65	No solid
SP3 : Ca	4,4'-dipyridyl	1 : 1 : 4	DMF:MeOH:H <sub>2</sub> O (1 : 0.5 : 0.5)	3	acetic acid	65	No solid
SP3 : Ca	4,4'-dipyridyl	1 : 1 : 4	DMF:MeOH:H <sub>2</sub> O (1 : 0.5 : 0.5)	3	formic acid	65	No solid
SP3 : Sr	4,4'-dipyridyl	1 : 1 : 4	DMF:MeOH:H <sub>2</sub> O (1 : 0.5 : 0.5)	3	HCl	65	amorphous
SP3 : Sr	4,4'-dipyridyl	1 : 1 : 4	DMF:MeOH:H <sub>2</sub> O (1 : 0.5 : 0.5)	3	HNO <sub>3</sub>	65	amorphous
SP3 : Sr	4,4'-dipyridyl	1 : 1 : 4	DMF:MeOH:H <sub>2</sub> O (1 : 0.5 : 0.5)	3	acetic acid	65	amorphous
SP3 : Sr	4,4'-dipyridyl	1 : 1 : 4	DMF:MeOH:H <sub>2</sub> O (1 : 0.5 : 0.5)	3	formic acid	65	No solid
SP3 : Cu	4,4'-dipyridyl	1 : 1 : 4	DMF:MeOH:H <sub>2</sub> O (1 : 0.5 : 0.5)	3	HCl	65	amorphous + crystalline

SP3 : Cu	4,4'-dipyridyl	1 : 1 : 4	DMF:MeOH:H <sub>2</sub> O (1 : 0.5 : 0.5)	3	HNO <sub>3</sub>	65	amorphous + crystalline
SP3 : Cu	4,4'-dipyridyl	1 : 1 : 4	DMF:MeOH:H <sub>2</sub> O (1 : 0.5 : 0.5)	3	acetic acid	65	Crystalline
SP3 : Zn	4,4'-dipyridyl	1 : 1 : 4	DMF:MeOH:H <sub>2</sub> O (1 : 0.5 : 0.5)	0.5		65	amorphous
SP3 : Zn	4,4'-dipyridyl	1 : 1 : 4	DMF:MeOH:H <sub>2</sub> O (1 : 0.5 : 0.5)	1		65	amorphous + crystalline
SP3 : Zn	4,4'-dipyridyl	1 : 1 : 4	DMF:MeOH:H <sub>2</sub> O (1 : 0.5 : 0.5)	2		65	amorphous
SP3 : Zn	4,4'-dipyridyl	1 : 1 : 4	DMF:MeOH:H <sub>2</sub> O (1 : 0.5 : 0.5)	2.5		65	amorphous + crystalline
SP3 : Zn	4,4'-dipyridyl	1 : 1 : 4	DMF : EtOH (1 : 1)	2		65	amorphous
SP3 : Zn	4,4'-dipyridyl	1 : 1 : 4	DMF:EtOH:H <sub>2</sub> O (1 : 0.5 : 0.5)	2		65	amorphous
SP3 : Zn	4,4'-dipyridyl	1 : 1 : 4	DMF : DMSO/ H <sub>2</sub> O (1 : 0.5 : 0.5)	2		65	amorphous
SP3 : Zn	4,4'-dipyridyl	1 : 1 : 4	DMF:H <sub>2</sub> O (1 : 1)	2		65	amorphous
<b>SP3 : Zn</b>	<b>4,4'-dipyridyl</b>	<b>1 : 1 : 4</b>	<b>DMF:H<sub>2</sub>O (1 : 1)</b>	<b>1</b>		<b>65</b>	<b>crystalline</b>
SP3 : Zn	4,4'-dipyridyl	1 : 1 : 4	DMF : EtOH (1 : 1)	1		65	amorphous
SP3 : Zn	4,4'-dipyridyl	1 : 1 : 4	DMF : MeOH (1:1)	1		65	no solid
SP3 : Zn	4,4'-dipyridyl	1 : 1 : 4	DMF : MeOH (1:1)	2		65	no solid
<b>SP3 : Mg</b>	<b>4,4'-dipyridyl</b>	<b>1 : 1.5 : 8</b>	<b>DMF</b>	<b>2.5</b>	<b>HCl</b>	<b>80</b>	<b>crystalline</b>
SP3 : Ca	4,4'-dipyridyl	1 : 1.5 : 8	DMF	2.5	HCl	80	amorphous
SP3 : Sr	4,4'-dipyridyl	1 : 1.5 : 8	DMF	2.5	HCl	80	amorphous
<b>SP3 : Ba</b>	<b>4,4'-dipyridyl</b>	<b>1 : 1.5 : 8</b>	<b>DMF</b>	<b>2.5</b>	<b>HCl</b>	<b>80</b>	<b>crystalline</b>
SP3 : Mn	4,4'-dipyridyl	1 : 1.5 : 8	DMF	2.5	HCl	80	amorphous + crystalline
SP3 : Cu	4,4'-dipyridyl	1 : 1.5 : 8	DMF	2.5	HCl	80	amorphous
SP3 : Zn	4,4'-dipyridyl	1 : 1.5 : 8	DMF	2.5	HCl	80	amorphous
SP3 : Al	Piperazine	1 : 7 : 5	H <sub>2</sub> O	10	HNO <sub>3</sub>	210	amorphous + crystalline

**Table A.10** Calculation of SP, MCH<sup>+</sup> and MC ratios at 65 °C from UV-vis absorption data.

Vial	Metal	Outcome	A <sub>SP</sub>	A <sub>MCH<sup>+</sup></sub>	A <sub>MC</sub>	SP/MC	MCH <sup>+</sup> /MC	SP/MCH <sup>+</sup>
1	Mg	3	3.88384	0.04834	0.00365	1064.0658	13.2438	80.3442
	Ca	2						
	Cu	2						
	Zn	2						
2	Mg	3	3.57006	0.18334	0.02453	145.5385	7.47411	19.4723
	Ca	3						
	Cu	2						
	Zn	1						
3	Mg	3	3.09077	0.43455	0.00374	826.4091	116.1898	7.11258
	Ca	3						
	Cu	1						
	Zn	1						
4	Ca	1	2.7836	1.69791	0.01315	211.6806	129.1186	1.63943
	Cu	1						
	Zn	1						
5	Mg	2	3.1193	0.00581	0.0117	266.6068	0.4966	536.8847
	Sr	3						
	Ca	3						
	Mg	1						
6	Sr	3	3.04094	0.01366	0.02214	137.3505	0.6170	222.6164
	Ba	3						
7	Ca	1	3.02361	0.00951	0.01339	225.8111	0.7102	317.9401
	Sr	3						
	Mg	1						
	Cu	2						
	Zn	2						
8	Sr	3	3.05598	0.0129	0.02155	141.8088	0.5986	236.8977
	Ca	3						
	Mg	2						
9	Sr	3	3.37391	0.02105	0.03899	86.53270	0.5399	160.2808
10	Mg	1	3.57695	0.00173	0.0115	311.0391	0.150435	2067.6011
	Ca	1						
	Sr	1						
	Ba	1						
11	Ca	1	3.40751	0.00759	0.00974	349.8470	0.7793	448.9473
	Mg	1						
	Mg	3						
	Mg	2						

Vial	Metal	Outcome	ASP	AMCH+	AMC	SP/MC	MCH <sup>+</sup> /MC	SP/MCH <sup>+</sup>
12	Mg	1	4.29041	0.01562	0.09712	44.1764	0.1608	274.6741
	Ca	1						
	Ca	2						
	Sr	3						
	Ba	2						
	Zn	1						
13	Ca	2	1.41571	0.03553	0.02514	56.3130	1.41329	39.8455
	Sr	2						
14	Ca	1	1.34139	0.3622	0.00764	175.5746	47.4084	3.7035
	Sr	2						
	Cu	3						
15	Ca	1	1.28538	0.29031	0.00784	163.9515	37.0293	4.4276
	Sr	2						
	Cu	3						
16	Ca	1	1.42345	0.04665	0.02779	51.2217	1.6787	30.5134
	Sr	2						
	Cu	4						
17	Ca	1	1.46369	0.17428	0.01869	78.3141	9.3248	8.3985
	Sr	1						
18	Sr	4	2.89628	0.01763	0.03106	93.2479	0.5676	164.2813
	Ca	2						
	Mg	1						
	Ba	2						
	Zn	3						
19	Zn	3	1.19707	0.00825	0.00628	190.6162	1.3137	145.0994
20	Mg	4	3.56935	0.23996	0.02495	143.0601	9.6176	14.8748
	Ca	2						
	Sr	2						
	Ba	4						
	Zn	2						
	Cu	2						
	Mn	3						